Fall 2019

Thermomechanical analysis of rock asperity in fractures of enhanced geothermal systems

Chao Zeng

Department: Civil, Architectural and Environmental Engineering

THERMOMECHANICAL ANALYSIS OF ROCK ASPERITY IN FRACTURES OF ENHANCED GEOTHERMAL SYSTEMS

by

CHAO ZENG

A DISSERTATION

Presented to the Faculty of the Graduate School of the

MISSOURI UNIVERSITY OF SCIENCE AND TECHNOLOGY

In Partial Fulfillment of the Requirements for the Degree

DOCTOR OF PHILOSOPHY

in

CIVIL ENGINEERING

2019

Approved by:

Dr. Wen Deng, Advisor
Dr. Xiong Zhang
Dr. Matt Insall
Dr. Baojun Bai
Dr. Andreas Eckert

ABSTRACT

Enhanced Geothermal Systems (EGS) offer great potential for dramatically expanding the use of geothermal energy and become a promising supplement for fossil energy. The EGS is to extract heat by creating a subsurface system to which cold water can be added through injection wells. Injected water is heated by contact with rock and returns to the surface through production well. Fracture provides the primary conduit for fluid flow and heat transfer in natural rock. Fracture is propped by fracture roughness with varying heights which is called asperity. The stability of asperity determines fracture aperture and hence imposes substantial effect on hydraulic conductivity and heat transfer efficiency in EGS.

Firstly, two rough fracture surfaces are characterized by statistical method and fractal analysis. The asperity heights and enclosed aperture heights are described by probability density function before cold water is pumped into fracture. Secondly, when water injection and induced cooling occurs, the thermomechanical analysis of single asperity is studied by establishing an un-symmetric damage mechanics model. The deformation curve of asperity under thermal stress is determined. Thirdly, deformation of fracture with various asperities on it in response to thermal stress is analyzed by a new stratified continuum percolation model. This model incorporates the fracture surface characteristics and preceding deformation curve of asperity. The fracture closure and fracture stiffness can be accurately quantified by this model. In addition, the scaling invariance and multifractal parameters in this process are identified and validated with Monte Carlo simulation.

ACKNOWLEDGMENTS

PhD study is a short time from the length of life but it has imposed significant impact on my thought, attitudes and values.

I would like to express my deepest appreciation to my advisor, Dr. Wen Deng. He gave me the chance to work with him and the freedom to select my favorite topics about four year ago. I would like to thank my committee member, Dr. Xiong Zhang. His inspiration and assistance enlightened me greatly. The most impressive in my mind is his own experience on how to dig into a new area. A thank you to Dr. Matt Insall, an expert from mathematical department. Sincere thanks to Dr. Baojun Bai. Lastly, thanks Dr. Andreas Eckert for being my committee member. Besides my committee, Dr. Chenglin Wu is also appreciated sincerely for his training and leading me into the mechanics world.

I also take this opportunity to record my sincere thanks to all the colleagues in the same office: Dr. Chuang Lin, Xiaolong Xia, Dr. Junnan Cao, Dr. Kerry, Dr. Ruichang Guo, Elieh, Javad, Beshoy, Sara, Mehrad, and other friends in other department: Yandong, Dustin, and Xinzhe Yuan.

In the spiritual aspect, I am grateful to almighty God for his love and mercy. In his family, I know a lot of lovely people: Dr. Mingzhen Wei, Dr. Binqi Zhang, Dr. Jinwei Zhang, Dr. Xin Li, and Lan Li etc. In addition, Ross and Sheri, Tom and Helen also taught me to how to find truth and to appreciate our creator.

Finally, thanks my parents, younger sister, and my girlfriend.

TABLE OF CONTENTS

Page

LIST OF ILLUSTRATIONS

Page

LIST OF TABLES

Page

1. INTRODUCTION

1.1. ENHANCED GEOTHERMAL SYSTEMS

A naturally occurring geothermal system, known as a hydrothermal system, is defined by three key elements: heat, fluid, and permeability at depth. Heat the extracted resource from subsurface, fluid the delivery material and permeability provides the pathway for fluid flow. Most hydrothermal system is close to volcanic region where the hot magma is close to the surface. Therefore, hydrothermal system tends to be distributed along the Earth's plate boundaries, although they may also be found at intra-plate locations. Its usage started more than one thousand year ago, such as cooking food, shower etc. The disadvantage of this system is confined to limited locations. Most areas are infeasible for hydrothermal exploitation. The enhanced geothermal system, also called engineered hydrothermal system, is created to expand usage of hydrothermal resources. An enhanced geothermal system (EGS) is a man-made reservoir, created where there is hot rock but insufficient or little natural permeability or fluid saturation. In an EGS, fluid is injected into the subsurface under carefully controlled conditions, which causes pre-existing natural fracture to reopen, creating permeability.

Most EGS rock is granite for its high heat capacity and low permeability. In geological aspect, geothermal resources comes from igneous intrusion in the upper crust. Granite, as an igneous rock, is a desirable rock in EGS. Besides that, it requires low permeability because the heat in the rock can be maintained, not quickly dissipated. That is why it is also called hot dry rock. According to the estimates of Muffler [1], a cubic kilometer of granitic magma at 800ºC contains 3×1018 J of heat, which is equivalent to

the heat content of 480 million barrels of crude oil. After intrusion in the crust, magma loses heat through conduction and convection. When the permeability of the host rock and the intrusion are low, a hot dry rock geothermal resource is developed. This impinges technical problem on geothermal exploitation. How to extract heat from low permeability rock can be tackled by technology in oil and gas industry. For brittle granite, natural fracture is widely distributed in the rock mass due to tectonic stress near the plate boundary.

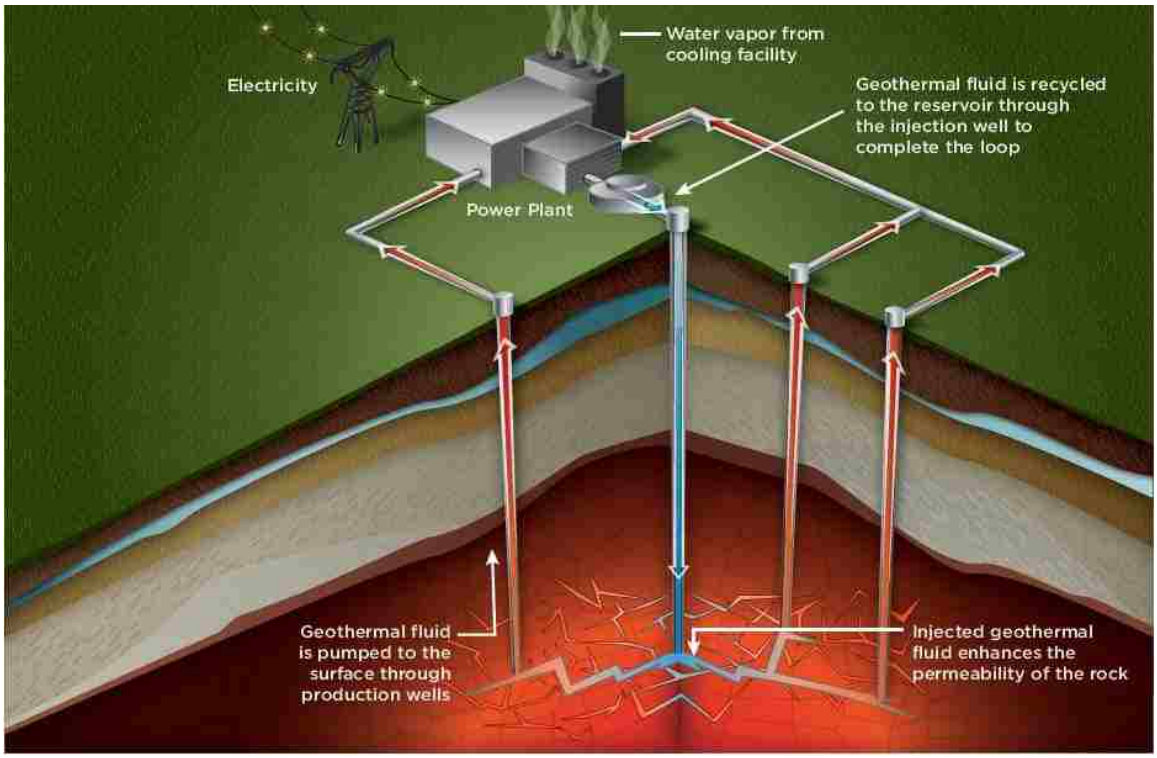

Figure 1.1 An Illustration of Enhanced Geothermal Systems.

By controlling the pump rate of fluid, natural fracture can be reopened. Because they are sheared induced fracture, not tensile fracture. Natural fracture network provides

the main conduit for fluid circulation throughout the now-fractured rock and to transport heat to the surface where electricity can be generated. The sketch of enhanced geothermal system is shown in Figure 1.1, which is from department of energy report in 2012.

Drill and injection wells are constructed into the hot rock reservoir with low permeability. Then, cold water is injected at sufficient pressure to reopen natural fracture and create fracture network. Continue operation until there is enough fractured volume to create a reservoir. The hot water is pumped to plant and recycled for next injection. It shows that fracture plays pivotal role in the heat extraction and fluid circulation. Water mainly flows in fracture, the fracture aperture determines the hydraulic transmissivity and heat transfer rate.

Fracture is propped by discrete roughness on fracture surface. In subsurface, the fracture is stable and can sustain high in situ stress. However, this stability would break down due to cooling effect. When cold water is pumped into fracture, the cooling occurs between cold water and hot rock. Significant thermal stress is induced in this cooling process, therefore propping asperities would undergo thermomechanical process. The essential difference between expansion of fracture aperture and shrinkage of fracture aperture is determined by the cooling rate. If the cooling is rapid, only the small region near the surface is subjected to thermal stress while the in situ stress loads on the asperities. In this circumstance, the asperities deform and even break. Because the fracture aperture is of particular importance on the fluid circulation and heat conduction, the deformation of asperity is the key point to analyze variation of fracture aperture. The fracture aperture variation by this destructive deformation of asperity is briefly discussed in this dissertation and further elaboration will be worked on recently.

1.2. OVERVIEW

Luo et al. [2] conducted laboratory hydrothermal experiments on artificially fractured granite sample. The “area ratio” is termed to define the roughness of fracture surface. With increase of area ratio, larger fracture aperture and higher hydraulic conductivity can be resulted. In addition, the fracture aperture decreases with increasing rock temperature owing to thermal expansion effects. A perfect exponential relationship between rock temperature and fracture aperture also found.

Isaka et al. [3]conducted uniaxial compression test on granite subjected to pre-heating to heigh temperature and then undergoing slow cooling and rapid cooling. The mechanical properties deteriorate much seriously under rapid cooling than slow cooling. Micro-cracks are created in granite under rapid cooling. This irreversible thermal shock demonstrates the damage of granite under rapid cooling. This can be applied to enhanced geothermal system and nuclear waste disposal. The thermal deterioration and damage are also observed by cyclic heating and cooling with circulating water by Zhu et al. [4].

McDermott and Kolditz [5] came up with a geomechanical model for fracture deformation under hydraulic, mechanical and thermal loads. The deformation of surrounding rock and asperity use theory of elasticity in one unit of fracture void space. This small model was then extended to fracture scale by fractal analysis.

Tran [6] analyzed thermally-induced secondary cracks on existing fracture surface by cooling effect. The subsequent change of fracture aperture and its effect on hydraulic flow is also discussed. The critical condition for secondary crack initiation is the temperature difference between injection fluid and hot rock. In the understanding of thermal fracture creation, several authors made great endeavor. For example, Chen and

Marovelli [7] conducted an experiment to analyze thermal stress in a rock disk subjected to an external thermal shock by cold water. Perkins and Gonzalez [8] as well as Kocabas [9] proposed analytical models to investigate the state of stresses induced by cold fluid injection. Ghassemi et al. [10] developed an integral equation to calculate thermally induced stresses associated with the cooling of a planar fracture in a hot rock.

It presents that granite is susceptible to rapid cooling effect and is likely to result in micro-cracks. Most research focus on solid granite without fracture. In the context of geothermal system, the asperity on fracture surface is likely to deform and even damage under severe cooling. The objective of this study is to analyze the thermomechanical analysis of fracture asperity in response to rapid cooling effect and its macroscopic characterization.

1.3. DISSERTATION ORGANIZATION

This dissertation is composed of nine sections, as follows:

Section 1: The engineering background of this research is introduced. The prerequisite for geothermal exploitation is hot and dry granite. Fracture is indispensable to provide conduit for fluid circulation and heat conduction. Asperities on fracture surface is of particular significance to open fracture. The stability of asperity entails quantitative analysis.

Section 2: To know fracture deformation under thermal shock, rough fracture surface requires characterization. Probability density function and spectral density function are used to characterize asperity height and spatial distribution. The correlation

length and fractal properties are determined by spectral analysis and fractal analysis. This work is based on the smooth transition zone study by Oglvie et al. [11].

Section 3: The two-dimensional fractal analysis in Section 2 is not accurate to characterize heterogeneity and cluster distribution of asperities. However, these features affect void space and thus fluid circulation. Therefore, to incorporate these feature in the analysis method, multifractal based hierarchical cascade is employed. Besides these features, the critical percolating threshold and fractal dimension of percolating cluster can also be determined. In this sense, both the mechanical features and hydraulic features are combined in this model. This statistical model is based on the stratified percolation model by Nolte et al.[12] .

Section 4: After characterization of fracture surface and aperture in preceding sections, fracture deformation in response to stress is analyzed. In fracture deformation, three key components should be considered: asperity deformation, mechanical interaction of asperities and deformation of surrounding rock. They are analyzed in different sections in this section. Their effect on fracture closure is discussed. This analysis is based on the joint deformation model by Hopkins[13].

Section 5: Asperity deformation by stress loading is analyzed in this section. Most research assumed elastic deformation of asperity and attribute nonlinear stress-displacement property to increasing contact areas as fracture deforms. However, asperity damage at the tip is considered as another resource of nonlinearity. Damage mechanics constitutive model is established to characterize asperity deformation in both mechanical and thermomechanical circumstances. The deformation curve of asperity deformation is obtained in this section.

Section 6: As a porous rock, asperity deformation should consider the effect of porosity distribution. The porosity effect on the reduction of mechanical property and crack initiation is analyzed.

Section 7: With large temperature difference, damage occurs at the connect circle between hemispherical asperity and surrounding rock. This crack initiation and propagation in respect to thermal stress and overburden loading are quantified. Fracture mechanics analysis is employed in this section.

Section 8: In analysis of fracture deformation, most research assume elastic deformation of cylindrical asperity. However, asperity is irregular and more like hemisphere. In hemispherical geometry is used, too large stress on tip of asperity should be tackled. The hemispherical asperity with damage can resolve this problem. Therefore, comparison of fracture deformation under cylindrical asperity and hemispherical asperity is conducted to know the possible difference induced by simplistic asperity geometry.

Section 9: The conclusion is drawn on this study and future work to extend this study is presented.

2. FRACTURE TOPOGRAPHY

2.1. INTRODUCTION TO FRACTURE TOPOGRAPHY

There is increasing awareness of the great effect fractures have on the mechanical and transport properties of rocks in enhanced geothermal systems. The fracture in granite may range in scale from extremely small microcracks, with a characteristic length scale small than the grain size of the rock, up to large fault systems in high tectonic stress area. The mechanical properties of rocks, described by their bulk elastic constants and shear strength, are known to be strongly dependent upon the presence and geometrical properties of fractures [14, 15]. Microscopic models of two contacting rough surfaces have been used to derive the elastic properties of single fracture including both normal and shear stiffness [16, 17], and to predict friction, wear, and the stability of shear behavior in rock joints. In all these models, a controlling influence is exercised by the aperture of the two interacting surfaces. The shape, size, and number of asperity contacts and the local slope of the surfaces are particularly important parameters in such models.

The fracture is propped by rough asperities with various height distribution. The asperities serve as obstacles in the flow channels. The fluid flows around the asperities. Fluid channeling is the result of asperities distribution in the fracture surface. In addition, the mechanical properties of fracture in response to normal and shear loading also dependents the distribution of asperities in the surface. Under the stress loading, the real contact area only accounts less than 50% of the nominal contact area in the fracture surface. The various asperity heights cause the different extent of matching of two surfaces which influence the stiffness and modulus of rock mass. Therefore, it is

important for us to study the way the geometry of fracture surface affect the mechanical, hydraulic properties of the fractured rock mass.

The numerical simulation has been widely accepted to study these properties in fracture due to the scarcity of rock samples on some conditions and cumbersome to obtain the sample with specified properties. As the first step, the accurate simulation entails the approximation of the natural fracture. Due to the effect of asperities or roughness on the mechanical and hydraulic properties of fractured rock mass, the detailed features of fracture surface should be maintained in the synthetic fractures. Several different methods have been used in the creation of numerical synthetic fracture. Amadei and Illangsekare [18] created synthetic fractures with unmatched fractal surface to study flow and solute transport in fracture. Brown [19] differentiated the long wavelength and short wavelength differently to create synthetic fractures. That is, the two fracture surfaces have perfect matching at short wavelength and becomes independent at long wavelength. This characteristics of fracture surface is also observed in natural rock fractures[20]. Glover et al. [21] improved that method and smoothed the transition length between matching and independence of two fracture surfaces. Pyrak-Nolte and Morris [22] used the stratified percolation theory to construct fractal aperture without explicit representation of fracture surfaces. In all these approaches, the one with good comparison to the natural fracture is preferable. Even though the fractal feature of fracture surface is incorporated in some synthetic fracture models, waviness and unevenness of fracture surface are neglected. The more accurate synthetic fracture is necessary to obtain more reliable results in the following analysis. Therefore, the model from Glover et al [21] will be constructed step by step in this section.

In this section, I will briefly describe the mathematical foundation of the geometrical parameters that describe fractures with rough surface. Then, the numerical techniques to create fracture is elaborated. The properties of fracture surface are analyzed based on synthetic fractures surfaces. Finally, the key parameters are stressed for analysis in the following section.

2.2. MATHEMATICAL DESCRIPTION OF FRACTURE SURFACES

The mathematical description of rough fractures is well reviewed in books[23, 24]. The key parameters to create the numerical synthetic fracture will be emphasized in this section. That is, the step-by-step procedure to generate the numerical fracture from profiling data is of main interest in this section. Firstly, the mathematical functions to define the fracture and aperture are classified. Then, the specific parameters in these functions are listed.

2.2.1. Mathematical Functions. It is best to begin with a definition of a fractal fracture in rock. By fractal fracture, we mean a fracture occupying three dimensional space with two surfaces, each with a fractal dimension between 2 and 3. In general, a statistical description of either of the surfaces that goes to make the fractal fracture is given by specifying two basic functions: (1) the probability density function for heights and (2) the power density spectrum. The probability density function describes the distribution of the surface heights about the mean value without regard to the horizontal spatial position, and the power density spectrum describes the texture or spatial correlation of heights on the surface. When the surface heights have a Gaussian (normal) distribution, then the 2-D surface texture is described accurately by a combination of the

mean and standard deviation of the Gaussian distribution and the form of the power density spectrum. Natural fractures often have Gaussian heights [15]. However, if the height distribution were more complicated, then a complete description of 2-D structure would require more information.

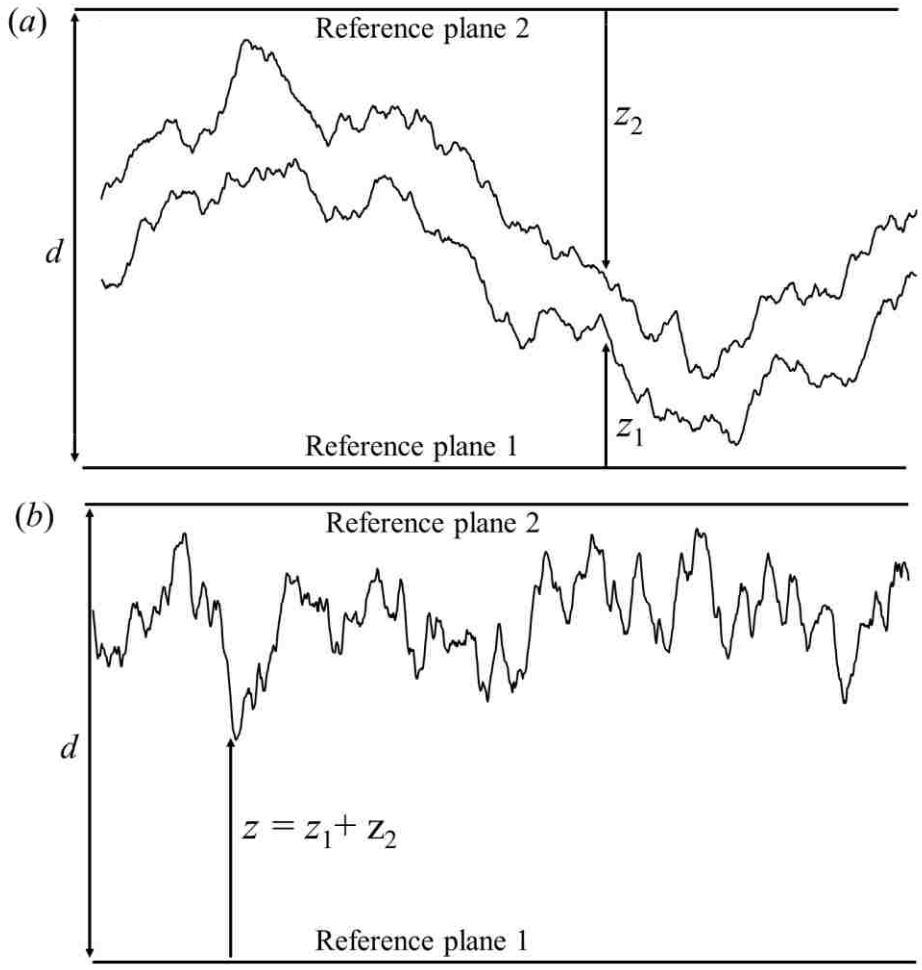

Figure 2.1 Illustration of Composite Topography of Fracture Surface. (a) Schematic cross section through a joint. The surface heights are measured from parallel reference planes fixed in each surface. (b) The "composite topography" of a joint is defined by summing the heights of both surfaces at each point along the joint. The aperture is the distance between "composite topography" and reference plane 2 in (b).

Before going to introduction of probability density function and power spectrum, the aperture between two rough surfaces has to be elaborated. Because the fracture surface is rough, the aperture between two rough surfaces is intractable to define. Therefore, the concept of "composite topography" introduced by Brown and Scholz [25] is used to quantify the aperture. The schematic of "composite topography" is shown in Figure 2.1(b). The distance between "composite topography" and reference 2 is the aperture. If we do not consider the closure of fracture, the distance between two reference planes d is constant, thus the aperture topography can be described by the "composite topography".

2.2.1.1. Probability density function. From standard statistics, the probability is defined as the ratio of the number of elements of a set conforming to a particular condition to the total number of elements. The probability function $P(z)$ is defined in the following manner. The $P(z)$ associated with the surface height z, is defined as the fraction of the surface having height $\leq z$. The $P(z)$ is the integral of the probability density function:

$$P(z) = \int_{-\infty}^{z} p(x)\,dx \tag{2.1}$$

The probability density function is therefore the derivative of the probability function, i.e.

$$p(z) = \frac{dP(z)}{dz} \tag{2.2}$$

The relation of $p(z)$ and $P(z)$ is shown in Figure 2.2.

2.2.1.2. Power spectrum. The power spectral density is the Fourier transform of the autocorrelation function. Thus, they are equivalent descriptions of the same aspect of

surface texture. The power spectrum is computed by breaking the surface profile into a sum of sinusoidal components, each with its own wavelength, amplitude, and phase (see Figure 2.3). The squared amplitude of each component is referred to as its power, and the graph with relation of power to inverse of wavelength is power spectrum. The power spectrum normalized in a particular way is known as the power spectral density. The power spectral density $G(k)$ has a power law relation with inverse of wavelength k:

$$G(k) = Ck^{-\alpha} \tag{2.3}$$

where C is the proportionality constant; α is the power spectrum exponent.

Power spectral density $G(k)$ provides a useful description of the surface roughness if one considers the spectral moments. The moments of the power spectral density function are defined as:

$$m_n = \int_{k_n}^{\infty} k^n G(k)\, dk \tag{2.4}$$

where m_n is the nth moment and $k_0 = 2\pi/\lambda_0$ at $n = 0$. m_0 is the variance of heights on the profile, m_2 is the variance of slopes [26], and m_4 is the variance of curvatures, also named kurtosis in rigorous mathematical definition.

In summary, once the probability density function for heights and the autocorrelation function for a surface are known, then a complete description of the roughness and an individual surface is obtained.

2.2.2. Detailed Fracture Parameters. To implement the probability density function of asperity height and power density spectrum practically, the specific fracture parameters are required to create synthetic fracture. Fractal fracture is composed of two fracture surface. Intuitively, the fracture parameters are classified into those associated

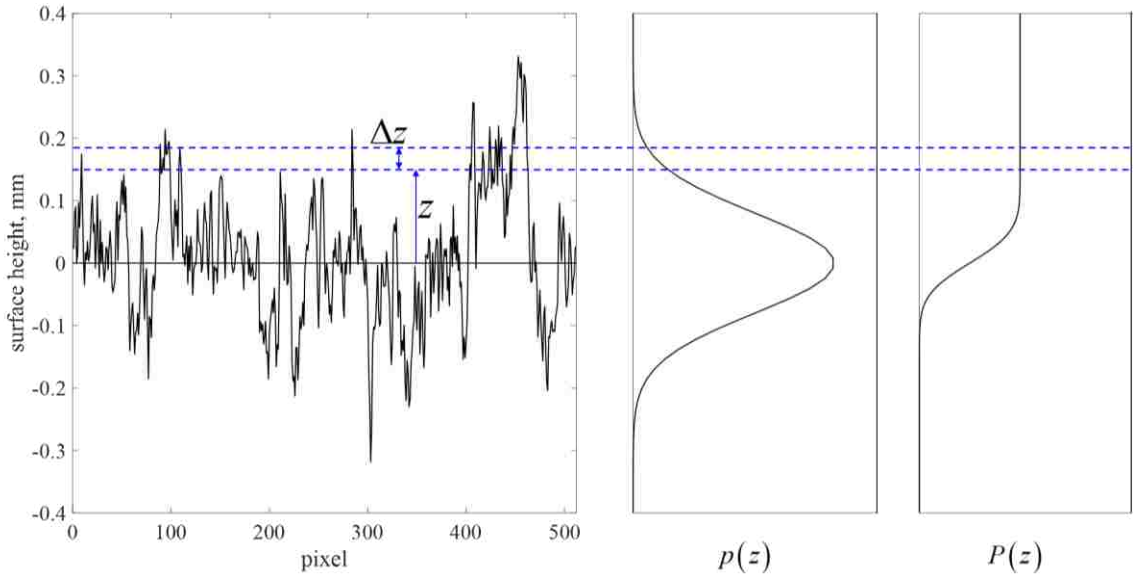

Figure 2.2 Illustration of the Probability Function for Surface Height. The height of the surface above the mean level is *z*. The probability density function $p(z)$ is approximately the fraction of the surface in the range of z and $z+\Delta z$. The cumulative probability function is the integral of $p(z)$ from $-\infty$ to *z*.

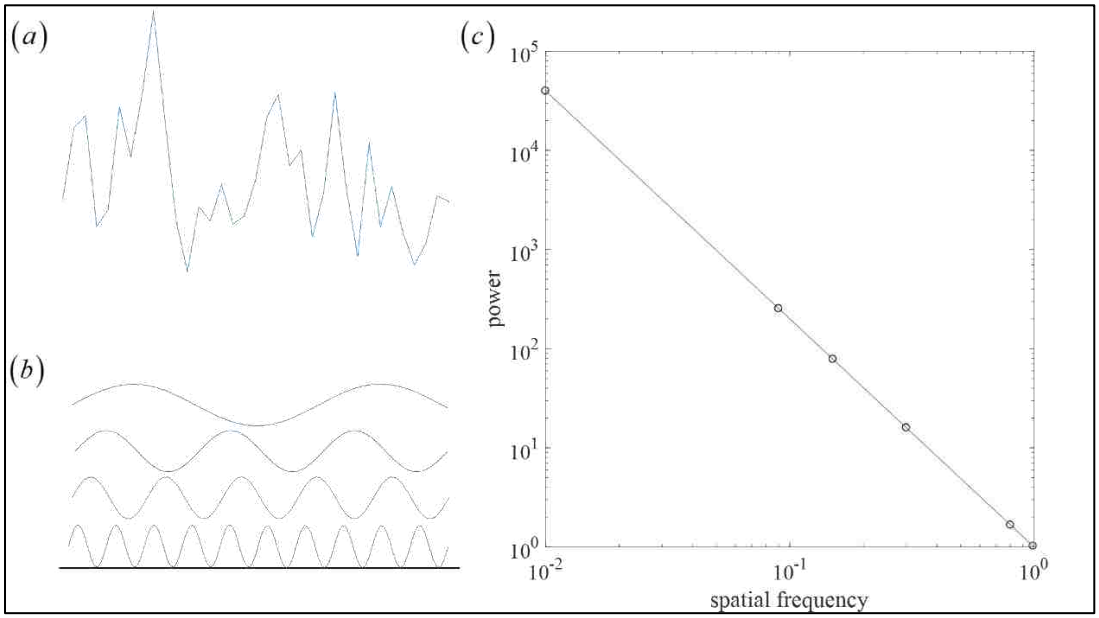

Figure 2.3 Illustration of the Power Spectrum of a Surface Profile. (*a*) Part of irregular fracture surface, (*b*) its sinusoidal components at different frequencies with amplitude A and wavelength λ, and (*c*) the relation of power and spatial frequency 1/λ for all sinusoidal components.

with individual surfaces, those defined for assembly of two surface, and arbitrary parameters. It is worth mentioning that these parameters are directly obtained from experimental testing. However, due to the limited experimental condition, these data are borrowed from literature in this section.

2.2.2.1. Surface parameters. (1) Standard deviation σ_s of asperity heights on each fracture surface. This is a measure of the roughness of the surface asperities.

$$\sigma_s^2 = \frac{1}{N}\sum_{i=1}^{N}\left(y_i - \bar{y}\right)^2 \tag{2.5}$$

Where y_i represents *N* discrete measurements of the heights of the surface, which has a mean value of $\bar{y}$.

(2) The fractal dimension D_f of each fracture surface. This is a measure of the scaling behavior of the surface, and contains information regarding the relative positions of asperities of different size on the surface. This parameter has relation with power exponent α by [19]:

$$D_f = \frac{7-\alpha}{2} \tag{2.6}$$

(3) The anisotropy of fractal dimension of the surface A_s, which allows the surface to have different fractal dimensions in different directions across the surface. In Equation (2.3), the wavenumber k denotes the average in *x* and *y* direction. Therefore, the surface is intrinsically assumed to be isotropic. Whereas the anisotropic surface is often observed in natural fracture, the anisotropy of fractal dimension in *x* and *y* direction has to be accounted.

2.2.2.2. Fracture parameters. (1) The matching parameters. The individual fracture surface follows the power law in Equation (2.3). However, when fit together to create aperture, the matching phenomenon occurs. That is, rough fractures are matched to some degree at long wavelength and relatively unmatched at short wavelength [27, 28]. This phenomenon shows in Figure 2.4. The data of surfaces are from Figure 2.1. Brown [19] came up with mismatch wavelength λ_c to differentiate the matching transition. But the transition point is abrupt. Isakov *et al*. [29] improved this concept with smooth transition between matched and unmatched segments. The difference of these two methods are shown in Figure 2.5 schematically. The matching of two fracture surfaces is defined as *R*. When *R* is 1, it means the two fracture surfaces are the same; when *R* is 0, it means the two fracture surfaces are totally independent. More parameters are introduced by Isokav *et al*. [29] in Figure 2.5(*b*). The second was verified and has better description with the natural rock. In this section, the second model is used to describe the matching fraction of two surfaces. The relations of these parameters in Figure 2.5 (b) are presented.

$$\lambda_{-} = \lambda_c \frac{2\lambda_c + \tau}{2\left(\lambda_c + \tau\right)} \tag{2.7}$$

$$\tau = \lambda_{+} - \lambda_{-} \tag{2.8}$$

where R^{+} and R^{-} are maximum matching fraction and minimum matching fraction to define the degree of matching at long and short wavelength, respectively. λ_{+} and λ_{-} are wavelength at the maximum matching fraction at minimum matching fraction, respectively. τ is the width of transition. All these values require determination from experimental testing.

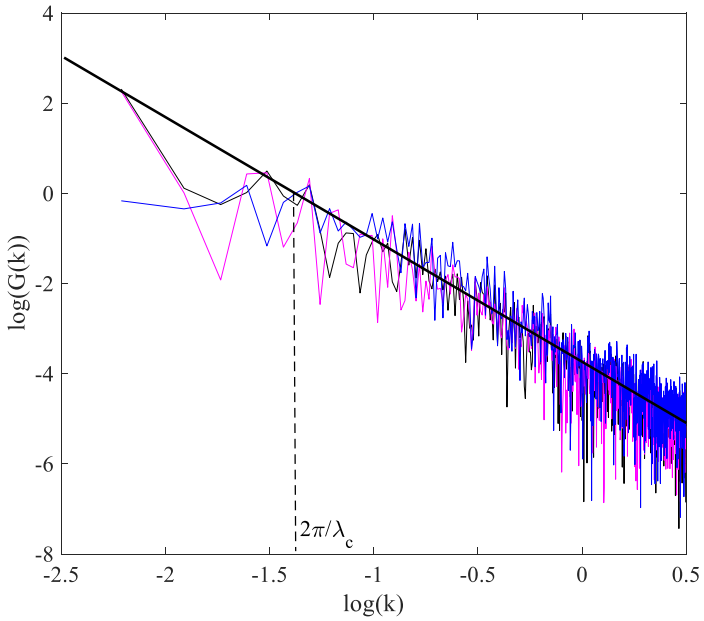

Figure 2.4 The Power Spectra from Two Fracture Surfaces and the Aperture. The black curve stands for top surface, the magenta curve standards for bottom surface, the green curve stands for the aperture. The black line is the average line to indicate the slope of the power spectra. The slope is -3. Wavelength at the mismatch point is λ_c. It shows that mismatch occurs at small wavelength and match well at the long wavelength.

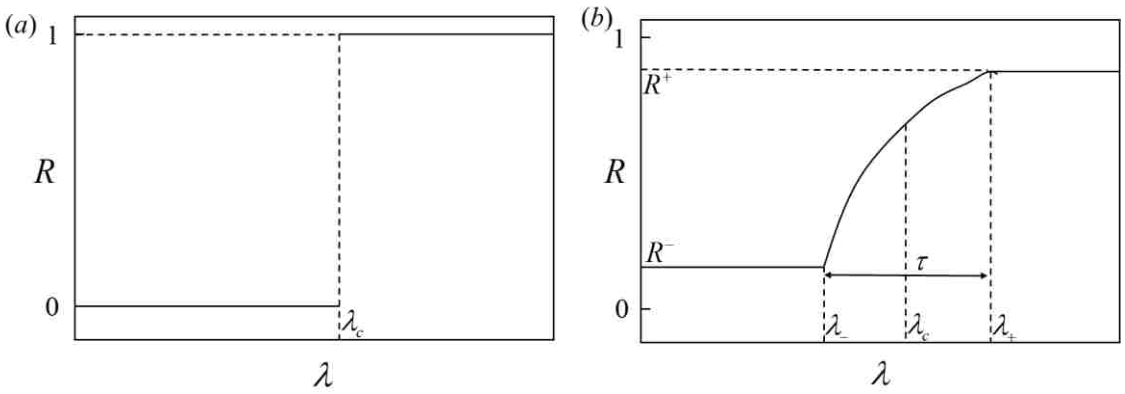

Figure 2.5 Approaches in the Matching of Fracture Surfaces. The horizontal axis is wavelength and the vertical axis is matching of both fracture surface. (a) The abrupt mismatch wavelength λ_c defined by Brown [19], (b) the smooth transition near the mismatch wavelength λ_c defined by Isakov *et al* [29].

(3) Standard deviation of the aperture σ_a. This parameter is a measure of the complexity of the aperture, i.e. the difference between the constriction and wide portions

of the aperture. The relation of σ_a and σ_s is shown in Figure 2.6. The equation for the covariance between two surfaces with mean values $\bar{y}$ and $\bar{z}$ is [30]:

$$C_{yz} = \frac{1}{N}\sum_{i=1}^{N}\left(y_i - \bar{y}\right)\left(z_i - \bar{z}\right) \tag{2.9}$$

If the surface *y* and *z* are completely uncorrelated, then $C_{yz} = 0$. For two completely correlated surfaces, $C_{yz} = \sigma_y^2 = \sigma_z^2$ since at each point, $y_i - \bar{y} = z_i - \bar{z}$. The variance of aperture is,

$$\sigma_a^2 = \frac{1}{N}\sum_{i=1}^{N}\left[\left(y_i - \bar{y}\right) - \left(z_i - \bar{z}\right)\right]^2 = \sigma_z^2 - 2C_{yz} + \sigma_y^2 \tag{2.10}$$

When two surfaces are completely uncorrelated, the variance of aperture should be twice the variance of an individual surface. When the surfaces are completely correlated, the variance of aperture is zero because the fracture is fully closed without open space.

(4) The fractal dimension of the aperture. This parameter can be obtained from the log-log slope of the power density spectrum of the aperture as a function of wavelength, shown in Figure 2.4. Because the existence of mismatch wavelength, the fractal dimension of aperture is confined to the slope near the small mismatch wavelength.

(5) The anisotropy in fractal dimension of the aperture.

2.2.2.3. Statistically average parameters. (1) The arithmetic mean height of each surface $\langle z_a \rangle_a$. This occurs at the peak of the probability distribution of heights. (2) The arithmetic mean aperture $\langle z_a \rangle_g$. It has the same physical meaning as $\langle z_a \rangle_a$. Both of them can be obtained from probability distribution of height and aperture.

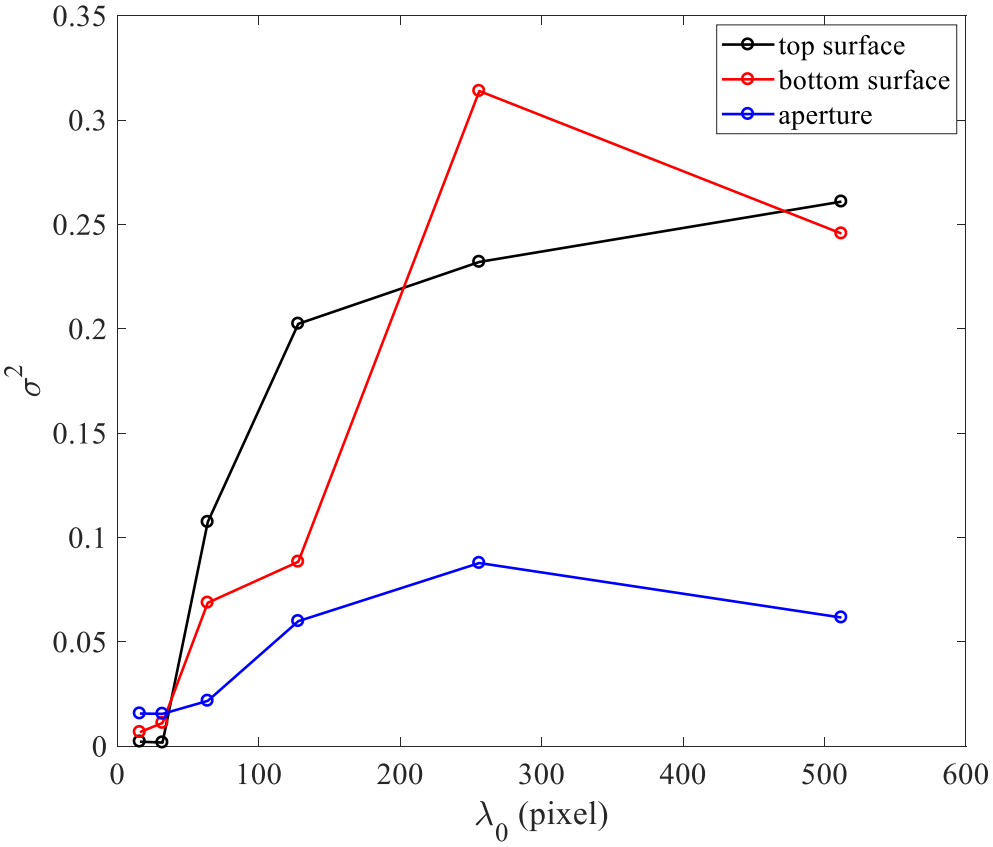

Figure 2.6 The Relation of Mean Square Roughness (σ_s^2 and σ_a^2) as a Function of Profile Length λ_0 in Unit of Pixel, at Any Physical Size. At large wavelength, the difference between surface and aperture is significant.

2.2.2.4. Basic statistics. These specific parameters on surface and aperture of granite are tested by Ogilvie et al. [11]. Their data will be directly listed in Table 2.1 and used for further generation of fracture.

2.3. SYNTHETIC FRACTURE GENERATION

By the data in Table 2.1, the probability density function and power spectral density function can be obtained. Then, all the required information to generate synthetic fracture is ready. One method of computing the power spectral density function just

Table 2.1 Rock Fractures Tested on Granite by Ogilvie et al [11].

Surface parameters	Standard deviation (U) (mm)	1.97
	Standard deviation (L) (mm)	2.07
	Fractal dimension (U)	2.25
	Fractal dimension (L)	2.16
	Anisotropy in fractal dimension(U)	0.88
	Anisotropy in fractal dimension(L)	0.86
	Physical size (mm)	95.9
Fracture parameters	Mismatch wavelength	4.5
	Transition length	40
	Wavelength λ_{-}	2.25
	Wave length λ_{+}	42.25
	Minimum matching fraction	0.1
	Maximum matching fraction	0.9
	Standard deviation	0.65
	Fractal dimension	2.64
	Anisotropy in fractal dimension	1.02
Arbitrary parameters	Arithmetic mean of surface (U)(mm)	1.71
	Arithmetic mean of surface (L)(mm)	1.71
	Arithmetic mean of aperture (mm)	1.33

Notes: the U after the name stands for upper surface, the L stands for lower surface. Some modifications have been made on the data for better presence in following section.

discussed is to take the Fourier transform of the topography. This calculation is the generalization of Fourier analysis and results in a series of sinusoidal components, which can be characterized by their wavelength, amplitude, and relative phase. This information, collectively known as the amplitude spectrum, is a series of complex number which contains both amplitude and phase information. The power spectrum is the modulus or square of the various amplitude components. The spectral synthesis method introduced by Peitgen and Saupe [23] is used to generate computer models of isotropic fractal surfaces. Two matrices are generated where each point in each matrix corresponds to that in the final matrix of Fourier components. These two matrices contain random number that are partially correlated to some degree. The degree of partial correlation depends upon the matching parameters. Finally, the inverse fast Fourier transform is implemented to convert the complex matrix into real space. The details of implementation refers to that book and the MATLAB® code is attached in Appendix A. The generated fracture surfaces and enclosed aperture heights are displayed in Figure 2.7, Figure 2.8 and Figure 2.9.

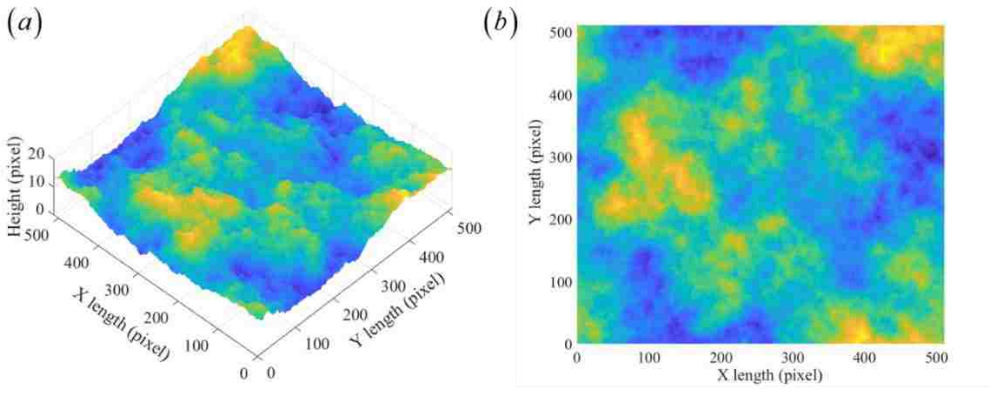

Figure 2.7 Top Synthetic Fracture Surface. (*a*) 3D view and (*b*) top view.

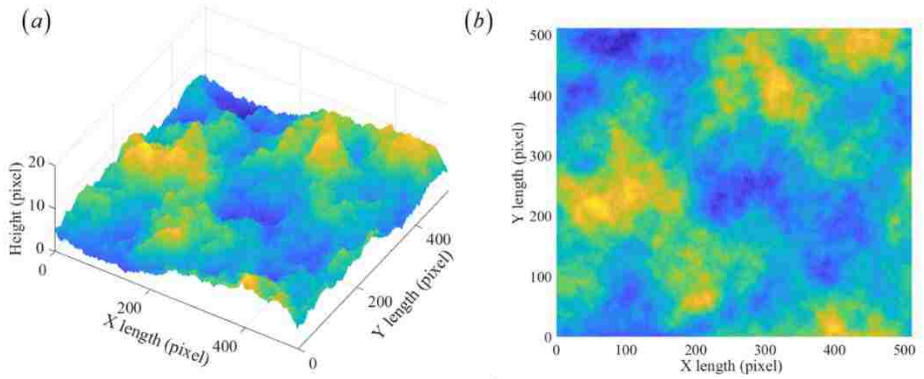

Figure 2.8 Bottom Synthetic Fracture Surface. (*a*) 3D view and (*b*) top view of numerical synthetic fracture at bottom surface.

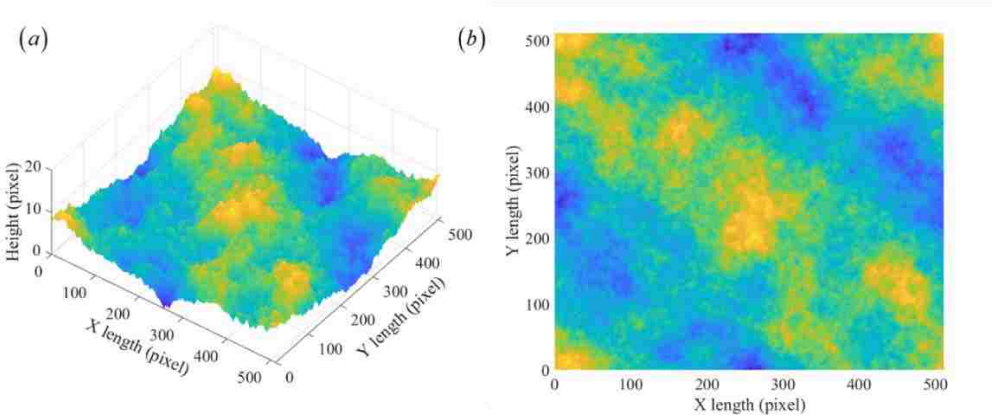

Figure 2.9 Synthetic Fracture Aperture. (*a*) 3D view and (*b*) top view of numerical synthetic fracture at aperture.

2.4. FRACTURE ANALYSIS

Because the aperture height is of essential interest for fluid flow and heat transfer. It characterizes the space between contacting asperities. The aperture height in Figure 2.9 is summarized and normalized. The probability density of aperture height is displayed in Figure 2.10. Ogilvie *et al.* [11] states that the distribution of aperture heights follows lognormal distribution. The number of small aperture takes more account in total

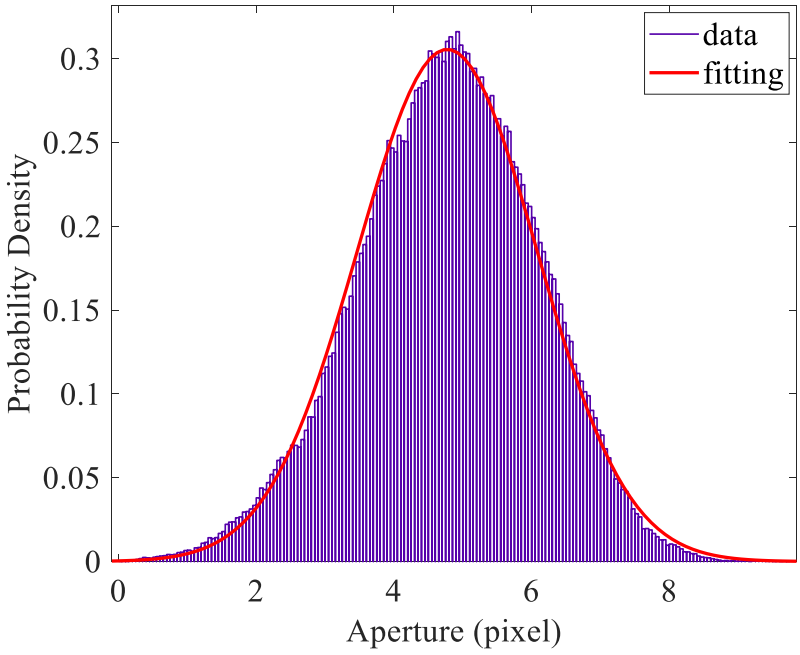

Figure 2.10 The Probability Density of Aperture Height of Synthetic Fracture. The data are fitted by Gaussian normal distribution. The mean and variance are 4.77 and 1.7, respectively.

apertures. They reached this conclusion by statistical analysis of 619 synthetic rough fractures by their private graphing software. The lognormal distribution of aperture height is also ascertained by Power and Tullis [28]. Hundreds of real faults surfaces are measured by profilimeter. However, Brown [15] presented the Gaussian distribution of aperture height by surface profilimetry of granite. This contradictory results is probably attributed to the different rock types they measured. For the fracture data in Table 2.1, the aperture height for this fracture is presented in Figure 2.10. The probability density of aperture height is Gaussian with mean 4.77 and variance 1.7. This result confirms with Brown's statement. However, it is not deterministic for this distribution. More investigation is required on the distribution of aperture height due to its significance.

The mean value of the normal distribution is more important than the variance. Higher mean value of aperture height means more open space between two fracture surfaces. Therefore, the mean value is analyzed in this section as a function of surface asperity distribution (standard deviation), fractal dimension, anisotropy, mismatch wavelength, and transition wavelength. Other parameters remain the same in Table 2.1.

The dependence of mean aperture on standard deviation of fracture surfaces is shown in Figure 2.11. The fracture aperture depends linearly upon the standard deviation. Standard deviation characterizes scattering of asperity distribution on the fracture surface. Higher deviation denotes more scattering of asperity and larger fracture aperture. In this sense, the non-uniform distribution of asperity has higher fracture aperture. This implicitly complies with the results of Hopkins [13]. The fractal dimension describes the proportion of high-frequency to low-frequency roughness and is a measure of surface texture. For natural fracture surfaces, fractal dimension D tends to fall approximately in the range $2 \leq D \leq 2.5$, with small values representing smoother surfaces. The variation in this range is investigated and the corresponding result is displayed in Figure 2.12. As the surface becomes rougher, the fracture aperture increase super-linearly. This result is kind of consistent with Figure 2.11. Non-uniform distribution and rougher distribution leads to larger fracture aperture. The anisotropy is also considered in this sensitivity study. For natural fracture surface, the roughness is usually not isotropic. The anisotropy is used to characterize this anisotropic roughness. When anisotropy is less than one, the anisotropy is transverse to *x*; when this value is one, the surface is isotropic; when this value is larger than one, the anisotropy is parallel to *x*. The anisotropy at which mean aperture minimizes in Figure 2. 13 is 0.78. The logarithmic scale is shown in horizontal *x* axis.

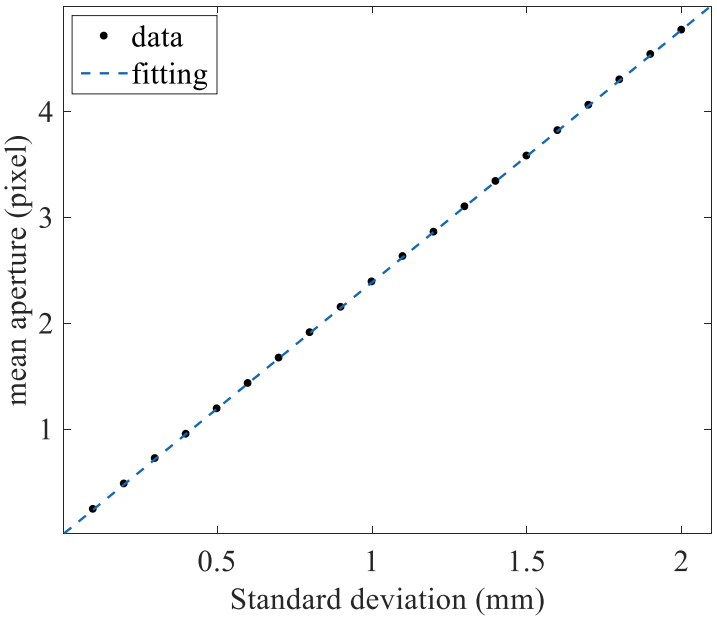

Figure 2.11 Mean Synthetic Fracture Aperture as a Function of the Standard Deviation of Surfaces. Other parameters refer to Table 2.1.

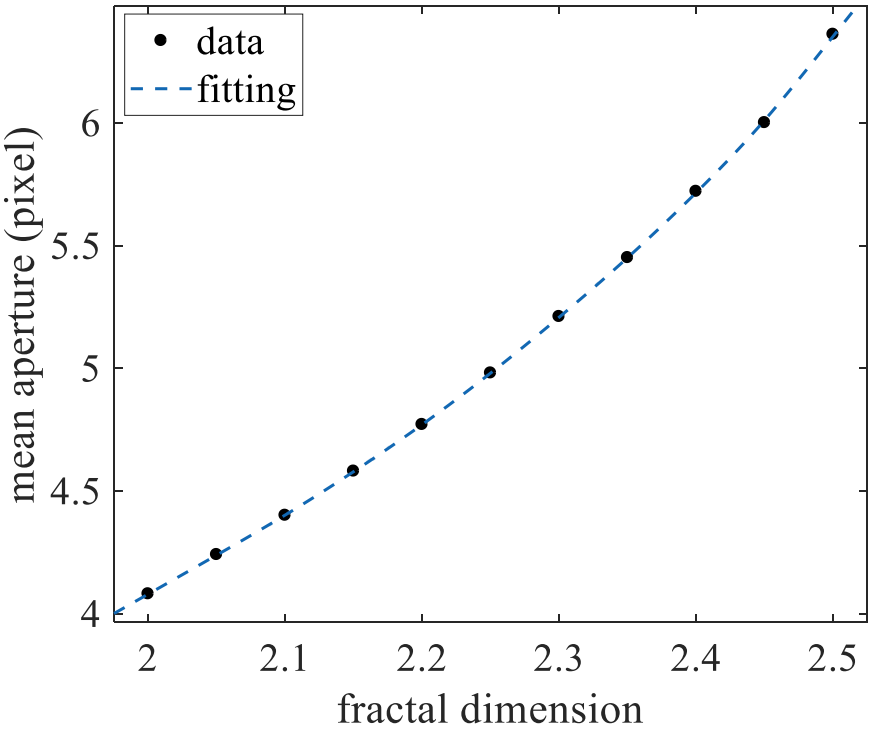

Figure 2.12 Mean Synthetic Fracture Aperture as a Function of the Fractal Dimension of Surfaces. Other parameters refer to Table 2.1.

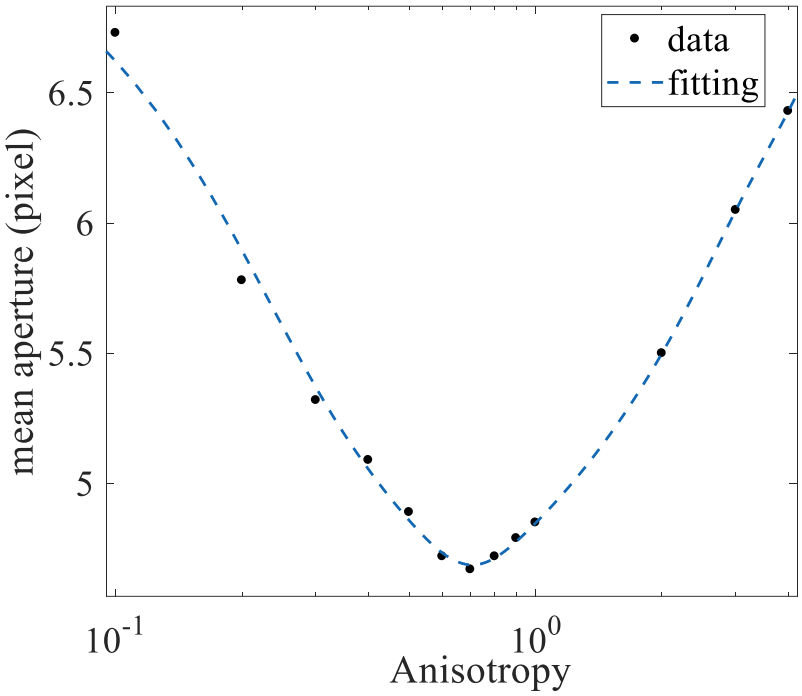

Figure 2.13 Mean Synthetic Fracture Aperture as a Function of the Anisotropy of Surfaces. Other parameters refer to Table 2.1.

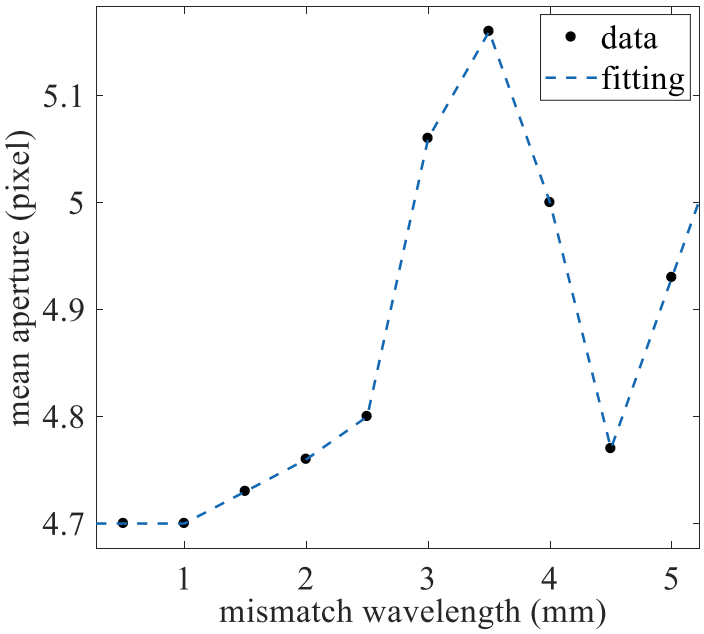

Figure 2.14 Mean Synthetic Fracture Aperture as a Function of the Mismatch Wavelength of Surfaces. Other parameters refer to Table 2.1.

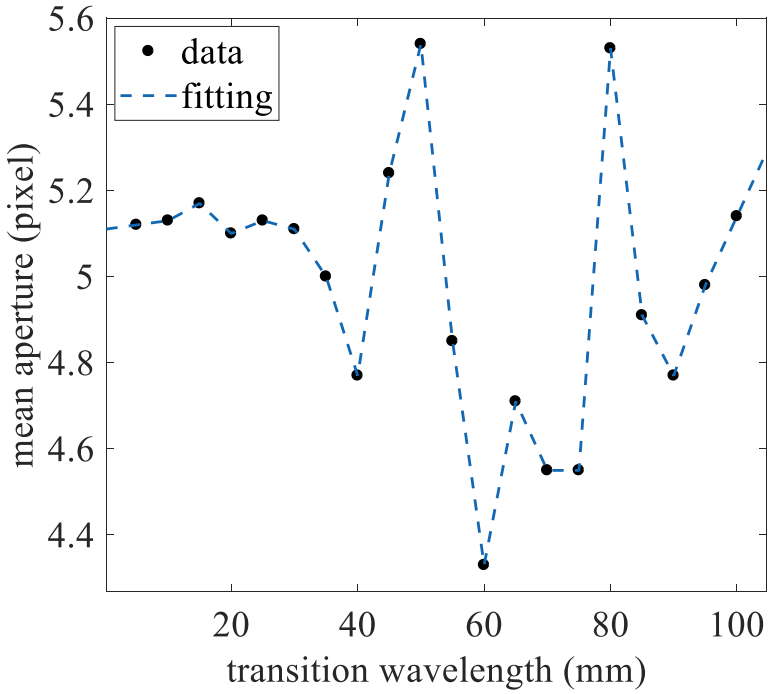

Figure 2.15 Mean Synthetic Fracture Aperture as a Function of the Transition Wavelength of Surfaces. Other parameters refer to Table 2.1.

It indicates the effect of anisotropy is not symmetric. The smaller part has more influence on the mean aperture. Furthermore, the mismatch wavelength and transition wavelength are also investigated in Figure 2. 14 and Figure 2. 15. The wiggles infers no monotonic relation between them.

2.5. DISCUSSION

Spectral analyses show that rough fractures are fractal or self-affine in nature. This means [19] that surface irregularities are present at all scales, with longer wavelength irregularities having larger amplitude and contributing more to overall roughness than short wavelength features. The border between two wavelength ranges is the mismatch wavelength. This value is found to have a strong impact upon flow,

controlling channeling effects and the related hydraulic behavior at the fracture scale [31]. The study on mismatch wavelength requires more details on its implication on physical phenomena, such as flow, chemical erosion, and hydrothermal effect. The fracture characterization provides an effective avenue for following analysis on normal loading. This fracture surface is not likely to be directly used in normal loading due to complicated details on the fracture surface. The small wavelength dominates and it is hard to be considered in loading condition due to its small size. However, further simplification based on this characterization makes the analysis reasonable. The anisotropy is added in this model to consider the anisotropic feature of the fracture surface. But this anisotropy is very simple and makes the cluster of the contacting region distorted and unrealistic. A more realistic analysis of fracture surface is multifractal analysis [32].

3. STRATIFIED CONTINUUM PERCOLATION MODEL

3.1. INTRODUCTION TO STATISTICAL MODEL

There has been strong interest in the ability of fractal geometry to describe many of the characteristics of seemingly structure-less patterns. Much of this interest has come after the realization that an impressive number of random systems exhibit scale invariance, also known as self-similarity; that is, certain parameters describing the system remain the same regardless of the scale of magnification. Scale invariance lies at the heart of the notion of fractal dimension [33].

For a random pattern to have scale invariance, the distribution of the sizes of the features which define the pattern must vary as a power law with some scale, *b*: $P(b) \propto b^{-(D+1)}$. The exponent D is the fractal dimension of the object. As such, the concept of fractal dimension is simply the consequence of power-law statistics governing size distributions. Power-law statistics ensure scale invariance. Invariance under transformation is a powerful and recurring concept in physics describing widely different phenomena. In many of these phenomena, invariance under scale transformation offers valuable insight into the physical origins of the phenomena and often provides for the use of powerful analytic tools for describing their structure. For instance, the scale invariance of fractal objects allows the analytic results of renormalization group theory to be used [34].

In application, real system rarely possess the same scaling properties for all scales. Namely, there are scales above or below which the scaling properties change. These scales are called cut-offs. Often the cut-offs can carry as much information about

the physical processes creating the pattern as the scaling properties of the patterns. Typically, when a fractal dimension is assigned to a pattern, this dimension is only valid for scales above a lower cut-off and below and upper cut-off. In fact, measurement of certain fundamental properties, such as contact area, depends directly on the cut-offs. Also the measurement of the fractal dimension can be influenced by cut-offs when the measurement scale approaches the cut-off scale. For these reasons, particular attention must be paid to the limits of the regimes of scaling when attempting to define the physical properties of a pattern.

With the power of fractal description comes considerable complexity, fractal objects take on a tremendous variety of forms, and sometimes several fractal dimensions can be defined for the same object. For example, a random percolation network at its critical percolation threshold has a fractal dimension of D = 1.89 [34]. At the same time, the fractal dimension of the backbone of the percolating cluster is D = 1.59 [35]. Similarly, in the case of the fracture surface, many fractal models can be used to describe the topography. The fracture contact areas can be viewed as random holes, or tremas (removed part) [33], which puncture a conductive sheet. Therefore, aperture between fracture surfaces can be modeled as lying on a random Sierpinski carpet.

Three types of random Sierpinski carpet, shown in Figure 3.1, are constructed interactively by removing successively smaller squares (or tremas) from the original black square. Even though they display different topography, they have the same spatial fractal dimension. In the carpet shown, 8 out of 9 sub-squares, of scale b = 1/3, remain at each level. This gives the carpet the approximate fractal dimension $D = \ln 8/\ln 3 = 1.89$. The fractal dimension of a Sierpinski carpet can be measured, in principle, by counting

the number of tremas larger than some set value. In practice, the counting is carried out by superposing grids with successively smaller spacing and counting the number of grid squares at each level which are occluded more than 50% by a single trema. The fractal dimensions are derived from the slope of ln (b2-N) vs. ln b, where b is the scale size of the grid and N is the number of squares occluded for that scale b. The quantity (b2-N) is the number of grid squares which remain uncut by tremas at this scale size. This fractal dimension is called box-counting dimension. There are several different dimensions widely used in description of fractal geometry [36]. The box-counting dimension is the simplest and most used one.

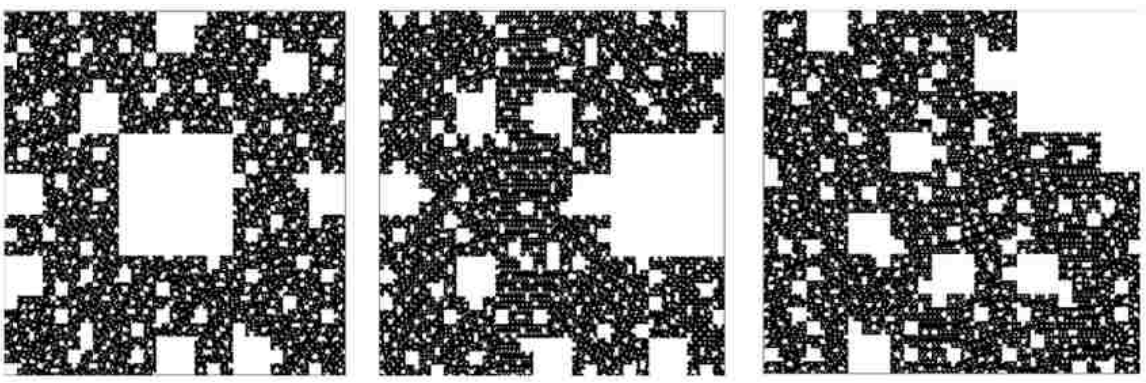

Figure 3.1 Three Types of Random Sierpinski Carpet with Five Size Levels of Recurrence. In spite of their different topography, the spatial fractal dimension $D = 1.89$ is the same but in a statistical sense [37].

The fluid flow in fracture follows percolation theory. The percolation theory is also used to construct the model. For standard percolation theory, two basic forms of percolation models are site percolation and bond-percolation, shown in Figure 3.2. In site percolation, the sites are occupied with a probability p. No flow can occur through an unoccupied site. In bond percolation, the bond are occupied with a probability p, and no

flow can occur through an unoccupied bond. The fundamental property of a random flow system is the existence of a critical probability pc, which defines the percolation threshold. For occupation probabilities below this critical probability, no connected path exists through the random network and the flow is totally occluded. At the percolation threshold, only a single percolating cluster exists. This percolating cluster has a fractal dimension of D = 1.89. For values of the occupation probability increasing above the critical density more connected paths can be found, and the connection between two opposing boundaries increases sharply. The critical probability is a function of the lattice dimension, and also of the specific model. This relation is shown in Figure 3.2c. The power of percolation theory comes from its ability to define the critical threshold parameter pc, as well as the functional form of the hydraulic conductivity near the percolation threshold. Because of scale invariance at the percolation threshold, the hydraulic conductivity slightly above the critical threshold obeys a power-law relations as a function of density: $k \propto \left(p - p_c \right)^t$, where k is the hydraulic conductivity in the region, p is the flow path density, pc is the critical density, and t is the exponent. As the system moves far above the percolation threshold, the random flow network can be characterized by applying the effective medium approximation [38] from which a homogeneous conductivity can be defined for the flow system.

The lattice percolation model provides the basis for percolation theory, but it falls short in the analysis of area fraction of percolation [39]. The area fraction denotes the ratio of area with aperture to total area in horizontal cross section. Therefore, the fracture aperture simulation entails more realistic percolation model. Based on the experimental analysis [40], the fracture aperture follows scaling invariance. The multifractal analysis is

used to quantify the statistical parameters of fracture surface and aperture, such as momentum exponent, singularity and fractal dimension function. The multiplicative cascade model is a desirable model to meet this multifractal and is implemented by Nolte and Pyrak-Nolte [12]. The basis of multiplicative cascade is introduction in the following section.

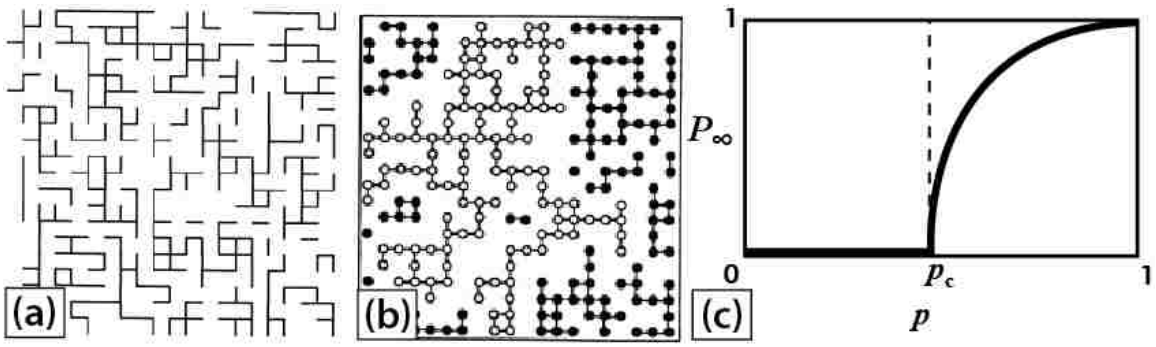

Figure 3.2 Illustration of Discrete Percolation Model. Schematic representation of (*a*) bond percolation, (*b*) site percolation and (*c*) the probability P_∞ as a function of the occupancy, p of the network [41].

3.2. MULTIPLICATIVE CASCADES

A multiplicative cascade is an iterative process that fragments a given set into smaller and smaller pieces according to some geometric rule and, at the same time, distributes the total mass of given set according to another rule.

Multiplicative cascade models are mathematical constructs appropriate to capture the intermittent and highly irregular behavior. Multiplicative cascades were initially proposed by Kolmogorov for turbulence modeling [42]. Currently the multiplicative cascade model has found applications in several areas to describe non-linear phenomena which have multiplicative structure [43].

Of interest in some cases are cascades in which features at larger scale overlap with features at smaller scales. Overlap mixes the effects at different scales, so that the processes at one scale are no longer independent of processes at other scales. Overlap converts the random cascade into a random process with multiplicative cascade and an approximately log-normal distribution of densities. Two random Cantor bars are shown in Figure 3.3. one without overlap, one with overlap. In both cases, the number of remaining lengths are 3 and the scale factor between two generations are 4. In the case of no overlap, the fractal dimension is D = ln3/ ln4 =0.79. In the case with overlap, on the other hand, the fractal dimension is smaller than this value. Because, the averaged length shrinks but the scale factor remains the same. The densities of the bar after three iterations are shown at the bottom of the Figure. By allowing overlap, regions of very high density occur. The high density produces an extended tail on the mass distribution. The properties of multiplicative cascades with continuous overlap, and relate them to problem in correlated percolation.

Stratified percolation is a correlated percolation model that generates fractal patterns through a self-similar cascade. Overlap of cascades is allowed, leading to approximately log-normal densities. This model is part of a larger class of correlated percolation systems, in which occupancy is conditionally dependent on local environments. Much of correlated percolation has been motivated through Ising percolation. Ising clusters in two dimensions comprise equilibrium system with near-neighbor exchange interactions and long-range correlation. The connectivity of clusters in the Ising model has been related to the geometric critical behavior of percolation

systems. In addition to equilibrium Ising percolation, other correlated percolation systems have also been studied.

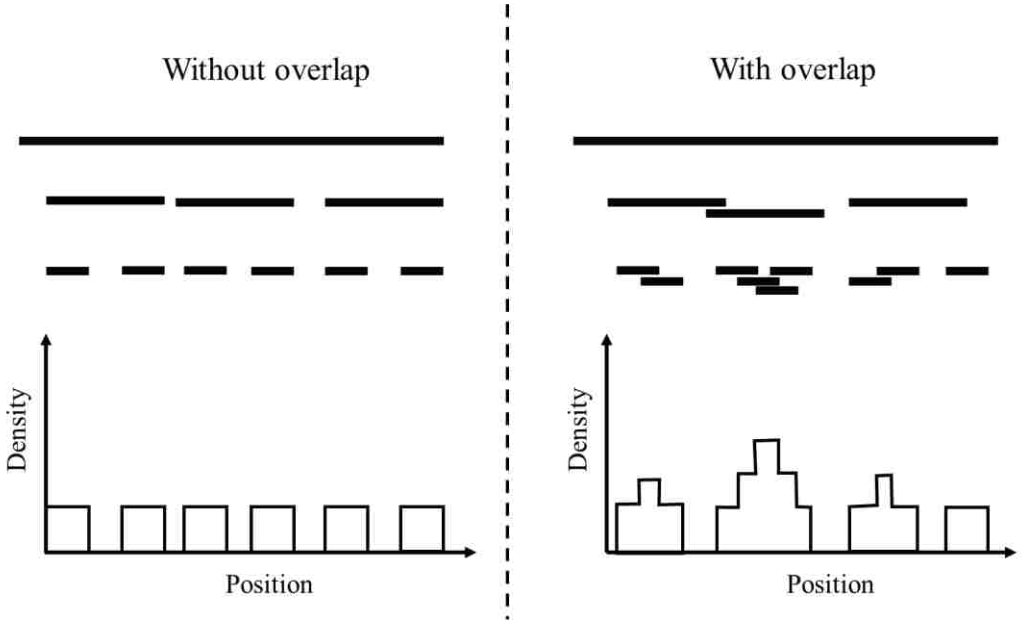

Figure 3.3 Random Cantor Bars. Without overlap, the fractal dimension is D = 0.79. With overlap, the resulting mass distribution is multifractal.

Much of continuum percolation theory is based on random continuum percolation. A continuum percolation pattern is shown in Figure 3.4a. Squares are randomly positioned within the region of interest. The pattern is generated with one generation having 800 squares. The stratified percolation pattern is shown in Figure 3.4b. This pattern is slightly below the percolation threshold because two opposing boundaries are not connected by black squares. The percolation threshold is usually defined for infinite region, but the numerical region is impossible to draw infinite region. The periodic boundary condition is used for four boundaries as a compromise. When the square is intersect with one boundary, part of it exceeding the boundary will be moved to

the corresponding part by periodic boundary condition. The other noticeable difference between two patterns resides in the cluster size. Standard continuum percolation pattern has small cluster size and disconnected to each other. However, stratified continuum percolation pattern has large cluster size and some are clumped together. The clustering is a typical characteristics of correlated percolation. This feature is recognized in the natural fracture. Figure 3.5 shows the conductive path or hydraulic path in tensile fracture [44]. Conductive electricity is always used to measure the distribution of asperity and void space in fracture. Both of them shows clusters of white space which means contacting asperities. This pattern is similar to Figure 3.4b where the white space also denotes the contacting asperities. For the correlated percolation, the critical percolation density of scaling parameters are of particular interest in describing the cluster size. In the following, the percolation property of this model is analyzed.

3.3. PERCOLATION PATTERN FORMATION

Stratified percolation patterns are generated by a recursive algorithm that defines a self-similar cascade of random sites. The construction may be regarded as applying random continuum percolation on successively smaller scales. Figure 3.6 shows this construction in four generations. The scale factor is b = 3.78 and the number of sites in each generation is N = 4. In the first generation, N sites are randomly placed. The N second squares having edge scaled by b is placed in the second generation. The algorithm repeats, no randomly placing N sites in each of the N squares in second generation. In the third generation shown in Figure 3.6, the number of squares are 43 = 64. It can be deduced that the total squares in nth generation is Nn, where N is the number of squares

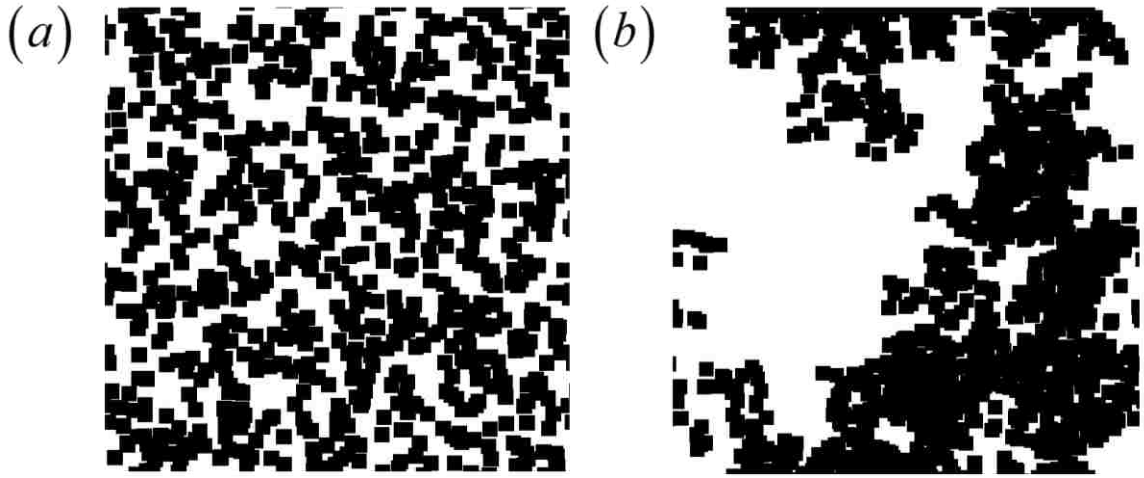

Figure 3.4 Presentation of Standard Continuum Percolation Pattern and Stratified Continuum Percolation Pattern. (*a*) Standard continuum percolation pattern and (*b*) stratified continuum percolation pattern. The number of squares is 800 and scale factor of 30 in (*a*). The number of generation is 5, and scale factor of 2.37 in (*b*). The black squares denote void space in fracture and the white space denotes contacting regions.

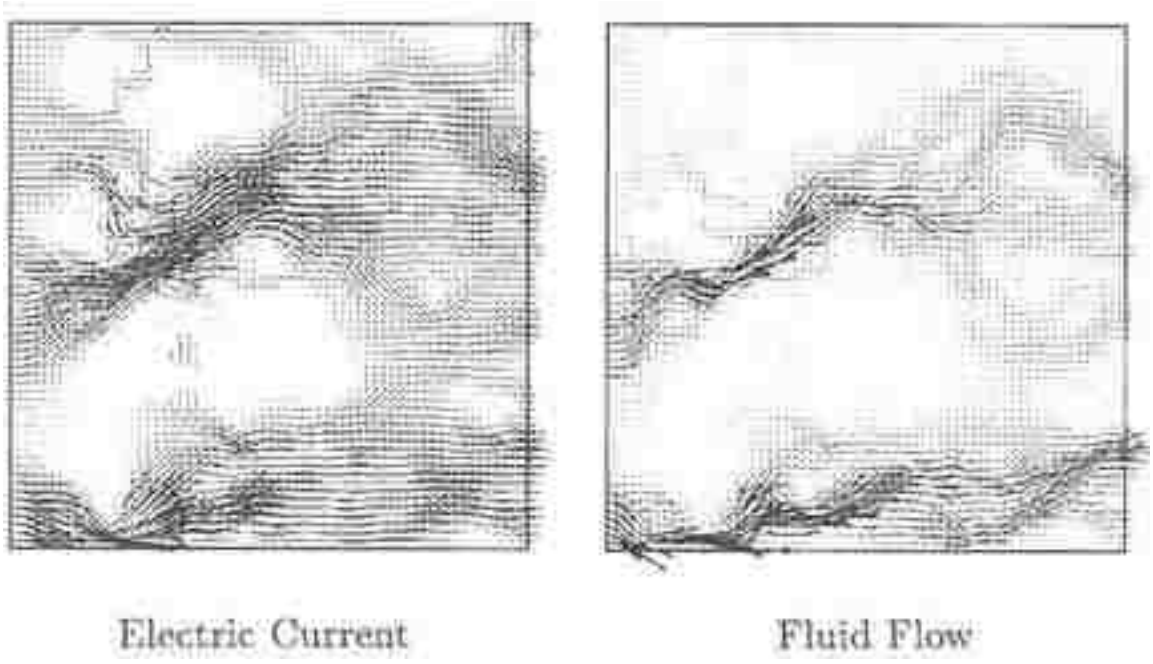

Figure 3.5 The Electric Current and Fluid Flow in Fracture [44]. The grey lines denote the flow line and the white area are contacting asperities. The cluster of white area means the clumping of contacting asperities.

per generation, and *n* is order of generation. It's worth noting that the largest square work as an initial state and is finite in size. However, the critical percolation and scaling exponents are defined in infinite region. To mitigate this deficiency, the periodic boundary condition is applied on the four outer edges on largest square. This periodic condition is applied only on the largest square. For "child" square, it is allowed to overlap and overhang the smaller regions.

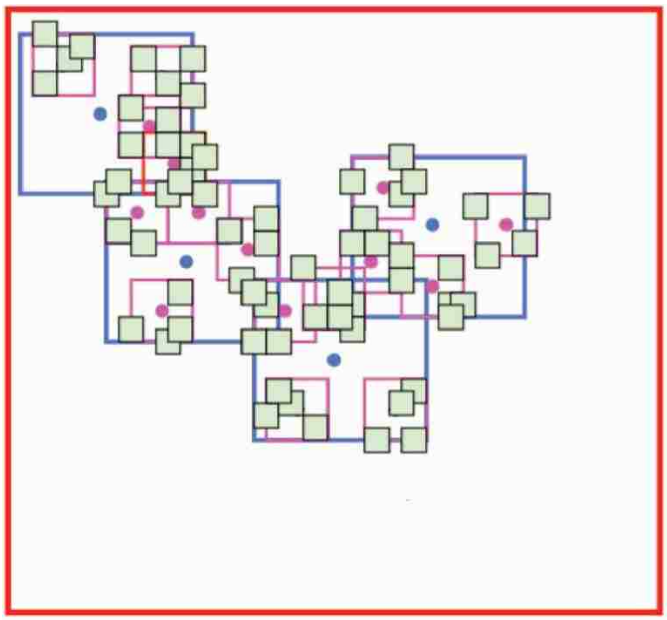

Figure 3.6 Recursive Construction of a Stratified Percolation Pattern [45]. The Figure includes three generations with a scale factor of 3.78 between two generations. The first, second and third generations are shown in red, light blue and magenta, respectively. The light green squares represent the plotted points. Overlaps of the smaller light green squares result in a variable aperture distribution. This Sierpinski carpet model is two-dimensional pattern of Cantor bar with overlap in Figure 3.3.

The stratified percolation construction is intrinsically a continuum construction. Because the squares is randomly placed without grid. At each scale, the sub-squares are centered randomly within the next larger generation, such that each generation is a

continuum percolation plot of its own. Even at the smallest level, when the final squares are plotted, the squares are placed randomly as a continuum plot. In practice, placement of squares is not that easy as seen in Figure 3.6. The geometry information of the squares is stored in numerical matrix. That is, the data has grid, like pixels on the geometry. To maintain the continuum pattern of percolation, the side of final squares cannot be as small as one pixel. In that condition, the model becomes discrete site percolation and the continuum pattern is lost. However, the size of final squares cannot be large in case of

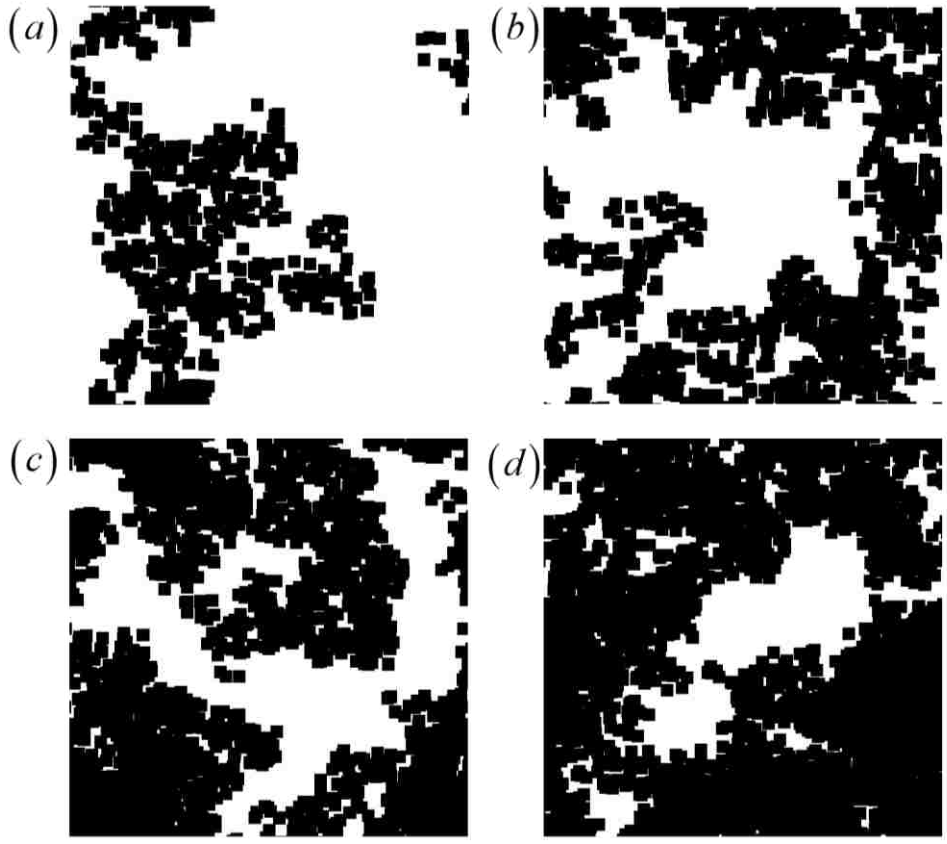

Figure 3.7 Examples of Stratified Percolation Patterns with Size of Final Squares 4 × 4 Pixels and the Largest Square 300 × 300 Pixels. The scale factor and number of generation for all of them are $b = 2.37$ and $n = 5$. The difference is the number of sites in each generation: (*a*) $N = 5$, (*b*) $N = 6$, (*c*) $N = 7$, and (*d*) $N = 8$.

small scale factor and small number of generations. Based on these considerations, the largest square are 300 × 300 pixels and the size of final squares are 4 × 4 pixels [12].

Examples of stratified percolation patterns are shown in Figure 3.7 for different numbers of sites with same scale factor and number of generations. In Figure 3.7a, the top and bottom edges are not connected by black squares but this arrangement is close to the percolation. That means the fraction of area is slightly below the percolation threshold. The area fraction of black squares is 24%. In Figure 3.7b, the top and bottom edges are connected which means percolation occurs in this pattern. The area fraction is 45%. But one cannot draw the conclusion that the percolating area fraction is between 24% and 45%. The percolating area fraction is applicable in the infinite region. The specific value of the percolating area fraction requires elaboration and more detailed analysis. It will be discussed in following section. Figure 3.7c and 3.7d also have percolation between two opposing edges. Their area fraction occupied by black squares are 64% and 72%. In addition, the clumped structures are obvious in four Figures, which is the feature of the percolation model.

Stratified percolation has much in common with curdling. Curdling is a process whereby an originally uniform mass clumps together into many small regions with high density [33]. The curdling process, especially self-similar processes, involve a cascade in which the mass sequentially breaks into smaller subsets of larger subsets. Many models involving curdling have been developed. For example, Multifractal lattices have been generated through cascade processes [46, 47]. The cascade in stratified percolation is obvious, leading also to a curdled structure.

3.4. PERCOLATION PATTERN STRUCTURE

The covered area of a percolation pattern is one of the key parameters used to characterize the system. The critical percolating threshold is usually expressed as covered area fraction in continuum model. The definition of area fraction per generation is calculated in the identical manner as for standard continuum percolation. For N squares of reduced size b plotted within a square region of unit area, the result from standard continuum percolation is:

$$a(N,b) = 1 - \left(1 - \frac{1}{b^2}\right)^N \tag{3.1}$$

where $a(N,b)$ is called the area fraction per generation. A recursive expression for the total area fraction of the stratified percolation pattern can be defined by applying (3.1) for the changing area fraction of each successive generation. For n generation, this recursive expression is:

$$\begin{aligned} A(n,N) &= 1 - \left[1 - \frac{A(n-1,N)}{b^2}\right]^N \\ &\vdots \\ A(1,N) &= a(N,b) \end{aligned} \tag{3.2}$$

A simpler, non-recursive approximate expression is obtained by expanding Equation (3.2) as:

$$A(n,N) = a\left[a + (1-a)a^2\right]^{n-1} \tag{3.3}$$

This equation would be exact if periodic boundary condition were applied to each generation. However, in current construction, the periodic boundary condition is only applied for the largest square. Therefore, Equation (3.3) is approximate, and

underestimate the true area fraction. The total area fraction for n = 5 generation with b = 2.37 is plotted in Figure 3.8, as a function of the area fraction per generation $a(N,b)$ for N varying from 3 to 10. The data are obtained from Monte Carlo simulations, and are compared with Equation (3.3).

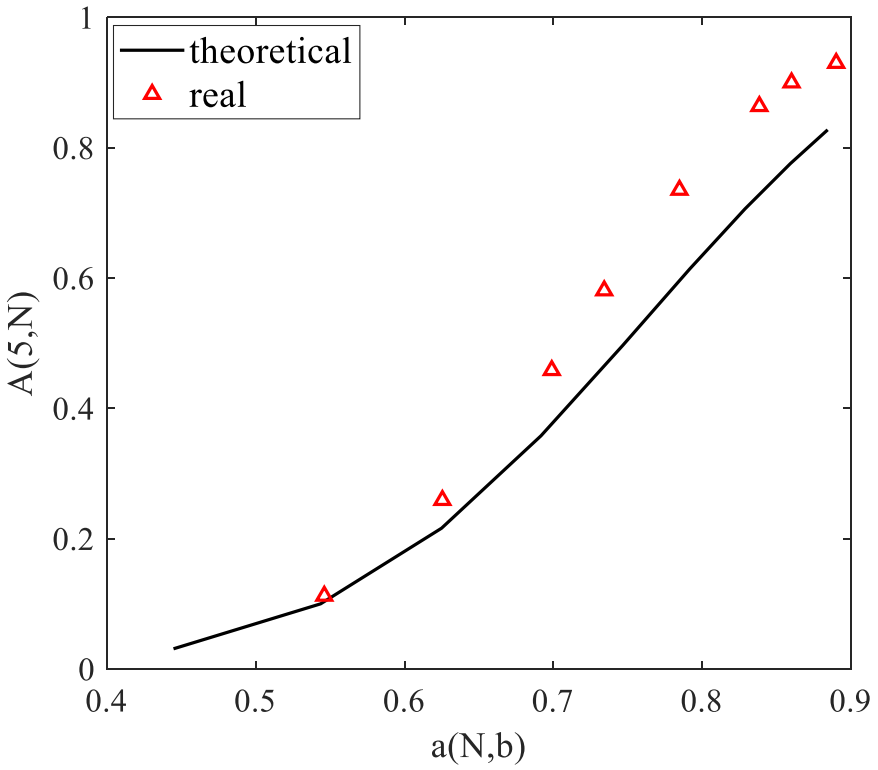

Figure 3.8 The Final Occupied Area Fraction by the Stratified Pattern as Functions of Initial Area Fraction with b = 2.37 and n = 5. The number of points N vary from 3 to 11. The curve is calculated from Equations (3.1) and (3.2), and the red markers is calculated by Monte Carlo simulations.

The patterns in Figure 3.7 are two dimensional; positions are either covered or not. A third degree of freedom can be gained by considering the density of covered positions. The density of sites is obtained during the plotting of the pattern by counting the number of times that a given position is covered by a plotted square. An example with

five generations are displayed in Figure 3.9. The white areas represent zero density; the number of overlap is colored in 3.9a and 3.9b. The correlations introduced during the cascade algorithm are clearly visible. Regions of high density and low density are separately clumped. The distribution of site numbers in each pixel is shown in Figure 3.10. The density of occurrence of a specific density is plotted as a function of site number. The probability density is not Gaussian, and is approximately log-normal. Log-normal distribution are characteristics of multiplicative cascades [48, 49]. The long tail of high densities is caused during the cascade construction as many squares overlap with one another. The density of sites can be equated with distributions of apertures for a fluid-flow network. The long tail of large “apertures” has been found to be particular relevant for aperture distribution in fractures in rock [50].

3.5. FRACTAL STRUCTURE

The stratified percolation patterns are fractal within the limits of the upper and lower cutoff lengths. The upper cutoff length is the initial sample size and the small cutoff length is the size of final squares. Within these limits, the black and white patterns are scale invariance and are characterized by a fractal dimension. The degree of homogeneity of the two-dimensional patterns is characterized using lacunarity. When the density of sites is considered, the patterns are multifractal and exhibit a distribution of fractal dimensions and Lipschitz-Hölder exponent. All of these aspects of the stratified patterns are discussed in this part. The two dimensional properties are discussed first, followed by the multifractal analysis.

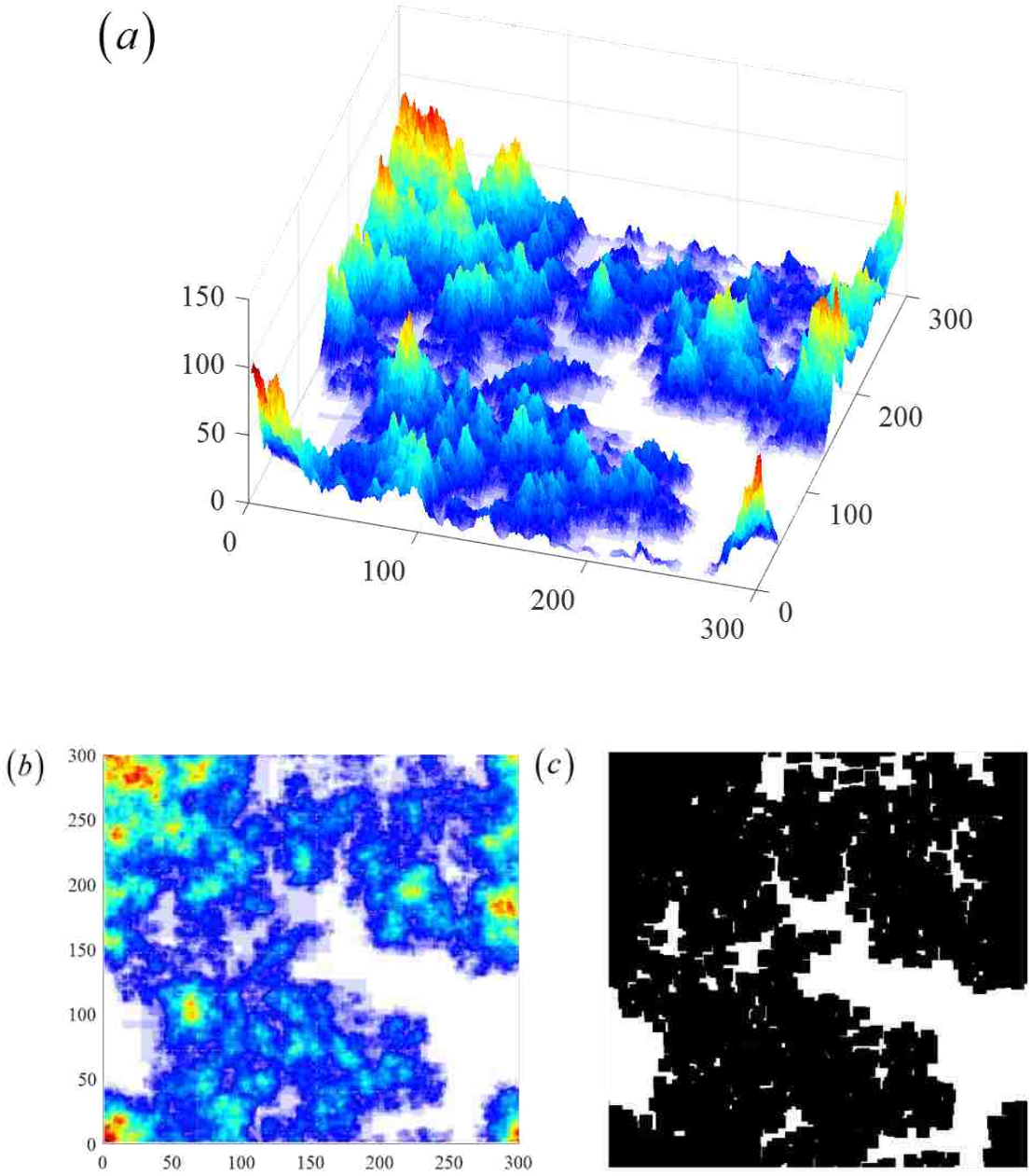

Figure 3.9 Density of Sites for Stratified Continuum Percolation with $N = 8$, $b = 2.37$, $n = 5$. The density of sites is strongly correlated, reflecting the overlapping cascade construction process. (*a*) the three dimensional representation; (*b*) the two dimensional representation with all generation effect involved; (*c*) the two dimensional representation with final generation effect considered.

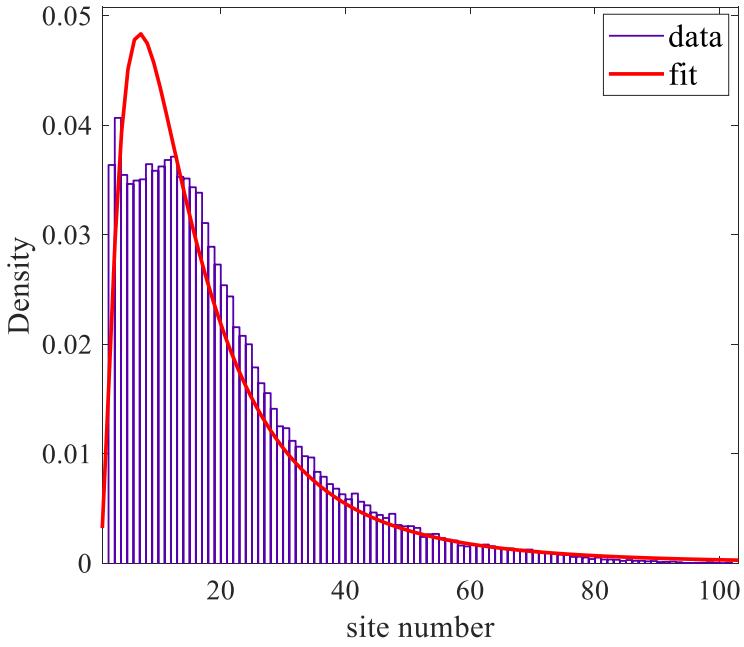

Figure 3.10 Distribution of the Site Number for Figure 3.9 Showing the Frequency of Occurrence for Different Densities. The distribution has a long tail of large densities that is approximately described by a log-normal distribution. The normalized histogram is fitted by log-normal distribution. The mean and variance are 19 and 216, respectively.

The fractal dimension of the full stratified patterns can be estimated by considering the cascade construction of the patterns. The fractal dimension is usually obtained by box-counting method. However, that is numerical calculated fractal dimension. The analytical version is derived by Nolte and Pyrak-Nolte [12]. The detailed derivation refers to their work and their analytical form of fractal dimension is simply presented at here. After some approximation, the fractal dimension is:

$$D = 2 + \frac{n-1}{n} \frac{\ln\left\{a(N,b)\left[1-a(N-1,b)\right]+a(2N)a(N-1)\right\}}{\ln b} \tag{3.4}$$

This can be roughly verified by the first generation scenario. In that condition, n = 1 holds and D = 2 applies. This is consistent with standard continuum percolation pattern in Figure 3.4a. The fractal dimension is 2 for standard continuum percolation pattern. For

scenario of more generations, the comparison between theoretical form by Equation (3.4) and numerical calculation by box-counting method is presented in Figure 3.11. The details on box-counting method is shown in Figure 3.12. The difference is noticeable. It comes from the approximate formula in Equation (3.4). Based on the statement by Nolte and Pyrak-Nolte [12], the error is within 10% for theoretical formula. From this sense, the difference is in the expected range. In addition, to evaluate the sensitivity of generation number on the fractal dimension, two cases with different number of squares are considered. The corresponding fractal dimensions are plotted in Figure 3.12. It shows that fractal dimension is statistically invariant and is an intrinsic properties of percolation model. It concludes that the fractal dimension can be approximately derived and has a reasonable agreement with numerical results by box-counting method.

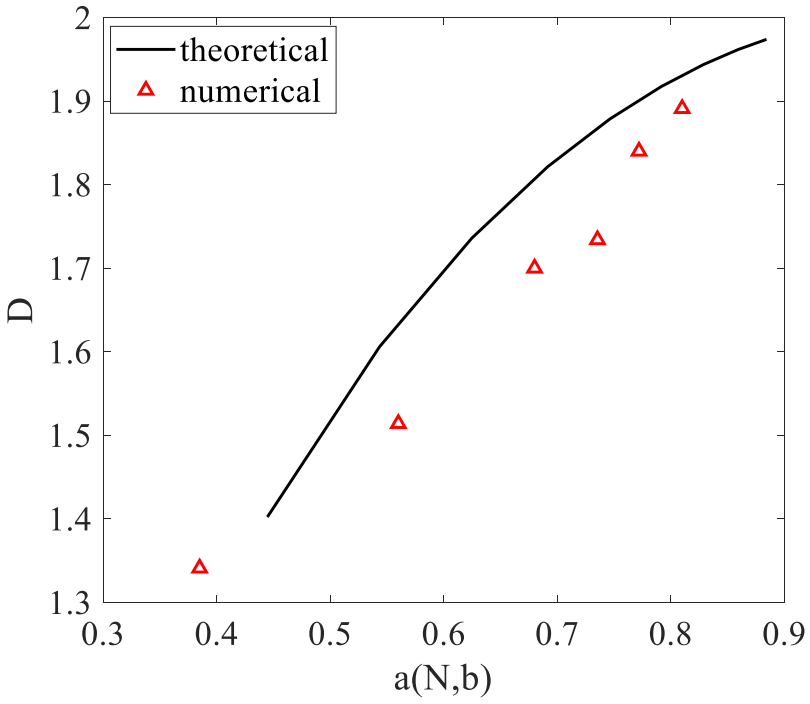

Figure 3.11 Fractal Dimension *D* vs. the Area Fraction per Generation for $n = 5$, $b = 2.37$, *N* Varying from 3 to 11. The difference is noticeable, but the trend is almost the same.

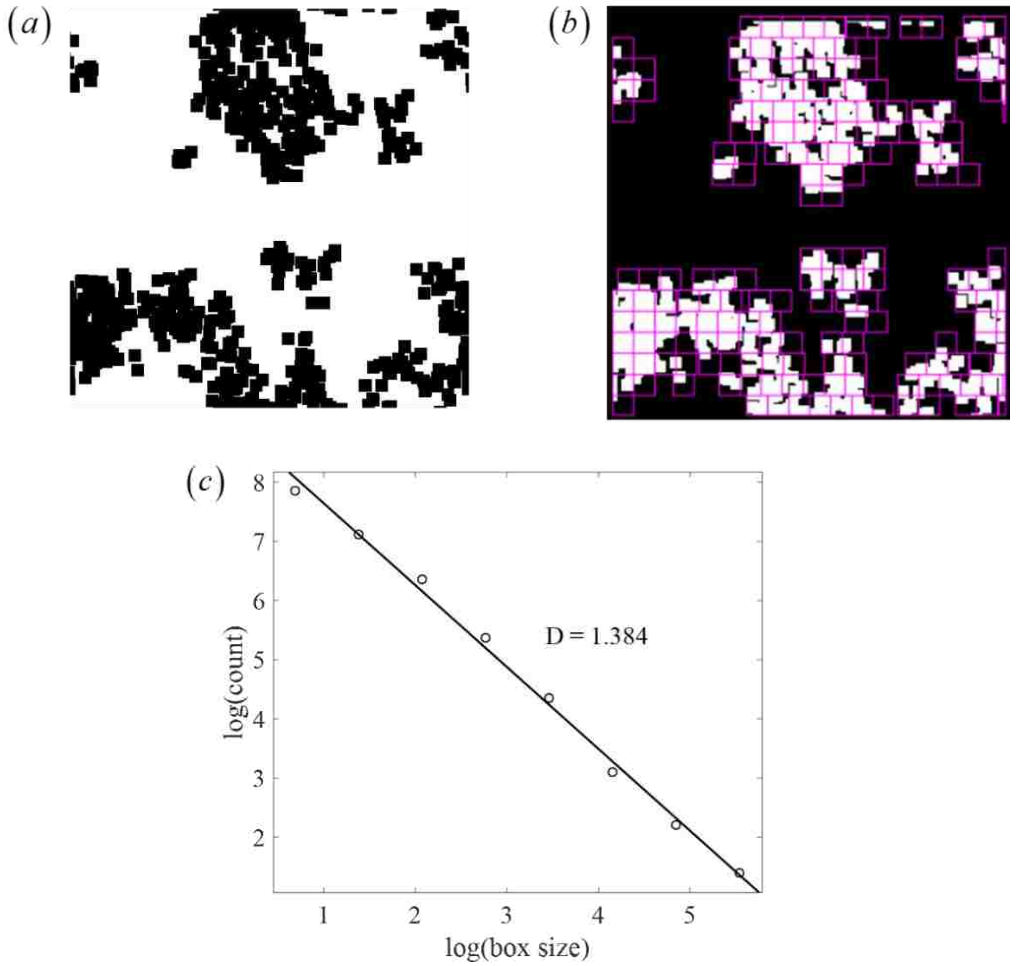

Figure 3.12 The Calculation of Fractal Dimension by Box-Counting Method. (*a*) the binary image created by stratified percolation model at $n = 5$, $N = 5$ and $b = 2.37$; (*b*) one screenshot on box-counting with grid displayed; (*c*) the log-log plot of number of box and box linear size to calculate the fractal dimension $D = 1.284$.

For two dimensional structure, the fractal dimensional can not only characterize the texture of structure. Lacunarity is introduced by Mandelbrot to analyze the turbulence [33]. Lacunarity is a counterpart to the fractal dimension that describes the texture of a fractal. It has to do with the size distribution of the "gap" in the texture. Roughly speaking, if a fractal has large gaps or holes, it has high lacunarity; on the other hand, if a fractal is almost translationally invariance, it has low lacunarity. Different fractals can be

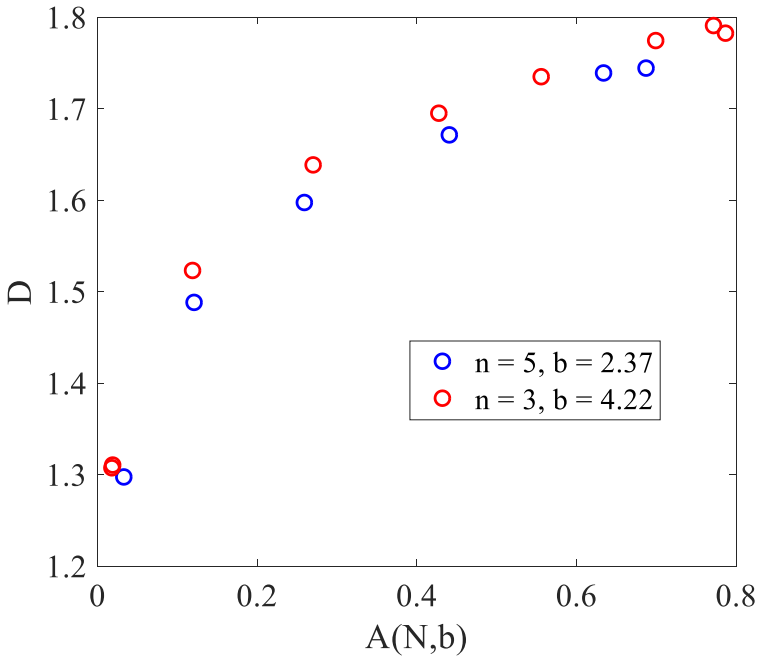

Figure 3.13 The Fractal Dimension *D* with Respect to Total Area Fraction in Two Different Generations.

constructed that has the same dimension but that look widely different because they have different lacunarity. Lacunarity analysis is now used to characterize patterns in a wide variety of fields and has application in multifractal analysis in particular.

In many patterns or data sets, lacunarity is not readily perceivable or quantifiable, so computer-aided methods have been developed to calculate it. Box-counting lacunarity is the most widely used version. It is measured by box counting with varying box size. In current pattern, the lacunarity can be defined as:

$$\Lambda(L)=\frac{\left\langle A^2(L)-\langle A(L)\rangle^2\right\rangle}{\langle A(L)\rangle^2} \tag{3.5}$$

The numerator is the variance based on area fraction in a particular generation. $A(L)$ is the shorthand notation for $A(n,N)$ with box size L from Equation (3.2) and (3.3). The

denominator is the squared average of area fraction with box size L. This is one of the definitions of lacunarity.

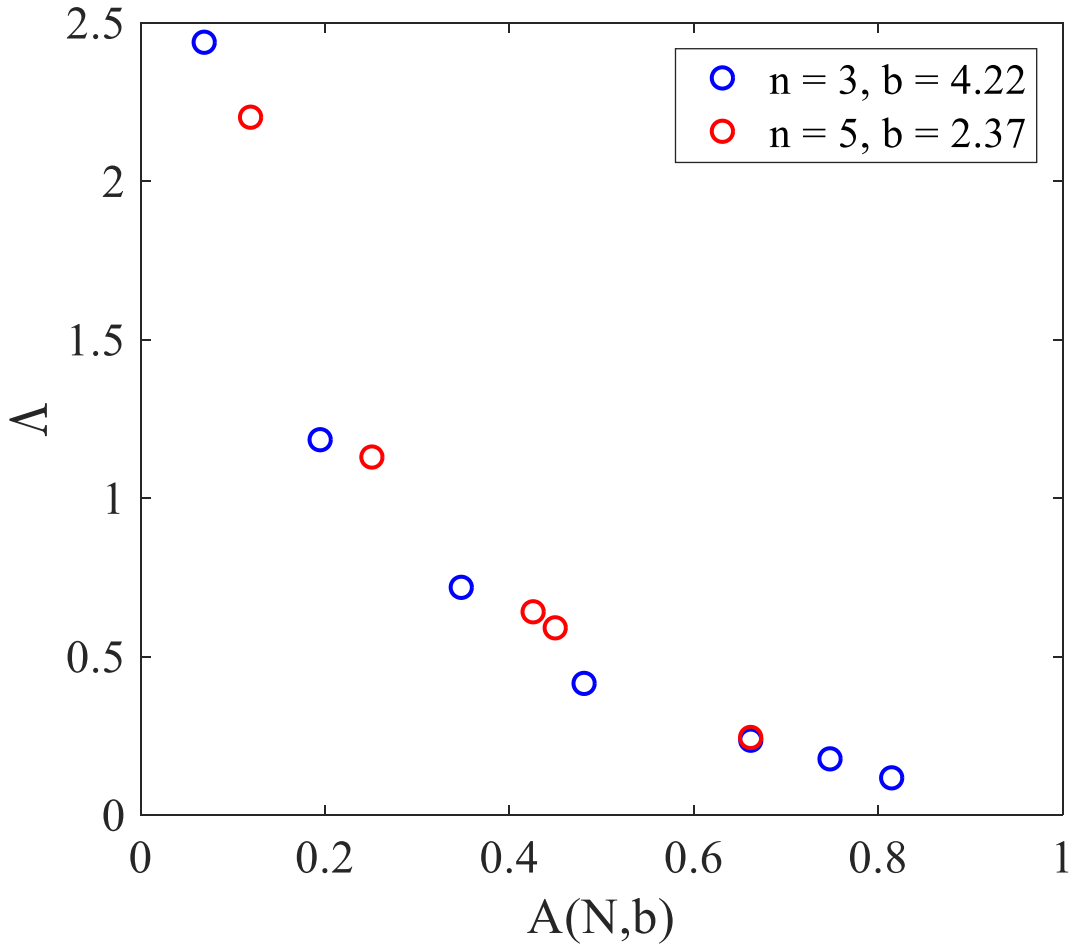

Figure 3.14 The Lacunarity Takes on Approximately Universal Behavior When Plotted vs the Final Area Fraction. Two different generations are considered, *n* = 5 and *n* = 3.

Considering the feature of box-counting method that the size of squares logarithmically shrink by a factor of 2 in each scale, the preferable calculation of lacunarity from numerical aspect is:

$$\Lambda = \frac{1}{n}\sum_{i=1}^{n}\Lambda\left(2^{i}\right) \tag{3.6}$$

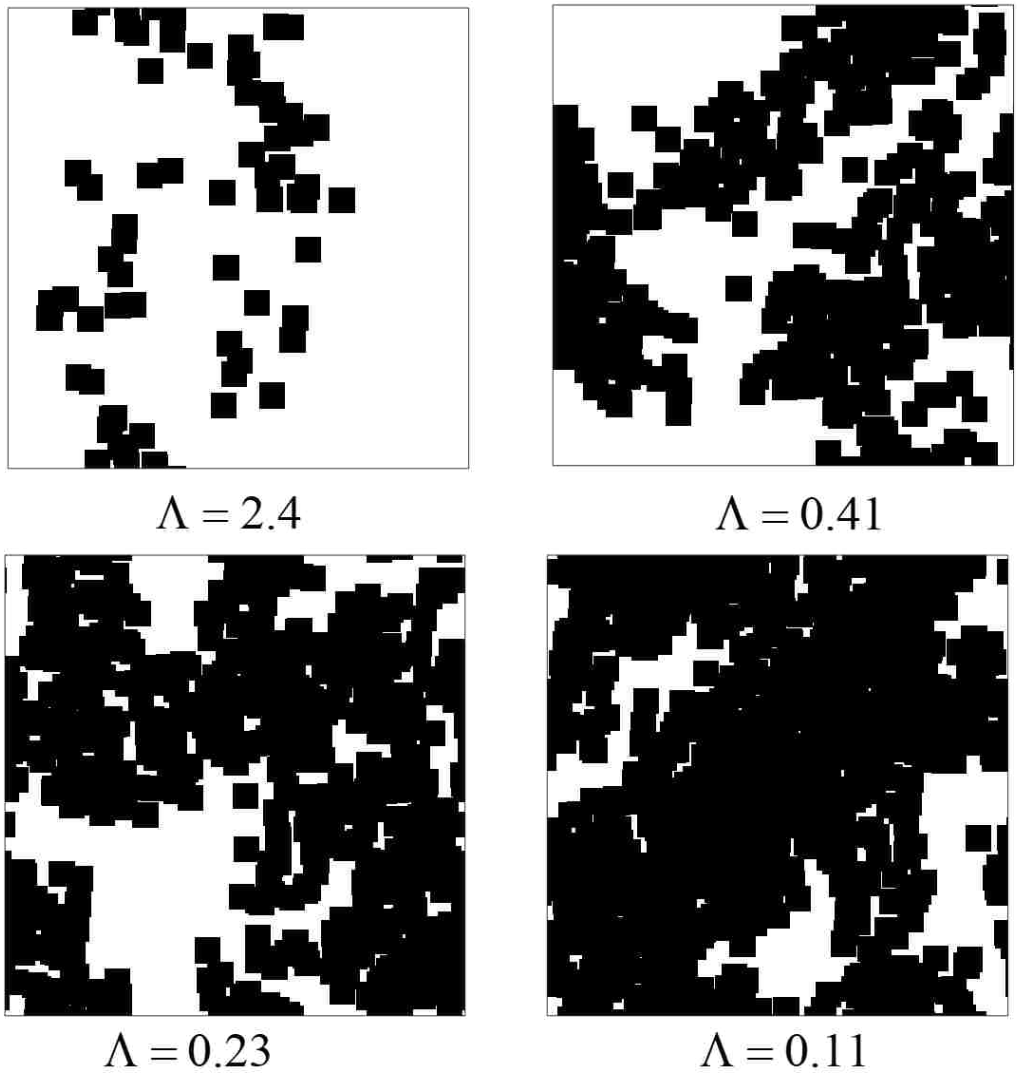

Figure 3.15 Four Patterns of Black Squares with Different Lacunarity. All of them are created with n = 3, b = 4.22.

The measured lacunarity for Monte Carlo simulations of stratified percolation patterns with two generations are given in Figure 3.14 as a function of the final area fraction. In Figure 3.14, Λ decreases sharply when the area fraction is small and with increasing covering area, Λ slowly approaches to zero. As stated before, lacunarity characterizes heterogeneity of the texture in the spatial dimension. When the region of

interest is fully covered by black squares, it becomes homogenous and results in zero lacunarity. Sliding box scanning is the usual way to run the Monte Carlo simulations. More details on this methods refers to Wikipedia. The MATLAB code to implement it is attached in Appendix C.

Four scenarios in Figure 3.14 are selected to illustrate the physical meaning of Λ in Figure 3.15. Three generations with scaling factor b = 4.22 are created. The smaller "hole" in the region, the smaller Λ is.

Fracture dimensions offer a systematic approach to quantifying irregular patterns that contain an internal structure repeated over a range of scales. In preceding two-dimensional fractal analysis, the fractal dimension D and lacunarity Λ are both calculated by box-counting method. The disadvantages of the box-counting technique is that the process does not consider the amount of mass inside a box and is not able to resolve regions with high or low density mass. Multifractal methods are suited for characterizing complex spatial arrangement of mass because they can resolve local densities. In practice, a way to quantify local densities is by estimating the mass probability in the ith box as:

$$P_i(L) = N_i(L) / N_T \tag{3.7}$$

where $N_i(L)$ is the number of pixels containing mass in the *i*th box and N_T is the total mass of the system. Also important is to quantify the scaling (or dependence) of P_i with box size *L*. For heterogeneous or non-uniform systems, the probability in the *i*th box $P_i(L)$ varies as:

$$P_i(L) \sim L^{\alpha_i} \tag{3.8}$$

where α_i is the Lipschitz-Hölder exponent characterizing scaling in the *i*th region or spatial location. These exponents reflect the local behavior of the measure $P_i(L)$ around the center of a box with diameter *L*, and be estimated from Equation (3.8) as:

$$\alpha_i = \log P_i(L) / \log(L) \tag{3.9}$$

Note that similar α_i values are found at different positions in an image. The number of boxes $N(\alpha)$ where the probability P_i has exponent values between α and $\alpha + d\alpha$ is found to scale as:

$$N(\alpha) \sim L^{-f(\alpha)} \tag{3.10}$$

where $f(\alpha)$ can be defined as the fractal dimension of the set of boxes with exponent α. Multifractal measures can also be characterized through the scaling of the *q*th moments of P_i distributions in the form:

$$\sum_{i=1}^{N(L)} P_i^q(L) = L^{(q-1)D_q} \tag{3.11}$$

where D_q is the generalized fractal dimensions defined as:

$$D_q = \lim_{L \to 0} \frac{1}{q-1} \frac{\log \sum_{i=1}^{N(L)} P_i^q(L)}{\log L} \tag{3.12}$$

The exponent in Equation (3.11) is known as the mass exponent of the *q*th order moment, $\tau(q)$:

$$\tau(q) = (q-1) D_q \tag{3.13}$$

From Equation (3.12), we can see that when $q = 0$ all the boxes have a weight of unity, the numerator becomes $N(L)$, and D_q becomes:

$$D_0 = \lim_{L \to 0} \frac{\log N(L)}{\log(1/L)} \tag{3.14}$$

This form is exactly the box-counting dimension used in two-dimensional fractal analysis. It means that monofractal is a special case of multifractal and only considers the homogeneous texture. The other two special moments are $q = 1$ and $q = 2$. The corresponding dimensions are entropy dimension and correlation dimension, respectively. They have physical significance but is not widely in measure of fracture surface. In Equation (3.12), the higher order of q takes more accounts on the low mass density since P_i is in the range of 0 and 1. Therefore, the weights on different mass density can be implemented by different q. The correlation of fractal dimension $f(\alpha)$ and mass exponent $\tau(q)$ is connected by the Legendre transformation:

$$f\left[\alpha(q)\right] = q\alpha(q) - \tau(q) \tag{3.15}$$

and

$$\alpha(q) = \frac{d\tau(q)}{dq} \tag{3.16}$$

The significance of Equation (3.15) and (3.16) is feasible measure of fractal dimension $f(\alpha)$ for varying α.

In practice, the Equation (3.12), (3.15) and (3.16) can be applied to continuum percolation model in this section. The mass density $P_i(L)$ can be calculated by the density of sites in Figure 3.9. One example with *n* = 5, *b* = 2.37 is used to analyze fractal

dimension and mass moment. The pattern of this example is show in Figure 3.16. The white “hole” is non-uniformly distributed in the region of interest. This heterogeneity structure can be quantitatively described by $\tau(q)$, $\alpha(q)$ and $f(q)$. As a comparison, the fractal dimension and lacunarity from monofractal analysis are also calculated. For pattern in Figure 3.16, the fractal dimension is 1.75 by fix-grid scan and lacunarity is 0.2894 by sliding box scan. In multifractal analysis, the D_0 is calculated by $D_0 = -\tau(0)$ which is Equation (3.13) at $q = 0$. Reading from Figure 3.17, it is exactly 1.75 for D_0. Besides this box-counting dimension, the different slope on two side of $q = 0$ characterizes the range of $\alpha(q)$. It shows that $\alpha(q)$ in the negative q is larger than that in the positive q. It means that mass density of small “hole” has more weights in the geometry than large “hole” in the region. This statement comes from the fact that moment $q > 0$ magnifies the contribution of boxes with large “hole” and $q < 0$ magnifies the contribution of boxes with small “hole”. The change of $\alpha(q)$ is shown in Figure 3.18 associated with fractal dimension $f(q)$. Their correlation is plotted in Figure 3.19. It shows highly heterogeneity in the pattern by the un-symmetric shape. To illustrate this point, an extreme example can be taken. If the pattern is homogeneous, the fractal dimension $f(q)$ only has one value located at the peak point. This fractal dimension value is exactly for the largest cluster in the random percolation system in Figure 3.4*a*. In this circumstance, $f(q)$ degenerates to D_0 and the curve shape is more like a δ function.

In addition, the heterogeneity can also be read from f(q) vs α(q) in Figure 3.20. Three different patterns are created with different number of squares in each generation. The information for these patterns are n = 5, b = 2.37 and N = (5, 7, 8). They are kind of clumping together due to very close fractal dimension. The peak of each curve represents

box-counting dimension (q = 0). That means, as increase of area fraction due to more squares in each generation, curve shifts on that auxiliary black line. All curves are tangent to that line. When large N is used, the asymptotic value for the peak would be 2 and that is the maximum fractal dimension in two-dimensional system. The symmetry can be an indicator of homogeneity of the system. For the curve in Figure 3.20, the large α(q) takes more portions, leading to large scaling in patterns and the non-uniform distribution of scaling properties. The associated MATLAB code is attached in appendix C as well.

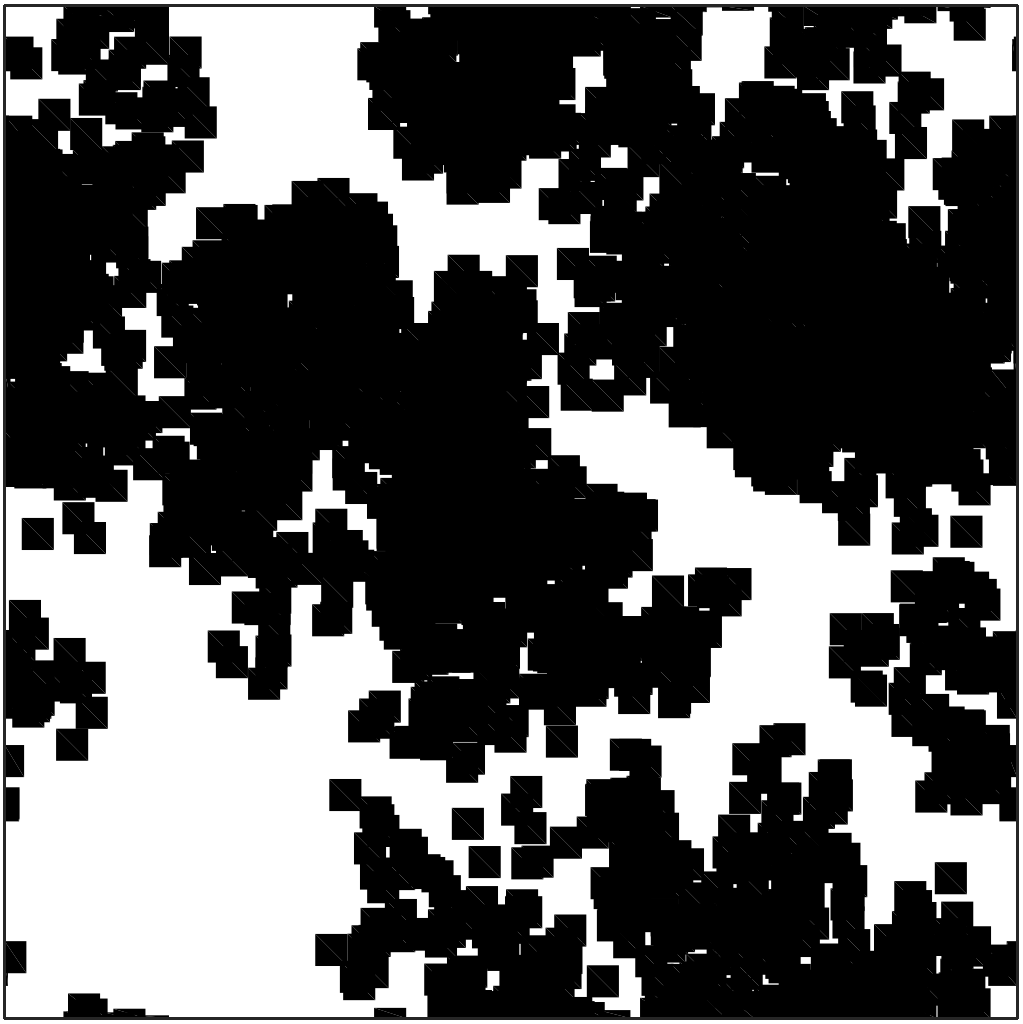

Figure 3.16 One Pattern with $n = 5$, $b = 2.37$.

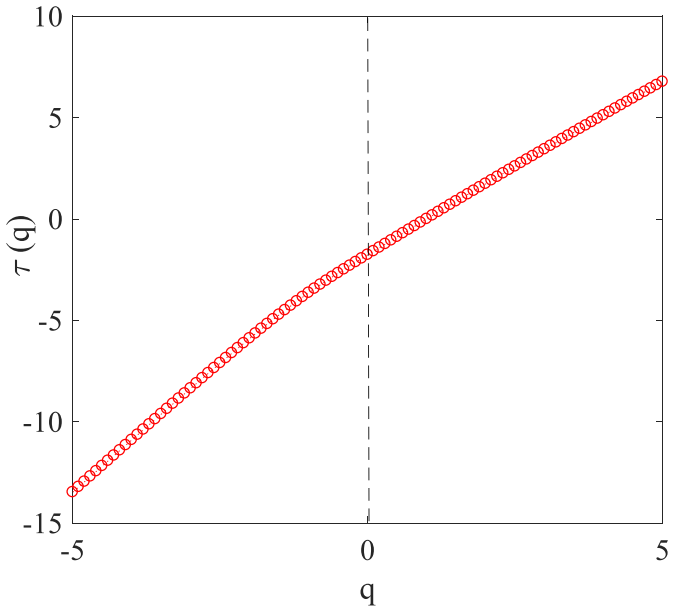

Figure 3.17 Mass Exponent $\tau(q)$ with Respect to q for the Pattern in Figure 3.16.

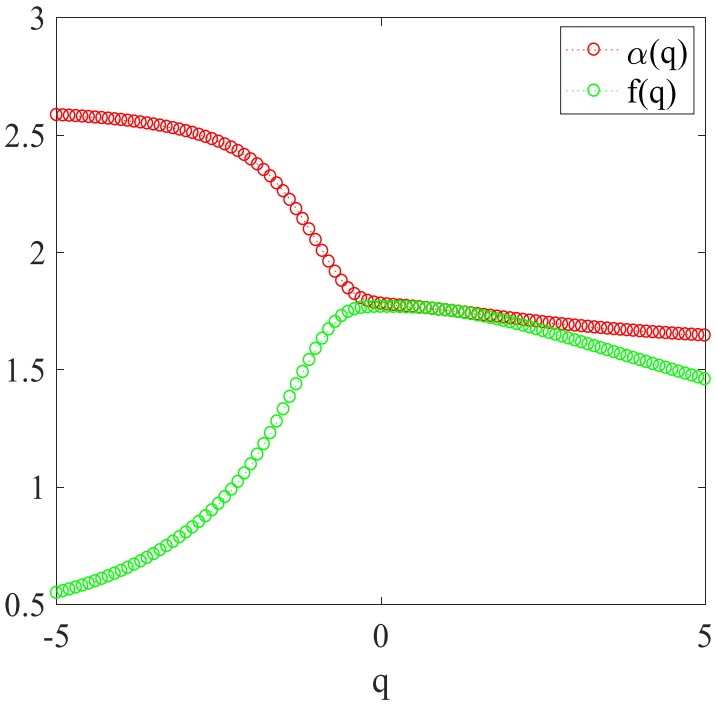

Figure 3.18 Lipschitz-Hölder Exponent $\alpha(q)$ and Fractal Dimension $f(q)$ with Respect to q for the Pattern in Figure 3.16.

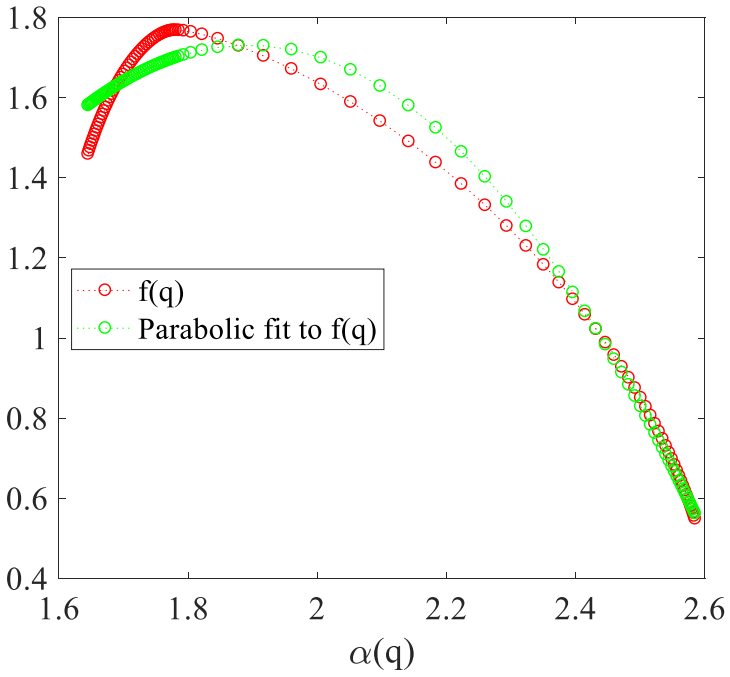

Figure 3.19 The $f(\alpha)$ Curve for Pattern in Figure 3.16.

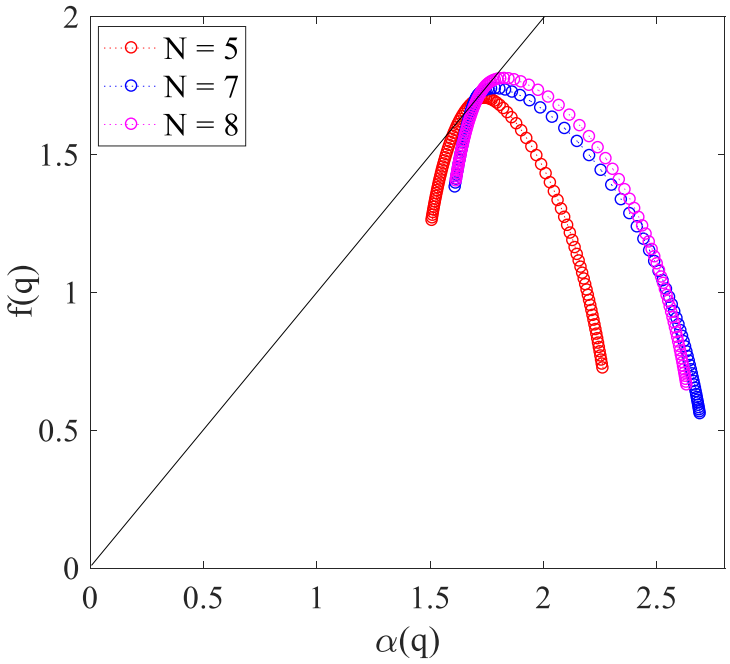

Figure 3.20 The $f(\alpha)$ Curves for Patterns with N = 5, 7 and 8. The curves are all tangent to the line $D = \alpha$.

3.6. SUMMARY

The stratified continuum percolation model incorporates hierarchical cascades of Cantor bar and percolation model. The overlap in the cascades results in multifractal feature of pattern, which resembles the statistical characteristics of fracture surface and aperture [40]. This model is two dimensional, the height distribution can be simulated by the density of sites in each pixel and was successfully used by Pyrak-Nolte et al.[51]. The main motivation of this model comes from the simulation of fluid flow conduits in a fracture. That means that the simulation is based on the fluid flow and on roughness distribution on the fracture surface, then calculate the aperture distribution. From this aspect, the calculation of fluid flow becomes easier, but increases the difficulty of surface characterization at the same time. At any rate, currently no comprehensive model can efficiently and accurately characterize both the fracture surface and the aperture and their deformation as well.

4. FRACTURE DEFORMATION MODEL

4.1. INTRODUCTION TO FRACTURE DEFORMATION

In enhanced geothermal systems, before injected water is pumped into the subsurface, fracture or joint in subsurface remains stable and open. This open fracture is propped by the roughness or asperities on two opposing surfaces. The initial state of asperities requires determination before thermomechanical analysis. Therefore, this section intends to analyze the fracture deformation under loads.

The deformation of fractures went a long way to obtain the current understanding. Initially, the fracture is not assumed to be rough and the perfectly flat surfaces sustains loads elastically. However, the stress-strain curves for fracture loading is nonlinear cannot be explained by this flat surface assumption. With advance of measurement technology, the roughness on the surface can be quantified as in Section 2. Then, the elastic deformation, plastic deformation or even crushing of asperities under different magnitudes of loads are assumed to explain the reason for nonlinear stress-strain curve. In these, Hertzian contact model is widely used as the deformation model for single asperity. Later, Archard [52, 53] proposed that asperities on surfaces remain undamaged even under high loading and concluded that the nonlinear properties is probably attributed to new contact of asperities. The asperity deformation is still elastic even though it undergoes plastic deformation in initial several loading cycles. His statement was verified by Dyson and Hirst [54], Halliday [55]. The asperities were assumed the primary contributor to macroscopic deformation of fracture. Greenwood and Williamson [56] did the breakthrough work on the deformation fracture by numerous asperities on

surfaces. One rough surface was contacted upon a flat surface and the distribution of asperities was assumed to follow Gaussian distribution. The tip or curvature of asperity is treated as spherical and the deformation of asperities follows Hertzian contact model. They take account of the import fact that the elastic deformation of the macroscopic surfaces of the plane and sphere alter the forces on the asperities, and use an iterative process to calculate self-consistent displacement and pressure distribution. The total number of contacting asperities increases proportionally to the load while the average size of a microscopic contacting asperity is almost load independent.

However, the interaction between asperities has not been addressed in preceding models. The conditions for these model to be valid is long distance between contiguous asperities. As shown in Section 2, the asperities is closely clustered on fracture surface. Therefore, their interaction should be carefully justified and taken into account. The interaction was observed experimentally by Williamson and Hunt [57], Pullen and Williamson [58]. The other significance for their work is the fact that material displaced from the contacting regions must reappear by raising some part of the non-contacting surface. Non-contacting surface denotes the void space between contacting asperities or other lower asperities. This infers that deformation of asperities brings bulk deformation of the material surrounding the joint. Usually the bulk material is long enough, bulk deformation on two half bulk can be analyzed by analogy to loading on half-infinite plane. The later has known solution. The bulk deformation would influence the surface shape and the pressure distribution on contacting asperities.

Therefore, fracture deformation model should incorporate deformation of asperity, bulk deformation of surrounding rock and interaction of asperities. In this

section all of them are considered in the model. This model is similar to that used by Hopkins [13]. The following section follows these three components of deformation and validate this model with existing experimental data from literature. It is worth noticing that the asperity is assumed to be cylinder shape in this section and consider as hemisphere in thermomechanical analysis.

4.2. ASPERITY DEFORMATION

As a simple case, the asperity is assumed as rod erected on fracture surface. The design is termed by Gangi [59] as "bed of nails" model. Gangi assigned power law distribution to rod's height and the cross section area is proportional to height. This "bed of nails" model can be used in this section to capture nonlinear closure curve (displacement – loading stress plot). For single asperity, the asperity deformation can be calculated from Hooke's Law for elastic materials (nonlinear deformation is not considered for simplicity):

$$F = \frac{EA}{L_0}\Delta L \tag{4.1}$$

where ΔL is the displacement of asperity due to force F uniformly loaded on top of asperity. A is the cross section area of rod, $A = \pi a^2$, a is the radius of rod. E is Young's modulus of asperities. L is the initial length of asperity at unstressed state. The lateral expansion of asperity in the loading is negligible and not considered in this study. For the shape of asperity, hemispherical contacting asperities are widely used geometry to mimic deformation. That real geometry will be considered in later section and the framework of deformation is constructed in this section.

4.3. HALF-SPACE DEFORMATION

The bulk deformation of surrounding rock takes a primary portion in the fracture deformation. Due to small size of asperity compared to surrounding rock, usually less than 2 mm, and the surrounding rock can be treated as an infinite half space. The load F on surrounding rock is the same to the problem that a load is distributed over circular area on the half space and solve the displacement of plane surface. This solution is well known as Boussinesq solution for a concentrated force acting on the boundary of a semi-infinite solid. For point inside the loaded area, displacement in the direction of the force is:

$$u_i = \frac{4\left(1-v^2\right)F}{\pi^2 Ea}\int_0^{\pi/2}\sqrt{1-\frac{r^2}{a^2}\sin^2\theta}\,d\theta \tag{4.2}$$

where *v* is Poisson's ratio; *r* is the distance from the center of the asperity.

For points outside the loaded area, displacement in the direction of the force is:

$$u_o = \frac{4\left(1-v^2\right)Fr}{\pi^2 a^2 E}\left[\int_0^{\pi/2}\sqrt{1-\frac{a^2}{r^2}\sin^2\theta}\,d\theta-\left(1-\frac{a^2}{r^2}\right)\int_0^{\pi/2}\frac{d\theta}{\sqrt{1-\frac{a^2}{r^2}\sin^2\theta}}\right] \tag{4.3}$$

The sketch of semi-infinite surface deformation is shown in Figure 4.1a. This situation is analogous to displacement of surrounding rock by rigid asperity loading. The elastic deformation of asperity is considered in Section 4.2. The displacement profile along the radial direction on the semi-infinite surface is shown in Figure 4.1b. The properties used to calculate this graph are: E = 20 GPa, v = 0.25, F = 100018 N, a = 1 mm. The displacement in the asperity area is enclosed by two red dash lines. It shows that

displacement is not uniform in the asperity area, and maximizes in the center of asperity area. The formula for maximum displacement is:

$$u_{\max} = \frac{2\left(1-v^2\right)F}{\pi aE} \tag{4.4}$$

At r/a = 5, the displacement u/umax ≈ 0.1. It means that the displacement outside of loading area is still significant. This is just the presentation for one rigid asperity, and becomes more obvious when bunches of asperities locates together. While in the real simulation the stress on the asperity remains constant from in-situ stress, the displacement at three different asperity radius are plotted in Figure 4.2 with same loading stress. It shows that large asperity takes more loads. This is an important result in terms of joint stiffness, which depends on the average displacement across the fracture. If the tall asperities are clustered together to form large contact areas, the average displacement across the fracture will be greater than if the asperities are dispersed. This point will be elaborated in later section.

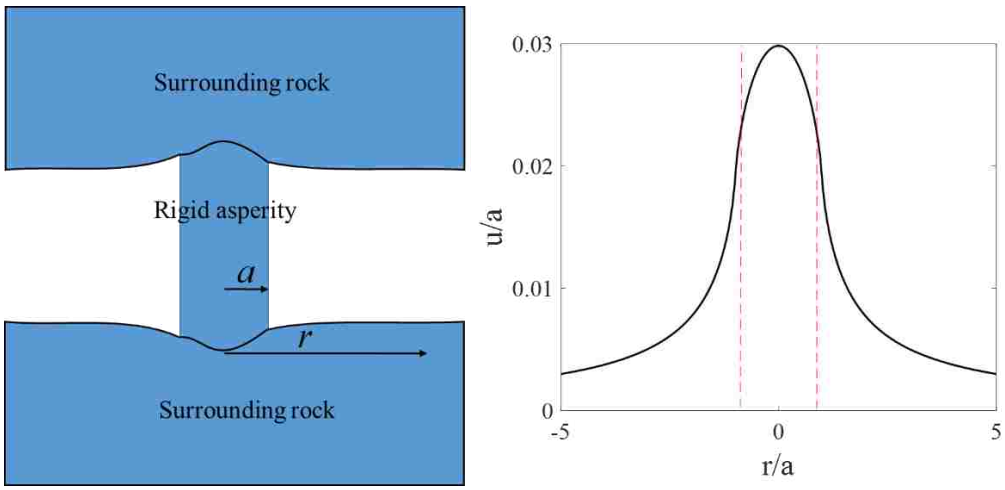

Figure 4.1 Half-Space Deformation by Rigid Asperity Loading. (*a*) The sketch and (*b*) the displacement along the radial direction.

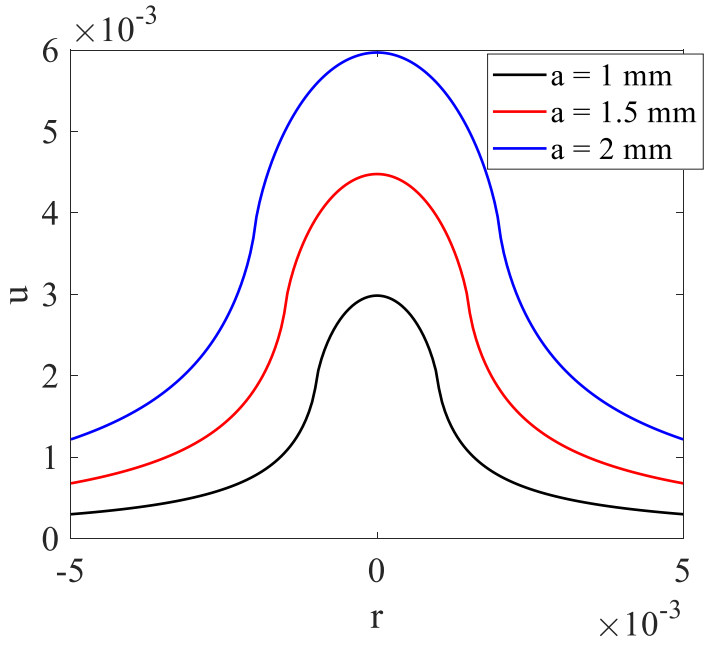

Figure 4.2 The Displacement along Radial Direction at Different Radius of Rigid Asperities.

Even though the displacement under and outside of asperity area in the semi-infinite surface are calculated by Equations (4.2) and (4.3), the complicated form is intractable to numerous asperities on fracture surface. Therefore, the average displacement of surrounding rock under asperities area is:

$$\bar{u} = \frac{1}{\pi a^2} \iint u_i dr d\theta \tag{4.5}$$

The integral is to calculate the volumetric displacement and $\bar{u}$ denotes average displacement of surrounding rock under asperity area.

4.4. MECHANICAL INTERACTION OF ASPERITIES

The mechanical interaction of asperities is a simple extension to Section 4.3. In Figure 4.2b, loading on asperity also causes some displacement outside of asperity. When

other asperities are loaded in the surrounding, that displacement induced by individual asperities at a particular position is superposed together under the assumption of small deformation theory. For example, two asperities *i* and *j* are located in the position shown in Figure 4.3. The loading on asperity *i* causes displacement beneath j to be:

$$\bar{u}_{ij} = \frac{1}{\pi a^2}\int_{r_1}^{r_2}\int_{\theta_1}^{\theta_2} u_o(r)\, d\theta dr \tag{4.6}$$

The loading on asperity *i* causes displacement beneath *i* to be:

$$\bar{u}_{ii} = \frac{1}{\pi a^2}\int_0^a u_i(r)\cdot 2\pi r dr \tag{4.7}$$

where double subscripts *ij* denote displacement beneath asperity *j* caused by loading on asperity *i*, depending on the equality of *i* and *j*. $\bar{u}_{ij}$ is the average displacement beneath *j* by loading on asperity *i*, *a* is the radius of asperity *j*.

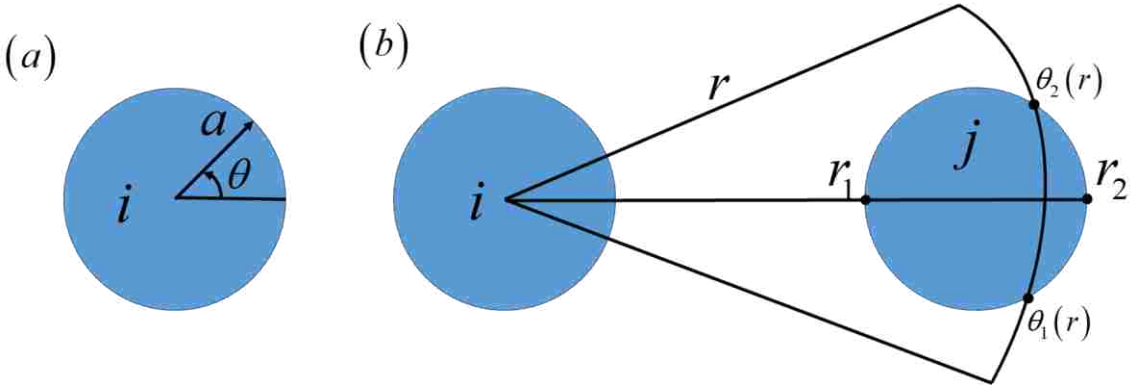

Figure 4.3 The Geometric Relation of One Asperity and Two Asperities in Mechanical Interaction. (*a*) One asperity *i* and (*b*) two asperities *i* and *j*. In (*b*), the closest point on *j* to center of *i* is r_1 and longest distance to center of *i* is r_2. The angles of arc intersected with *j* counter clockwise are $\theta_1(r)$ and $\theta_2(r)$.

Based on simple geometric calculation (referring to Figure 4.3), the effect of particle *i* to particle *j* can be expressed as the function:

$$\bar{u}_{ij} = \frac{1}{\pi a^2}\int_{r_1}^{r_2} u_0(r)\cdot 2r\cdot \arccos\left[\frac{R^2+r^2-a^2}{2Rr}\right]dr \tag{4.8}$$

where *R* is the distance between two asperity centers.

The underlying assumption used in Equations (4.7) and (4.8) is uniform radius of asperity. If the asperity radius varies, two radius symbols should be used instead. Therefore, the total average displacement beneath asperity i is the superposition of displacement caused by its own loading and other loadings:

$$\bar{u}_i = \sum_{j=1}^{N} \bar{u}_{ji} \tag{4.9}$$

where *N* is the total number of asperities in the region. Both Equations (4.7) and (4.8) are included in this form.

An example is taken for illustrate the influence of mechanical interaction of asperities. Two cylindrical rigid asperities erect on the semi-infinite surface. The loading parameters and mechanical properties are: E = 20 GPa, v = 0.25, a = 0.5 mm, F = 1 kN. The distance between two cylindrical is dist. Two dist are selected: dist/a = 2 and dist/a = 6. The configuration of model is shown in Figure 4.4a. The displacement profile along horizontal direction is shown in Figure 4.4b. The high plateaus corresponds to average displacement beneath rigid asperities. With longer distance between two asperities, the average displacement beneath rigid asperities decrease gradually. When the distance is long enough, the mechanical interaction of asperities vanishes and the displacement beneath each asperity is the same as in Figure 4.1*b*. Therefore, the clumping of asperity substantially increases the deformation of surrounding rock. This clumping property is characterized by multifractal analysis in Section 3. In addition, the deformation between

asperities is significant in Figure 4.4*b*. It reaches half of deformation beneath asperity when *dist*/*a* = 2. This significant effect of deformation cannot be neglected since it squeezes fracture aperture and leads to more contacting asperities between two tall asperities.

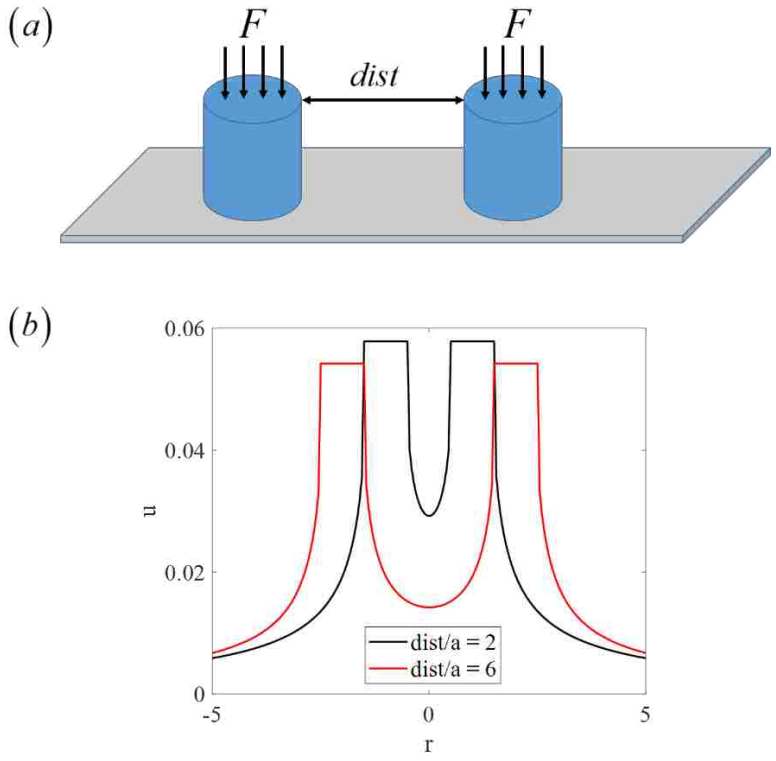

Figure 4.4 Mechanical Interaction of Two Rigid Asperities Loading on Semi-Infinite Elastic Plane. (*a*) The configuration of model and (*b*) the resulting displacement.

4.5. FRACTURE DEFORMATION

Section 4.2 introduces deformation of single elastic asperity, and Section 4.4 introduces the deformation of surrounding rock caused by mechanical interaction of rigid asperities. Combination of them tells the compression of elastic asperity and surrounding solid rock. With presence of more than one asperity in the fracture surface, this

combination can only solve the fracture displacement with asperities having same heights. For the varying heights, either specified stress condition or specified displacement condition does not determines how many asperities will come into contact. When the number of contacting asperities is unknown, that procedure in Section 4.2 and 4.4 is not enough to obtain total displacement or stress between fracture surfaces. Therefore, more constraints are required to find the solution. In this section, the fracture deformation with varying heights of asperities will be determined. The constraints to reach that deformation is introduced below.

For simplicity, consider a single asperity between two half space. The ketch of asperity in fracture is shown in Figure 4.5. The initial length of asperity is L_0. After loading, its length becomes L, and also cause displacement of half space $\bar{u}_i$. The resulting fracture aperture is b. The deformation of asperity is $\Delta L = L_0 - L$. In addition, the relation $L = \bar{u}_i + b$ holds. Combining these two equations, the equation for deformation is:

$$\bar{u}_i + b + \Delta L = L_0 \tag{4.10}$$

Equation (4.10) applies for contacting asperity. If the adjacent asperity with lower height and does not contact with both fracture surface, the inequality for deformation is:

$$\bar{u}_i + b > L_0 \tag{4.11}$$

Variable b is unknown beforehand. It can be determined by iterative scheme. Other variables are from preceding sections in this section. The loading displacement d is more widely used as a boundary condition, therefore it is used in the iterative procedure as $d = L_0 - b$. It says that force is linear to these displacement variables and is favorable to

work as independent variable in the calculation. The structure of fracture has to be known. In this way, the positions of asperities and their heights are known. If loading displacement is specified, that is, *d* is known, the force on each asperity can be calculated by Equations (4.10) and (4.11) with iteration. If loading force is specified, fracture deformation can be calculated by Equations (4.10) and (4.11) without iteration. The MATLAB code is attached in Appendix C.

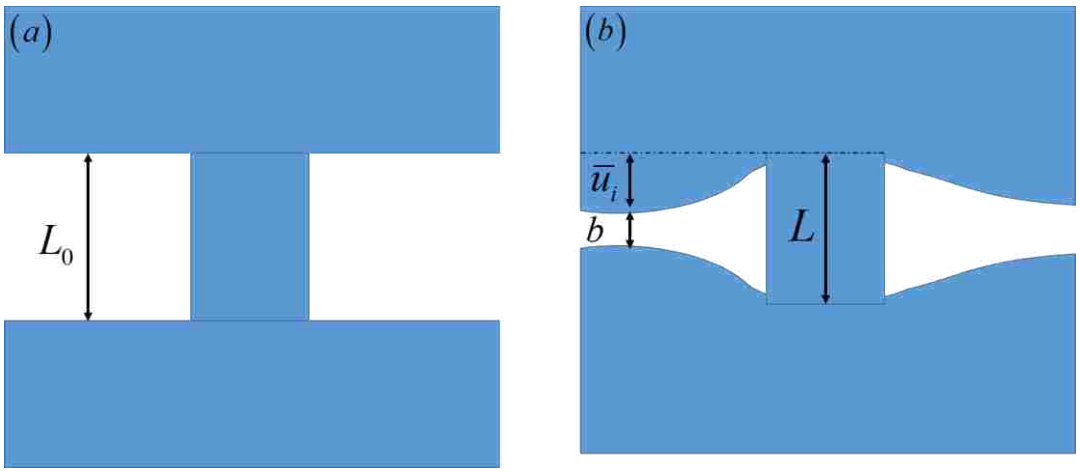

Figure 4.5 Geometric Relation in Fracture Deformation. (*a*) The initial unstressed state of single asperity with length L_0, (*b*) the stressed state of single asperity with length L, the displacement of surrounding rock on one side is $\bar{u}_i$ and the fracture aperture outside the influence distance is b.

4.6. VALIDATION OF FRACTURE DEFORMATION MODEL

As stated, the position and heights information about asperities are required before specific calculation. To ensure that the model calculated force with the correct magnitude, tests are constructed that allows model results to be compared to analytical solutions. As a simple case, the asperities has equal radius of 0.5 mm and are spaced 0.5 mm apart. The height is assume to 3.5 mm for all of them. Total number of asperities are

50 in a row. The properties for both asperities and surrounding rock are E = 20 GPa, v = 0.25. The force on each asperity is shown in Figure 4.6b. The force is non-uniform distributed. The asperities at the edge takes more force than the middle one. Because asperities at the edge has less interaction effect than the middle. The surface has less indentation and leads to relatively taller asperities than the middle. The total force taken by asperities is 53.98 kN. Therefore, more force is loaded on them. This result complies with our expectation. In addition, the relative importance of interaction and self-deformation of asperities can be compared in this example. Take the 30th asperity for example, it is subjected to deformation by other 49 asperities and its own deformation. The loading force on it is 1.05 kN reading from Figure 4.6b. Its own deformation is 0.234 mm and the deformation induced by other asperities is 0.266 mm. The total deformation is 0.5 mm. It shows that asperity deformation is less than the surrounding rock deformation. Therefore, it demonstrates the significance of surrounding rock deformation.

More realistic case is asperities with varying heights. Taken an example of height distribution as $L_0 = 3 + 0.5\sin\left(6\pi x / 73.5\right)$, where x is the distance to first asperity. The origin is at the center of first asperity. Other parameters remain the same as that example with equal height. The force on each asperity is shown in Figure 4.7b. The total force taken is 19.1 kN, much less than that in uniform height even though the displacement is the same. Three ‘hills’ in Figure 4.7b correspond to three humps in Figure 4.7a. Therefore, fracture deformation is related to asperity distribution and cluster of asperities sustains more weights than discrete asperities. This statement is consistent with Hopkins [13].

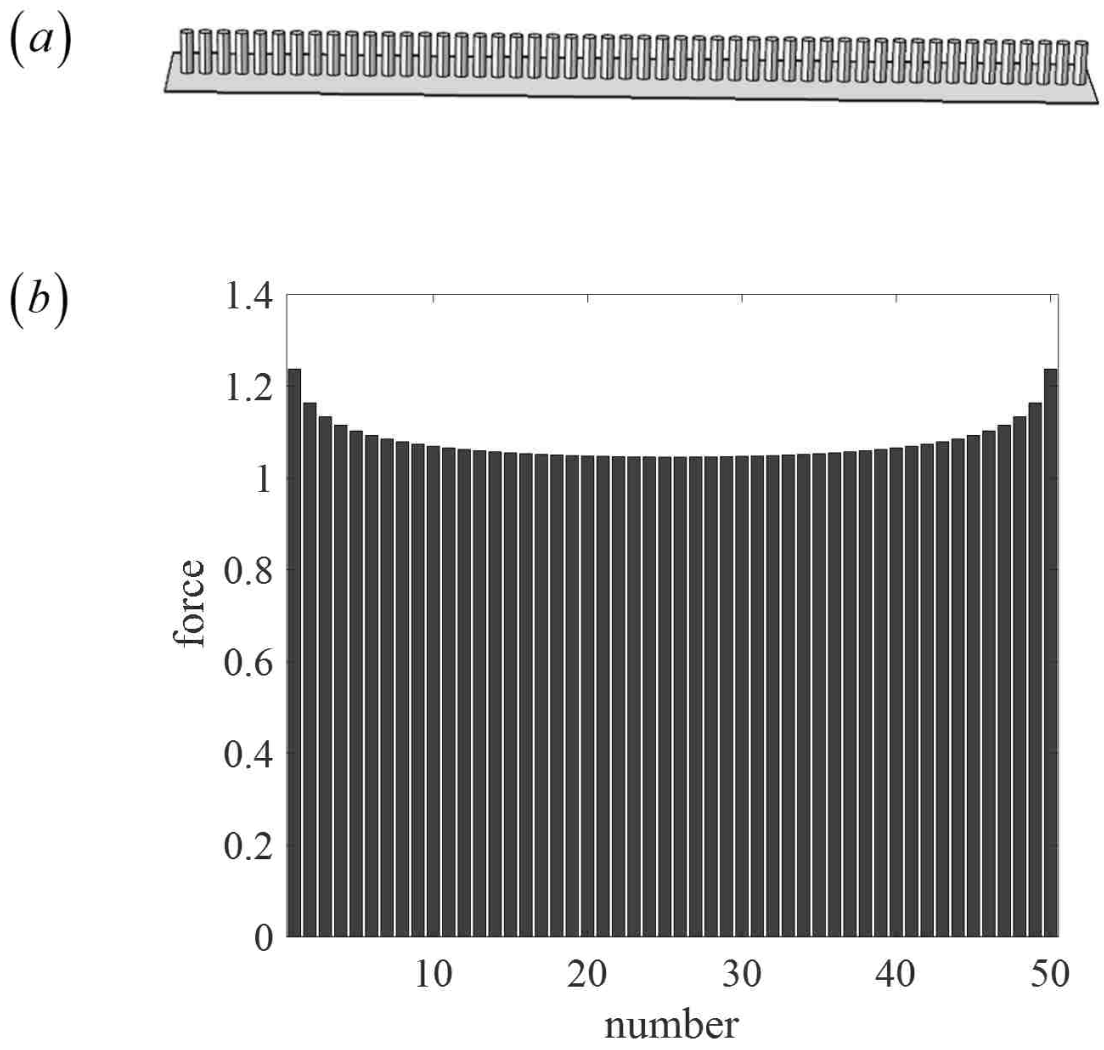

Figure 4.6 Force Distribution on Row of Asperities with Equal Height under Specified Displacement. (*a*) The configuration of asperities and (*b*) the force loaded on each asperity for uniform height.

After having a basic understanding of fracture deformation, a well-known model is used to validate our fracture deformation model. A rigid punch presses on a semi-infinite half-space and the loading area is circular. The configuration of this model is shown in Figure 4.8.

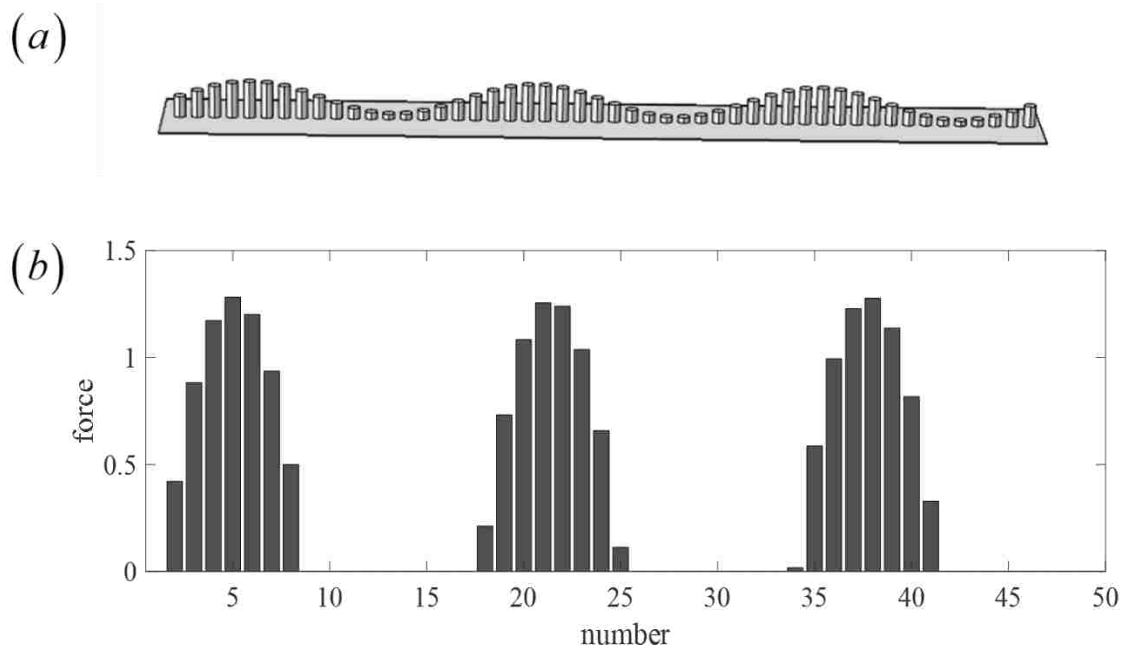

Figure 4.7 Force Distribution on Row of Asperities with Sinusoidal Height under Specified Displacement. (*a*) The configuration of asperities and (*b*) the force loaded on each asperity for sinusoidal heights.

Because the punch is assumed to be absolutely rigid, the displacement beneath the punch is constant and is given by:

$$u = \frac{P\left(1-v^2\right)}{2aE} \tag{4.12}$$

where P is the total load on the punch, a is the punch radius, v is the Poisson's ratio, E is Young's modulus.

The distribution of stress across the punch is given by:

$$\sigma\left(r\right) = \frac{P}{2\pi a\sqrt{a^2 - r^2}} \tag{4.13}$$

where r is the distance from the center of the punch.

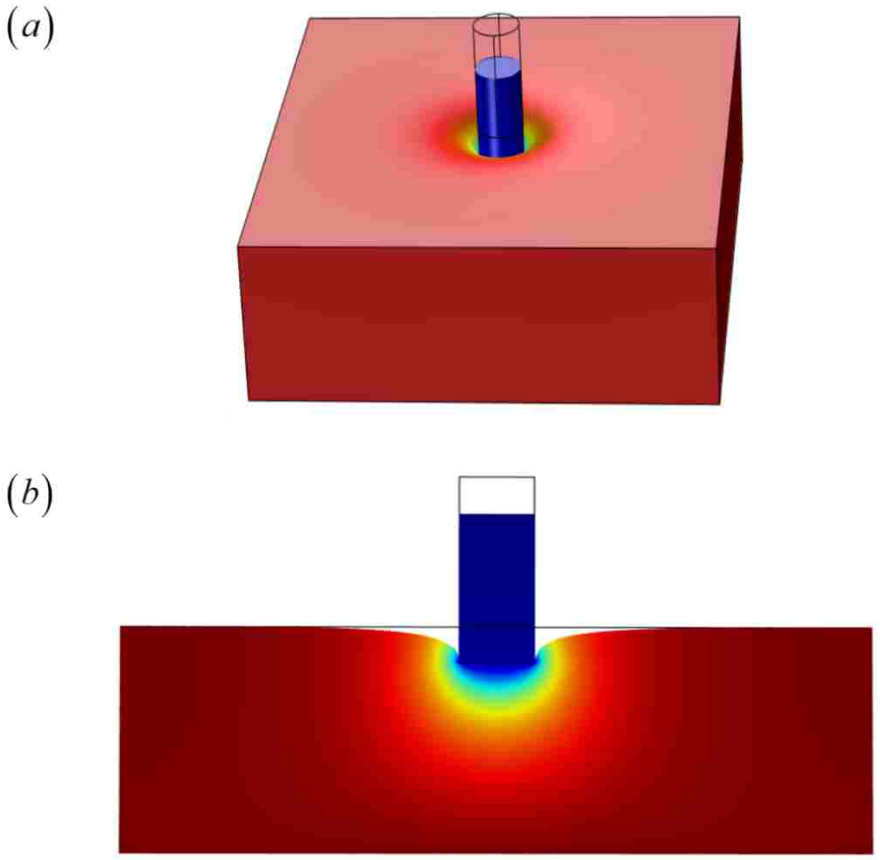

Figure 4.8 A Rigid Punch Presses on a Semi-Infinite Half-Space. (*a*) Three-dimensional display and (*b*) cutting plane display.

This rigid punch test can be simulated by fracture deformation model in this section. Due to circular loading area, the arrangement of circles has to form a large circle and rings can form in this arrangement shown in Figure 4.9. The number of inner circles to fill the outer circles of radius *a* is:

$$n = \frac{\pi a^2}{4b^2} \tag{4.14}$$

where *a* is the radius of rigid punch or outer circle and *b* is the radius of small disks or inner circles. Inversely, if the number of inner circles is known, the radius of small disks

can be determined by Equation (4.14). Based on geometric relation that the inner circles along radial direction can optimally fit the outer circle, this relation holds:

$$a \approx b(2m - 1) \tag{4.15}$$

where m is the number of rings. In Figure 4.19, two inner rings present. Substituting into Equation (4.14), the equation is:

$$n \approx \frac{\pi}{4}(2m-1)^2 \tag{4.16}$$

Both m and n are integer. Therefore,

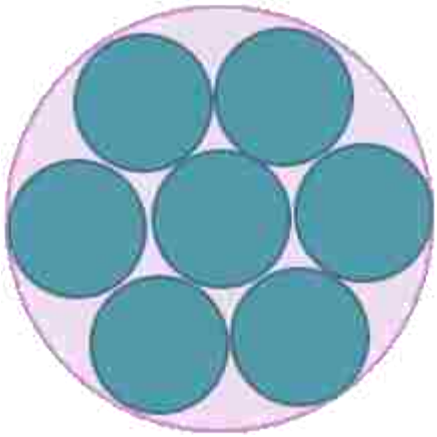

Figure 4.9 The Arrangement of Inner Circles to Fill the Outer Circles.

In addition, to satisfy the condition that the punch is rigid, the disks used to model the punch are given high Young's modulus. The used parameters are Es = 20 GPa, v = 0.25, Ep = 2000 GPa, a = 0.5 mm. The number of inner circles are 19, 62, 132 and 226. The corresponding radius of disks are 0.1017 mm, 0.0563 mm, 0.0389 mm and 0.0297 mm. The configuration of circular disks is shown in Figure 4.10. The height of cylinders

is set to 2 mm, and the specified displacement is 0.2 mm. The analytical total force is calculated by equation:

$$P = \frac{2auE}{1-v^2} \tag{4.17}$$

where u is the specified displacement for rigid punch.

For the numerical total force, it is obtained by summation of force on individual disk. The force on disks is obtained by formation deformation model. The small modification is required due to rigid punch and only half space. The total force is termed as numerical total force and presented in Table 4.1.

Table 4.1 The Comparison of Total Force

No. of rings	No. of disks	Disk radius (mm)	Total force (numerical)	Total force (analytical)	Diff. (%)
3	19	0.1	3.9355	4.2667	7.76
4	38	0.0714	4.045		5.2
5	62	0.0556	4.0872		4.21
6	95	0.0455	4.1285		3.24
7	132	0.0385	4.14		2.97
8	176	0.0333	4.1575		2.56
9	226	0.0294	4.169		1.8

It shows that numerical total force gradually approaches the analytical total force. The difference is also shown in last column. With reduce of disk radius, the total area

they occupied also approaches real area of rigid punch. The real area is 0.7854 mm^2. The area for numerical disks are 0.5969 mm^2, 0.6086 mm^2, 0.6021 mm^2, 0.6179 mm^2, 0.6147 mm^2, 0.6131 mm^2, 0.6137 mm^2.

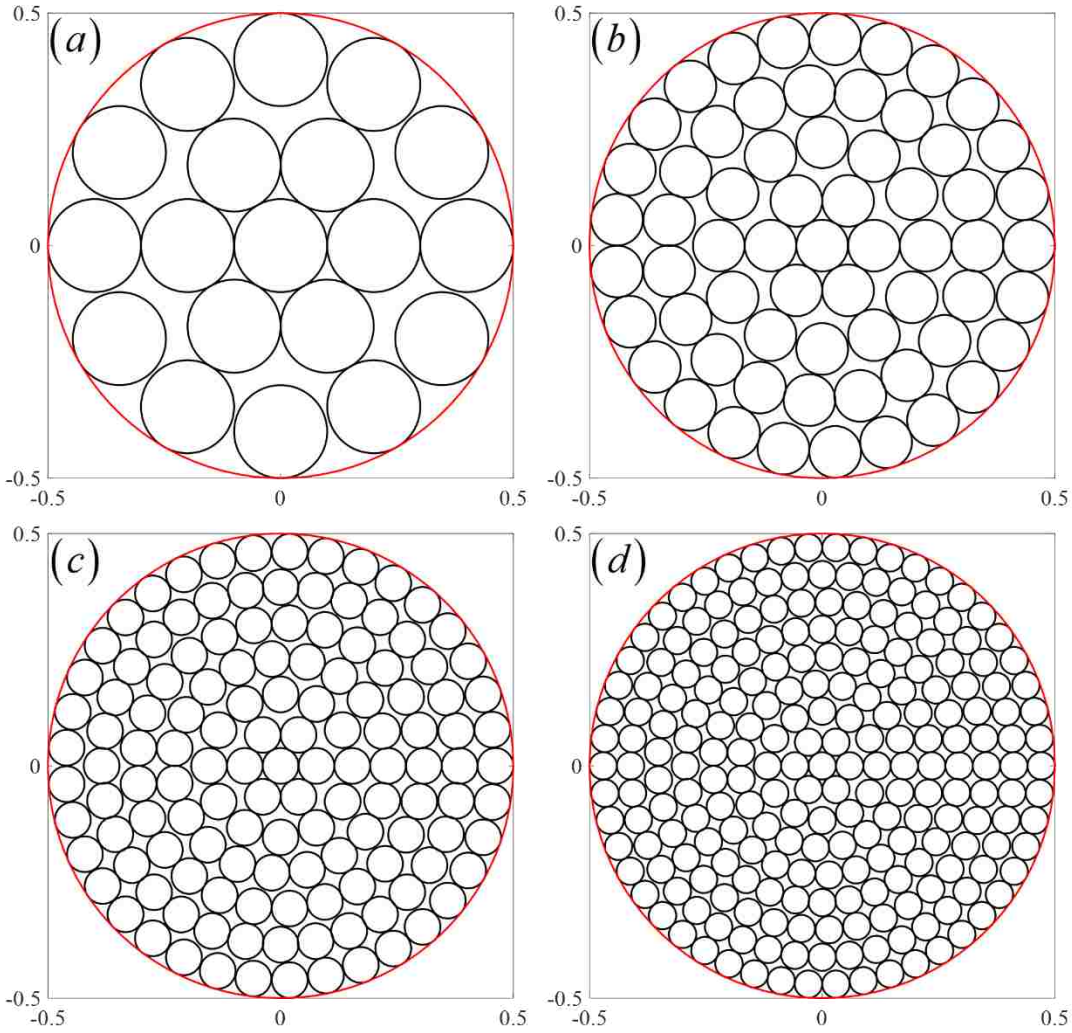

Figure 4.10 The Configuration of Circular Disks in Numerical Method.

Besides the total force on the circular rings, the stress distribution along radial direction can also be compared with analytical solution. For analytical solution, the stress

distribution is given by:

$$\sigma(r) = \frac{P}{2\pi a\sqrt{a^2 - r^2}} \tag{4.18}$$

This stress is inversely proportional to distance to center of rigid punch. When r approaches edge of punch, it becomes infinite. The numerical stress distribution is calculated from disk along radial direction. Because stress is independent on θ, the sequential disks along radial direction is selected and the stress is calculated as:

$$\sigma_i = \frac{f_i}{A_i} \tag{4.19}$$

where f_i is the force loading on that disk and A_i is its area, σ_i is the average stress on that disk. The stress comparison is shown in Figure 4.11. Only one case is presented. With more rings considered, two curves become smooth and closer to each other.

In summary, a fracture deformation model is established with cylindrical geometry of asperities. The fracture deformation has three components: asperity deformation, mechanical interaction of asperities, half-space deformation. The half-space deformation dominates the fracture deformation. Even though the asperity is simple, the significance of asperity distribution can still be captured. The asperity cluster can sustain more loads than discrete asperities. That explains the cluster distribution of asperities in Section 3. This model takes advantage of circular cross section of asperities. In this circumstance, the stress distribution induced by loading on asperities is well known [60]. It is easy to group individual disks to large geometry, like the rigid punch test. This concept is used to validate fracture the deformation model with the rigid punch test.

However, this cylindrical assumption of asperities is oversimplified. The hemispherical geometry of an asperity is more often used in the literature. The Hertzian contact model is found to be unrealistic in terms of high stress concentration on the tip of the asperity. Therefore, a more realistic model is required to replace the cylindrical asperities. Other parts can remain the same. This is the objective of next section.

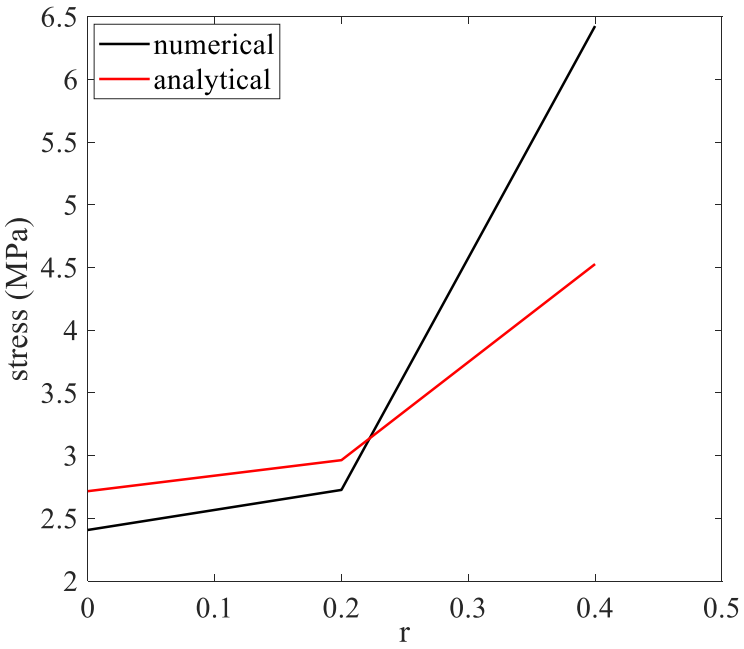

Figure 4.11 The Stress Distribution with Respect to Distance from Center of Rigid Punch for Three Rings.

5. DEFORMATION OF HEMISPHERICAL ASPERITY

5.1. INTRODUCTION TO ASPERITY DEFORMATION

Enhanced geothermal systems (EGS) provide an alternative energy solution by injecting water into hot rock and recycling the heated water for baseload electricity generation as clean energy [61, 62]. The report of a Massachusetts Institute of Technology study predicted a potential of 100 GWe of cost-competitive electricity capacity could be achieved by EGS in the next 50 years in the United States with suitable investment and improvements to existing technology [62]. In the study of EGS mechanisms, the energy production efficiency is mainly influenced by reservoir permeability, water production rate, rock thermal conductivity and injection temperature; among these factors, reservoir permeability is the most important one [63, 64]. It has been well recognized that fractures, generated either by hydraulic fracturing or by shearing reactivation in geothermal reservoirs, play a critical role in the determination of reservoir permeability and the control of flow and heat transport. Changes of fracture network could result in a significant impact on the energy production efficiency of EGS as well as the recycling rate of injected working fluid [64, 65]. Although various working fluids have been suggested such as CO_2 [66], ammonia, n-Butane and neopentane [66], water is the most popular working fluid considered in EGS. Great efforts have been made to study the impact of fracture networks on EGS for energy production efficiency and water loss rate in which case the energy and water as working fluid are two of the most important resources for human society needs [67]. Such efforts include using the fracture continuum method [68], the single porosity method [69], the dual porosity method [70],

and the discrete fracture network method [71]. Among these fracture network studies, however, the geomechanical effects are seldom considered. Geothermal reservoirs are mainly developed in tectonically stressed sedimentary basins at depths of approximately 3 km to 5 km with temperatures of up to 350˚C [72]. By injection of cold water into hot dry rock (HDR) to be heated up, large temperature differences exist between the injected water and the HDR of the ambient geothermal reservoir. This temperature difference could exert thermal stress on the rock and have a geomechanical impact on each fracture. Similar thermal effects also are present in other problems such as deep earth energy storage, CO_2 sequestration and enhanced oil recovery. By assuming fractures as equivalent porous media, Pandey et al. [73] analyzed the thermo-elastic effect on fracture aperture and concluded that the cooling effect by water injection could induce fracture opening in the vicinity of the injection well and closure of fractures at far field locations. In their analysis, only the rock matrix contraction due to cooling had been considered. The Soultz-sous-Forêts pilot site study verified such occurrences of a thermal contraction zone at the reinjection zone [74]. In other aspects, thermal stimulation to generate secondary fracture opening by injecting cold water into primary fractures was studied [75]. Multiple secondary thermal fractures could be created and propagate perpendicular to main fracture with different rates and final lengths for distinctive temperature difference. This fracture initiation by thermal shock of reservoir rock were demonstrated in experiments [76] as well as in analyzed theoretical models [77, 78].

In contrast to the fractures generated by hydraulic fracturing for shale oil recovery, most fractures in EGS are pre-existing and self-propping fractures [79]. The geomechanical integrity of self-propping asperities is therefore important to the integrity

of fracture networks in EGS. Nevertheless, extant studies have not yet paid much attention to the geomechanics of the self-propping asperities, especially when fractures with self-propping asperities are subject to degradation due to large thermal stress caused by sudden cooling effects. Thermal stress due to the rock/water temperature difference by cold-water injection can damage fracture self-propping asperities, reduce fracture aperture, and even close the fractures. This study aims to bring such thermal effects to the attention of EGS studies, encouraging researchers to study how such thermal effects could affect the self-propping asperity integrity. Through finite element analysis by assuming idealized asperity shape as semi-sphere, we have demonstrated the failure of fracture asperity when the water/rock temperature difference reaches critical values under various overburden pressures.

5.2. PROBLEM STATEMENT AND METHODOLOGY

To explore the thermal effect on self-propping fracture asperities and keep our problem focused, we considered an idealized fracture which has parallel plates as walls and a pair of semi-spheres as asperities (Figure 5.1*c*); high resolution real-world fracture mapped by optical profilometry [80] will be considered in our future work due to the duration limit of this study. The semi-spheres prop a fracture open by bearing overburden pressure. When the injected water is exposed to the high temperature of the surrounding rock matrix, the asperities are subject to a sudden large thermal stress, and pore pressure changes are negligible compared to corresponding large thermal stress on an asperity [81]. Such thermal stress could damage self-propping asperities and deteriorate fracture network integrity in EGS. To investigate its possible impact on EGS, a quantitative

model had been developed to describe the mechanical response of the asperity to the thermal stress by considering a damage based constitutive law on asperities [82]. Due to the symmetry of the semi-sphere pair contact, only one semi-sphere was considered.

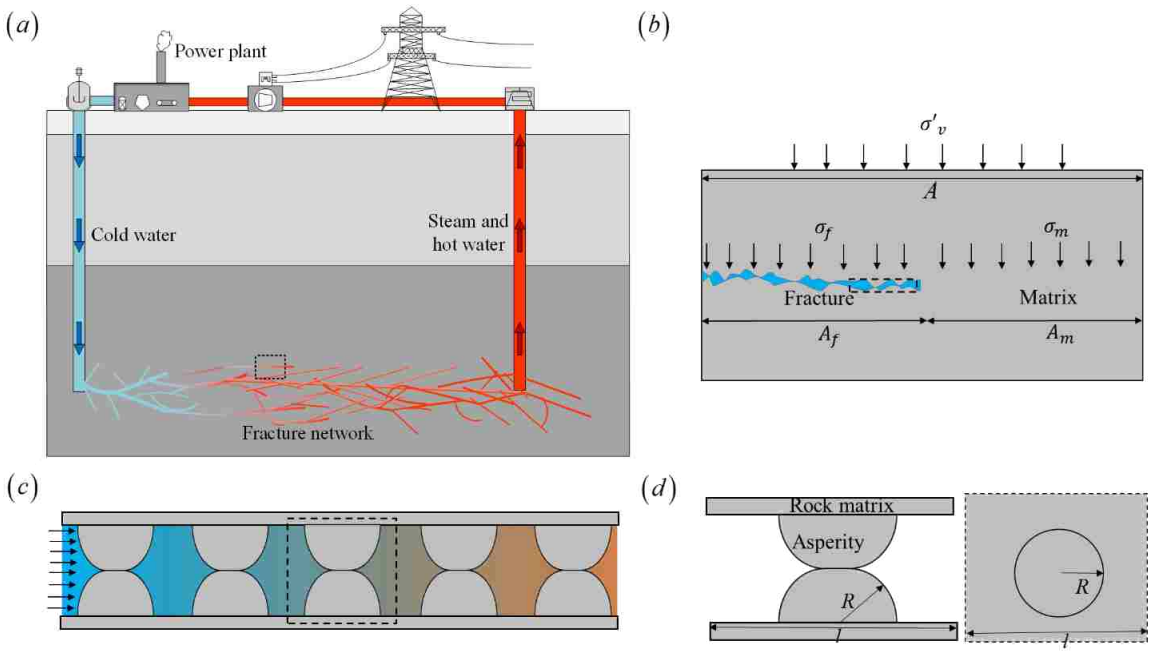

Figure 5.1 Sketch of Enhanced Geothermal System and Asperity Distribution of Interest. (*a*) Schematic of typical enhanced geothermal systems (EGS), (*b*) the fracture configuration and stress distribution in fractured zone, (*c*) the idealized asperity distribution on the surface of rough fracture, (*d*) idealized asperity pair bonding with rock matrix in one unit cell at frontal view (left) and top view (right).

5.2.1. Mapping of Loading Stress on Asperity. The large in-situ stress in deep formation does not uniformly load on fracture surface and rock matrix at its average magnitude in the fractured zones. The real loading stress on asperity is much lower than the nominal in-situ stress. A simple mapping method was used in this study to calculate the loading stress on asperities; for more accurate but complicated methods readers may refer to the work by Hopkins [13]. In our model, in-situ stress distribution along depth

was specified as in Soultz-sous-Forêts geothermal project [83]. Overburden pressure σ_v was taken to be a linear function of EGS depth z (in a unit of m): $\sigma_v = -1.3 + 25.5z$ kN/m^2, and pore pressure was also modeled as a linear function of depth z: $u = 0.9 + 9.8z$ kN/m^2. We defined the net pressure difference between σ_v and u as effective overburden pressure $\sigma'_v = \sigma_v - u$. As demonstrated in Figure 5.1*b*, when a fracture is present at certain depth of fractured zone, the fracture asperities only take up a small portion of the loading compared to rock matrix body. The far-field overburden pressure is balanced partially by pressure on fracture surface and pressure through rock matrix body, respectively (Figure 5.1*b*). In this model, a conservative 2:1 model of pressure on rock matrix to pressure on fracture surface was specified. That is, $\sigma'_v A = \sigma_f A_f + \sigma_m A_m$ applies based on the force balance and $A_f = 2A_m$. The physical presentation of these symbols are in Figure 5.1*b*. Need to note that the configuration of fracture in geothermal reservoir has small aperture but large depth. The sketch in Figure 5.1*b* is exactly the cross section in the depth direction. The assumed relation of area occupied by fracture and rock matrix is appropriate [84]. We also assumed that asperities on the fracture surface had the same spherical shape (Figure 5.1*c*) and size to simplify analysis. The contact area of asperities in fractures is generally known to be less than 40% of the total surface area of the fracture [13]. In this model, we set the contact area of asperities to be 30% of the fracture surface area. That means that the ratio of asperity area to unit cell area is 30%, $\pi R^2/l^2 = 30\%$ as shown in Figure 5.1*d*. The fluid pressure is related to injection pressure and site along the straight line path from production well to injection well. In this regard, the force or pressure loading on asperity pair can be correlated to far-field overburden pressure with the

embedded effect of pore pressure/fluid pressure. In the following part of this paper, this relation frequently will be used.

5.2.2. Thermal Conduction. The temperature field within the asperity is determined by the heat exchange between the low-temperature water with temperature T_w and the high-temperature rock matrix with temperature T_r. The temperature difference between the rock and water is $\Delta T_{w\text{-}r} = T_r - T_w$. This cooling process can be interpreted as the thermal unloading process. The governing equation for this heat exchange is written as:

$$k\nabla^2 T + q = \rho c \frac{\partial T}{\partial t} \tag{5.1}$$

where T is the temperature within the asperity; q denotes the rate of heat generated inside the medium; k is the apparent thermal conductivity of the medium; ρ is the bulk density of medium; c is the specific heat or heat capacity of the medium, and t is the time. In this study, we assumed the cooling process occurs immediately after the injection of water. Since size of asperities is much smaller than that of matrix rocks, the injected water can cause a much faster cooling of asperities, which are completely immersed in the water, compared to the fracture walls. At the same time, the water has not been significantly heated up immediately. Therefore, for the boundary conditions, the temperature of the connection between asperity and rock matrix was set as constant T_r while the free surface of asperity was assumed at the inlet water-temperature T_w before the water had been heated. The spatial temperature distribution in asperity was obtained by solving Equation 5.1. In this calculation, a temperature change ΔT defined as $\Delta T = T_r - T$ is the change of asperity temperature after the heat exchange between water and rock matrix reaches equilibrium. The ΔT of the asperity is critical in our study and will be coupled with the

asperity geomechanical process. A thermo-mechanical process was modeled by adding ΔT to the constitutive model described below by considering thermal expansion of asperity.

5.2.3. Asymmetric Damage Mechanics Model. The failure of quasi-brittle heterogeneous materials such as rocks is mostly due to propagation and intersection of pre-existing micro-cracks [85, 86]. A macroscopic representation of micro-crack development was qualitatively described by continuum damage mechanics [82]. A damage variable was generally introduced to characterize surface density of intersection of micro-cracks, as justified by principles of irreversible thermodynamics [87]. In our work, an isotropic damage variable is used to model deterioration of elastic modulus:

$$E = E_0(1 - D) \tag{5.2}$$

where E is the degraded elastic modulus; E_0 is initial Young's modulus; D is an isotropic damage variable and satisfies the criterion $0 \leq D \leq 1$. The value $D = 0$, corresponds to a state in which the rock is intact (without degradation of Young's modulus), while the value $D = 1$, corresponds to, complete loss of bearing capacity and (almost) no stiffness of the asperity material (rock).

The stress-strain relationship, by considering the thermal expansion ($\Delta\varepsilon ij = \alpha\Delta T\delta ij$), can be expressed as,

$$\sigma_{ij} = \left[\bar{\lambda}\varepsilon_{ij} - (3\bar{\lambda} + 2\bar{\mu})\alpha\Delta T\right]\delta_{ij} + 2\bar{\mu}\varepsilon_{ij} \tag{5.3}$$

where σ_{ij} and ε_{ij} are the stress and strain tensor, respectively; δ_{ij} is the Kronecker delta; and α is the coefficient of thermal expansion. The $\bar{\lambda}$ and $\bar{\mu}$ are damaged Lamé's constants defined as $\bar{\lambda} = \frac{Ev}{(1+v)(1-2v)}$, $\bar{\mu} = \frac{E}{2(1+v)}$, where v is Possion's ratio.

To determine *D*, by combining the uniaxial compression/tension test results and the results of indirect Brazilian disk tests conducted on granites [88-90], we imposed asymmetric triangular stress-strain profiles with peak strengths followed by the residuals (Figure 2*a*). Similar profiles had been used as well [82]. A bilinear elastic response was assumed prior to reaching the peak for both compressive and tensile loading conditions. The reduced stiffness in the second linear stage represents the propagation of micro-cracks. After reaching the peak, an instantaneous reduction in strength was introduced to represent the brittle nature of rock failures in both tensile and compressive loading conditions. A linear softening behavior was given to the tensile loading case based on the micro-crack coalescence. A flat residual strength was used in the model of the compressive loading scenario, to represent the residual confining effects [91]. A maintenance of small residual value (0.01% of initial value) was kept to reduce the computational instability. The damage variables for tension and compression were calculated respectively as follows,

$$D_t = \begin{cases} 0 & 0 < \varepsilon < \varepsilon_{ti} \\ \left(1 - \frac{\varepsilon_{ti}}{\varepsilon}\right)\left[1 - \frac{\frac{\sigma_{to}}{\sigma_{ti}} - 1}{\frac{\varepsilon_{tr}}{\varepsilon_{ti}} - 1}\right] & \varepsilon_{ti} < \varepsilon < \varepsilon_{tr} \\ 1 - \frac{\sigma_{tr}}{\sigma_{ti}}\frac{\varepsilon_{ti}}{\varepsilon} - \frac{\frac{\sigma_{tu}}{\sigma_{ti}} - \frac{\sigma_{tr}}{\sigma_{ti}}}{\frac{\varepsilon_{tu}}{\varepsilon_{ti}} - \frac{\varepsilon_{tr}}{\varepsilon_{ti}}}\left(1 - \frac{\varepsilon_{ti}}{\varepsilon}\right) & \varepsilon_{tr} < \varepsilon < \varepsilon_{tu} \\ 1 & \varepsilon > \varepsilon_{tu} \end{cases} \tag{5.4}$$

and

$$D_c = \begin{cases} 0 & \varepsilon_{ci} < \varepsilon < 0 \\ \left(1 - \frac{\varepsilon_{ci}}{\varepsilon}\right)\left[1 - \frac{\frac{\sigma_{co}}{\sigma_{ci}} - 1}{\frac{\varepsilon_{cr}}{\varepsilon_{ci}} - 1}\right] & \varepsilon_{cr} < \varepsilon < \varepsilon_{ci} \\ 1 - \frac{\sigma_{cr}}{\sigma_{ci}}\frac{\varepsilon_{ci}}{\varepsilon} & \varepsilon_{cu} < \varepsilon < \varepsilon_{cr} \\ 1 & \varepsilon < \varepsilon_{cu} \end{cases} \tag{5.5}$$

where the symbol σ represents maximum principal stress σ_1 in (5.4) and minimum principal stress σ_3 in (5.5). The value ε is the equivalent principal strain: $\varepsilon = \frac{\sigma}{E}$. The subscripts *t* and *c* stand for tension and compression, respectively. The subscript *i* signifies the elastic limits; the subscript *o* the peak strengths; the subscript *r* indicates the residual strengths; and the subscript *u* the ultimate failure. Although the tangential stiffness in each linear segment remains constant, the secant stiffness is proportionally reduced, describing the irreversible damages. The elastic unloading process at each stage and the following reduced secant stiffness are also illustrated in Figure 5.2*a*. The parameters used to define the constitutive law in this study are based on the uniaxial experimental values [88] for granite in consideration of significant confining pressure [92] and laboratory loading difference [93]. It should be noted that the constitutive law profile described above is the projection of the failure surface in the principal stress space (σ_1, σ_2, σ_3), which can be divided into tension and compression zones as follows:

$$\bar{\sigma}_f = \begin{cases} |\sigma_1| & 0 < \sigma_3 < \sigma_2 < \sigma_1 \\ |\sigma_3| & \sigma_3 < 0 < \sigma_2 < \sigma_1 \;||\; \sigma_3 < \sigma_2 < 0 < \sigma_1 \;||\; \sigma_3 < \sigma_2 < \sigma_1 < 0 \end{cases} \tag{5.6}$$

where $\bar{\sigma}_f$ defines the failure surface. Note that, the absence of cohesion in brittle rocks [94] limits the ratio between compressive and tensile strengths giving $\left|\frac{\sigma_1}{\sigma_3}\right| < 0.1$ in compression zone. The failure surface in the principal stress coordinate is plotted in Figure 5.2*b*. The indices 1-4 correspond to the linear segments illustrated in Figure 5.2*a*. Following a tension-positive sign convention, the first quadrant shown in Figure 5.2*a* is in tension, and the third quadrant is in compression. The pyramidal failure volume constructed by the failure surface (Figure 5.2*b*) quantifies the failure zones in the

principle stress space as found in the experiments. An asymmetric constitutive relationship was then established for the modeling of rock failures under complex loading conditions.

By solving (5.1), (5.3) and equilibrium Equation (5.7) given below together, we can obtain the distribution of ΔT, σ_{ij}, ε_{ij} and D within the asperities, and estimate damage and deformation of asperities.

$$\sigma_{ij,i} + F_j = 0 \tag{5.7}$$

where F_j is the body force tensor.

In our modeling, we firstly applied σ'_v to the asperity contact, which represents a self-propping situation before applying any cold-water injection, i.e. $\Delta T_{w\text{-}r} = 0$. Then, we used obtained stress and strain distributions as the initial stress and strain status for further calculation. For the boundary conditions, the displacement of the asperity/rock matrix interface is fixed in the tangential direction which can be interpreted as rigid connection between the asperities and the rock matrix.

In our study, two asperity damage mechanisms were investigated, including the contact induced damages and the thermally induced radial crack propagations. The mechanical performance of the self-propping asperity was evaluated through the force-displacement response. Then the cooling process due to water injection was modeled to exhibit interaction between the two damage mechanisms. A quantified failure prediction was reached by the characterization of such interaction. At the end, we correlated our modeling results with actual field data to provide meaningful interpretations of the modeling results.

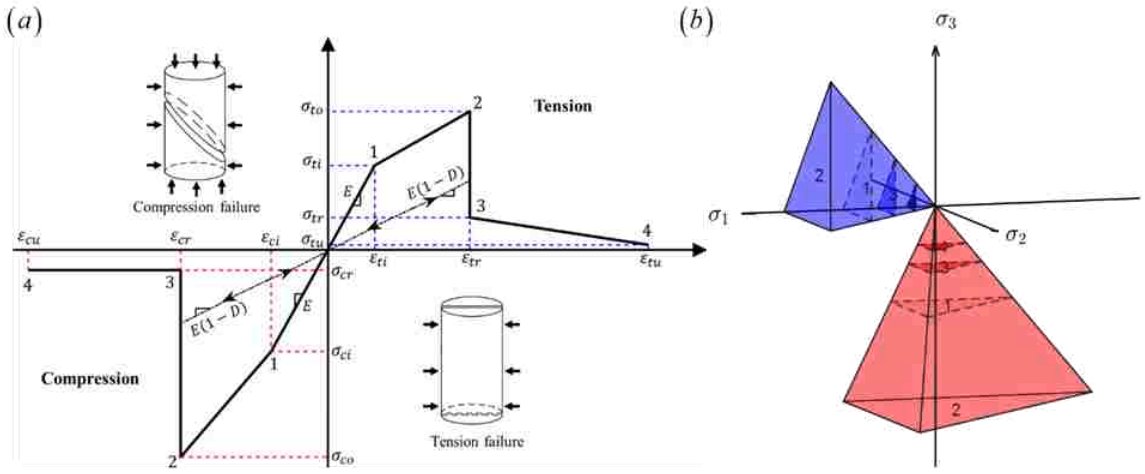

Figure 5.2 Elastic Damage-Based Tension-Compression Asymmetric Constitutive Relation: (a) the stress-strain curve, 1: linear elastic limit; 2: peak strength; 3: residual strength; 4: ultimate failure; (*b*) Failure surface in three-dimension principal stress space, therein blue color denotes tension zone and red color denotes compression zone.

5.3. NUMERICAL RESULTS

The result from numerical simulation is presented in this part.

5.3.1. Initial Stress-Strain Response. Before applying any thermal effect, we need to know the initial stress status of the self-propping asperity at varying depth in the deep earth. To reconstruct the stress status of asperities, we conducted the strain-controlled loading to obtain a complete stress-strain characteristics for asperities numerically. The stress-strain relationship is plotted as a dashed curve in Figure 5.3. By connecting the peak values of the dashed curve in a monotonically increasing manner, we can re-create the stress-strain relationship under stress-controlled loading mode as indicated by solid curve in Figure 5.3. Each stress drop after the peak in the strain-controlled loading mode indicates a local damage within the asperity contact zone. From the stress-controlled perspective, the monotonic increments of strain, which cause

snapping of stress and result in plateaus as illustrated by the solid line in Figure 5.3, indicates large vertical crushes of the asperity.

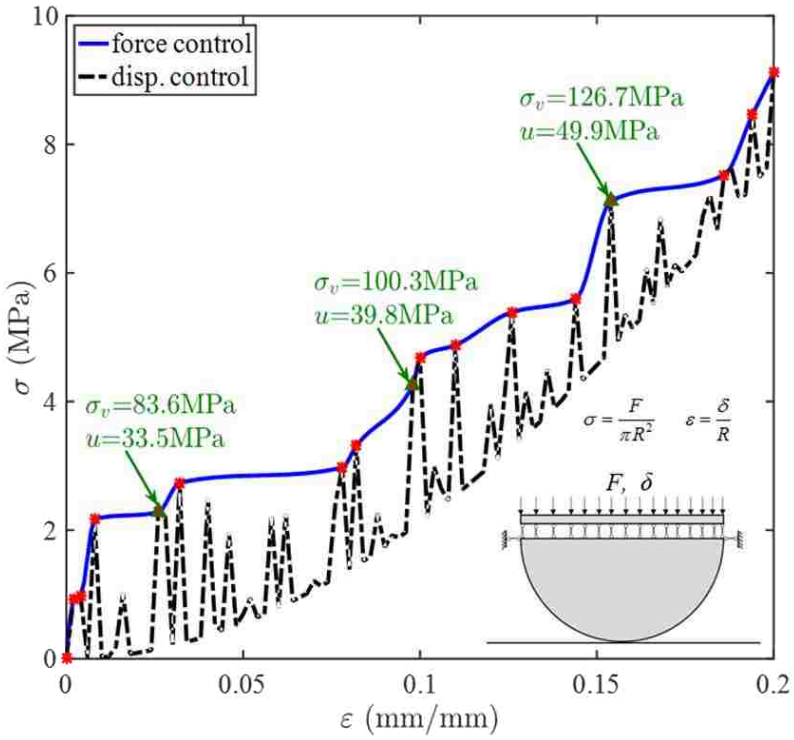

Figure 5.3 The Relation of Stress on Top of Asperity and Strain (Deformation/Radius) at Force Control Loading (Blue Line) and Displacement Control Loading (Black Dash Line). Overburden pressure σ_v and corresponding pore pressure u at three typical strain conditions are shown as well.

The Hertzian contact model was used to analyze the deformation of contacting asperity under normal stress [25, 95]. But it was criticized by Beeler and Hickman [96] that the excessive strain of contacting asperity at prescribed normal stress cannot be accommodated. For example, asperity strain, defined as the ratio of mean value of asperity deformation to asperity tip radius of curvature, is used to quantify the vertical deformation of contacting asperity. Asperity strains during experiment at 7 MPa

macroscopic normal stress range are typically 0.14 [96]. In this study, with the uniform height assumption of asperities on fracture surface, the asperity strain is approximately 0.15 at normal stress of 7 MPa. The result is very close to the experimental data. Whereas, the Hertzian contact stress is about 19 GPa at asperity strain of 0.14 based on the equation $\langle \sigma_c \rangle = 0.42E^* \sqrt{\delta/R}$ in Beeler and Hickman's work [96]. Thus, the normal loading-displacement relation in this study can replicate the similar result with experimental data, but the Hertzian model cannot accommodate excessive asperity strain at prescribed normal stress.

5.3.2. Boundary Setting for Thermo-Mechanical Analysis. To capture the deformation behavior of mated asperity pair by cooling, the temperature distribution within asperity and rock matrix is required. The temperature distribution around the asperity is decided by heat convection in fluid and heat conduction in solid rock. Therefore, another hydrothermal simulation is conducted separately. The simulation is implemented in COMSOL® *Multiphysics*. The considered region is one unit cell as shown in Figure 5.4*a*. Notice that this region is the same as that in Figure 5.1*d* comprising one single asperity pair. Based on the assumed ratio of real contact area to nominal surface area 30% in Section 5.2.1, the edge length of rock matrix block is l=8.1 mm. Two layers are set for the rock matrix in either side of asperity: the one connecting asperity is regular solid domain and the other one is infinite element domain. Their lengths are $a = b$ = 3 mm. The thermal parameters of solid and water are from Table 5.1. The cold water flows along positive x direction. The transverse direction (y-z plane) are symmetric boundaries for both solid and fluid. One difference compared to asperity model in this study is the contacting state of asperity pair. The asperity pair is artificially

separate to reduce the mesh singularity near the asperity tip. The inlet and outlet for thermal boundary condition of water are constant temperature and open boundary condition. The temperature at utmost solid surface in *x*-*y* plane is set to constant temperature. The hydraulic condition of water at the inlet and outlet are flow rate $Q=6\times10^{-8}$ m^3/s and outflow boundary condition. The cross section in the *x*-*z* plane crossing the center of asperity is presented in Figure 5.4*b*. Because of the equivalent length in the *x* direction and *y* direction, the cross section in the *y*-*z* plane crossing the center of asperity should be the same as Figure 5.4*b*. This is a simple model focusing on single asperity to demonstrate the thermal conductivity effect.

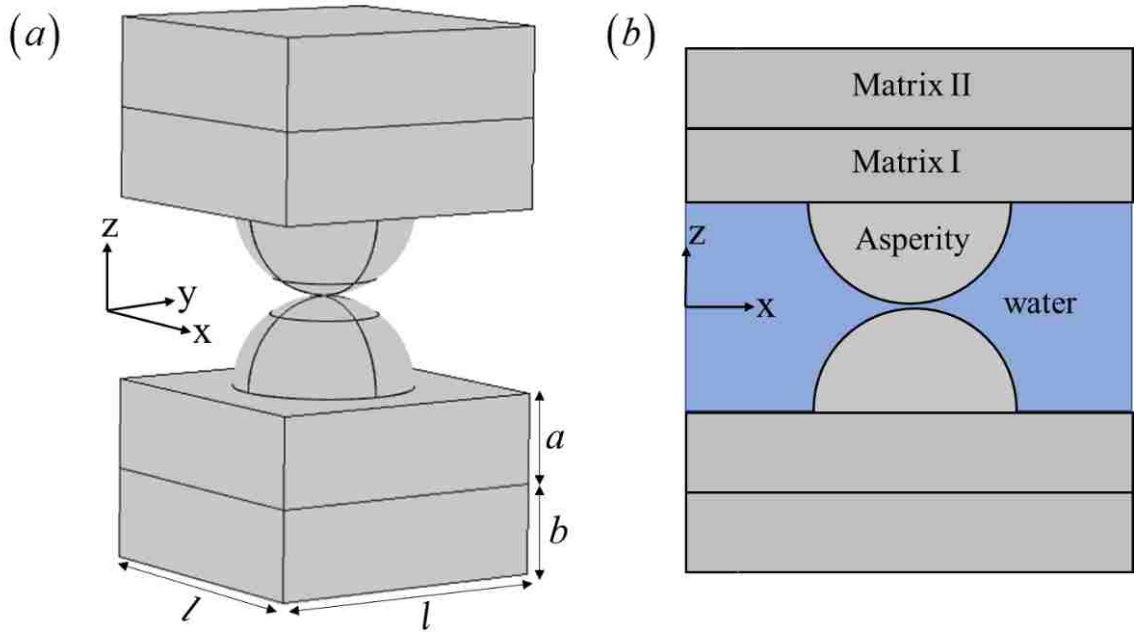

Figure 5.4 Schematic Diagram of Single Asperity Model to Illustrate the Hydrothermal Simulation: (*a*) 3D view and (*b*) cross section in the *x*-*z* plane. Matrix I: nearby rock matrix domain, Matrix II: infinite element domain of rock matrix in simulation.

Table 5.1 Model Data Used in Simulation

Category	Parameter name	Value
Elastic parameters	Young's modulus, E	111.36 GPa
	Poisson's ratio, v	0.25
Thermal parameters	Heat capacity, c	790 J/kg·K
	Thermal conductivity, k	10.7 W/m·K
	Reservoir temperature, T_r	350˚C
	Injection water temperature, T_w	50˚C
	Granite density, ρ	2750 kg/m^3
Geometric parameters	Hemisphere radius, R	2.5 mm
Compression parameters	Elastic limit stress, σ_{ci}	294 MPa
	Peak compressive strength, σ_{co}	600 MPa
	Residual compressive strength, σ_{cr}	58.2 MPa
	Elastic limit strain, ε_{ci}	2.64×10^{-3}
	Residual compressive strain, ε_{cr}	6.87×10^{-3}
	Ultimate compressive strain, ε_{cu}	1.0×10^{-2}
Tension parameters	Elastic limit stress, σ_{ti}	24.54 MPa
	Peak tensile strength, σ_{to}	40.2 MPa
	Residual tensile strength, σ_{tr}	9.42 MPa
	Ultimate tensile stress, σ_{tu}	1.5 MPa
	Elastic limit strain, ε_{ti}	2.2×10^{-4}
	Residual tensile strain, ε_{tr}	6.65×10^{-4}
	Ultimate tensile strain, ε_{tu}	1.5×10-3

The temperature distribution around the asperity pair is shown in Figure 5.5. Only the temperature distribution in the solid domains display for better illustration. The three

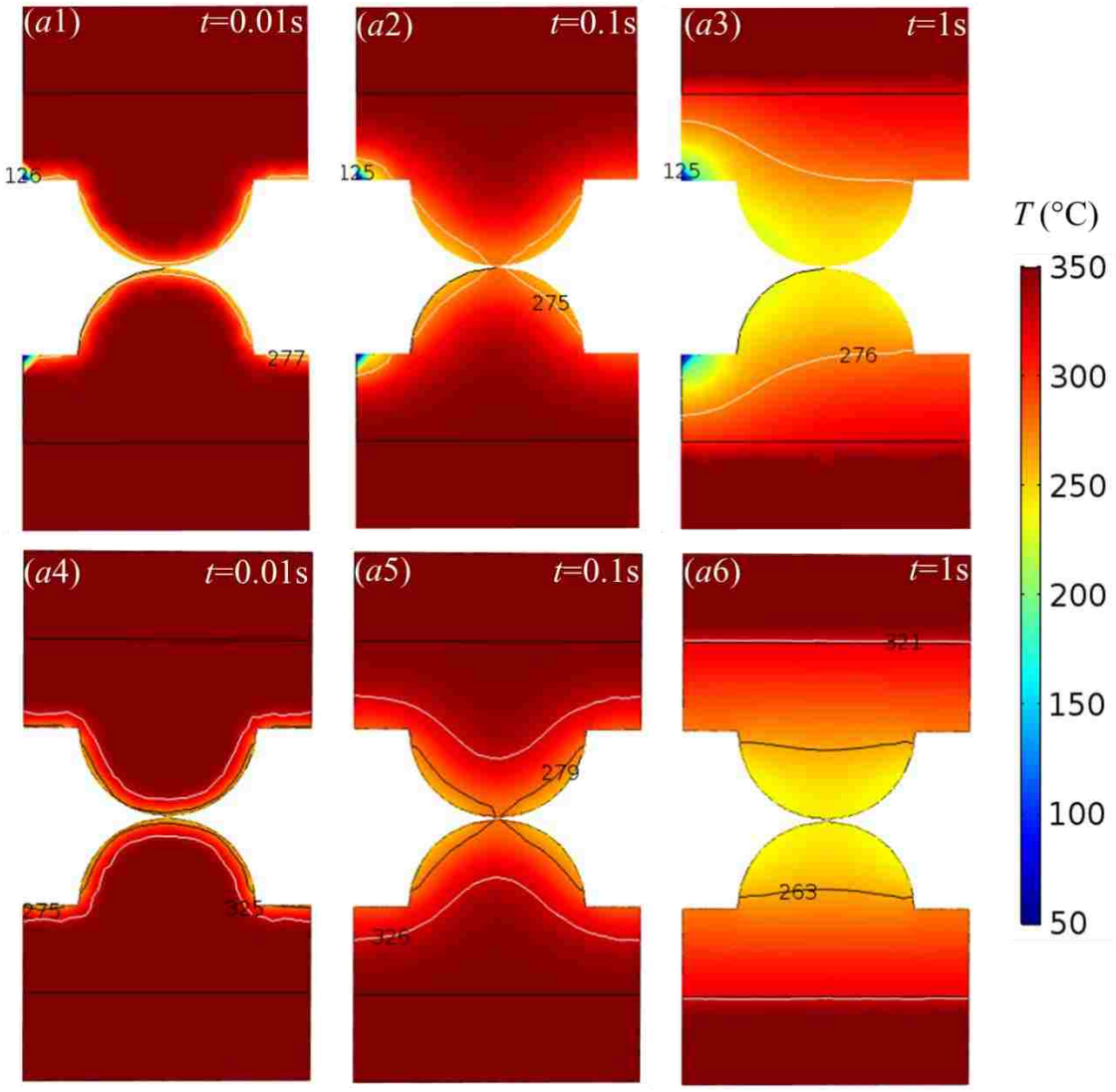

Figure 5.5 The Temperature Distribution at Three Instants of Time around the Asperity. (*a*1)-(*a*3) are cross-sections in the *x*-*z* plane through center of single asperity shown in Figure 5.4, (*a*4)-(*a*6) are cross sections in the *y*-*z* plane through center of single asperity shown in Figure 5.4.

graphs in the first row (*a*1-*a*3) are temperature distribution at three time steps (*t* = 0.01s, 0.1s and 1s) in the *x*-*z* plane crossing the center of asperity. The blue spots near the entrance indicate low temperature from inlet boundary condition. As the temperature contour moves faster in the fluid domain than in the solid domain, the thermal front

propagates faster in fluid domain. This can be more obvious in the temperature maps (*a*4-*a*6) in the *y*-*z* plane crossing the center of asperity. The asperity pair extruded into fluid domain has more rapid temperature change. The real temperature distribution around the surface of asperity is not uniform as seen from Figure 5.5(*a*6). To simplify the calculation in ABAQUS®, the constant temperature on the spherical surface is set. More accurate temperature distribution around the asperity will be considered in further work. In addition, the temperature drop in the rock matrix is small compared to asperity.

In our numerical implementation in ABAQUS®, the asperity was firstly loaded to prescribed overburden pressure, which simulated initial conditions of asperity before cooling. Then, gradually increased temperature difference $\Delta T_{w\text{-}r}$ was applied on the outer surface of the asperity while the loading pressure was kept constant. The schematic illustration of loading process are displayed in Figure 5.6*a*. This intends to simulate the contact of water and rock at different site along fracture direction. Because the cold water near the injection well would be heated up and hence the temperature difference of warm water and hot rock reduces along fracture direction. The premise for rapid cooling of asperity while constant temperature of fracture matrix is the instantaneous touching moment of cold water and hot rock. Two reasons can substantiate this point.

Heat transfer in fluid and solid is mainly controlled by convection and conduction, respectively. In the transfer direction perpendicular to fracture surface, the thermal conduction within the solid and solid/fluid interface can be characterized by thermal diffusivity of the solid. From the parameters in Table 5.1, the thermal diffusivity of solid is about 5×10^{-6} m^2/s by $\alpha = k/\rho c_p$. For the small size of asperity (R=2.5 mm), the time scale for this cooling can be roughly estimated to be 1.25 s by $\Delta t = R^2/\alpha$.

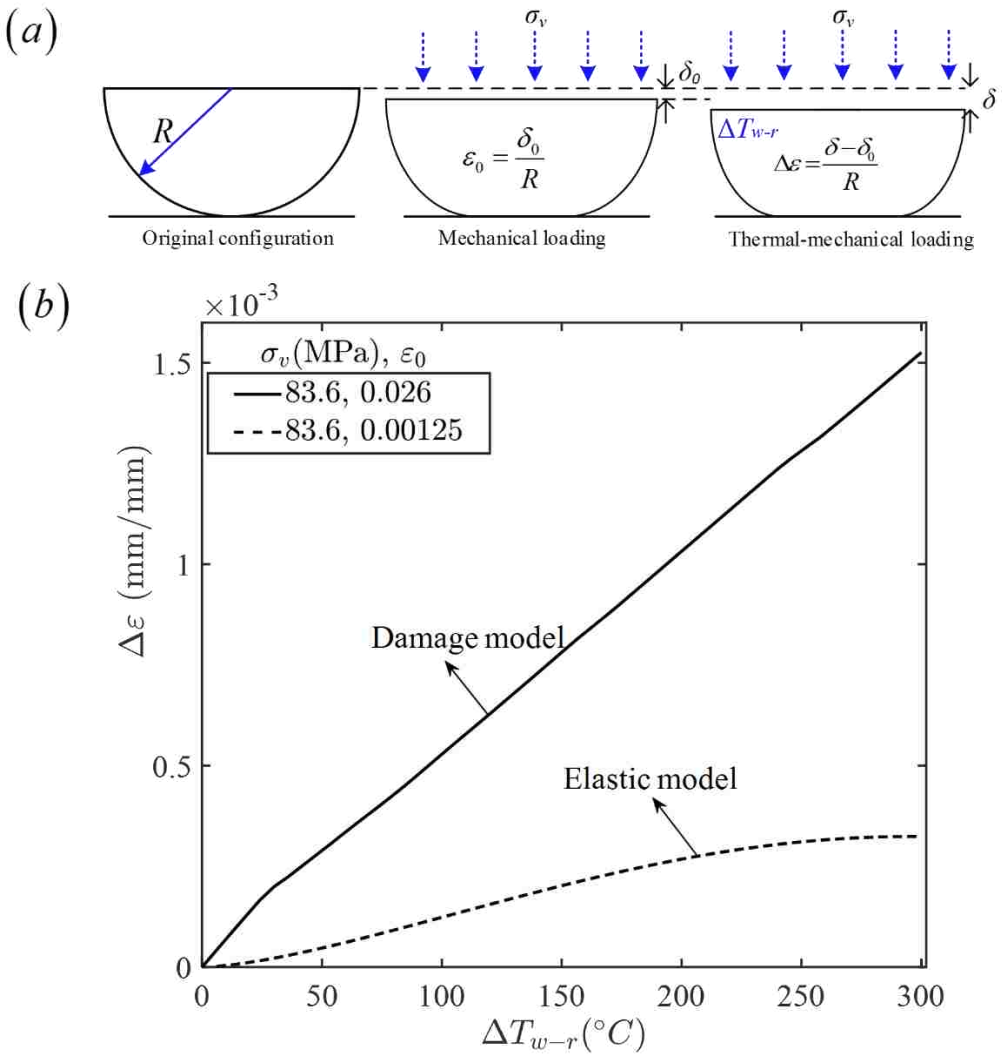

Figure 5.6 Deformation of Asperities under Cooling Effect. (*a*) Illustration of deformation process, (*b*) asperity deformation with response to rising temperature difference for damage model and elastic model on solid asperity.

In this sense, the time to asymptotically reach steady state is approximately 1.25 s. In the transfer direction longitudinal to fluid flow, the thermal convection within the fluid can similarly be characterized by hydraulic diffusivity of the fluid. The hydraulic diffusivity of water in geothermal test is typically in the order O(101) m2/s [97]. The time scale for cold water to flow through the asperity pair is about 2.5×10-5 s. Hence, this

local thermal non-equilibrium causes insufficient heating of water. It also means that the impact of thermal diffusion is much smaller than the convection in the fracture. Considering the small size of asperity to rock matrix and exposure of asperity surface to cold water, the variation of temperature in the rock matrix is negligible. However, for a long term of EGS heat production, the rock matrix will eventually be cooled down. The fixed asperity/rock matrix boundary condition becomes invalid. Therefore, the proposed asperity failure mechanism below only works at the early production stage of EGS.

5.3.3. Temperature-Strain Response under Cooling. The thermal loading of damage model firstly is compared with standard elastic model. The elastic model is set up in ABAQUS® CAE with the same parameters as in Table 5.1. The same mesh size and loading procedure shown in Figure 5.6*a* is followed in elastic model. The comparison of thermal loading of damage model and elastic model are displayed in Figure 5.6*b*. The initial vertical strain due to mechanical loading is larger for the damage model at low temperature compared to elastic model. Because the elements near the contact region are damaged (D=1) or partially damaged (0<D<1) in the mechanical loading stage and the induced thermal stress would cause some damage near the contact region. With increasing temperature, more elements will lose bearing capacity for damage model, leading to approximately linear relationship between ΔT and $\Delta\varepsilon$. For the elastic model, with increasing contact area, higher loading can be withstood and the curve asymptotically levels off with increasing temperature difference.

To understand the “temperature”-“strain” response of the asperity when subject to cooling process, three typical overburden pressure σ_{v1} = 83.6 MPa, σ_{v2} = 100.3 MPa, and σ_{v3} = 126.7 MPa, and their corresponding pore pressure u_1 = 33.5 MPa, u_2 = 39.8 MPa,

and u_3 = 49.9 MPa were selected for the "temperature"-"strain" test. Here, the "temperature" is actually the temperature difference between the hot rock and injected cool fluid, and the "strain" is the induced strain change due to the cooling effect. The corresponding depths of these overburden pressure were referred to the top, middle and bottom of regular EGS reservoir (3 km ~ 5 km). Three overburden pressure scenarios are depicted in Figure 5.7 with corresponding initial strain ε_0. With fixed temperature difference, the higher overburden pressure leads to the lower vertical deformation of asperity by cooling effect, which indicates the overburden pressure could inhibit the

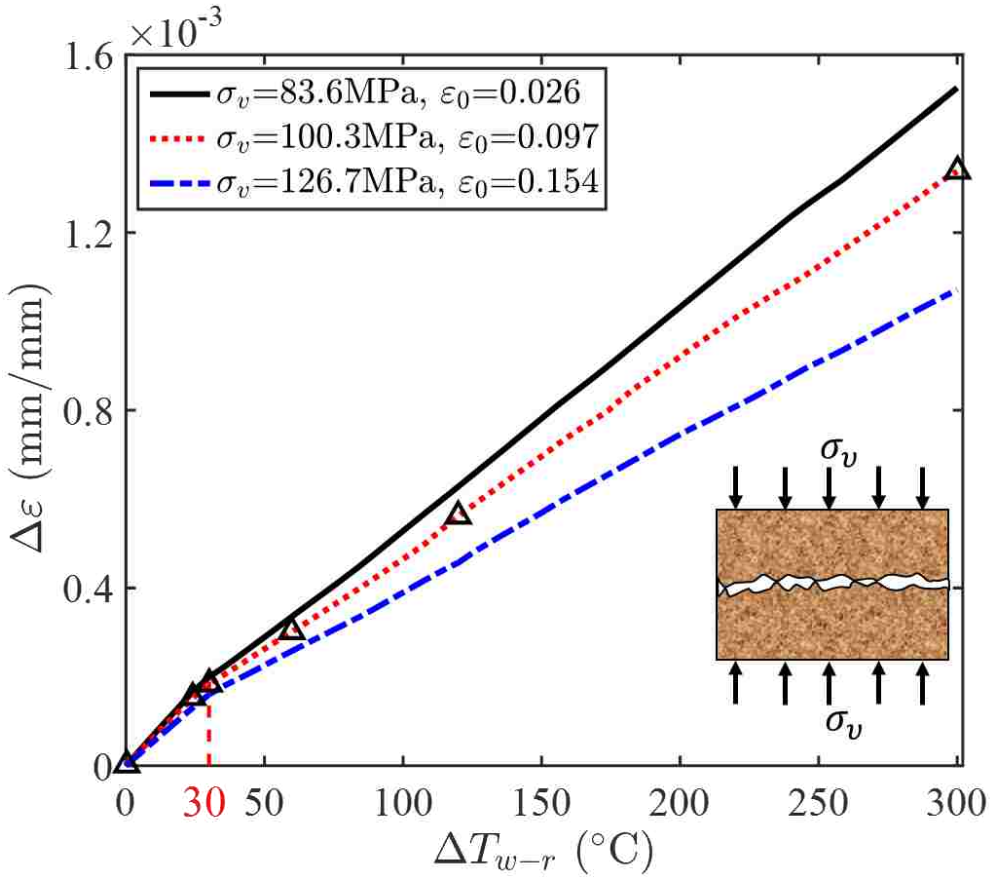

Figure 5.7 The Effect of Water-Rock Temperature Difference on Strain Change at Three Overburden Pressure Cases, Critical Strain Changes to Define Asperity Failure is Delineated by Horizontal Dash Line.

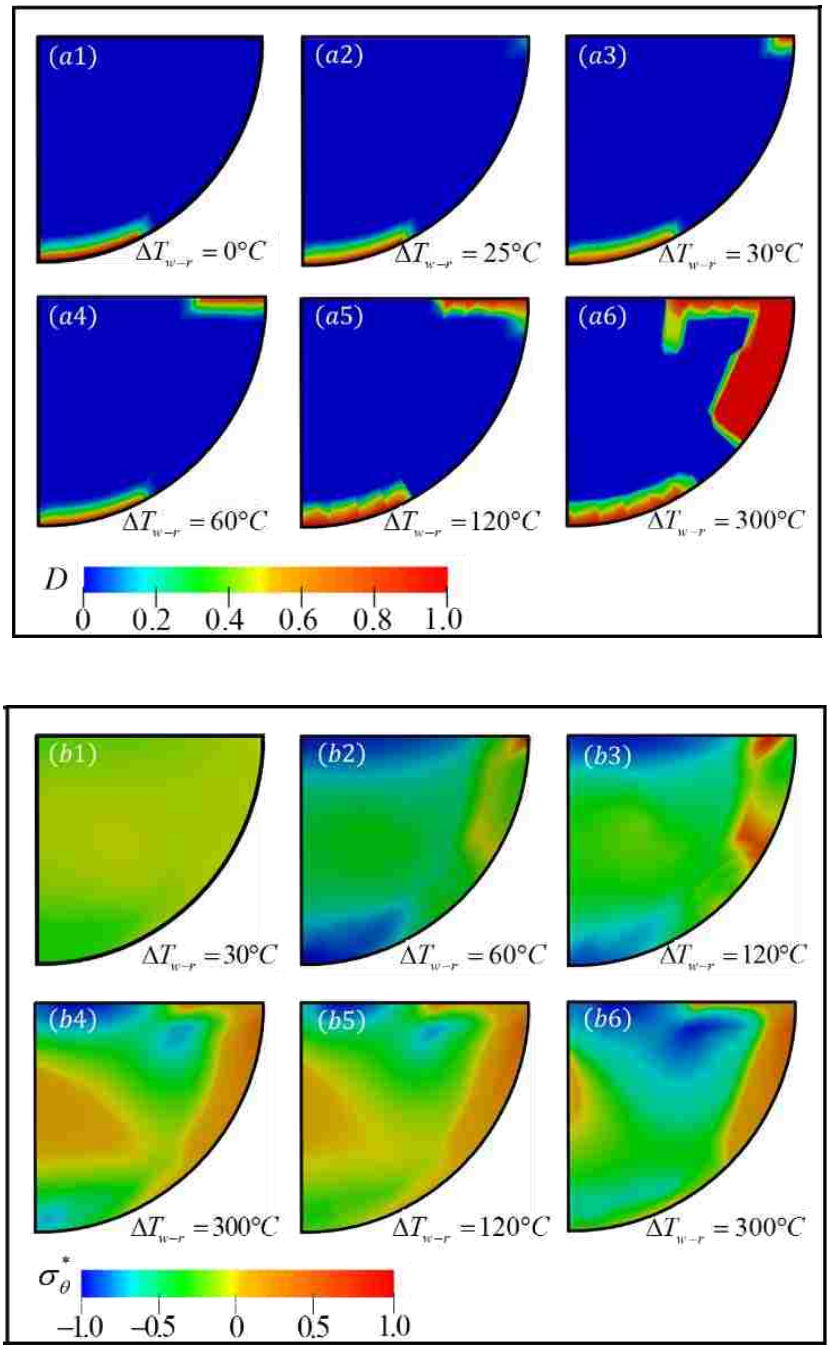

Figure 5.8 Damage Value Contour and Normalized Hoop Stress Contour at Different Temperature Difference. (*a*) The contour of damage variable *D* and (*b*) normalized hoop stress σ_θ^* at overburden pressure σ_v=100.3 MPa. Normalized hoop stress is defined as $\sigma_\theta^* = 2\frac{\sigma_\theta - \sigma_{\theta,min}}{\sigma_{\theta,max} - \sigma_{\theta,min}} - 1$, where $\sigma_{\theta,max}$ and $\sigma_{\theta,min}$ are spatially overall maximum and minimum hoop stress in each temperature difference case, in this normalization, hoop stress is mapped into [-1,1].

deformation caused by cooling process. A bilinear trend can be observed for the variation of $\Delta\varepsilon$ with respect to $\Delta T_{w\text{-}r}$ with different slopes (Figure 5.7). The turning points for different overburden pressure cases are almost at the same $\Delta T_{w\text{-}r} \approx 30^{\circ}\text{C}$. This fact can be interpreted as that σ_v in horizontal orientation of fracture has little effect on turning point.

We took the case of σ_v = 100.3 MPa as an analysis example to better understand this invariant of temperature difference on vertical deformation. The damage variable and hoop stress contours at six spots with different $\Delta T_{w\text{-}r}$ (triangles in red dash line in Figure 5.7) are plotted in Figure 5.8. It is noticed that there is only vertical contact damage at the contact area of the asperity before $\Delta T_{w\text{-}r}$ reaches 30 ˚C and the initiation of radial cracks occurs once $\Delta T_{w\text{-}r}$ reaches 30 ˚C (Figure 5.8(*a*3)). After the initiation of a radial crack, the vertical stiffness is reduced due to continuing radial cracking. This radial cracking induces vertical stiffness reduction, however, gives a smaller vertical strain response compared to vertical contact damage.

5.3.4. Asperity Damage Process. In this study, it was observed that the asperity had two damage mechanisms: the contact damage and the cracking inside the asperity. The contact damage has already existed when bearing the earth overburden pressure before applying any thermal effect (Figure 5.8(*a*1)). After applying the cooling process due to cold fluid injection, the cracking inside the asperity could initiate. Both two damage mechanisms could potentially lead to a failure of the asperity. To determine which damage mechanism exerts primary control on the asperity failure when the asperity is subject to cooling process, we used the same three overburden pressure schemes as described above in Section 5.3.3 for this asperity failure mechanism study.

As shown in Figure 5.8(*a*1), the contact damage has already existed due to the in-situ overburden pressure at initial condition $\Delta T_{w\text{-}r} = 0$. Prior to the turning point temperature difference, i.e., $\Delta T_{w\text{-}r} = 30$ ˚C, thermal effect of temperature difference only extends vertical elastic compression but not sufficiently induces fracture closure, and the damage area near the asperity contact point is barely changed. The fracture-related hoop stress is also presented in Figure 5.8*b*. To emphasize the redistribution and sign of hoop stress in asperity by change of temperature difference, hoop stress σ_θ is mapped into the range [-1, 1]. Figure 5.8*b* shows that the change in σ_θ mainly comes from the induced ΔT gradient within the asperity. As $\Delta T_{w\text{-}r}$ exceeds the turning point, the large shrinkage of semi-sphere with fixed top surface causes significant σ_θ. When the tensile strength is exceeded, a radial cracking initiates near the edge of top surface. As the temperature difference increases, the radial cracking near the top surface grow towards the center, leading to a reduction in effective contact area at the asperity-matrix connection. At the radial crack, the thermal strain has no constraints, and thermal stress is released. Consequently, σ_θ is redistributed and intensified at other parts as demonstrated in Figure 5.8*b*. As $\Delta T_{w\text{-}r}$ continues to increase, the radial crack deviates downwards in Figure 5.8(*a*6) since the σ_θ going downwards is larger than that going radially forward [98]. At this moment, the radial crack length is maximal at current overburden pressure and labeled as critical crack length a_c. Then, crack deviates downwards at two spots in Figure 5.8(*a*6).

More detailed mechanical analysis on the fracture propagation refers to Section 4. The deviation of fracture propagation is due to the combined effect of thermal stress and overburden pressure retards the cracking.

5.4. DISCUSSION

The asperity failure is discussed in this part. In the mechanical loading, the asperity has vertical damage and in the thermomechanical loading, the asperity has both vertical and circumferential damage. The quantitative analysis and presentation is shown.

5.4.1. Asperity Failure Mechanisms. In the asperity damage study, it is clear that the contact damage can hardly cause any failure of asperity by cooling (Figure 5.8). The asperity failure by cooling is mainly attributed to the cracking inside the asperity. Two asperity failure mechanisms could exist: shearing and spalling.

When the radial cracking initiates (Figure 5.8(*a*3)), the asperity becomes fragile to any shear disturbance in the fracture. Although there is no shear failure occurs in our simulation, it is mainly due to our pure compression loading for simplification. In the real geothermal reservoir, shear force ubiquitously exists in the fracture network. This radial cracking could directly lead to the shear failure of the asperity and therefore a potential closure of the fracture.

When the cracking propagates downwards as shown in Figure 5.8(*a*6), due to the brittleness of granite rock, cracked parts are most likely detached from the asperity and flushed away by the injected fluids. Spalling process of asperity surface will occur. After detachment of the damaged parts, the rest of asperity gets exposure to cold fluid and the same cooling process occurs. The evolution of asperity configurations can be illustrated in Figure 5.9*a*. Notice that the crack propagates downward and along outer surface after reaching the critical crack length (second sketch in Figure 5.9*a*). The remaining part beneath radial cracks length is cut off artificially to renew the new geometry in order to reduce computational cost. It’s reasonable because that part is disconnected with rock

matrix and has no support of compressive loading, leading to negligible influence on stress distribution in other regions within asperity. The damage contour of renewed asperity is shown in Figure 5.9*b*. With elevated temperature difference, crack initiates at the edge of asperity, then propagates radially, and eventually deviates downwards to detach a large chunk. It's noticed that temperature difference at crack initiation is changed to $\Delta T_{w\text{-}r}$=60 ˚C. It's probably due to stress redistribution in new asperity configuration. This spalling gradually "peel" the asperity and reduce its effective force-bearing volume, and the asperity would break at constant overburden pressure.

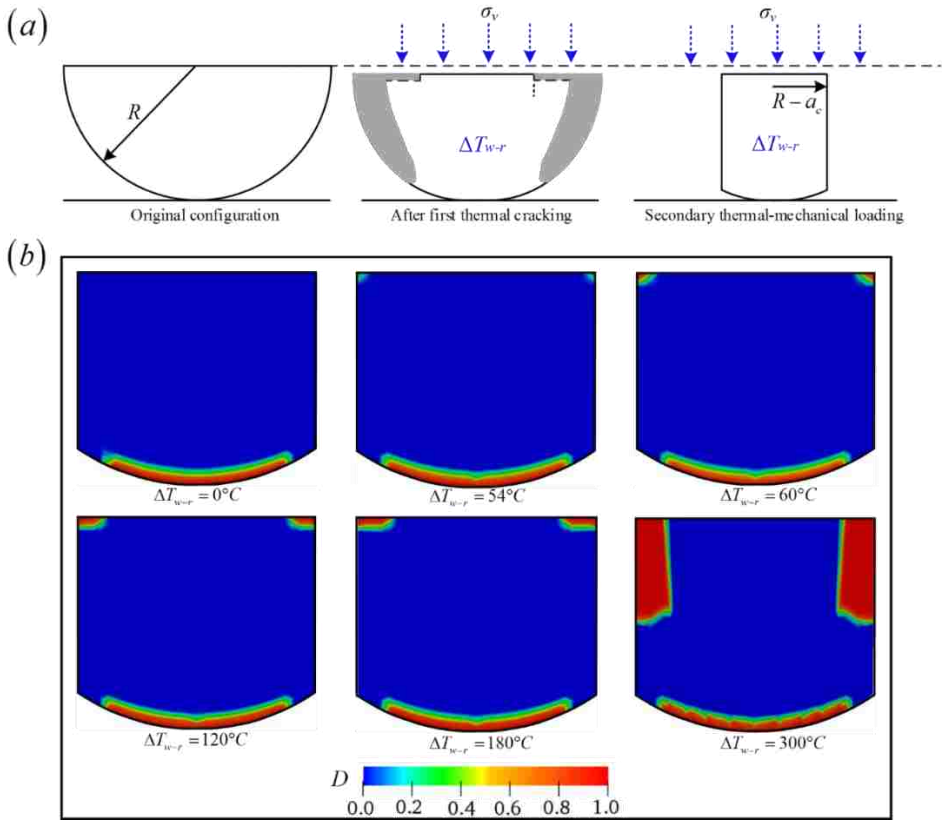

Figure 5.9 Secondary Thermal-Mechanical Loading with Rising Temperature Difference. (*a*) Illustration of asperity configuration at different stages (*b*) damage variable contour with elevated temperature difference at secondary thermal-mechanical loading at overburden pressure σ_v=100.3 MPa.

This failure phenomena can be indirectly validated by flow-through experiments on fractured cores in the literature review. Kamali-Asl et al [99] performed a series of flow-through experiments on artificially fractured granite. The amount of dissolved minerals in the effluent is much higher than estimated from chemical analysis. It highlights other process taking effects in the flowing experiments. Rutqvist [100] observed irreversible change of permeability that significantly deviated from supposedly reversible permeability. This difference is attributed to inelastic shortening of fracture asperity. Isaka et al. [3] and Kumari et al. [101] observed damage of fracture surface after rapid cooling of hot granite in laboratory experiment. This surface damage is highly related to the rate and extent of cooling. All of these experiments provide evidence to the topography change of fracture surface by cooling.

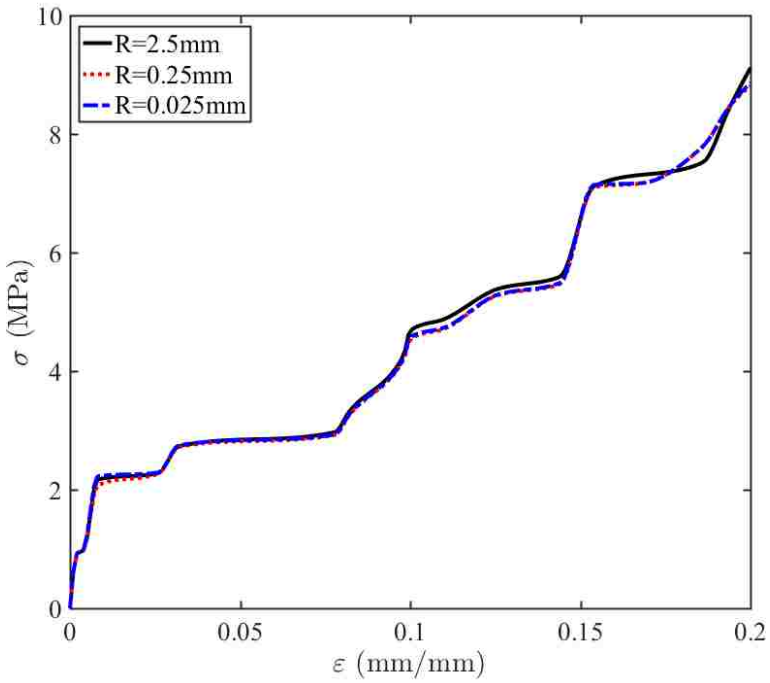

Figure 5.10 Correlation of Loading Stress and Vertical Strain for Three Different Asperity Radii.

5.4.2. Sensitivity of Asperity Size. The fracture surface constitutes different sizes of asperities. The viability of this model to different sizes of asperities is analyzed herein. Based on the work of Sharifzadeh et al. [102], most asperities have wide range of height from micrometers to millimeters. In this study, two more asperity radii, which were 0.25 mm and 0.025 mm respectively, were chosen to further analyze the size

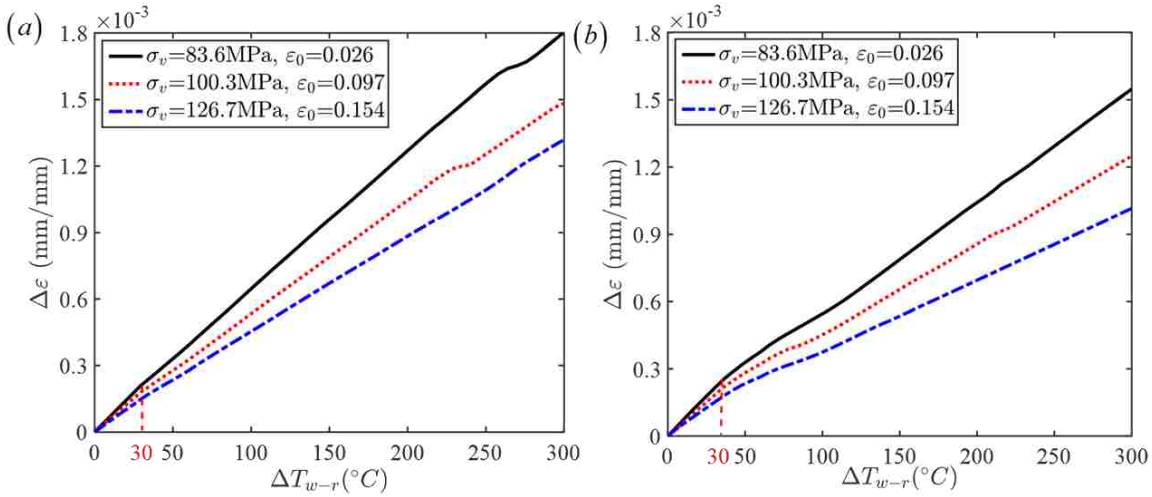

Figure 5.11 Strain Change with Response to Different Water-Rock Temperature Difference for Asperity Radius: (*a*) *R*=0.25 mm, (*b*) *R*=0.025 mm.

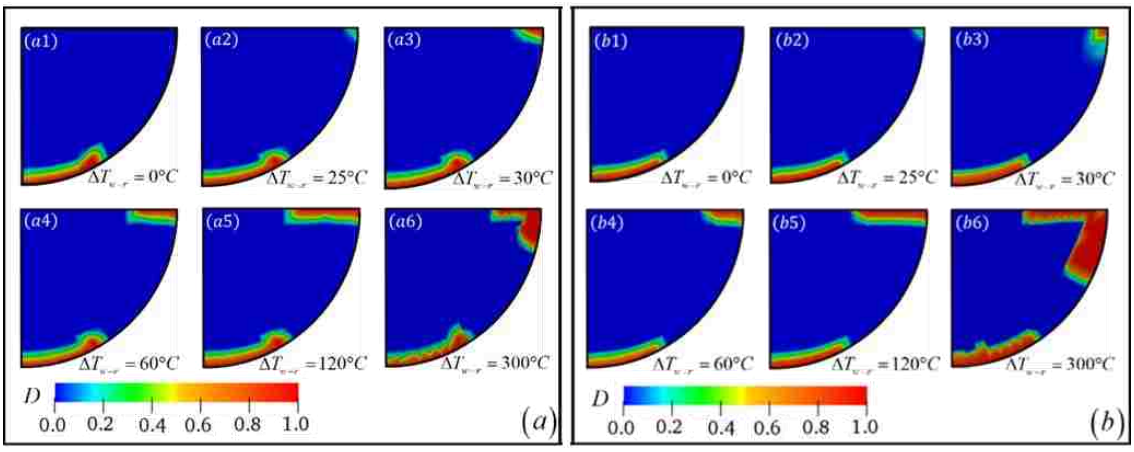

Figure 5.12 Contour of Damage Variable *D* at Overburden Pressure σ_v=100.3 MPa for Asperity Radius at (*a*) *R*=0.25 mm and (*b*) *R*=0.025 mm.

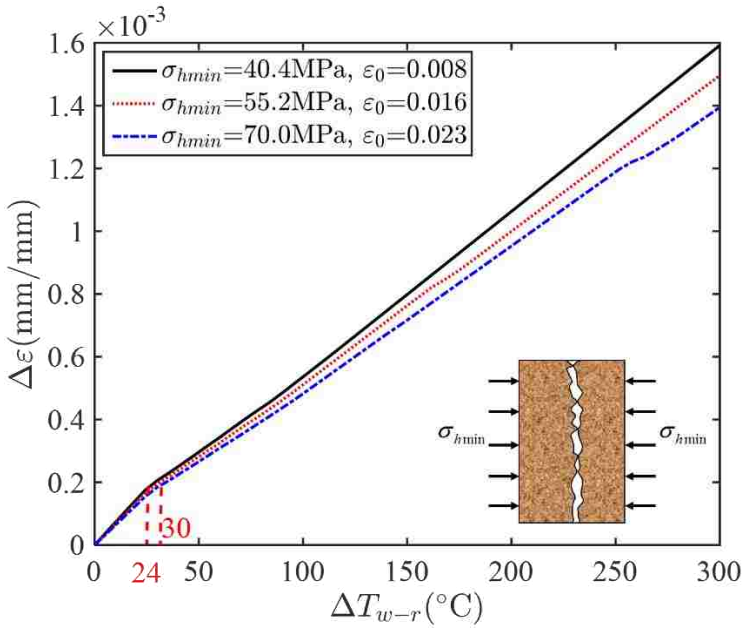

Figure 5.13 Strain Change with Respect to Water-Rock Temperature Difference for Vertical Fracture Orientation.

sensitivity of failure mechanisms of asperities. The same mapping method is used to correlate the loading pressure on asperity to the overburden pressure as introduced above. Similar as Figure 5.3, the force-controlled loading curve is shown in Figure 5.10. The difference of the mechanical deformation of asperities with three different radii is minor. The vertical strain change by temperature difference is shown in Figure 5.11. Two stages in curves can be noticed but not that obvious as in Figure 5.7. The turning point is still the same, around 30 ˚C. Taking σ_v=100.3 MPa as an example, the damage variable contours at six spots of temperature difference are shown in Figure 5.12. The radial cracking shows the same trend as the counterpart with the asperity radius of 2.5 mm. Overall, it shows no significant size sensitivity in this model to analyze failure mechanisms and vertical deformation of asperity by cooling effect.

5.4.3. Effect of Fracture Orientation. Due to the lower porosity of granite in deep formation (about 2%), natural fractures and hydraulic fractures are two main pathways for heat transfer. Field tests showed that minimum principal stress of subsurface formation was generally horizontal, so the shearing failure or dilation of natural joints was vertical or near vertical [64, 103] and new hydraulic fractures were most likely in vertical or oblique direction [104]. The laboratory injection experiment on granite also provides evidence on the oblique or near vertical propagation of hydraulic fractures [105]. Horizontal injection and extraction wells could be designed for EGS [63]. Hence, the analysis of oblique or near vertical fracture orientation is necessary. As a lower bound of the tectonic stress in the horizontal direction, the vertical orientation of fractures is considered in the part to delimit the minimum deformation of asperity.

Taking the in-situ stress in Soultz-sous-Forêts site as an example [83], the compression stress on asperity was from far-field horizontal minimum stress σ_{hmin}. The bounds for σ_{hmin} in depth of 3~5 km is between 40.4 MPa and 70.5 MPa. In this regard, three horizontal minimum stress 40.4 MPa, 55.2 MPa and 70.0 MPa were chosen to show the horizontal deformation of asperity by cooling. As expected, the same turning point of temperature 30 ˚C can be observed in Figure 5.13. The bilinear curves are in the same trend as those in Figure 5.7. However, the turning point of blue dash curves is different from the other two curves. At σ_v = 70.0 MPa, the turning point is 30˚C while it is 24˚C at overburden pressure smaller than 70.0 MPa. It verified the mitigation of radial cracking by overburden pressure, as like mitigation of vertical deformation at higher overburden pressure in Figure 5.7.

5.4.4. Thermal and Overburden Pressure Effect on Asperity Cracking. To quantify the effect of overburden pressure and temperature difference on the asperity cracking, we firstly investigated the evolution of radial crack length. For the horizontal orientation of fracture, the evolution of radial crack length is shown in Figure 5.14*a* at four different overburden pressure scenarios. The radial cracking of all scenarios initiates at 30 ˚C and propagates radially with elevated temperature difference. When it reaches the critical crack length a_c, cracking starts to deviate downwards in two spots as shown in Figure 5.8. The temperature difference at which cracking starts to deviate downwards is defined as critical temperature difference ΔT_c since it indicates the most fragile status of asperity to any shearing disturbance and a start of the asperity spalling. Figure 5.14*a* shows that the critical crack length keeps the same but the critical temperature difference increases with overburden pressure. The fracture propagation analysis on radial cracking is analyzed in Section 7. Radial crack propagation terminates when the energy release rate G is less than the fracture toughness G_c. The correlation of critical temperature difference and loading pressure on asperity is (see Section 7):

$$G_c = \frac{8a_c}{\pi E}\left[-\frac{E\alpha\Delta T_c}{1-\nu} + \frac{\nu}{1-\nu}\frac{R^2\sigma}{(R-a_c)^2}\right] \tag{5.8}$$

where a_c is the critical crack length; σ is the loading pressure on top of asperity; G_c is the fracture toughness. In Equation (5.8), the relation of ΔT_c and σ is linear. From Section 5.2.1, relation of loading pressure on top of asperity σ and tectonic pressure σ_v and σ_{hmin} is linear. Therefore, the relation of ΔT_c and σ_v (or σ_{hmin}) is also linear.

The correlation of critical temperature difference and overburden pressure are presented in Figure 5.14*b*. Two numerical data points are fitted by linear function: $\Delta T_c = 1.234\sigma_v + 42.06$. The minor divergence of discrete points could be due to mesh size

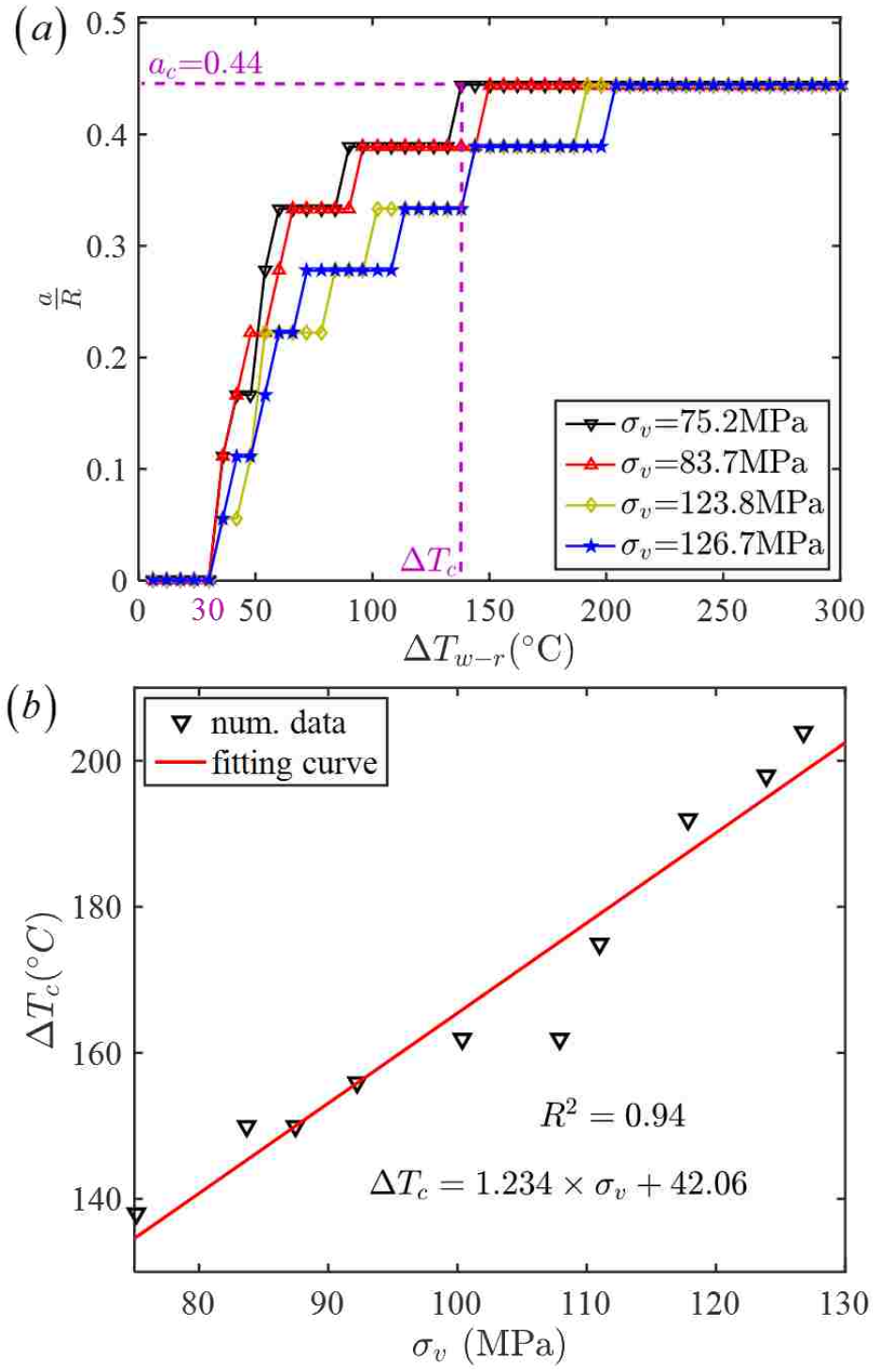

Figure 5.14 Crack Information at Different Temperature Difference for Horizontal Fracture. (*a*) Evolution of crack lengths at different temperature difference and (*b*) critical temperature difference at different overburden pressures for horizontal fracture, the fitting equation is $\Delta T_c = 1.234\sigma_v + 42.06$.

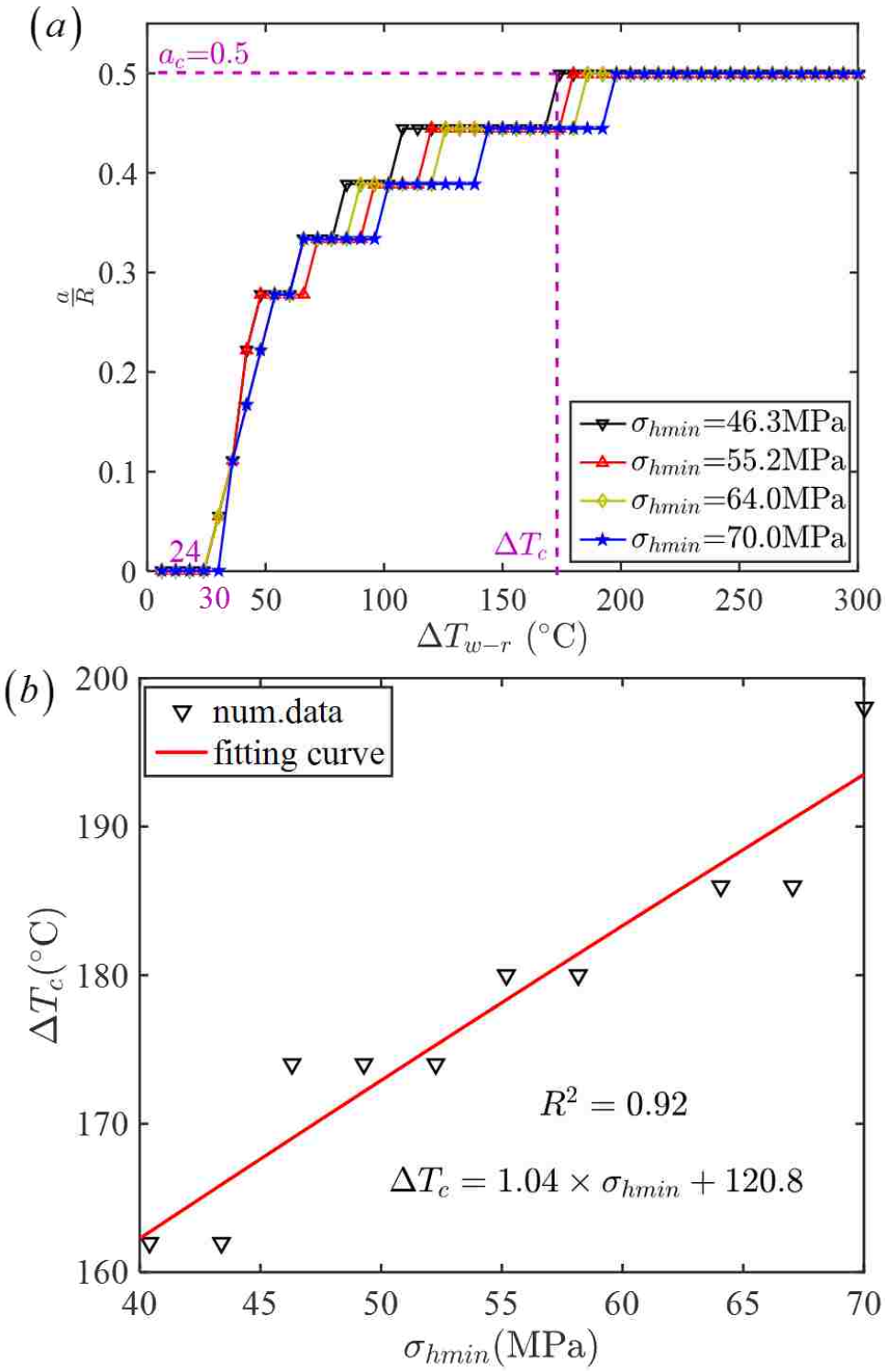

Figure 5.15 Crack Information at Different Temperature Difference for Horizontal Fracture. (*a*) Evolution of crack lengths at different temperature difference and (*b*) critical temperature difference at different overburden pressures for vertical fracture, the fitting equation is $\Delta T_c = 1.04\sigma_{hmin}+120.8$.

restraint. It shows clearly the constraints of overburden pressure on radial cracking and failure of asperity.

For the vertical orientation of fracture, the evolution of critical crack length with respect to temperature difference and overburden pressure is shown in Figure 5.15*a*. With difference in critical crack length in Figure 5.14*a* for the horizontal fracture, the critical crack length ratio is at 0.5 for the vertical fracture. This is attributed to the fact that smaller overburden pressure leads to less constraint on radial cracking. Also we need to know that the larger critical crack length indicates the smaller radius (R-a_c) in Figure 5.9*b* and more likely to have shear failure and thermal spalling. Similarly, the numerical correlation of critical temperature difference and overburden pressure is fitted by linear function: $\Delta T_c = 1.04\sigma_{hmin} + 120.8$ shown in Figure 5.15*b*.

5.4.5. Conventional Upscaling to Fracture Scale. The deformation behavior of single asperity pair in preceding analysis can be used to analyze the macroscopic behavior of fracture at fracture scale. Existing models about rough fracture deformation originated from a statistical description of loaded rough surfaces was proposed by Greenwood and Williamson [95]. The spherical topography of asperities was assumed in that seminal work. The mechanical behavior of contacting asperity under normal loading was simplified to follow Hertzian contact theory, which was demonstrated to be unrealistic by other researchers [96]. The asperity model in this study replaces Hertzian contact model to represent the deformation of roughness under mechanical loading or thermal stress.

When two rough fracture surfaces are loaded to contact, the concept of composite topography from Brown and Scholz [25] is used to represent the topography of rough

surface. Two reference planes are set and the height of asperity in top surface is denoted as z_2 and the height of asperity in bottom surface is denoted as z_1. The composite topography are $z=z_1+z_2$ and the separation of two reference planes is d, as shown in Figure 5.16*a*. The probability p that any asperity makes contact with opposite fracture surface is

$$p = \int_d^\infty \varphi(z)dz \tag{5.9}$$

where $\varphi(z)dz$ is the probability that a particular asperity has height z in the range z+dz. Assuming that the force F exerted by a single asperity is a function of the local deformation $F=f(z-d)$, the total macroscopic resisting normal stress σ_n is

$$\sigma_n = \eta \int_d^\infty f(z-d)\varphi(z)dz \tag{5.10}$$

where η is the areal density of asperities on the surface. The form of $f(z-d)$, i.e., the force-displacement relation on one asperity, can be calculated from Figure 5.3. For the prescribed mechanical properties in this study, the asperity strain and normal stress in the base line are used to define the deformation behavior of asperity. This would underestimate the normal stress. The corresponding force and displacement relation is (Figure 5.16*b*),

$$f(z-d) = 116\pi R^2 \left(\frac{z-d}{R}\right)^{1.879} \tag{5.11}$$

where R is the radius of spherical asperity. Substituting (5.11) into (5.10) yields

$$\sigma_n = \eta \int_d^\infty 116\pi R^2 \left(\frac{z-d}{R}\right)^{1.879} \varphi(z)dz \tag{5.12}$$

For the probability density function $\varphi(z)$, the detail of calculation for approximately Gaussian distribution and inverted chi-square distribution refers to appendix D by Brown and Scholz [25].

In addition, the hydraulic conductivity at the fracture scale can also be calculated in this process. First, the hydraulic aperture needs to be calculated. The mean value of asperity deformation as a function of closure is [96],

$$\langle \delta_a \rangle = \int_d^{d_0} (z-d)\varphi(z)dz \tag{5.13}$$

where d_0 is the surface separation at σ_n=0. Notice that d in Equation (5.13) depends on σ_n, which means that the separation of two reference plane reduces with loading. Thus, the mean aperture of open space in fracture $\langle h \rangle$ are,

$$\langle h \rangle = \int_0^d (d-z)\varphi(z)dz - \langle \delta_a \rangle \tag{5.14}$$

where the integral in the right-hand side denotes the statistically mean value of aperture at the initial state. The initial average aperture subtracts mean value of asperity deformation is equivalent to the transient mean aperture of fracture.

Then the hydraulic aperture can be obtained by the theoretical formula [106],

$$e^3 \approx \langle h \rangle^3 [1 - 1.5\sigma_h^2 / \langle h \rangle^2][1-2c] \tag{5.15}$$

where $\langle h \rangle$ is the average aperture size, from Equation (5.14), σ_h is the standard deviation of the aperture size, and c is the contact area between the fracture surfaces. σ_h can be found from the probability density function in Brown and Scholz [25] and c can also be obtained from probability density function.

The fracture permeability is then given by

$$k = \frac{e^3}{12} \tag{5.16}$$

The cubic law is used in the calculation of permeability from Equation (5.16).

The macroscopic force and permeability at fracture scale can be obtained from the equations from (5.9) to (5.16). The coefficients m_0, m_2, m_4, σ and d_0 in the probability

density function $\varphi(z)$ are determined by surface profiling prior to experimental measurement of closure [96].

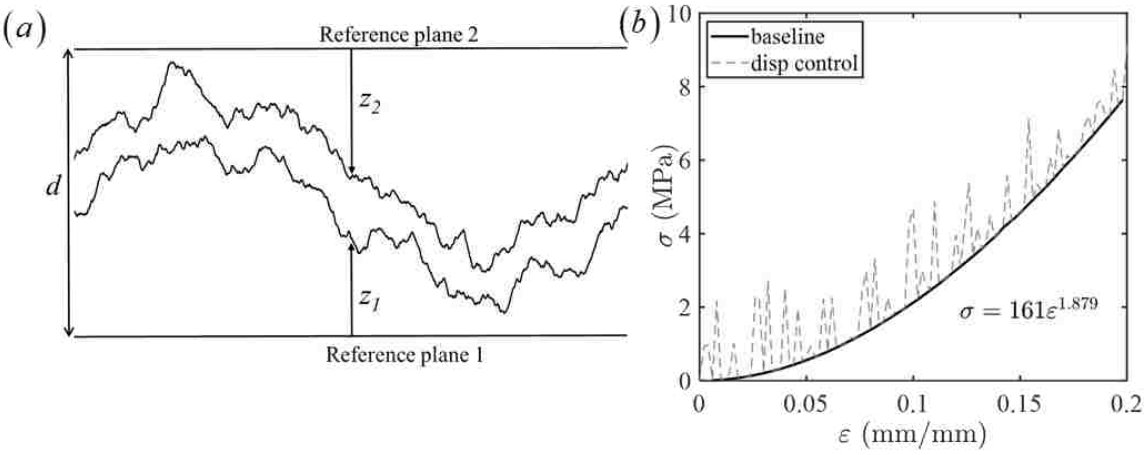

Figure 5.16 Deformation Curve of Asperities. (*a*) Two rough surfaces in contact. The actual topography is defined by upper surface heights z_2 measured with respect to the upper reference surface and lower surface heights z_1 measured with respect to the lower reference surface. (*b*) The fitting of base line in Figure 5.3.

This damage of asperity is irreversible. The normal stress and permeability calculated from Equation (5.12) and (5.16) can be used to analyze the long-term effect of thermal effect. The stress-permeability relation in asperity scale is the key to analyze the thermal effect in reservoir scale and long-term term. Current stress-permeability models [107, 108] did not consider this damage in their models. This upscaling can be used to supplement or refine those stress-permeability models.

5.5. SUMMARY

This section presented the comprehensive study of asperity failure under sudden cooling process under the EGS scenario. The effect of pore pressure, overburden

pressure, asperity size and fracture orientation were analyzed in this section. The main findings are summarized as follows:

(1) Thermo-mechanical analysis was conducted to investigate the deformation and potential failure of asperity. The results demonstrated the likelihood of fracture closure under the combined overburden pressure and injection-cooling process. Two major asperity damage mechanisms, which were contact damage and cracking within the asperity, potentially leading to fracture closure were revealed and analyzed. The contact damage dominates compressive deformation of the asperity, but it cannot induce the asperity failure by itself. The radial cracking inside the asperity counteracts compressive deformation of the asperity, and this cracking induced spalling and shear failure is responsible for the asperity failure and the possible fracture closure. Based on the significant effect of the thermal spalling and shear failure, the thermal cracking dominates the failure of asperity in EGS fractures. Further, the evolution of cracking of asperity shows significant impact of temperature difference on radial crack length, while the overburden pressure partially counteracts this deterioration. It demonstrates that considerable thermal stress is a primary factor of asperity damage in cooling process.

(2) The generality of this model was verified by considering the sensitivity of the asperity size. It shows the same failure patterns with varied asperity radius.

(3) The horizontal and vertical fracture orientations were considered in this study to resemble the real configuration of fracture distribution in EGS. Bilinear curves of $\Delta\varepsilon$ in response to $\Delta T_{w\text{-}r}$ and σ_{hmin} reveal the similar failure patterns of the asperity in possible all fracture orientations.

In addition, the deformation curve of hemispherical asperity can be used as a good substitute to cylindrical asperity in Section 4. This model has more realistic asperity geometry and incorporates the damage of asperity tip. This extension to thermomechanical analysis will be explained in last section.

6. DEFORMATION OF POROUS ASPERITY

6.1. BACKGROUND

Understanding the stress-induced deformations of asperities is critical to control deformation of fracture and gain insight on induced seismicity in geothermal problems. However, modeling the deformation of the contact asperities is challenging due to the rock heterogeneity and the complicated damaging and fracturing process under combined thermal-mechanical loadings. Laboratory experiments have shown various cracking patterns of rocks under thermal loading including fracture branching, coalesces, and spalling [109-111]. The failure of the quasi-brittle granite is mostly due to the propagation and intersection of pre-existing micro-cracks [82, 86]. This macroscopic representation of micro-crack development can be qualitatively described by damage mechanics [85, 112]. The damage variable is generally introduced to characterize surface density of intersecting micro-cracks following the thermodynamic principle [87]. The reduced material stiffness can then be calculated using the damage variable [113]. In the context of geothermal system, damage mechanics has been used to couple with hydrothermal effect to analyze the stress or permeability variation under crack propagation and nucleation [114-116].

To account for the heterogeneity of the materials, the probabilistic description was introduced into the damage model framework [117]. This probabilistic damage model (PDM) has then been widely used in rock mechanics due to its good depiction of macroscopic rock behavior by incorporating the spatial distribution of mechanical properties or structures. It is relatively easy to describe and calibrate the microstructures

and rock heterogeneity using the statistical distributions. The relatively low computational cost (compared with other computationally intensive method, such as Monte Carlo method [118]) and well-behaved convergence provide flexibilities in modeling problems with the complex boundary conditions and the mechanical contact. Liu et al. [119] established a mesoscale numerical model for thermal loading induced rock fracture problem. The coefficients of thermal expansion of mineral grains were varied to observe the effect of heterogeneity on the damaging process.

In the present work, we conducted a three-dimensional thermal-mechanical finite element model of two hemispherical asperities in contact with the porosity dependent PDM. Based on the uniaxial compression/tension, and indirect Brazilian disk experiments on granites[89, 120], we proposed an asymmetric triangular/trapezoidal stress-strain profiles describing both elastic and softening stages of the material behavior. An isotropic damage variable was introduced based on the proposed stress-strain profiles. The porosity effect on the material stiffness and strength was quantified using the energy-based effective medium theory [121]. The Weibull distribution function was implemented to consider the probabilistic characteristics of the porosity and the corresponding effects on the material stiffness and strength.

In the computational model, constant loading pressure on the top of asperity was maintained while asperities underwent the variation of the temperature field. The shrinkage of asperity would initiate crack at the connected position of asperity and rock block. This crack would propagate radially towards the center of connected circle. In this study, damages and this radial cracking induced by contact and displacement constraints from the fracture aperture were considered. The associated stiffness reduction in the

asperities was identified and characterized. The interaction between the contact induced damage and the radial cracking dominant deformation mechanisms was quantified using the analytical model. At the end, a semi-analytical fitting model was utilized to obtain the deformations with the overburden pressure and average temperature differences input. In addition, the effect of porosity on this coupled failure mechanism has been investigated. Field data were collected and compared with the modeling results providing predictions on fracture closure.

6.2. POROSITY DEPENDENT FAILURE CRITERION

For the compacted granite, the porosity is rarely considered in the mechanical analysis. However, porosity, particularly the porosity distribution, influences the compressive mechanical behavior of the granite significantly [122]. In addition, higher amount of pre-existing micro-cracks, pores and voids reduces the stiffness of the rock skeleton and contributes to the increase in the induced cracks at peak stress. As a part of granite block (in Figure 5.1), porous structure and porosity effect of asperities should be incorporated to mimic real response of fracture surface. Porous granites, as shown in Figure 6.1*a-b* [123], typically have statistical distributions in both elastic modulus and strength which significantly affect the average properties. This effect is typically quantified using Nur's critical porosity model [124]:

$$K = K_{solid}\left(1 - \frac{\phi}{\phi_c}\right) \tag{6.1}$$

$$G = G_{solid}\left(1 - \frac{\phi}{\phi_c}\right) \tag{6.2}$$

where ϕ is porosity, ϕ_c is critical porosity or percolation porosity and set to 0.4 for crystalline granites [125] . K_{solid} and G_{solid} are bulk and shear modulus of solid phase in granites. K and G are the bulk modulus and shear modulus of dry porous granites.

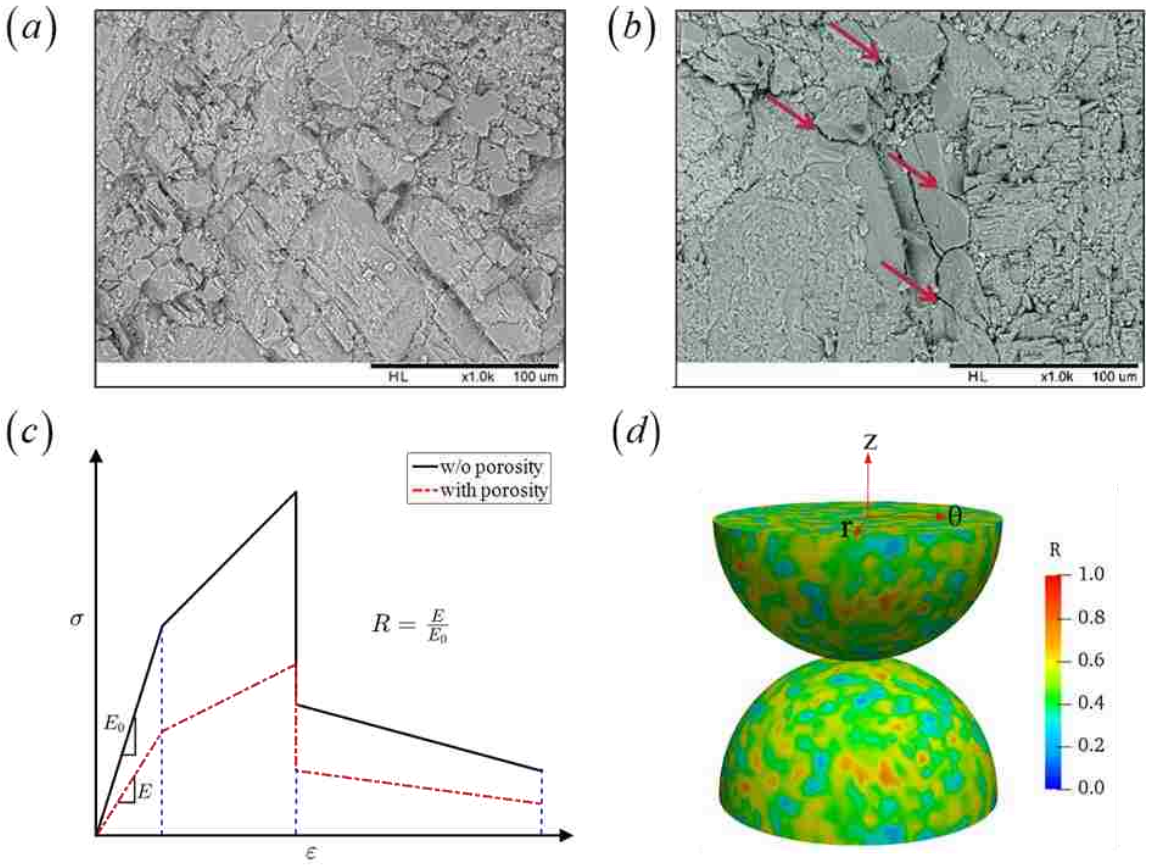

Figure 6.1 Microstructure of Granite. (*a*) Before loading and (*b*) after loading [123], red arrows pointing at microcracks, (*c*) strength reduction due to porosity, (*d*) spatial distribution of reduction factor.

Hence, the elastic strain energy of dry granite is:

$$W_e = \frac{3}{2}\varepsilon_{kk}^2 K \tag{6.3}$$

where W_e is the elastic strain energy density, ε_{kk} is the trace of the strain tensor. Based

on laboratory result, the variation of the strains at rupture is independent of the porosity [122]. Therefore, the failure strains ($\varepsilon_{c0}\ and\ \varepsilon_{to}$) introduced in Equations (5.4) and (5.5) stay unchanged while the Young's modulus and strength are reduced correspondingly by a reduction factor (R) defined below,

$$R \equiv \frac{W_e(K)}{W_e(K_{solid})} = \frac{K}{K_{solid}} = 1 - \frac{\phi}{\phi_c} \tag{6.4}$$

Petrophysical heterogeneity analysis widely adopts the Weibull distribution [126] to research the structural strength, fatigue, and other problems of rocks, which have obtained some satisfactory numerical simulation effect and good consistency with the experiments [116, 127]. The porosity distribution is assumed to follow the Weibull distribution $f(\phi)$,

$$f(\phi) = \alpha\beta\phi^{\beta-1}e^{-\alpha\phi^{\beta}} \tag{6.5}$$

$$\phi_m = \alpha^{\frac{1}{\beta}}\Gamma\left(1+\frac{1}{\beta}\right) \tag{6.6}$$

$$\lambda^2 = \alpha^{-\frac{2}{\beta}}\left[\Gamma\left(1+\frac{2}{\beta}\right) - \Gamma^2\left(1+\frac{1}{\beta}\right)\right] \tag{6.7}$$

$$\Gamma(z) = \int_0^{\infty} x^{z-1}e^{-x}dx \tag{6.8}$$

where α and β are scale and shape parameters, respectively. ϕ_m and λ are the mean and standard deviation, respectively. $\Gamma(z)$ is the Gamma function.

From Equation (6.8), the probability distribution function $f(R)$ for reduction factor *R* is then calculated as:

$$f(R) = \phi_c\alpha\beta[R^{-1}(\phi)]^{\beta-1}e^{-\alpha\left[R^{-1}(\phi)\right]^{\beta}} \tag{6.9}$$

$$R^{-1}(\phi) = \phi_c(1-R) \tag{6.10}$$

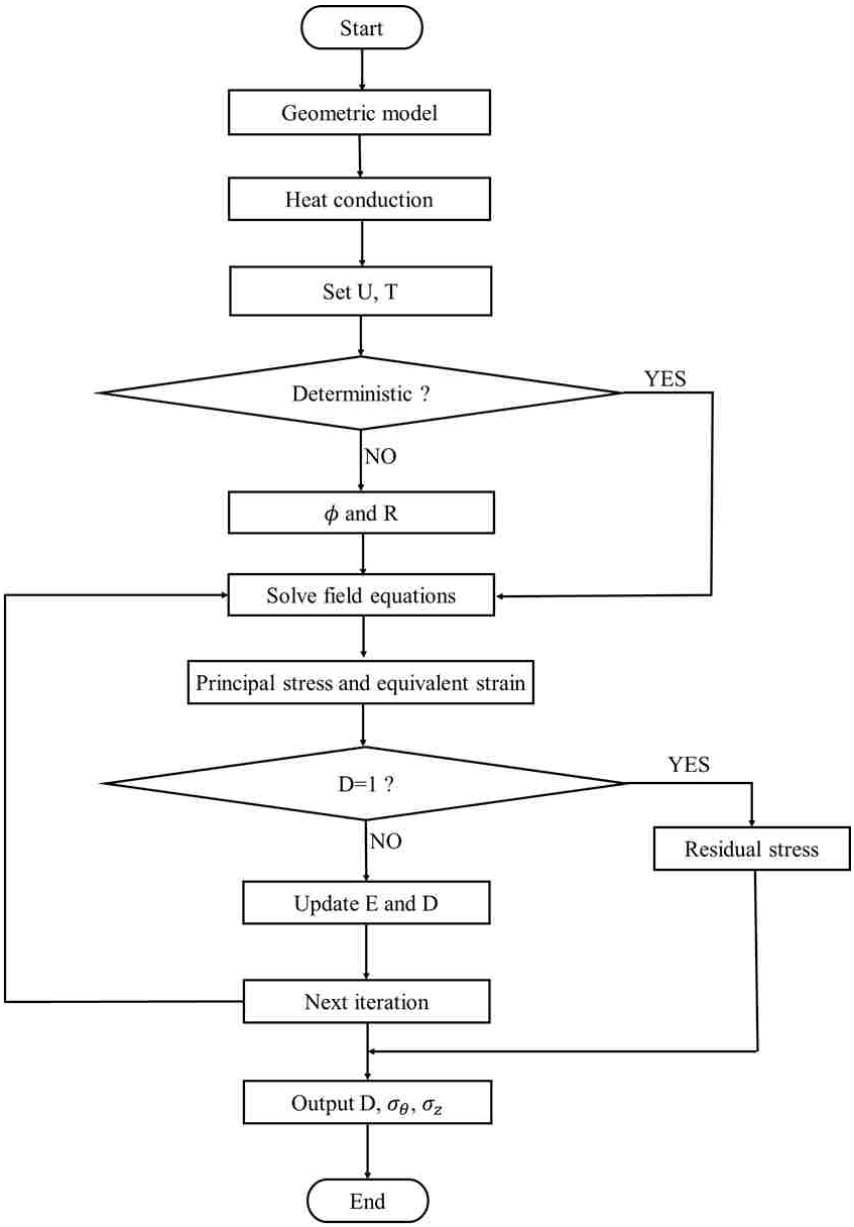

Figure 6.2 Flow Chart of UEL Subroutine.

where $R^{-1}(\phi)$ is inverse function of $R(\phi)$. Since the actual ϕ is in the range between 0.1% to 30% [128], $R(\phi)$ monotonously decreases in the range between 0.996 to 0.0893 as ϕ increases. A typical spatial distribution of R in the model is shown in Figure 6.1*d*. In the numerical analysis, the standard deviation versus the mean porosity ratio is fixed

($\frac{\lambda}{\phi_m} = 0.5$) simulating the actual porosity distribution. The mean porosity is varied to investigate its effect on the failure process.

6.3. NUMERICAL IMPLEMENTATIONS

The thermal-mechanical coupling and the porosity dependent constitutive models are integrated using the user-defined element subroutine (UEL) on the ABAQUS® finite element analysis platform. The flow chart is presented in Figure 6.2. The porosity distribution input is determined prior to the analysis. This is followed by the coupled damage algorithm which allows the simultaneous computation of both temperature and displacement fields.

6.3.1. Random Porosity and Weibull's Distribution. The Weibull's distribution is implemented following the algorithm in Figure 6.3*a*. The mean porosity ϕ_m and the variation λ are determined first. The shape parameters α, β are determined from Equations (6.6) and (6.7). The Monte-Carlo method [118] is then applied to generate probabilistic material properties.

In this implementation, a random number U uniformly distributed in the range of (0, 1) is generated. Given the α, β, the porosity can be obtained as:

$$\phi = \left(-\frac{1}{\alpha}\ln(1-U)\right)^{\frac{1}{\beta}} \tag{6.11}$$

The corresponding strength reduction factors are then computed as illustrated in Figure 6.3*b*. Considering the gap between the physical range of porosity (0.001, 0.3) and the natural range of Weibull's distribution (0, ∞). Truncations are performed on the numerically generated porosity as shown in Figure 6.4*a* for several distributions of mean

(*a*)

Algorithm: ϕ, R

Data: $\phi_c, \phi_m \in [\phi_{min}, \phi_{max}]$, λ/ϕ_m, *Flag*, element number N, E_0, Weibull pdf $p(\alpha, \beta, x)$, $R = f(\phi, \phi_c)$.

$\phi_m, \lambda/\phi_m \rightarrow \alpha, \beta$
Do 1:N
  Generate uniform random number U.
  Do
    $\phi_0 = p(\alpha, \beta, U)$
    If ($\phi_0 <= \phi_{max}$) then
      If ($\phi_0 >= \phi_{min}$) then
        $\phi = \phi_0$
        Exit
      End
    End
  End do
  $R = f(\phi, \phi_c)$

  If (*Flag*=0) then
    Continue
  Else
    E=R*E_0
  End
End do

(*b*)

Algorithm: Update E, D

Data: principal stress: $\sigma_1, \sigma_2, \sigma_3$, equivalent strain:$\bar{\varepsilon}$, constitutive parameters: $\varepsilon_{ci}, \varepsilon_{cr}, \varepsilon_{cu}, \varepsilon_{ti}, \varepsilon_{tr}, \varepsilon_{tu}, \varepsilon_{tr}, \varepsilon_{tu}$

If $\sigma_3 < 0 < \sigma_2 < \sigma_1$ && $\left|\frac{\sigma_1}{\sigma_3}\right| < 0.1$
  $\bar{\sigma} = \sigma_3$
Elseif $\sigma_3 < \sigma_2 < 0 < \sigma_1$ && $\left|\frac{\sigma_1}{\sigma_3}\right| < 0.1$
  $\bar{\sigma} = \sigma_3$
Elseif $\sigma_3 < \sigma_2 < \sigma_1 < 0$
  $\bar{\sigma} = \sigma_3$
Else
  $\bar{\sigma} = \sigma_1$
End

If $\bar{\sigma} = |\sigma_3|$ then
  $\bar{\varepsilon} = \bar{\sigma}/E$
  If $\bar{\varepsilon} < \varepsilon_{cu}$ then
    E = residual
    D =1
  Elseif $\varepsilon_{cu} < \bar{\varepsilon} < \varepsilon_{cr}$ then
    Update E, D
  Elseif $\varepsilon_{cr} < \bar{\varepsilon} < \varepsilon_{ci}$ then
    Update E, D
  End
End

If $\bar{\sigma} = |\sigma_1|$ then
  $\bar{\varepsilon} = \bar{\sigma}/E$
  If $\bar{\varepsilon} > \varepsilon_{tu}$ then
    E = residual
    D =1
  Elseif $\varepsilon_{tr} < \bar{\varepsilon} < \varepsilon_{tu}$ then
    Update E, D
  Elseif $\varepsilon_{ti} < \bar{\varepsilon} < \varepsilon_{tr}$ then
    Update E, D
  End
End

Figure 6.3 Computational Algorithms of (*a*) ϕ and *R*, Update of (*b*) *E* and *D*.

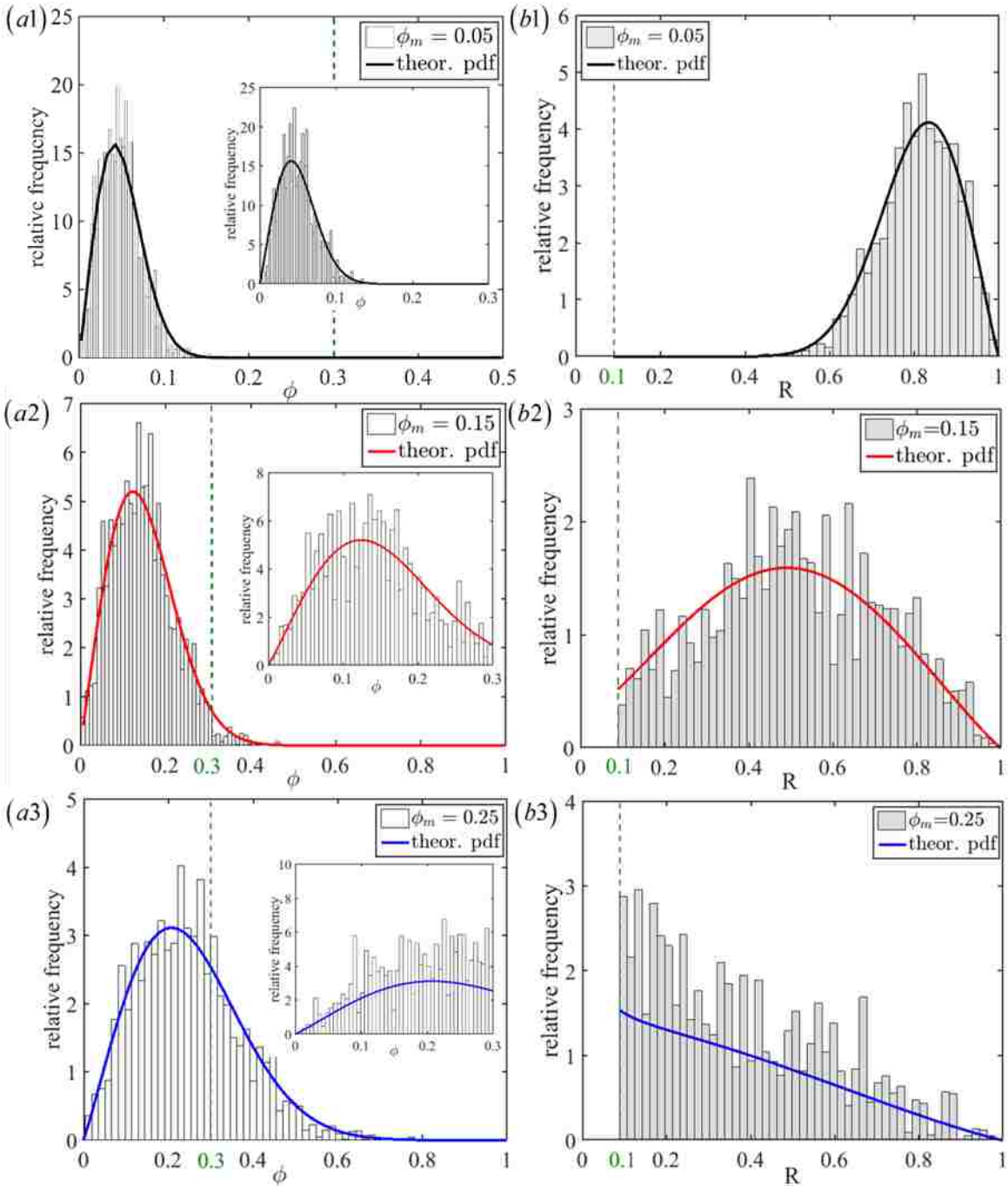

Figure 6.4 Display of Probability Density Function Used in Model. (*a*1, *a*2, *a*3) Numerical and theoretical Weibull distribution of different porosities (insets showing truncated porosity distribution), (*b*1, *b*2, *b*3) reduction factor distributions.

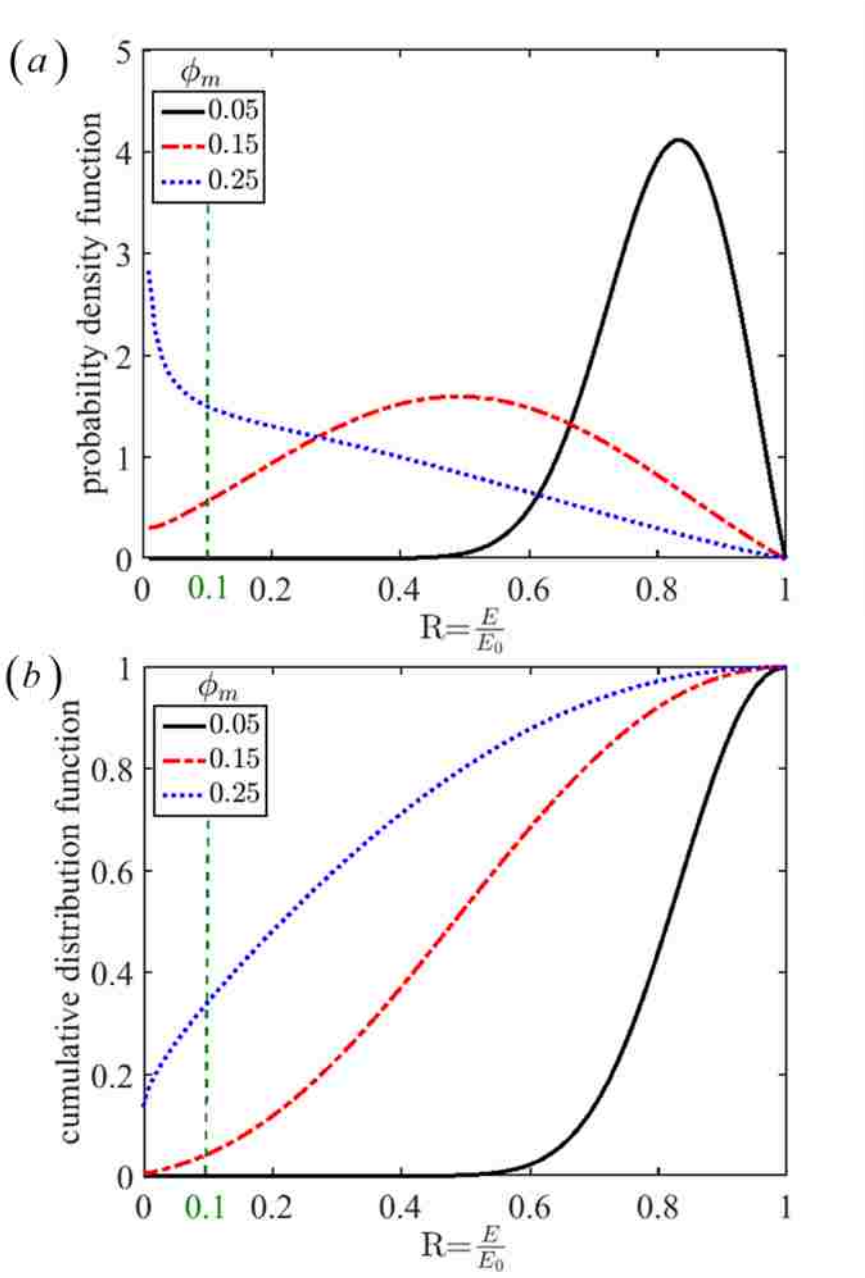

Figure 6.5 Probability Density Function and Cumulative Distribution Function. (*a*) Probability density function and (*b*) cumulative distribution functions of reduction factor at three porosities.

porosities. The corresponding strength reduction factors are then obtained with a truncated range of (0.1, 1.0) as shown in Figure 6.4*b*. These numerical inputs are then

fitted with a truncated probability distribution function. A Chi-square fitting criterion [129] is applied to ensure a high confidence in maintaining the original shape and accumulated probabilities, which are shown in Figure 6.5*a-b*. It should be noted that the porosity variation changes the distribution of strength reduction factor significantly. From the numerical results, the high porosity more likely gives a large strength reduction factor (blue lines).

6.3.2. Thermal-Mechanical Coupling and Damage Variable. The initial temperature of the top flat surface is set at the reservoir temperature, and the bottom curved surface is set as the water temperature. The temperature, as an additional degree of freedom, is obtained and coupled with the stress during the transient heat transfer process.

The numerical algorithm implemented is shown in Figure 6.3*b*. Tension and compression stress states are determined using Equation (5.6). Then, the equivalent strains are calculated. The tangent Young's modulus E and damage variable *D* are updated based on Equations (5.4) and (5.5) .The mechanical and thermal properties used are listed in Table 5.1.

6.4. RESULTS AND DISCUSSIONS

This section is discussed in three parts. In the first part, the response of contacting asperities under pure mechanical loading is investigated. Part of this result is presented in Section 5 The nominal stress and strain response are obtained from dividing the reaction force and displacement by the area of top surface and the radius of the asperity, respectively. In addition, this correlation of loading force and deformation of asperity is

validated with existing results. In the second part, the cooling process under constant pressure was investigated. The interaction between the contact induced damage and radial cracking was identified from the nominal strain responses. In the last part, the modeling results were compared with actual field data providing meaningful interpretations. The effect of porosity was also investigated by comparing with the results from deterministic model.

6.4.1. Mechanical Loading on Asperities. Two different cases are discussed: solid asperity and porous asperity. The effect of porosity is elaborated in the deformation.

6.4.1.1. Solid asperity. Neglecting the thermal and porosity effect, the contacting asperities show a gradual crushing failure described by the stress-strain responses in Figure 6.6. Responses from the displacement (solid line in Figure 6.6*a*) and the force controlled (solid line in Figure 6.6*b*) loading protocols are presented. The spikes in the displacement controlled response (Figure 6.6*a*) are mainly from the local crushing in the contact area. Linking these spikes, we obtain the relative smooth force controlled responses (Figure 6.6*b*) showing plateaus whenever the instability or snap-through occur due to the loss of local stiffness from contact. Both the displacement and force controlled responses show the increasing trend as the applied pressure increases. This indicates a relative stable deformation propagation under pure mechanical loading for solid asperities.

It’s worth noting that the asperities on the rough fracture surface are dispersed. The real contact area would increase with rising loading on the fracture surface. To simplify the calculation in this study, the contacting asperities are assumed to have the same curvature of contacting tip as the same assumption made by Greenwood and

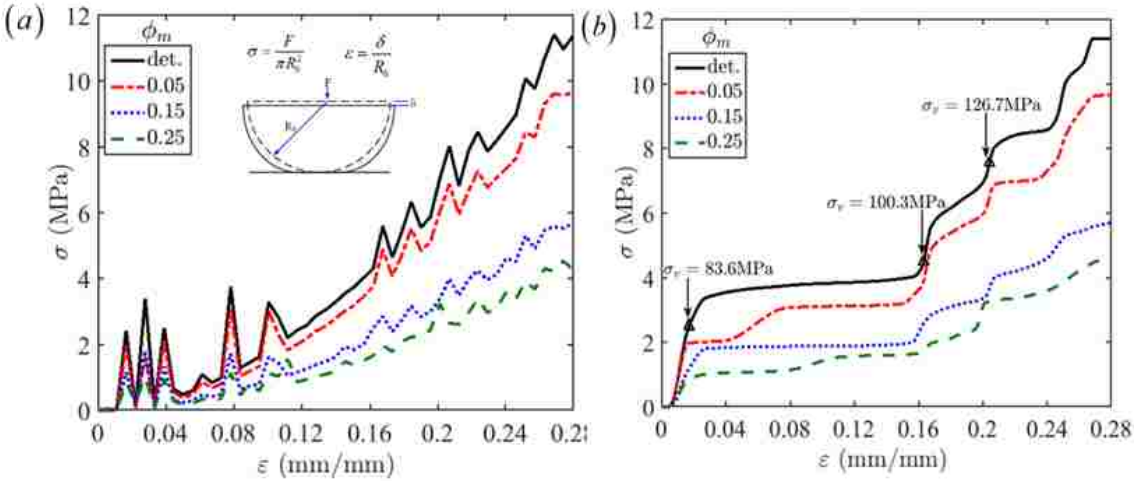

Figure 6.6 Stress Versus Strain Responses for Deterministic and Probabilistic Models under (*a*) Displacement and (*b*) Force Controlled Mechanical Loadings.

Williamson [56, 95]. In addition, considering the real contact area of asperities pairs maximally takes up 50% of the nominal area of fracture surface [22], the reasonable contact area of 27% is assumed for this study. That is, contacting asperities occupy 27% area of basic cell (comprising one asperity pair and residual void space). At here, the deformation of void space under loading is not considered. Therefore, the loading force on one basic cell can be calculated and is denoted as *P* in Figure 6.7. The correlation of loading force *P* and real contacting area *A* can be obtained by fitting the discrete data in numerical simulation and is shown in Figure 6.7. The power is 1.643 and is very close to the 1.5 in reference by Greenwood and Williamson [56, 95]. In addition to the power of calculation, this model can also get verified by the experimental data. In Beeler and Hickman's work[96], the asperity strain (defined as vertical deformation divided by radius of hemispherical asperity) at 7 MPa macroscopic normal stress range is typically 0.14. In this study, the normal stress corresponding to 0.14 asperity strain is approximately 4 MPa. The results are in the same order of magnitude. This small

difference is from the omission of deformation at void space region. The average nominal stress from purely elastic contact can be calculated by $\langle \sigma_c \rangle = 0.42E^* \sqrt{\delta/R}$ in reference[96]. The Hertizan contact stress is about 19 GPa at asperity strain of 0.14. It shows that the damage model can obtain the similar result with experiment but the Hertizan model is not physically plausible.

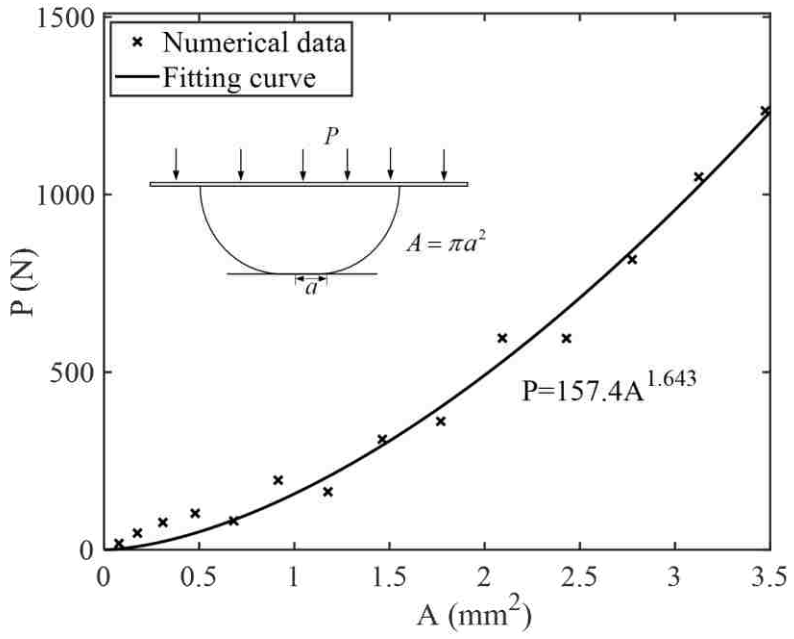

Figure 6.7 The Loading Force and Contact Area for Mechanical Loading of Solid Asperity in Numerical Simulation.

6.4.1.2. Porosity effect. Three different porosities ($\phi_m = 0.05, 0.15, 0.25$) are considered. The results show significant stress reductions in both displacement and force controlled responses as shown in Figure 6.6. As the porosity increases, the stiffness of the contacting asperity reduces. This reduced stiffness comes from the increased damaged area as presented in Figure 6.8. As shown in Figure 6.8*a*, two specific data points along

the force controlled response for the deterministic model and the case with porosity ($\phi_m = 0.15$) are selected. The associated damage contours show a significant increase of damaged area with $\phi_m = 0.15$.

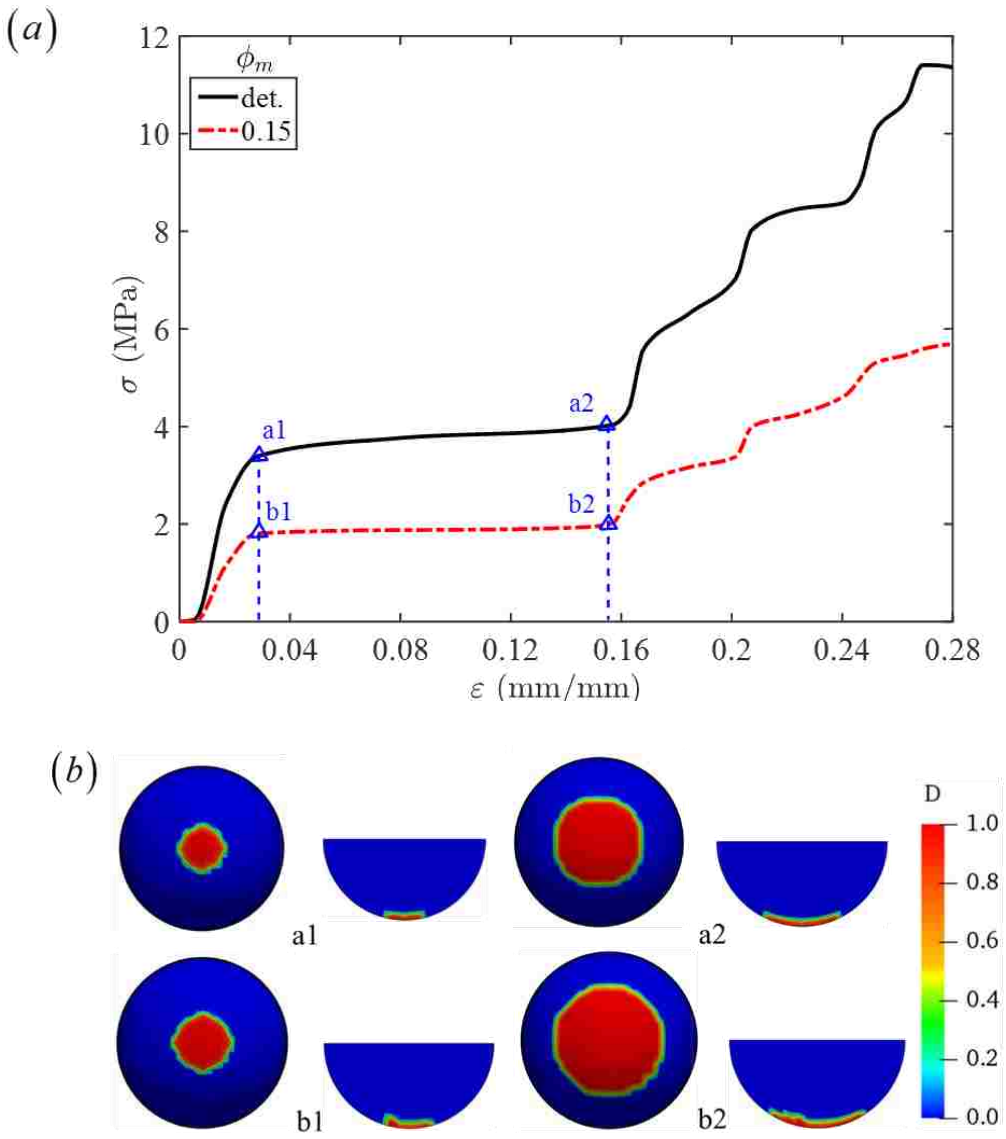

Figure 6.8 Response of Solid and Porous Asperities: (a) the stress-strain curve and (*b*) damage variable contour at critical points.

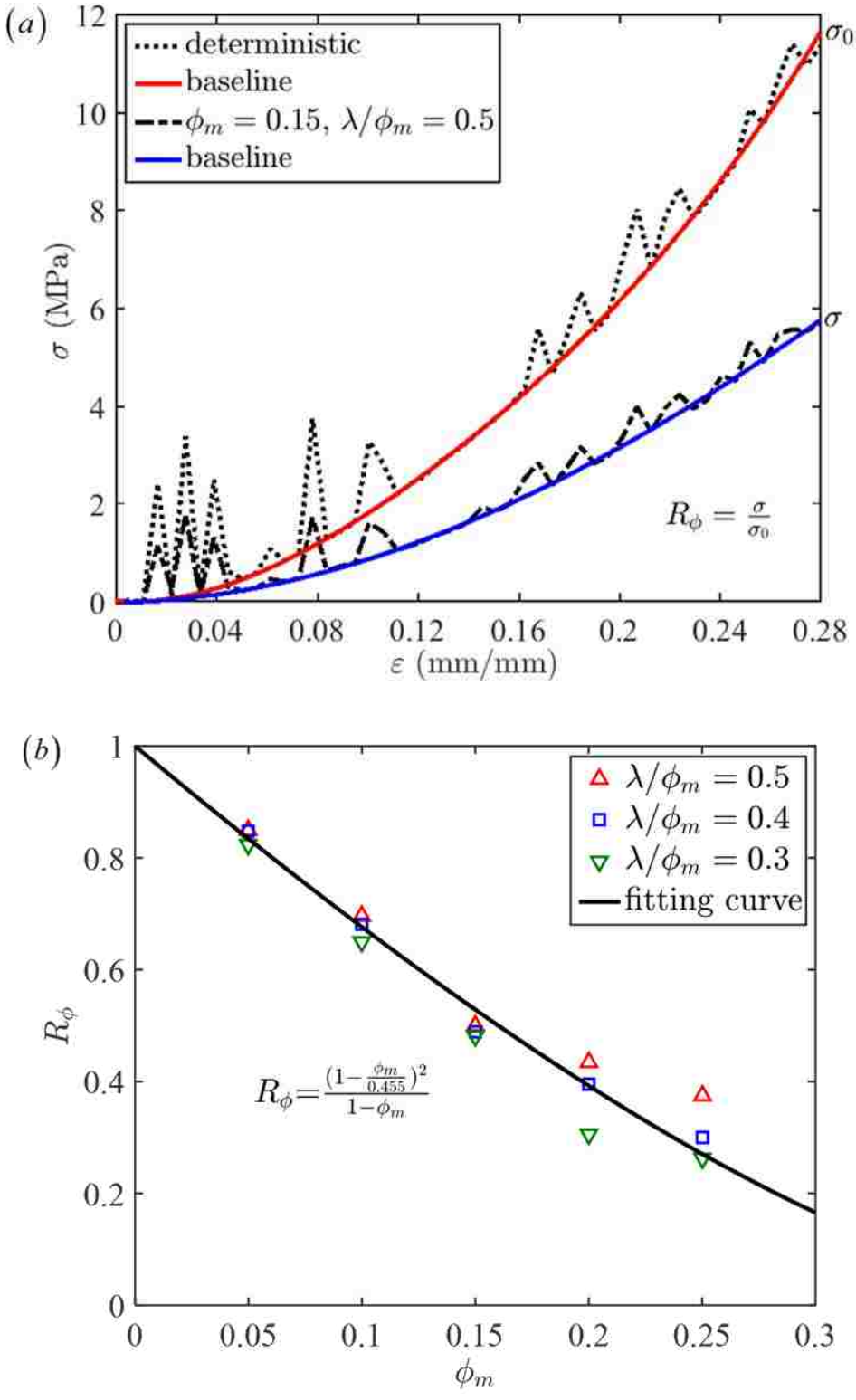

Figure 6.9 Comparison of Deterministic and Probabilistic Models. (a) At stress-strain curve and (b) fitting of reduction factor R_ϕ versus mean porosity ϕ_m.

To quantify this effect, an overall reduction factor R_ϕ is defined as the ratio between the baseline stress response of deterministic model and porous model as illustrated in Figure 6.9*a*. This effect is plotted in Figure 6.9*b*, an approximately linear relationship is observed between the increasing porosity and overall reduction factor R_ϕ by data fitting. This indicates a proportional reduction in vertical stiffness of the contacting asperities under overburden pressure.

6.4.2. Thermal-Mechanical Loading. Neglecting the porosity effect, the thermal-mechanical loading of the asperity is applied by maintaining the overburden pressures (σ_v) while increasing the temperature difference (ΔT) between cold water and hot asperity. During this process, the lateral component of displacement at the top surface of the asperity remains fixed. The temperature profile follows the solution obtained in the heat transfer process in the transient state. This loading procedure is illustrated in Figure 5.6*a*. Firstly, the thermal loading of damage model is compared with standard elastic model. The elastic model is set up in ABAQUS® CAE with the same parameters setting in Table 5.1. The same mesh size and loading procedure is followed in elastic model. The vertical deformation of asperity responding to increasing temperature difference is shown in Figure 5.6*b*. The thermal loading leads to smaller thermal deformation for elastic model compared to damage model on solid asperity in the whole stage. Because the element is always intact for elastic model, whereas the elements at contact region is damaged (D=1) or close to damage (0<D<1). With increasing temperature, more elements will loss bearing capacity for damage model, leading to approximately linearity. For the elastic model, with increasing contact area, higher loading can be withstood and the curve asymptotically flats out with increasing temperature difference.

For the thermal loading of porous asperity, three particular overburden pressure were selected spanning the feasible range in relationship with the actual exploration depth range (3-5 km) [83]. They are 83.6, 100.3, 126.7 MPa, Which can be mapped into the nominal pressure applied on the top surface of the asperity. The overall overburden pressure loads on the fracture surface and matrix rock region without fracture. The same asperity size on the fracture is assumed to calculate the force on each small basic region (composed of asperity pair and the cavity enclosed by two neighboring asperity pairs). The concept of this region is similar to that one in reference [5]. The force on this basic region is balanced by the stress on the asperity and fluid pressure in fracture. The fluid pressure (pore pressure) is set to hydrostatic pressure along the fracture length for simplification. Even though fluid pressure is function of various complicated factors, such as fracture length, flow rate, injection temperature etc., the total pressure drop between injection well and production is insignificant compared to temperature effect [130]. The detail for this mapping method refers to Section 5. The final mapping equation from global overburden pressure to loading stress on the top surface of asperity is:

$$\sigma = \left(\sigma_v - 2.46P_p\right)/0.54, \tag{6.12}$$

where P_p is the pore pressure at the depth of the asperity. Subtracting the initial strain (ε_0) caused by initial overburden pressure (σ_v), the fracture aperture closure ($\Delta\varepsilon$) is readily obtained and plotted against the temperature difference (ΔT) in Figure 10. As the temperature difference (ΔT) increases, which means that the asperities cool down to lower temperature, the fracture aperture closure ($\Delta\varepsilon$) increases over two linear stages with different slopes ($k_1 > k_2$). The critical temperature separating these two stages is about 30 °C. From the detailed analysis described below, we found the fracture aperture

closures of the two stages were mainly controlled by the contact induced damage and its interaction with radial fracture growth. These two stages were also found for cases with different overburden pressures (σ_v). As the overburden pressure increases, both slopes (k_1, k_2) reduce showing a pressure dependent fracture aperture closing behavior.

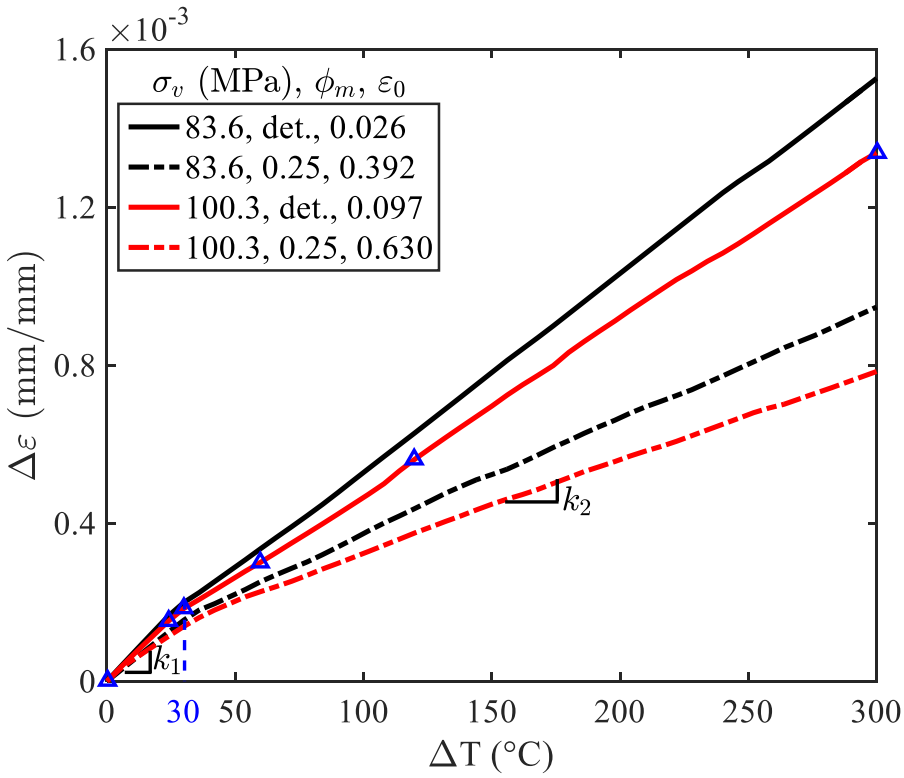

Figure 6.10 Fracture Aperture Closure versus Temperature Difference. (ε_0: initial strains before cooling, triangular symbols: selected temperatures for contour plots).

To examine and explain the two linear stages, we show the quarter-sectional contour plots of these state variables at ΔT at 0, 25, 30, 60, 120, and 300 °C under an overburden pressure of $\sigma_v = 100.3$ MPa as presented in Figure 6.11.

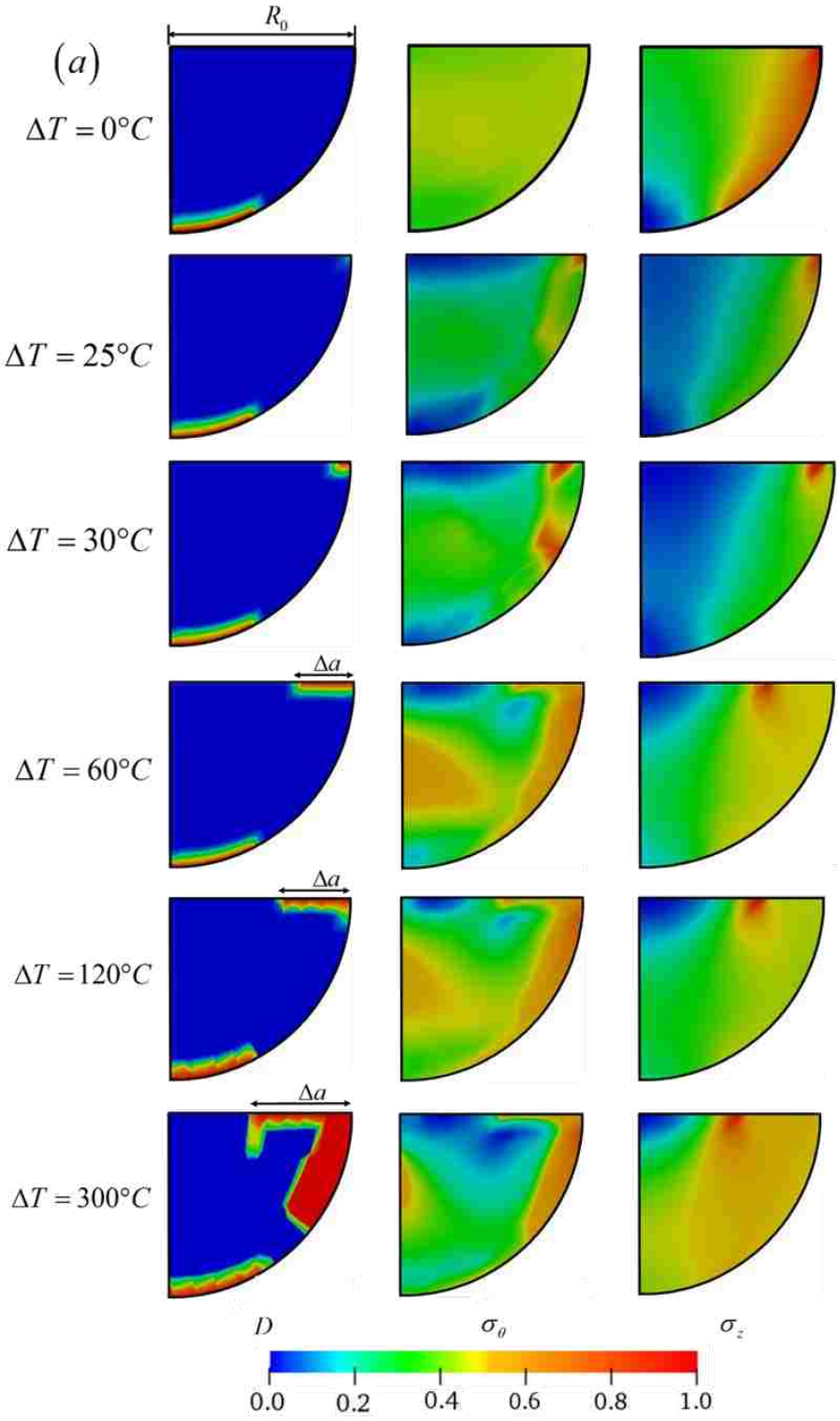

Figure 6.11 Damage Variable *D*, Hoop (σ_θ) and Vertical (σ_z) Stress Contours at σ_v=100.3MPa for (*a*) Deterministic Model; (*b*) Probabilistic Model at ϕ_m=0.25, λ/ϕ_m=0.5.

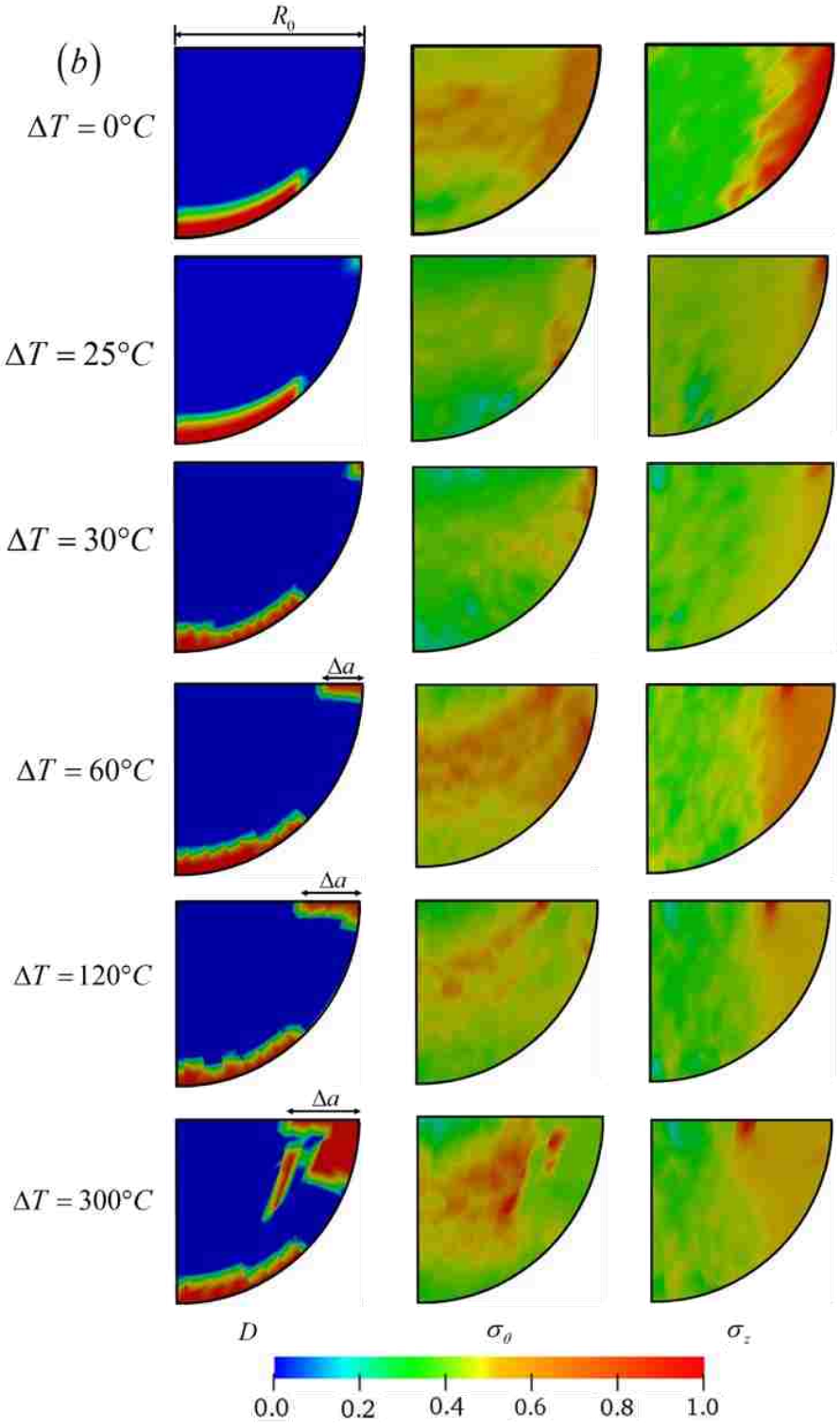

Figuure 6.11 Damage Variable *D*, Hoop (σ_θ) and Vertical (σ_z) Stress Contours at σ_v=100.3MPa for (*a*) Deterministic Model; (*b*) Probabilistic Model at ϕ_m=0.25, λ/ϕ_m=0.5. (cont.)

6.4.2.1. Contact dominant stage. Before ΔT reaches 30 °C, the thermal contraction in the asperity leads to stress release in the vertical direction (σ_z) comparing to the initial stress state due to overburden pressure loading. The contact induced damage zone remains without causing significant change of the overall vertical stiffness of the asperity. Therefore, a linear relation was found between fracture closure ($\Delta\varepsilon$) and ΔT with the slope k_1.

6.4.2.2. Radial fracture growth stage. When ΔT exceeds the critical temperature of 30 °C, the hoop stress (σ_θ) increases significantly due to the lateral constraint at the top surface. This introduces a radial fracture along with the increase of ΔT. However, as the radial crack propagates, the vertical stiffness reduces due to the loss of materials stiffness near the top surface. This causes intensified vertical stress near the contact zone leading to the increased damage in the bottom contacting zone. In this stage, the radial crack growth induced damage competes with the contact damage at the bottom giving rise to a reduced slope comparing to the first stage ($k_2 < k_1$). This is due to the reduction in the overall vertical stiffness of the contacting asperities. To quantify this competition, we define a damage ratio based on the volume integral of the damage variable over the top and bottom domain, $\gamma \equiv \frac{\int_{\Omega t} D dv}{\int_{\Omega b} D dv}$, where the top and bottom domain were separated by the geometrical center. Plotting r against ΔT in Figure 6.12, we found the critical points where the radial fracture occurs at ΔT= 30 °C and stop growing at ΔT= 150 °C for an overburden pressure of $\sigma_v = 100.3$ MPa, shown as the dashed lines. We also plotted the radial fracture growth in Figure 6.13a and found that the fracture initial temperature ΔT= 30 °C does not vary with different overburden pressures, however the fracture growth

termination temperature does. As the overburden pressure increases, the radial crack growth stops at higher ΔT. This is mostly due to the reduced hoop stress from the increased vertical compression. However, it is worth noting that the radial fracture growth terminates at the same length due to a constant fracture toughness of granites and fully constrained top surface in terms of lateral displacement. The energy release rate of the system increases slowly and reaches to a steady state. This can also be explained as the crack grows to the point at which the induced thermal stress is less than the tensile strength which arrests the radial fracture [98].

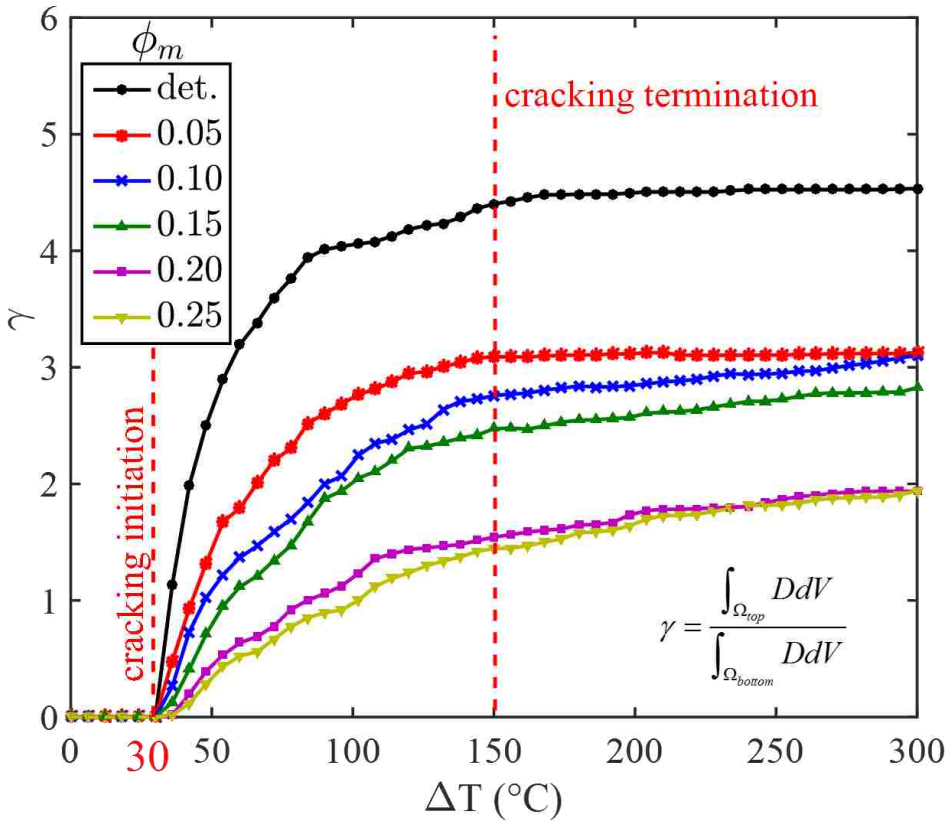

Figure 6.12 Damage Ratio γ with Respect to ΔT at Five Different Mean Porosity and Deterministic Model.

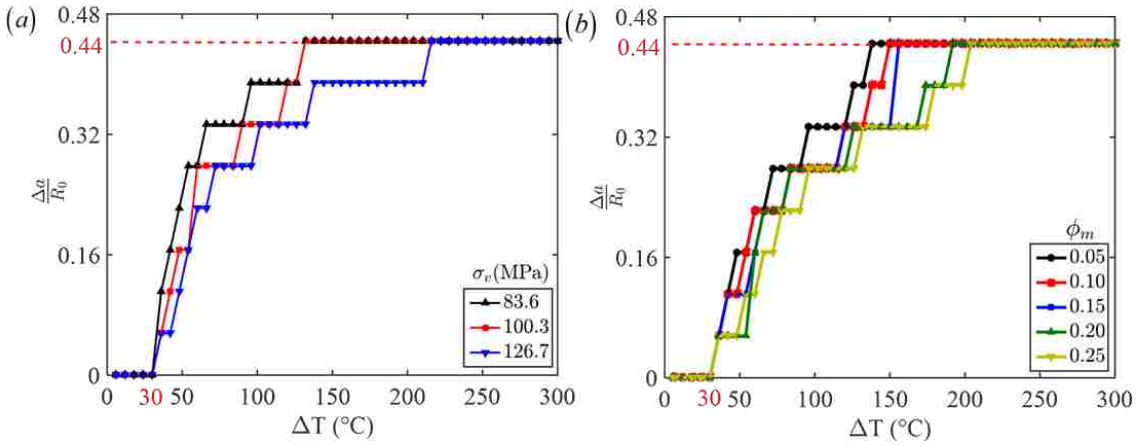

Figure 6.13 Relative Radial Crack Length $\Delta a/R_0$ versus Temperature Difference for (*a*) Deterministic Model; (*b*) Probabilistic Model at σ_v=100.3MPa and λ/ϕ_m=0.5.

6.4.2.3. Analysis and data fitting. An analytical model based data-fitting was also carried out to achieve a more efficient fracture closure prediction. Since the cooling process induced deformation is essentially elastic unloading, we could describe the fracture closure and temperature relation using the Hertzian contact theory [131], which gives the displacement and force response as follows,

$$\delta = \left(\frac{9F^2}{16R_0E^{*2}}\right)^{1/3} \tag{6.13}$$

where δ is the vertical displacement on the top of hemisphere. F is the force applied. R_0 is radius of hemisphere. $E^* = \frac{E}{1-\nu^2}$ is equivalent Young's modulus. δ and F relation follows the proportionality, $\delta \sim F^{2/3}$. Divided by $R_0\Delta T$ on both sides and combined with $\Delta\varepsilon = \frac{\delta}{R_0}$ and $\sigma_v = \frac{F}{\pi {R_0}^2}$, this proportionality gives the relationship between the stiffness and over burden pressure as $k_1 \sim {\sigma_v}^{2/3}$. We then fitted the numerical data with the derived functional form as shown in Figure 6.14*a* with close agreements. For k_2, we applied the

same functional form but considering a reduction caused by the radial fracture. A linear fitting was then obtained with close agreement as well as shown in Figure 6.14*b*. The competing failure mechanisms give us a pressure-dependent relation of k_2/k_1 as shown in Figure 6.14*c*. We then fit k_2 with varying overburden pressures as illustrated in Figure 6.14*d* with close agreement as well. With these fitting equations, we could directly obtain the fracture closure with known overburden pressure (σ_v) and temperature difference (ΔT).

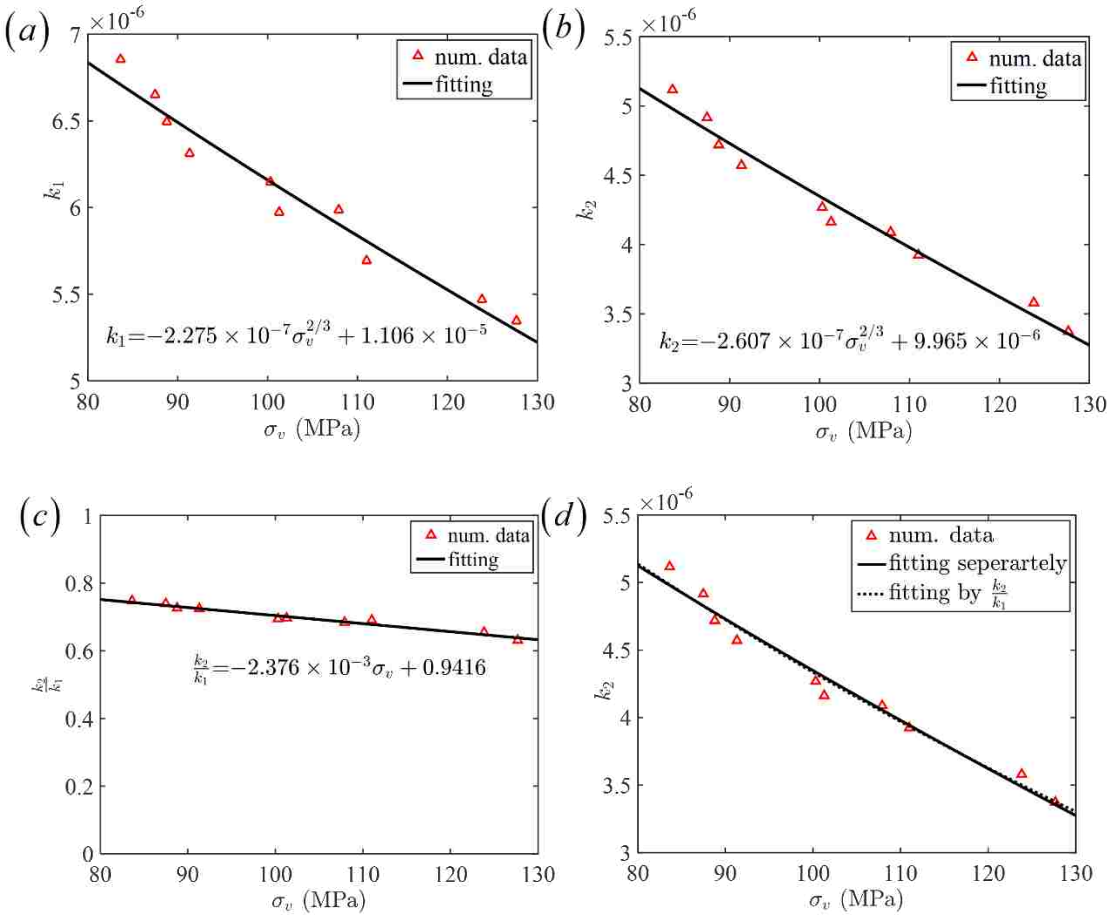

Figure 6.14 Fitting of Slope to Overburden Pressure. (*a*) Fitting of k_1 versus σ_v for deterministic model, (*b*) corresponding fitting of k_2 to σ_v, (*c*) ratio of k_1 to k_2 with respect to σ_v, (*d*) fitting of k_2 by equation in (*b*) and ratio in (*c*).

6.4.2.4. Effect on failure mechanism. Observing the fracture closure ($\Delta\varepsilon$) versus temperature responses (ΔT) in Figure 6.15 with varying overburden pressure (σ_v) and increasing mean porosities (ϕ_m), the bi-linear behavior remains, so does the result from deterministic model. Therefore, the reduced stiffness and strength of the asperity induced by porosity did not alter the two-stage failure mechanism. However, the increased mean porosity gives rise to the significant reductions in both k_1 and k_2. In the contact-damage dominant stage ($\Delta T \leq 30$ °C), the reduced stiffness due to porosity led to a significant reduction in the asperity stiffness. This is confirmed by a more uniformly distributed vertical (σ_z) and hoop stress (σ_θ) comparing to the deterministic model results as shown in Figure 6.11*b*. The reduced strength due to the porosity contributes to a significantly larger damage area near the contact as shown in Figure 6.11*b*. As the temperature entered the radial fracture growth stage ($\Delta T > 30$ °C), the initiation of radial fracture occurred. The identical critical temperature ($\Delta T_C = 30$ °C) indicates that the initiation of the radial fracture is not affected by the porosity. As temperature increases, we found a slight reduction in fracture growth rate and the delayed fracture arresting point as illustrated in Figure 6.11*b*. This fact is also corroborated with the evolution of damaging competition ratio γ shown in Figure 6.12. The damaged volume near top surface due to the radial fracture growth increases much slower than that of the bottom surface due to contact. As the porosity increases, this phenomenon becomes more apparent as shown in Figure 6.12 in terms of reduced γ. In addition, we compared the radial fracture growth as shown in Figure 6.13*b*. We found that the increasing porosity causes the slower fracture growth and higher ΔT to reach the fracture arrest length. In addition, the radial fracture stops at the same level, about 0.44 of the asperity radius, comparing to the deterministic model

without porosity. Therefore, the porosity induced reduction in stiffness and strength did not change the beginning and ending state of the radial fracture growth stage. However, the increasing porosity significantly added the amount of temperature difference (ΔT) to reach the fracture arrest length.

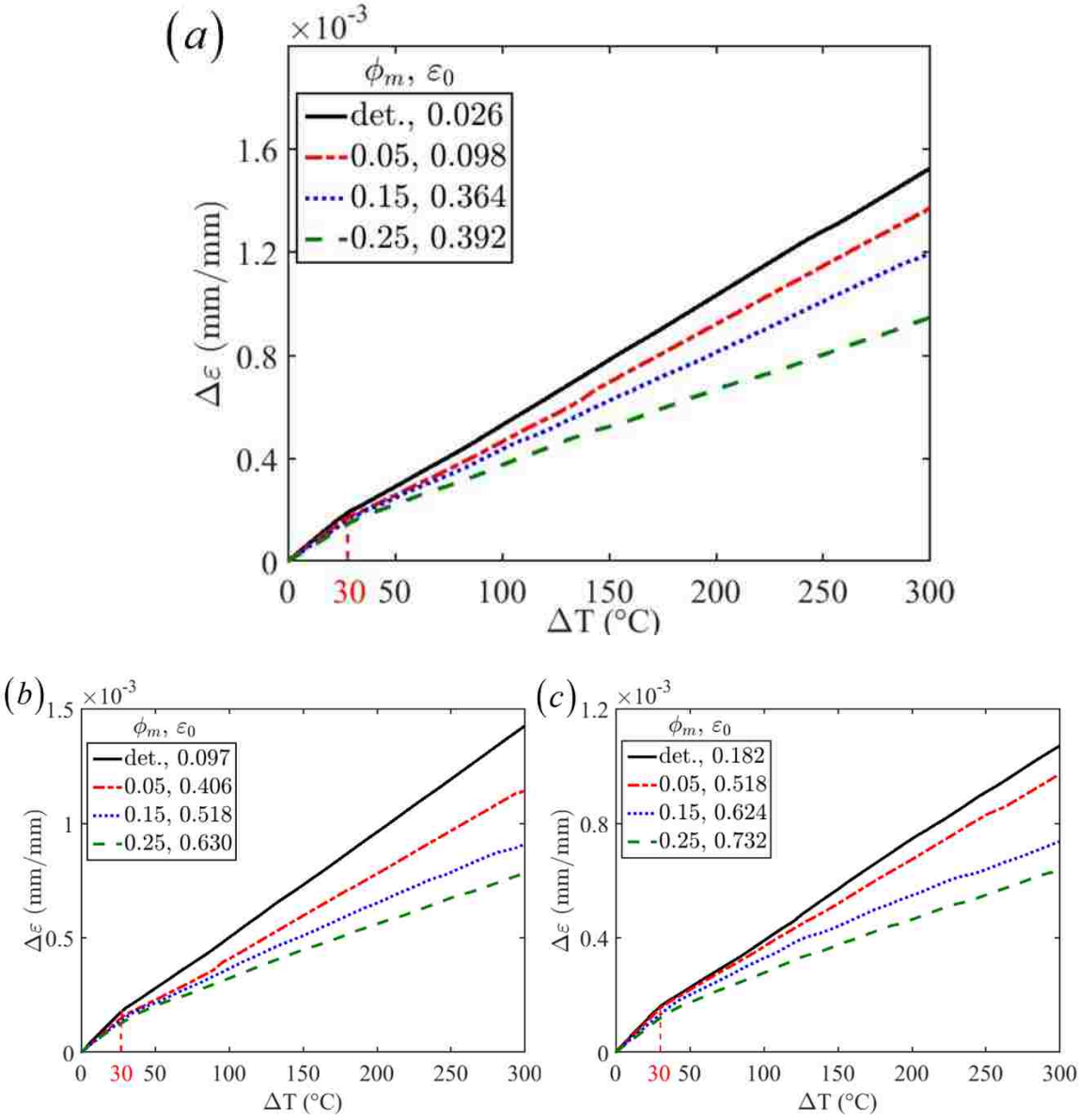

Figure 6.15 Effect of Temperature Variation on Asperity Strain Change at (*a*) σ_v=83.6MPa, (*b*) σ_v=100.3MPa and (*c*) σ_v=126.7MPa.

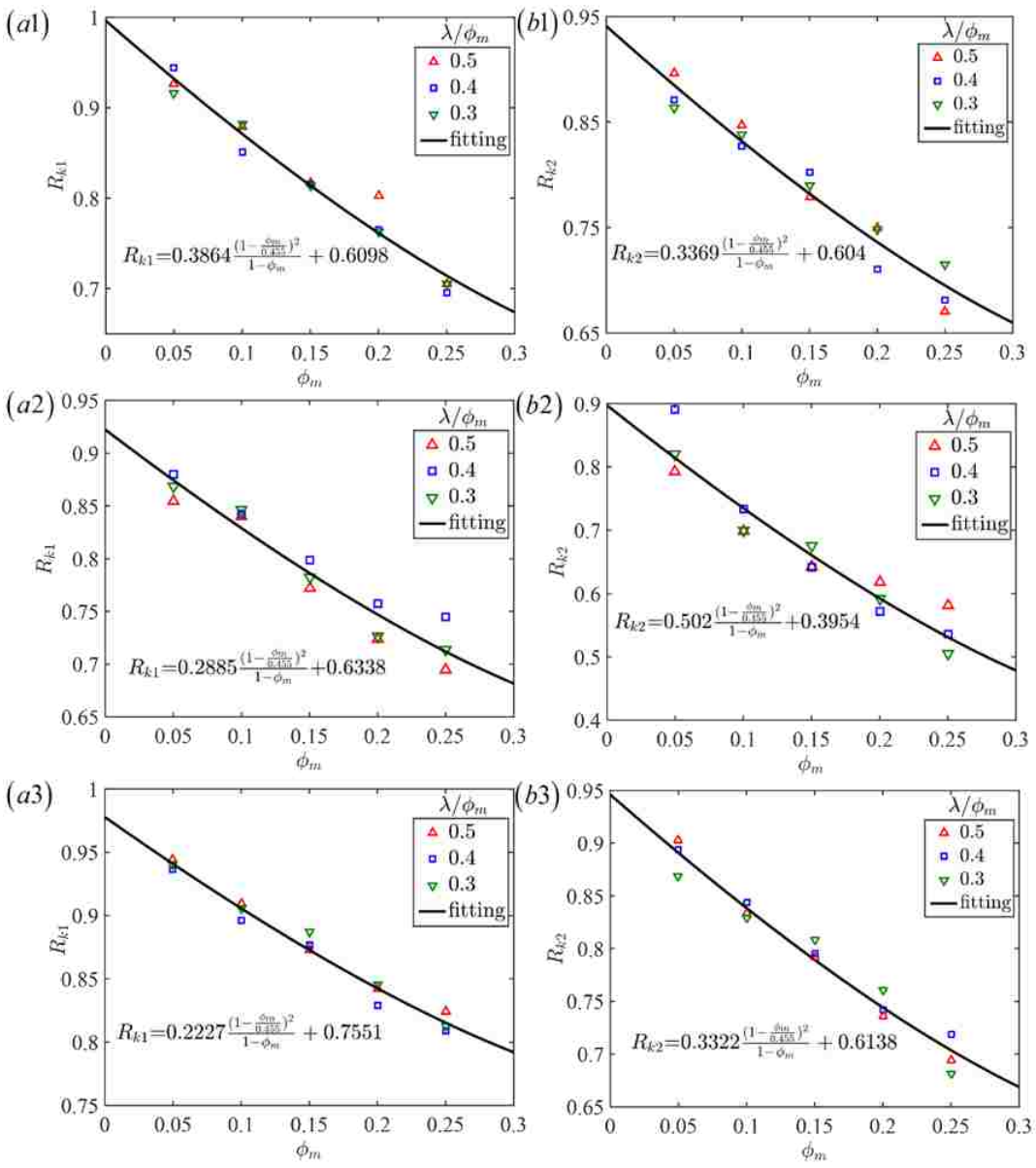

Figure 6.16 Fitting of Reduction Factor with Slope. (*a*1, *a*2, *a*3) Fitting of reduction factor R_{k1} for k_1 with respect to mean porosity ϕ_m and ratio λ/ϕ_m at σ_v=83.6MPa, σ_v=100.3MPa and σ_v=126.7MPa, (*b*1, *b*2, *b*3) the corresponding fitting of reduction factor R_{k2} for k_2.

6.4.2.5. Analysis and fitting. The correlation between the overburden pressure (σ_v) and both slopes in two stages ($k_1,\ k_2$) is obtained by fitting the numerical data.

However, we took advantage of the proportional reduction observed and conducted the

fitting with reduction factors ($R_{k_1} \equiv \frac{k_{1,por}}{k_1}, R_{k_2} \equiv \frac{k_{2,por}}{k_2}$) as shown in Figure 6.16. The increased overburden pressure gives rise to the additional increase in these reduction factors. Least-square fit was also used for fast extractions with close agreements. Similar analytical model based fitting were conducted for cases with porosities as shown in Figure 6.17. The results show an average lower fitting coefficients comparing to the case without porosity.

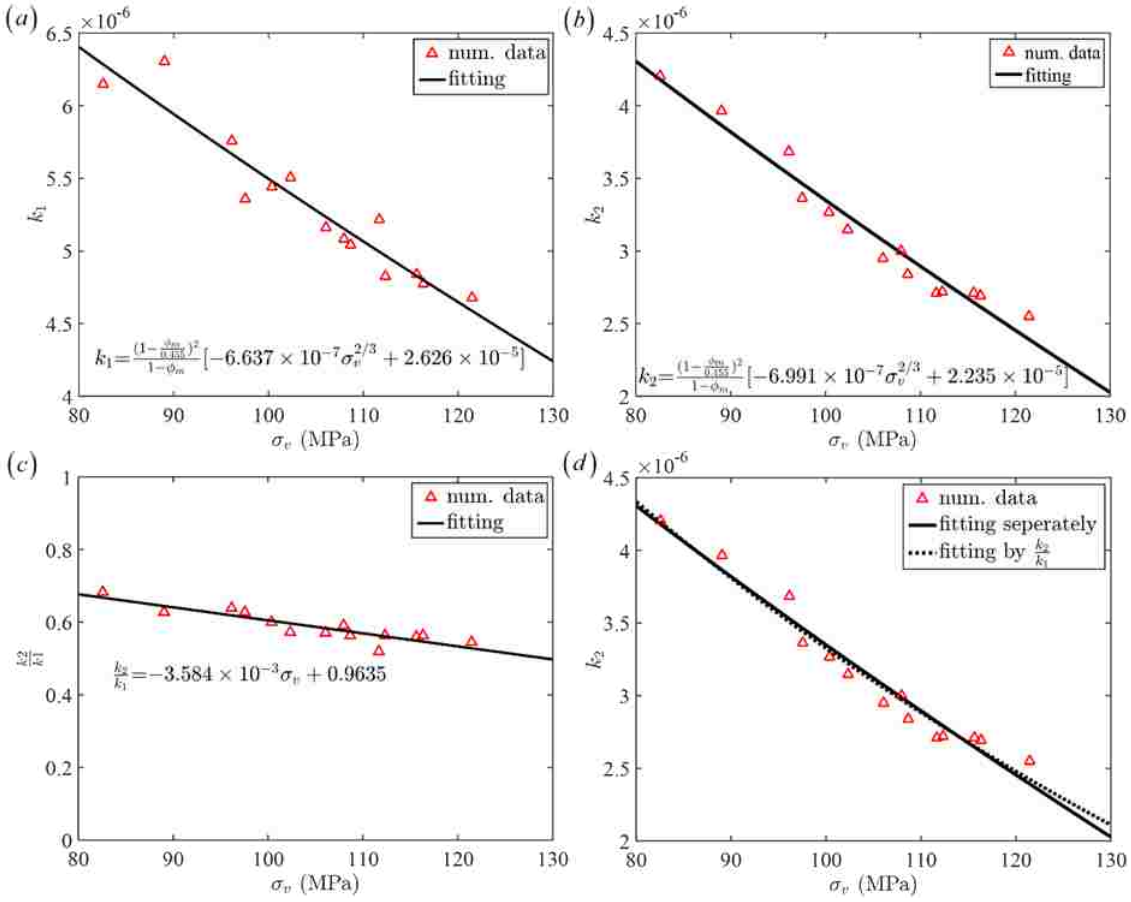

Figure 6.17 Fitting of Slope to Overburden Pressure for Probabilistic Model. Fitting of (a) k_1 and (b) k_2 with respect to σ_v for probabilistic model at ϕ_m=0.15, λ/ϕ_m=0.5. Fitting of k_2/k_1 (c) and k_2 (d) with respect to σ_v.

We collected all data as well as each corresponding least-square fit and compared them with the deterministic model results in Figure 6.18. As the overburden pressure increases, linear-wise reduction was found for both slopes k_1, k_2. However, the ratio between the two slopes ($k_2/\ k_1$) becomes more nonlinear due to the increased fracture process zone from the high porosity.

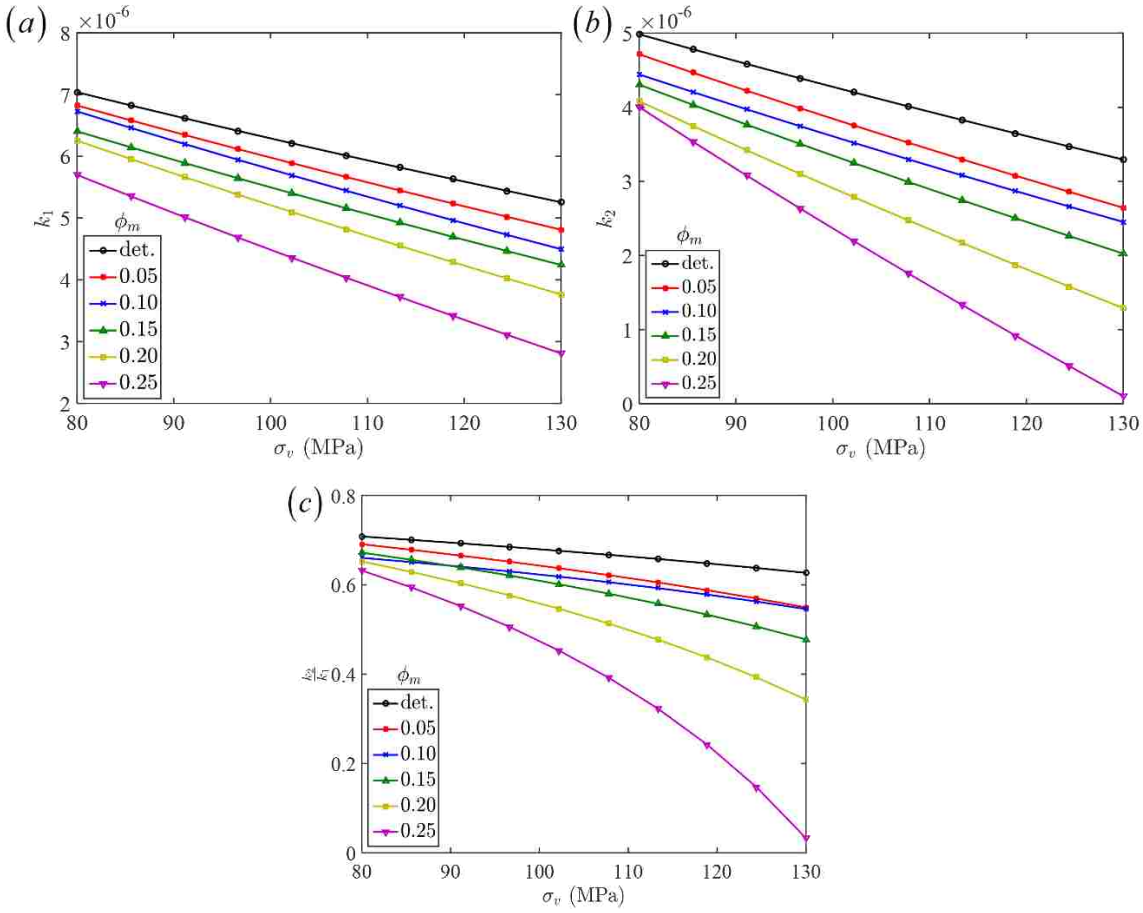

Figure 6.18 Fitting of Slopes Ratio to Overburden Pressure. Fitting of (a) k_1, (b) k_2 and (c) k_2/k_1 with respect to overburden pressure.

6.4.3. Fracture Aperture Closure Prediction. Given the analysis and fitting above, we could generate the critical fracture aperture closure ($\Delta\varepsilon_c$) contour given the

over-burden pressure (σ_v) and average temperature difference (ΔT_c) in Figure 6.19*a*. As shown in the contour plot, $\Delta\varepsilon_c$ increases rapidly as both σ_v and ΔT_c increase. The porosity leads to a significant reduction in $\Delta\varepsilon_c$ as observed from Figure 19*a*. Based on this result, the fracture aperture closures can be predicted by using the actual overburden-pressure and temperatures from the filed data [132]. We found that most of the data fell between these two $\Delta\varepsilon_c$ surfaces (with and without porosity). It is also worth mentioning that the high temperature difference used in the model is taken from the laboratory and field measurements. Laboratory experiments [133] show that the micro-cracks initiation near the injection point is mainly decided by rate of cooling. Considering the rapidly hydraulic diffusivity of water [97], the rapid cooling of hot rock is likely to occur. Secondly, the temperature of some geothermal reservoirs around the world is collected in the review paper [132]. From the data presented, the current highest reservoir temperature is in Northwest Geysers, at 400°C.

To evaluate the porosity effect, we also plotted the percentage difference between $\Delta\varepsilon_c$ with and without a porosity of 0.25 ($\frac{\Delta\varepsilon_d - \Delta\varepsilon_{0.25}}{\Delta\varepsilon_d}$, %) in Figure 6.19*b*. A distinct turning point was found at a critical temperature of 30˚C, below which the fracture aperture remains at a constant position. Above this temperature, we observe the enhanced porosity effect with high overburden pressure ($\sigma_v = 100.3, 130$ MPa). Opposite effect was found when we have low overburden pressure ($\sigma_v = 60$ MPa). The critical overburden pressure with a constant porosity effect of 18.57% is about 79 MPa. We then plotted the critical overburden pressure ($\sigma_{v,cr}$) under which the critical porosity effect remains constant (γ_{cr}) in Figure 6.19*c*. We found that the higher porosity it has, the higher critical overburden

pressures ($\sigma_{v,cr}$) and critical porosity effect (γ_{cr}) on the fracture aperture closures there are. It shows the effect of porosity on the failure of asperity.

The physical interpretations of this finding are threefold: (1) the porosity will reduce the fracture aperture closure; (2) the porosity effect is sensitive to the overburden pressure; (3) when the over-burden pressure exceeds a critical value (e.g., blue dotted horizontal line in Figure 22*b*), more porosity effect is expected with the increased temperature. Less porosity effect can be expected with increased temperature when this overburden pressure is below the critical value. We also plotted all the field data prediction and found that the porosity effect is in a wide range of 18.87%-81.41%.

6.5. SUMMARY

This section presents a comprehensive modeling and analysis of single pair of asperities deformed under the cooling process and overburden pressure. The results demonstrated the failure of deformable asperities under the combined thermal-mechanical loading. Two main failure mechanisms leading to the fracture aperture closures were revealed, which are the contact induced damage and the lateral constraint induced radial cracking. Each of the mechanisms as well as the interactions were quantified using numerical and analytical models.

It was also found that the porosity induces reductions in the overall stiffness and strength of the asperity. However, this does not alter the deformation mechanism. The presence of porosity causes delays in the radial crack growth and reduced fracture aperture closure. This reduction effect from porosity was also found sensitive to the overburden pressure and temperature.

The predication of fracture aperture closures was also obtained using the field data retrieved from the ongoing worldwide geothermal systems. The thermal-mechanical modeling and analysis provide insights into estimating deformations of porous asperities in complex operating conditions.

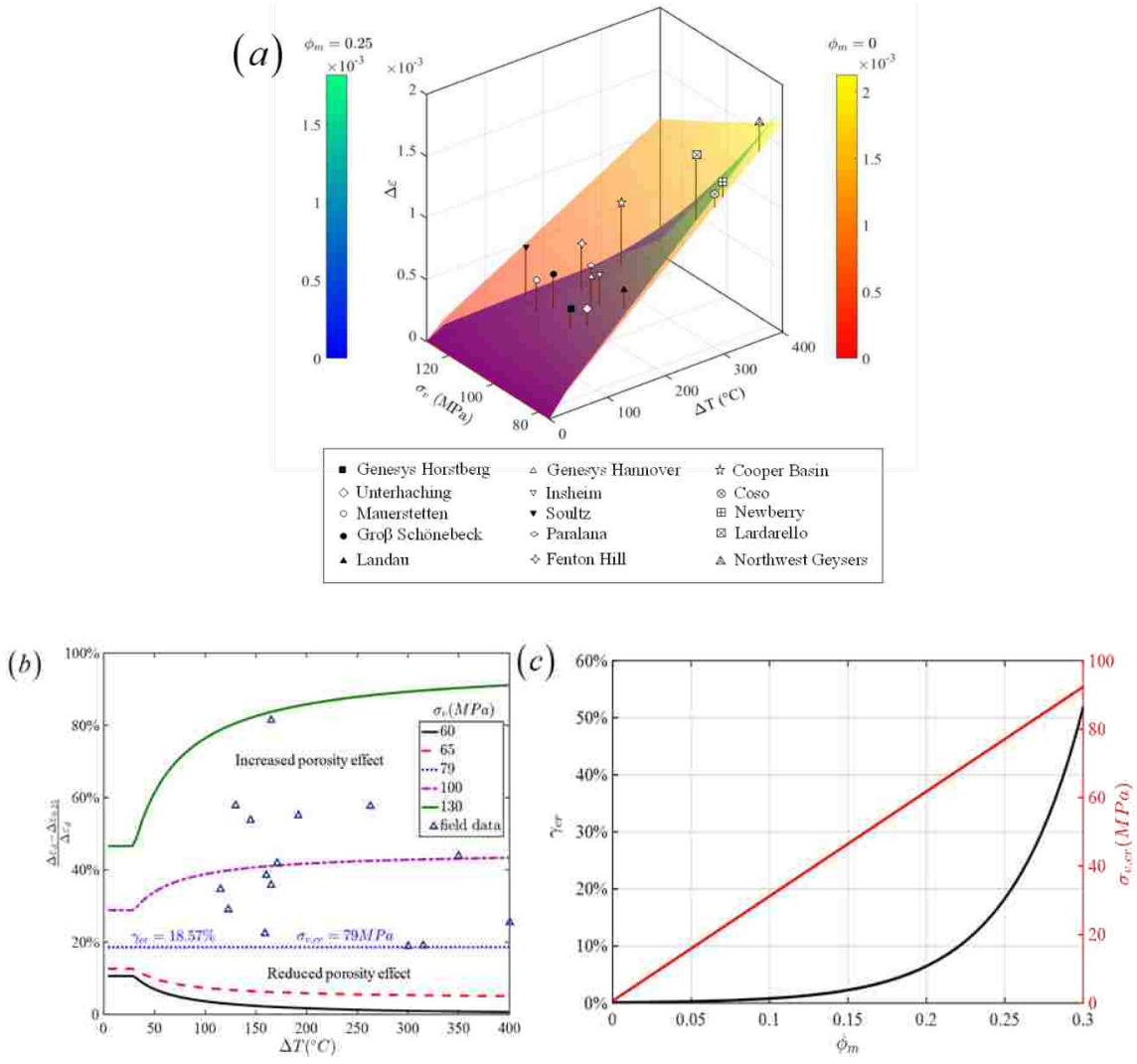

Figure 6.19 The Effect of Porosity on Fracture Parameters. (*a*) Strain change surface with respect to overburden pressure and temperature difference, ratio of strain changes at $\phi_m = 0.25$ to deterministic property with response to (*b*) temperature difference and (*c*) overburden pressure.

7. FAILURE PATTERN OF ASPERITY

7.1. INTRODUCTION TO ASPERITY FAILURE

Fracture as a major factor which greatly affect the fluid flow, heat recovery, colloid transport in environmental remediation, geothermal exploitation, and oil production. These natural and/or man-made fractures are mainly propped by nominal contact of uneven surfaces unless proponents are used. These discrete contacting roughness on fracture surfaces are called asperities. The importance of fractures on hydraulic transmissivity, flow channeling and heat recovery efficiency in fractures has long been acknowledged in areas such as the water flooding for secondary oil recovery [134, 135], the heat extraction in geothermal energy development [136, 137], and the high-level radioactive waste disposal storage [138, 139]. The integrity of asperity is essentially important in controlling fracture apertures in geological formation.

In natural fractures, multiple factors have been investigated for their influence on the deformation of asperity and the evolution of fracture aperture. Intensive work has been made to identify the individual effect of the thermal cooling [140], chemical erosion [141], elastic deformation [142] and pressure solution [143]. Attempts to couple those effects together have been made recently to comprehensively understand the evolution of fracture aperture. However, the inelastic deformation and/or failure of asperity caused by thermo-mechanical effects have been rarely considered in the investigations.

Taron *et al.* [144] conducted thermo-hydro-mechanical-chemical (THMC) coupled analysis of fracture asperity and found an irreversible reduction in aperture after a cycle of thermal loading and unloading. This abnormal change in aperture reduction

cannot be reasonably explained by elastic deformation models in their simulation. Accurate interpretation for this irreversible change of fracture aperture was not given in their paper. Lang *et al*.[145] also did THMC pore scale simulation of fracture sealing. While the initial contact stress between two contacting asperities was as high as 590 MPa, the temperature effects with a maximum 200°C temperature difference of fluid and rock on failure of asperity was ignored, leading to a lack of consideration for asperity failure in their study. Yasuhara *et al*. [143] conducted THMC coupled analysis on the evolution of fracture apertures in high-level radioactive waste storage. A significant temperature difference between water and rock was considered but thermal stress and inelastic behavior of asperity was disregarded. This lack of consideration for significant thermal stress could deviate their simulation results from the real fracture evolution. A more comprehensive study on the evolution of fracture apertures for granite rock at various temperature had been done both experimentally and numerically [146]. Their study inferred that there was a non-negligible effect of thermal effect on the fracture asperity failure when subjected to elevated temperature difference between water and granite. In the process of analyzing field data in Yucca Mountain drift scale test by Rutqvist [100], the irreversible permeability change had been observed in experimental data. This irreversible permeability change significantly deviated from reversible thermo-hydro-elastic solution through numerical analysis, and it was hypothetically attributed to inelastic compaction of fracture asperity.

To sum up, in current fracture studies, the effect of the temperature difference on the asperity integrity has not been extensively explored. We also has done thermo-mechanical coupled analysis on asperity failure and found two failure mechanisms of

asperity: contact failure and radial cracking in Section 6. However, the radial cracking was not theoretically explained in that work. The objective of this work is to investigate the mechanism of the radial cracking within the asperity under the cooling process by the cold fluid injection at various overburden pressure. A fracture mechanics based analytical solution is proposed to reveal radial crack propagation within the asperity. The effects of loading stress and temperature differences on the radial crack propagation are quantified through our analysis.

7.2. PROBLEM DESCRIPTION AND ANALYSIS METHODOLOGY

Natural fractures are usually maintained by the asperity self-propping. The size of asperity varies from tens of nanometers to several millimeters. In some engineering projects, e.g., enhanced geothermal systems, the cold fluid flows through fracture of hot rocks (temperature is even more than 300 °C) and thus, heat transfer occurs at fracture surface, shown in Figure 1. Along flow direction, injected fluid is heated up and rock is cooled down, the temperature difference between fluid and rock is varying. By considering the small size of asperity pairs, the cooling of the asperity is way faster than the cooling of the rock matrix. The considerable temperature difference between the invading fluid and hot asperity induces the asperity stress change and the shrinkage of contacting asperity. At the same time, the overburden pressure loading on asperity remains the same. This stress change and asperity shrinkage due the temperature difference could lead to a potential failure of asperity.

This potential failure of asperity by cooling and pressure loading has been analyzed in Section 6. In that work, asperity was idealized to hemisphere and bonded to

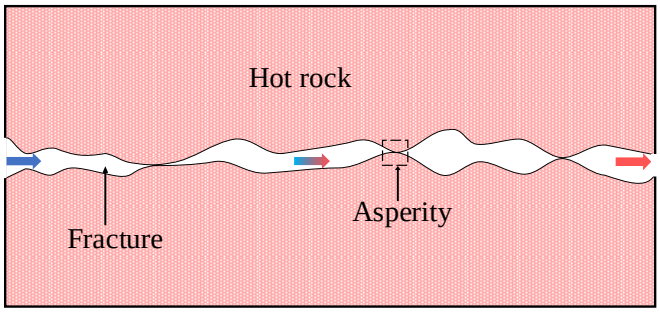

Figure 7.1 Cold Fluid Flows Through Fracture with Hot Matrix Rock.

stiff plate representing matrix rock. For simplicity and computational efficiency, one asperity bonding with overlying stiff plate was contacted with rigid surface to simulate real contacting of asperity pair (Figure 7.2*a*). Damage mechanics based asymmetric constitutive model was employed to simulate the deformation process of the asperity. Three-dimensional thermo-mechanical coupled finite element model was built to analyze the integrity of asperity under cooling and overburden loading. Two mechanisms of asperity failure were identified: the damage at contact zone and the radial cracking at top of asperity. The damage at contact zone was well explained by Hertzian contact model and damage mechanics, but the radial cracking was not fully investigated. Due to practical significance of asperity integrity, the condition to cause the radial cracking of asperities is crucial for the fracture evolution. An analytical model has been developed to understand the mechanism of the radial cracking by considering both thermal-mechanical analysis and linear elastic fracture mechanics.

7.2.1. Temperature Field and Boundary Condition. When asperity is much smaller than the rock matrix, the cold fluid injection could lead to the instant cooling of asperity but no temperature change of the rock matrix. In this study, the temperature of

cold fluid is denoted as T_w, and T_r denotes the initial temperature of hot rock. In consistency with our result in Section 5 and 6, the temperature of curved surface of hemisphere is set to T_w and temperature for top flat surface of hemisphere is constant, which is equal to T_r. Temperature distribution in asperity can be approximated as steady state. The sketch of heat conduction model is in Figure 7.2*b*. Spherical coordinates are used with axial symmetry (dash line). Steady-state heat conduction equation in spherical coordinates [147] can be given as

$$\frac{\partial}{\partial r}\left(r^2\frac{\partial T}{\partial r}\right)+\frac{1}{\sin\varphi}\frac{1}{\partial\varphi}\left(\sin\varphi\cdot\frac{\partial T}{\partial\varphi}\right)=0 \tag{7.1}$$

where φ is the angle rotating from axial symmetry, $\varphi\in\left[-\frac{\pi}{2},\frac{\pi}{2}\right]$, r is the hemispherical radius from center, $r\in[0,R]$.

Boundary conditions,

$$T\left(r,\frac{\pi}{2}\right)=T\left(r,-\frac{\pi}{2}\right)=T_r \tag{7.2}$$

$$T(r,\varphi)\ \textit{finite} \tag{7.3}$$

$$T(R,\varphi)=T_w \tag{7.4}$$

The analytical solution for this hemispherical heat conduction equation is,

$$T(r,q)=T_r+\sum_{m=0}^{\infty}C_m r^{2m+1}P_{2m+1}(q) \tag{7.5}$$

$$C_m=\frac{\int_0^1(T_w-T_r)P_{2m+1}(q)\,dq}{R^{2m+1}\int_0^1 P_{2m+1}^2(q)\,dq} \tag{7.6}$$

where $q=\cos\varphi$, $P_{2m+1}(q)$ is $(2m+1)$ degree Legendre polynomials of q, and R is the radius of hemisphere.

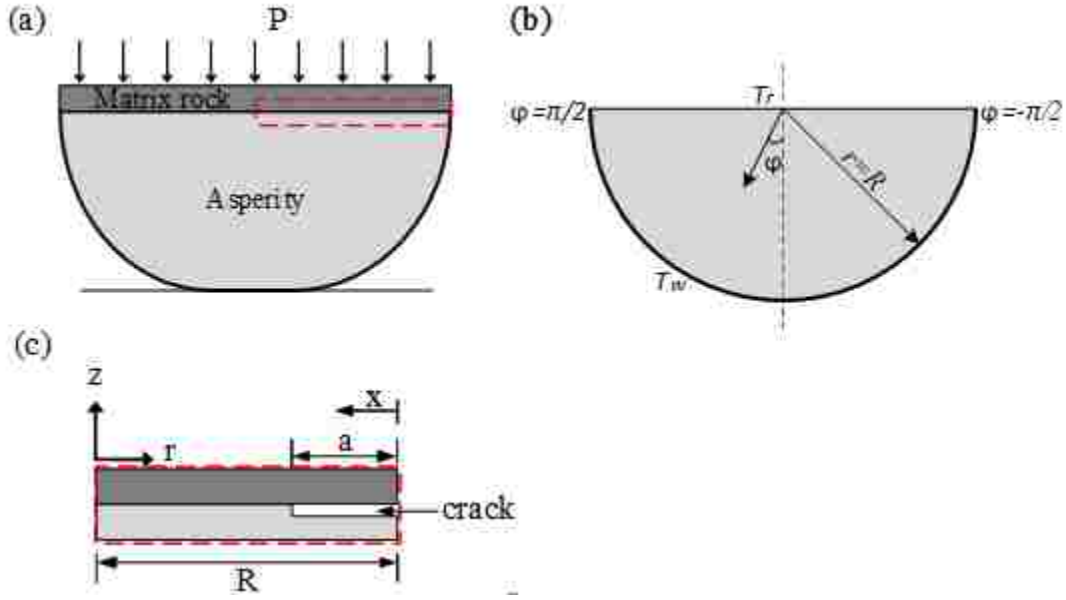

Figure 7.2 Sketch of Asperity Model to Fracture Mechanics Analysis. (*a*) 3D hemispherical contact model used in numerical simulation, (*b*) symmetric hemisphere with spherical coordinates to calculate temperature distribution and (*c*) simplified axisymmetric model.

7.2.2. Stress Distribution with Thermal Effect. The enclosed area by red dash rectangle in Figure 7.2*a* and 7.2*c* is where the radial cracking occurs. The stress distribution in this axisymmetric zone (Figure 7.2*c*) is analyzed in the following sections. Because it's a circular thin disk, cylindrical coordinates are set to the center of disk. The thickness of two layers is negligible compared to circular radius *R*. The stress-strain relation with thermal effect in radial and circumferential direction in lower layer (bright grey zone) are,

$$\varepsilon_r = \frac{1}{E}\left[\sigma_r - \nu\left(\sigma_\theta + \sigma_z\right)\right] + \alpha\Delta T \tag{7.7}$$

$$\varepsilon_\theta = \frac{1}{E}\left[\sigma_\theta - \nu\left(\sigma_r + \sigma_z\right)\right] + \alpha\Delta T \tag{7.8}$$

where E and ν are Young's modulus and Poisson's ratio of asperity, ε_r and ε_θ are radial strain and circumferential strains in lower layer, σ_r, σ_θ and σ_z are radial stress, hoop stress and vertical stress in lower layer respectively. α is the coefficient of thermal efficient, ΔT are temperature difference with reference to initial hot rock temperature, $\Delta T = T(r,q) - T_r$.

For the uniform shrinkage of the circular disk, the radial strain and the circumferential strain are the same, $\varepsilon_r = \varepsilon_\theta$. Regarding the constant temperature of the rock matrix, no lateral deformation is induced in upper layer (dark grey zone). By assuming the upper layer and lower layer bond well, no lateral deformation for the lower layer. It infers both ε_r and ε_θ in lower layer be zero,

$$\varepsilon_r = \varepsilon_\theta = 0 \tag{7.9}$$

In Figure 7.2*c*, the radial cracking length is symbolized by *a*. Pressure *P* from vertical lithostatic pressure loads on the top of the stiff plate. Based on the normal depth of enhanced geothermal formation (3~5 km), the vertical lithostatic pressure has a range of 75 MPa to 135MPa by referencing to the Soultz-sous-Forets geothermal project [74]. The corresponding loading pressure *P* on asperity is in the range of 2.0 ~ 7.5 MPa. The conversion of loading pressure *P* and vertical lithostatic pressure is elaborated in Section 5.2.1.

Thus,

$$\sigma_z = \frac{\pi R^2 P}{\pi (R-a)^2} \tag{7.10}$$

Combining Equations (7.7), (7.8), (7.9) and (7.10) gives hoop stress distribution in lower layer (bright grey zone),

$$\sigma_\theta = -\frac{E\alpha\Delta T}{1-\nu} + \frac{\nu}{1-\nu}\frac{R^2 P}{\left(R-a\right)^2} \tag{7.11}$$

7.2.3. Crack Propagation Analysis. The cracking of the granite (reservoir rock in enhanced geothermal systems) can be analyzed by linear elastic fracture mechanics. The propagation of cracks can be characterized by the relative value of energy release rate G and fracture toughness G_c. G is a measure of the energy available for an increment of crack propagation, and thus it is also called crack driving force. G_c indicates the energy needed for an increment of crack surface, so it's called resistant force. Thus, crack propagation criteria used at here are,

$$G \geq G_c \tag{7.12}$$

where G_c is a property of granite, set to 0.1 kJ/m^2 [148]. Because of the equivalence of energy approach and stress intensity approach, G can be calculated from stress intensity factor. For configuration in Figure 7.2*c*, Mode I fracture is the most likely cracking pattern along radial direction,

$$G = \frac{K_I^2}{E} \tag{7.13}$$

where K_I is Mode I stress intensity factor. Because crack face traction σ_θ is a function of r, weight function method is employed to calculate K_I for circular disk,

$$K_I = \int_0^a \sigma_\theta \sqrt{\frac{2}{\pi a}} \cdot \frac{1}{\sqrt{\left(1-\frac{x}{a}\right)}}\, dx \tag{7.14}$$

Weight function for radial constant displacement in circular disk is given in reference [149], only the first dominant term is used without much loss of accuracy.

Combining Equations (7.11), (7.13) and (7.14), energy release rate G is,

$$G = \frac{8a}{\pi E}\left[-\frac{E\alpha\Delta T}{1-\nu} + \frac{\nu}{1-\nu}\frac{R^2 P}{\left(R-a\right)^2}\right] \tag{7.15}$$

The radial crack propagation can be gauged by Equation (7.11). The material data in Equation (7.15) to calculate G is listed in Table 7.1. They are consistent with those used in the numerical simulation in Table 5.1.

Table 7.1 Material Data Used in Numerical Simulation and Analytical Model

Young's modulus, E	111.36 GPa
Poisson's ratio, ν	0.25
Initial rock temperature, T_r	350 °C
Initial water temperature, T_w	50 °C
Thermal expansion, α	8×10^{-6} 1/°C
Hemisphere radius, R	2.5 mm
Fracture roughness, G_c	0.1 kJ/m^2
Tensile strength, σ_t	6.7 MPa

7.3. RESULTS AND DISCUSSION

In this section, effects of overburden loading and thermal unloading on the radial cracking are investigated using our analytical model. The crack propagation is assessed by the comparison of energy release rates G and G_c. Whereas, the temperature difference facilitates the crack propagation due to the tensile hoop stress, the overburden pressure inhibits the energy release and the crack propagation by means of the compressive hoop

stress. Subsequently, their effects on critical crack propagation length are compared for analytical results and numerical results, and the comparison validates the accuracy of the analytical model. At the end, their comparative impacts on the crack propagation length are examined. It shows a higher impact of the temperature difference on the crack propagation length than the overburden pressure.

7.3.1. Crack Propagation. Crack starts to propagate when energy release rate G larger than fracture toughness G_c. G, as a function of crack length a, is plotted in Figure 7.3. The effect of overburden loading on energy release rate G is analyzed at here. The relation of G and crack length a under different overburden pressures are shown in Figure 7.3a. The temperature difference of water and rock is constant for this condition, $\Delta T_{w-r} = 30°C$. The overall trend of G with respect to a is a parabolic curve in small range of crack length. When G is larger than 0.1 kJ/m^2, crack extends. In the figure, two G – a curves intersect with G_c line (horizontal dash line). As shown in Figure 7.3a, there are two intersection points which have different indication of cracking. First intersection point indicates the length at which crack starts to extend, namely the pre-existing crack length. While the second intersection point means the end of extension, is the variable of interest in this study. Crack length corresponding to second interaction point is denoted as a_c. It will be used extensively in following analysis. At the same time, the effect of overburden pressure on G is clearly displayed. Higher overburden pressure has lower energy release rate which indicates restraint of crack propagation subject to overburden pressure. This can be explained more clearly by the hoop stress in Figure 7.3b. The vertical overburden pressure causes the compressive hoop stress in the asperity to counteract the tensile hoop stress which is the driving force for inducing cracks.

Compared at the disk edge, the overburden pressure has larger impact in the proximity of disk center.

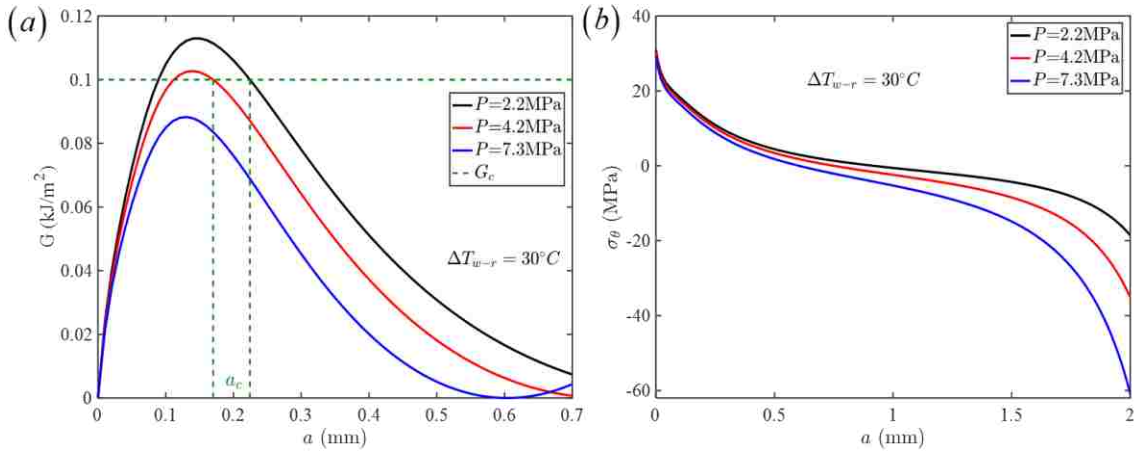

Figure 7.3 Strain Energy Release Rate and Hoop Stress Variation at Different Loading Pressure. (*a*) Strain energy release rate *G* with respect to crack length at three different overburden pressures at $\Delta T_{w-r} = 30°C$. (*b*) Associated hoop stress σ_θ along radial direction from edge.

Thermal effect: The effect of temperature difference on the G is shown in Figure 7.4. The constant overburden pressure for this scenario is P = 4.2 MPa. From Figure 7.4a, energy release rate is sensitive to temperature effect: only 5ºC variation can make a significant difference of the energy release rate. At this overburden pressure, cracking temperature is approximately 30ºC. The thermal effect on the energy release rate is opposite to the overburden loading effect. The higher temperature difference, which cause the larger tensile hoop stress near the disk edge, can cause the larger energy release rate.

7.3.2. Comparison of Numerical Simulation and Analytical Results. A damage mechanics based asymmetric model was developed to simulate the damage of asperity

under the impact of thermal effect and overburden loading. 22,384 elements for finite element simulation were set to model hemisphere.

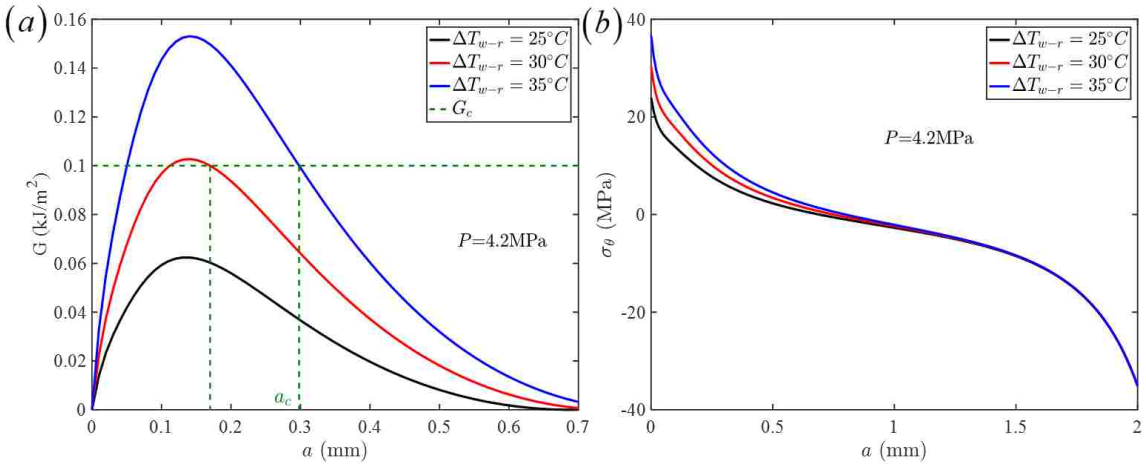

Figure 7.4 Strain Energy Release Rate and Hoop Stress Variation at Different Temperature Difference. (*a*) Strain energy release rate *G* with respect to crack length at three temperature difference at *P* = 4.2 MPa. (*b*) Associated hoop stress σ_θ along radial direction from edge.

The uniform edge length of each element is around 0.1 mm and about 25 elements are distributed along radial direction on the top of hemisphere. More details about numerical simulation can be referenced to Section 6. Some graphical results are presented at here to show the limit length of radial crack propagation. Figure 7.5*a* shows the damage variable *D* contours with increasing temperature difference at *P* = 4.2 MPa.

The Damage variable D is in the range of 0.0 ~ 1.0. 0.0 means the element is uncracked, and 1.0 means the element is fully damaged. Aggregates of damaged elements signify coalescence of micro-cracks and fracture. In Figure 7.5, contact zone and top

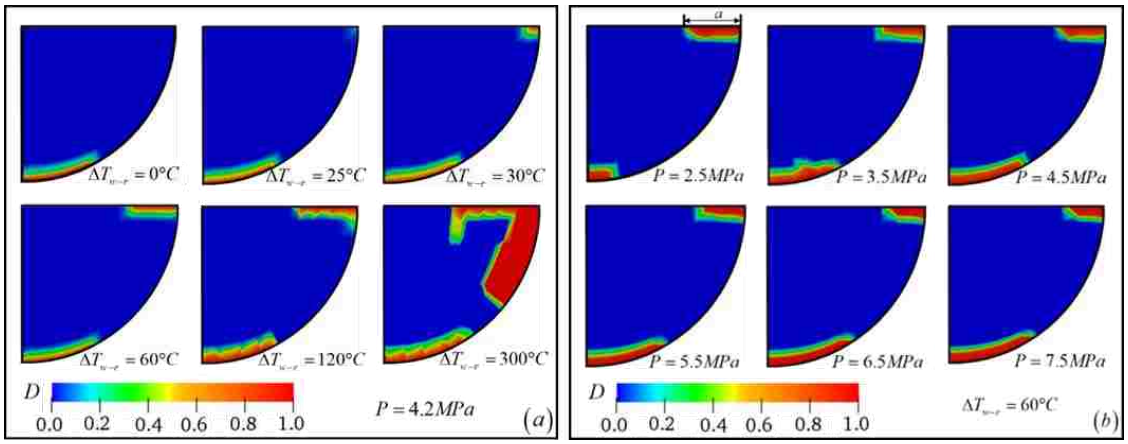

Figure 7.5 Damage Variable Contours with Difference Temperature Difference and Overburden Pressure. (*a*) The damage variable contours with elevated temperature difference of water and rock ΔT_{w-r} at P = 4.2 MPa. (*b*) The damage variable contour with increasing overburden pressure P at $\Delta T_{w-r} = 60°C$.

corner are red, indicating damage of element and cracking. A thin strip of red color on the top corner is the place of interest for the radial cracking. We can observe three stages for the radial cracking from damage variable contours. At ΔT_{w-r} less than 30ºC, no crack initiates at top corner. It starts to initiate and extend at when temperature difference is approximately equal to 30ºC. As ΔT_{w-r} increases, crack extends further towards center of asperity. Close to 300ºC, crack deviates downwards. Figure 7.5b shows the damage variable D contours with increasing overburden pressure at $\Delta T_{w-r} = 60°C$. For the broad range of overburden pressure from 2 MPa to 7.5 MPa (physically meaning of vertical depth of 3 km to 5 km), the radial crack length varies slightly. Specifically, higher overburden pressure causes smaller radial crack length, which demonstrates the restraint effect of the overburden loading to the radial cracking.

Comparison with Analytical Results: The crack length with response to elevated temperature difference at three different overburden pressures from numerical simulation

and analytical model is presented in Figure 7.6. Three stages of crack length variation can be clearly visualized for both numerical results and analytical results. Crack starts to extend at 30°C for both models. The threshold temperature difference can be well captured by both models. When temperature difference of water and rock is in between 30°C and 150°C, both numerical curves and analytical curves have steep slopes with slight difference. The zigzag shape of numerical curves is attributed to relative coarse mesh along radial direction. The edge length of each element in numerical simulation is roughly 0.1 mm along radial direction, damage of elements leading to jump of curves. Numerical curves and analytical curves have overall match in this range.

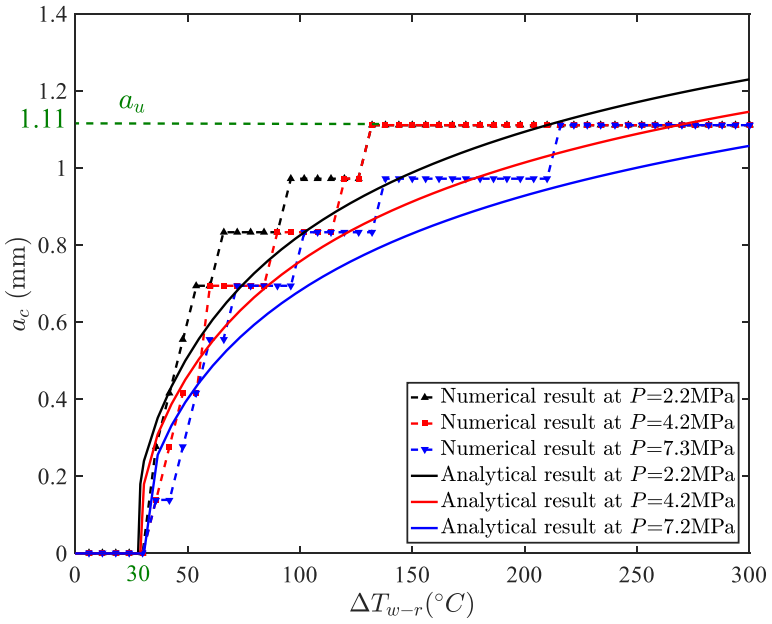

Figure 7.6 Comparison of Numerical Result and Analytical Result for the Effects of Temperature Difference on Critical Crack Propagation.

When temperature difference exceeds 150°C, there's an apparent discrepancy of trend of curves. For numerical results, the curves show the upper limit of crack length at

different overburden pressures, at 1.11 cm. This maximum crack length is denoted as a_u. After arrival of this limit, larger temperature difference has no effect on the radial cracking length. Notice that the red numerical curve at overburden pressure of 4.2 MPa depicts evolution of crack length in Figure 7.5a. The last damage variable contour shows the deviation of cracking downwards close to $\Delta T_{w-r} = 300°C$. It infers the deviation of crack propagation after curves levels out in Figure 7.6b for numerical results. However, analytical curves show an asymptotic increase of crack length a_c with elevated temperature difference. This discrepancy is the limitation of our analytical model to interpret deviation of cracking or kinking. Equation (7.13) is only valid to Mode I crack, not for shearing and tearing. The details analysis of this kinking can refer to Hutchinson and Suo [150], Ševeček et al. [151]. It can still be partially interpreted in ensuing paragraph by stress approach of our analytical model.

Corresponding to finite element condition, the hoops stress underneath maximum crack length a_u is analyzed to explain the kinking effect in numerical simulation. ϕ is defined as the angle rotating from right horizontal plate, shown in inset of Figure 7.7. ϕ = 5.7º corresponds to depth of two elements underneath crack length a_u, similarly, ϕ = 7.2º and ϕ = 8.6º are depths of three and four elements in numerical simulation at crack length a_u. Hoop stress σ_θ at those three vertical depths are plotted from analytical model in Figure 7.7. With depth underneath a_u goes downwards, σ_θ increases. The tensile strength for granite is set to σ_t = 6.7 MPa in simulation. It infers more likelihood for crack to deviate downwards than straightly radial extension.

Regarding Figure 7.6, the temperature differences required to reach maximum crack length a_u for different overburden pressure P is varied. Larger overburden pressure

instead retards this approaching. This opposition to crack from overburden pressure is explained by analytical model. This can be explained from Equation (7.11). Larger overburden pressure brings larger compressive stress to negate extensive driving force for Mode I crack, which slows down the arrival of maximum crack length. Hence, the numerical curves and analytical curves show similar pattern for effect of overburden pressure in Figure 7.6.

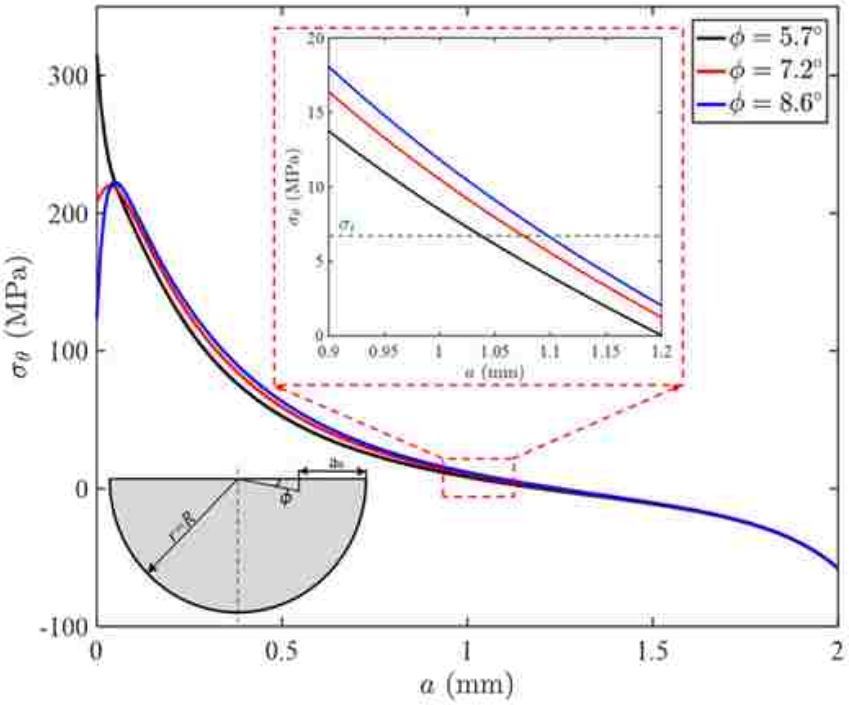

Figure 7.7 The Hoop Stress Distribution along Radial Direction toward Disc Center Calculated from Analytical Model. Inset indicates σ_θ distribution underneath maximum crack length a_u.

More elaborated analysis of overburden pressure effect on critical crack length is shown in Figure 7.8. The variation of critical crack length with response to increasing overburden pressure at three distinctive temperature difference scenarios is displayed.

The overall trend for critical crack length is inversely proportional to overburden pressure for both numerical and analytical results. As the same reason as before, the zigzag is due to coarse mesh of finite element simulation. The drop of one indent is around one edge length of element. Without this difference, the analytical results show good agreement with numerical results. Notice that the curve with ΔT_{w-r} equal to 60°C corresponds to scenario in Figure 7.5b. For three temperature difference scenarios, the reduction of critical crack length in the broad range of overburden pressure is only about 2 mm. As comparison, increase of critical crack length by temperature difference is about 1.11 cm from Figure 7.6. It indicates the greater impact of temperature difference on the radial cracking.

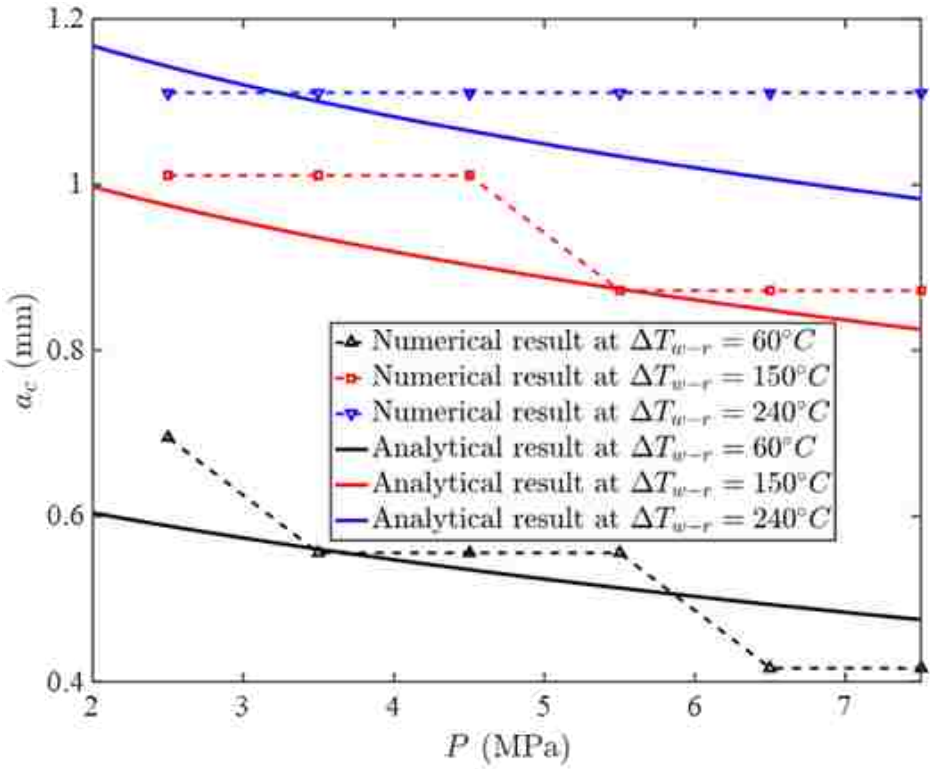

Figure 7.8 Comparison of Numerical Result and Analytical Result for the Effect of Overburden Pressure on Critical Crack Length.

7.3.3. Combined Effects of thermal Cooling and Overburden Pressure. After calibration of analytical model with numerical simulation, the quantified significance of temperature difference and overburden loading to radial cracking and the condition to induce radial cracking will be analyzed respectively in what follows.

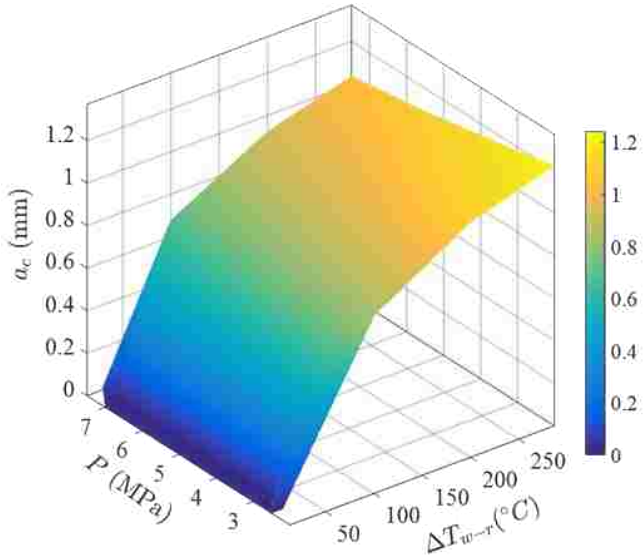

Figure 7.9 The Combined Effect of Overburden Pressure and Temperature Difference on Critical Crack Propagation Length from Analytical Model.

Comparative Significance: The critical crack length is important to the indication of the asperity failure. It's the combined outcome of overburden loading and thermal unloading. The variation surface of critical crack length a_c with response to the temperature difference ΔT_{w-r} and overburden pressure P is displayed in Figure 7.9. Slight decrease of critical crack length a_c shows with increasing overburden pressure and arbitrary fixed temperature difference. Whereas appreciable increase of critical crack length presents with elevated temperature difference and arbitrary fixed overburden pressure. Notices that analytical curves from Figure 7.6 and Figure 7.8 is the cutting

curve at prescribed overburden pressure and temperature difference respectively. The temperature difference shows greater impact on the cracking of asperity.

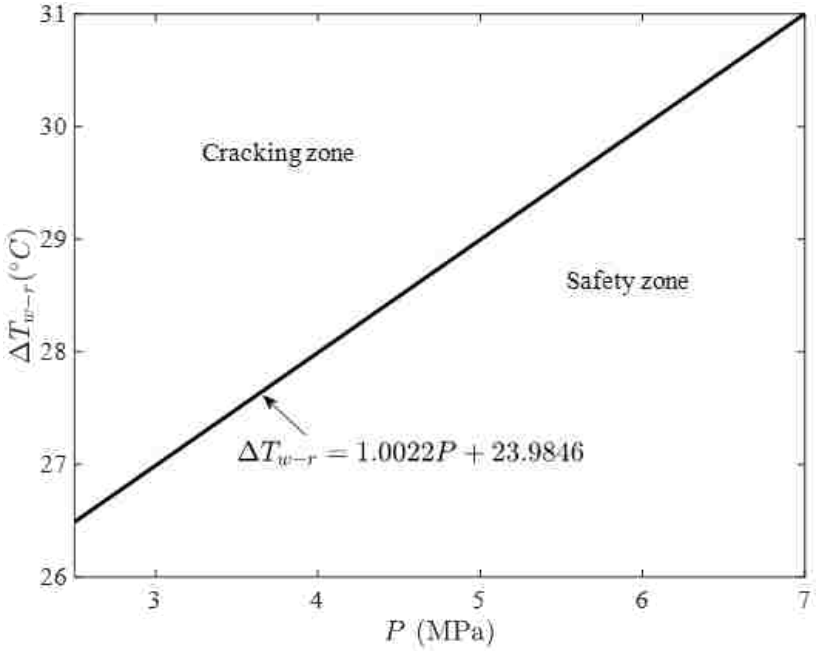

Figure 7.10 The Cracking Condition Defined by Combination of Temperature Difference and Overburden Pressure: Cracking Zone and Safety Zone.

Cracking Condition: When critical crack length a_c is zeros, it means safety of asperity on the top of asperity based on our analytical model. Therefore, extract the front intersection curve of crack length curve with $a_c = 0$ plane. That intersection curve is shown in Figure 7.10. It indicates the cracking zone ($a_c > 0$) and safety zone ($a_c = 0$). The critical boundary curve between two zones are fitted to be: $\Delta T_{w\text{-}r} = 1.022P + 23.9846$. It can apply to different scenarios with broader range of temperature difference and loading pressure. Specially, for the thermal-hydraulic-chemical-mechanical coupled analysis of asperity, it can be used with great convenience to assess the cracking issue of asperity.

When the data points fall into safety zone, cracking is not an issue, otherwise the failure of asperity on top of asperity should be considered in the coupled model.

7.4. SUMMARY

The integrity of asperities has significant effect on the aperture of natural fractures. Potential failure patterns of asperity under thermos-mechanical effects are identified in our previous numerical simulation: the damage at contact zone and the radial cracking on the top of asperity. The mechanism of the radial cracking is theoretically analyzed in this study. A linear fracture mechanics model is developed to investigate two main factors to radial cracking: the cooling process and the overburden loading. Firstly, analytical results is compared with previous numerical results with good agreement which validates the analytical model. Then, competing impacts of overburden pressure and thermal cooling are obtained. It shows that thermal cooling dominantly drives radial cracking, whereas overburden loading slightly counteracts this cracking failure of asperity. Combined effects on critical crack propagation length is presented. At the end, the cracking condition under such combined effects are quantitatively described. This can assist current multi-physics coupled analysis of asperities by introducing the thermal effect on the asperity radial cracking.

8. MECHANICAL ANALYSIS OF FRACTURE DEFORMATION

8.1. FRACTURE DEFORMATION

Before going to the thermomechanical analysis of fracture deformation in the circumstance of enhanced geothermal systems, the mechanical deformation of fracture should firstly be elaborated, that is, be verified by existing data. The fracture surface is complicated to characterize as shown in Section 2. It is due to three reasons. Firstly, it is time-consuming and resorts to high-tech device to measure the roughness of fracture, secondly, the measured data is not easy to analyze. For example, fractal analysis and multifractal analysis involve numerous parameters to be determined. Their determination is very sensitive to experimental operation. Thirdly, the fracture surface doesn't represent real condition. Because when rock sample with fracture is cored from subsurface or cut from core cube, the surface profile has changed due to stress relief or erroneous operation. Therefore, a quantity is required to directly or indirectly characterize fracture surface. Normal fracture stiffness was introduction by Goodman et al. [152] to describe the deformation of fracture. This parameter has been widely used in fracture deformation. Thus, its definition will be introduced in this section and it will be used as a parameter to validate our fracture deformation model.

This section will present as the following procedure. Firstly, the normal fracture stiffness is defined and the effect of asperity distribution on its variation will be analyzed. Two asperity geometry, hemisphere and cylinder, will be used as a comparison. Secondly, the fracture deformation with two asperity geometry will be compared with existing experimental data. The significance of each component will be highlighted.

Thirdly, the stratified continuum percolation model introduced in Section 3 will be used to specify asperity height. The resulting fracture deformation will be compared with experimental data as well.

8.2. NORMAL FRACTURE STIFFNESS

Fracture is exchangeable with the term joint in geoscience. The term “unit joint stiffness” is defined by Goodman et al. for a specimen containing a joint of length L and unit width. When subjected to a force normal to the joint, the specimen shorten by an amount that depends on the deformation of the fracture (confined to the roughness thin region) and the elastic compression of the solid material on eight side of the fracture. If the elastic deformation of the solid rock is subtracted from the total deformation, the resulting is the normal deformation of the fracture. If the fracture deformation is plotted as a function of force per unit length, then the slope of the resulting curve is to be the unit normal stiffness of the joint. The sketch of deformation and the deformation curve are shown in Figure 8.1 and Figure 8.2.

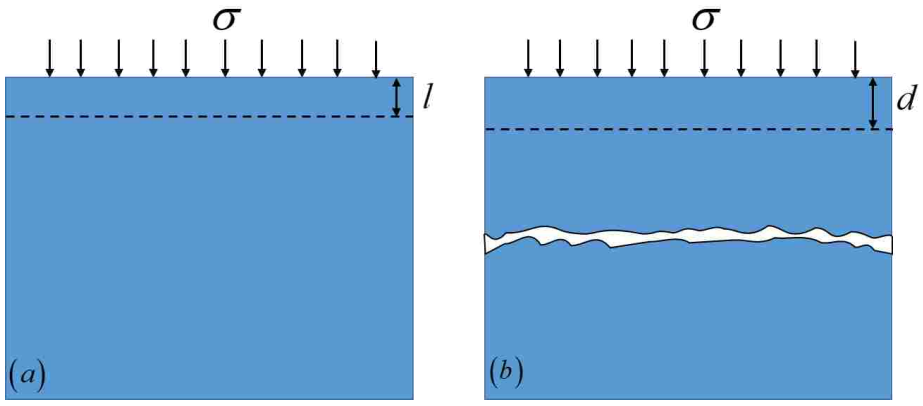

Figure 8.1 Fracture Deformation to Define Fracture Stiffness: (*a*) Elastic deformation of solid material and (*b*) deformation of fractured material.

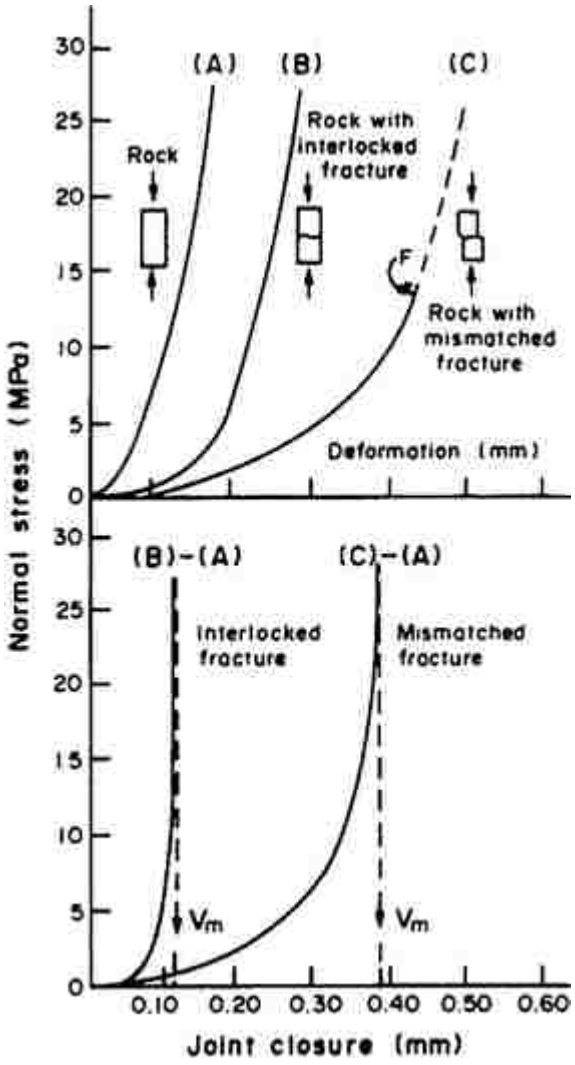

Figure 8.2 Normal Stress versus Rock and Joint Deformation for Intact Rock Specimen and Specimen with Single Fracture for Granodiorite [153].

The limiting cases of the definition is discussed. If the fracture is absent in the rock, the deformation caused by fracture is zero, leading to infinite normal stiffness. That is, the curve in Figure 8.2 is directly vertical. The physical interpretation is that the fracture is perfectly mated so that all deformation is due to that of the intact rock. If the fracture is wide enough, there is no contact between two opposite fracture surface, the

normal stiffness is zero. This corresponds to horizontal trend of curve in Figure 8.2. The physical interpretation is no contact between surfaces at zero stiffness.

In Section 4, fracture deformation is composed of three components: compression of asperity, deformation of two half-space by self-indentation and mechanical interaction. Recall that stiffness is defined in terms of the additional normal displacement due to the fracture. The additional displacement due to the fracture is the difference between fracture deformation and elastic deformation of solid materials (shown in Figure 8.1). In order to be consistent with the symbols in Section 4, the normal stiffness K can be calculated from:

$$K = \frac{\sigma}{2\bar{u} + \Delta L - 2l} \tag{8.1}$$

where σ is the applied stress in fractured rock specimen; $\bar{u}$ is the average normal displacement of half-space, defined in Equation (4.9); ΔL is compression of asperity, which will be either hemispherical asperity or cylindrical asperity, l is the displacement of the half-space that would occur if the fracture were perfectly mated (shown in Figure 8.1*a*).

The calculation of four variables in Equation (8.1) is discussed at here. The $\bar{u}$ can be readily calculated from Equations (4.9). The ΔL has two possible variables depending on hemispherical asperity or cylindrical asperity.

For cylindrical asperity, ΔL can be calculated from Equation (4.1),

$$\Delta L = \frac{FL_0}{\pi E a^2} \tag{8.2}$$

where F is the force acting on individual cylindrical asperity; L_0 is the initial length of asperity, E is the Young's modulus of asperity, a is the cross-sectional radius of cylindrical asperity.

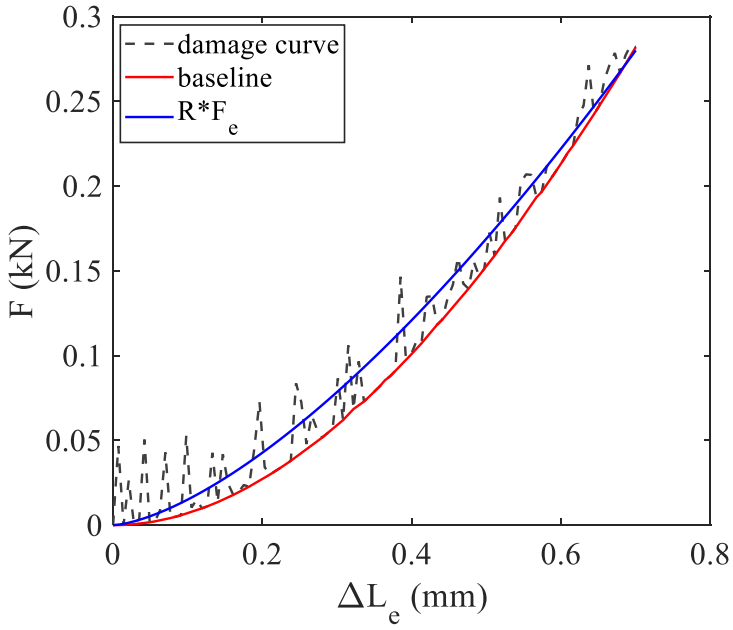

Figure 8.3 The Approximation of Damage Contact Model with Production of Elastic Contact Model with a Reduction Factor R.

For a hemispherical asperity, ΔL can be calculated from Section 5. The procedure to obtain the deformation curve is explained below.

For elastic standard Hertzian contact model, the displacement and force relation is:

$$\Delta L_e = \left[\frac{9\left(1-\nu^2\right)^2 F_e^2}{2aE^2} \right]^{1/3} \tag{8.3}$$

where ν is the Poisson's ratio. This equation is for elastic deformation of a hemisphere. However, when stress loading on asperity exceeds tensile strength, damage occurs as

analyzed in Section 5. The damage effect can be represented by a reduction factor, *R*. Therefore, the force of hemispherical asperities considering damage is:

$$F = RF_e \tag{8.4}$$

This reduction factor *R* can be determined by comparison of stress-strain curves for damage model in Figure 5.6*b* versus the elastic Hertzian contact model. Because the stress-strain curve is size independent, this factor multiplier is valid.

With the parameters in Table 5.1, the R is found to be 0.0054. After this reduction is multiplied, the approximation of new model to damage contact model is shown in Figure 8.3. There is still slight difference due to different power in the equation. The power for hertzian contact model is 1.5 for blue curve, but it is 1.845 for red curve. This small difference can be neglected due to constraint of allowable displacement in the real situation. For hemispherical contact, the displacement cannot be too large to in order to meet hertzian contact assumption. It is worth mentioning that this reduction factor R is much less than 1, meaning the less stress can be sustained by damage contact model. Conversely, under the same loading, the displacement of hemispherical asperity is much larger than that in elastic standard hertzian contact model. Combining Equations (8.3) and (8.4), the displacement equation for hemispherical asperity with damage feature is:

$$\Delta L = \frac{1}{R^{2/3}}\left[\frac{9\left(1-\nu^2\right)^2 F^2}{2aE^2}\right]^{1/3} \tag{8.5}$$

This equation establishes the relation of displacement and force on hemispherical asperity considering damage. This compression formula can be compared with cylindrical asperity in Equation (8.2). The underlying assumption of Equation (8.5) is that length of asperity is twice of radius of asperity cross section. This assumption is imposed

on Equation (8.2) to be L0 = 2a. The Hertzian Equation (8.3) is also compared. The comparison curve is shown in Figure 8.4. The parameters used refer to Table 5.1. The black curve is very close to the y axis. It shows that cylindrical asperity has smallest deformation and hemispherical asperity has largest deformation at the constant force loading on asperity. This result is very interesting because cylindrical asperity is widely used in the fracture deformation analysis for its simplification. However, this usage underestimates the deformation effects of asperity and would be likely to neglect their significance on fracture deformation. Hopkins [13] made the statement that asperity deformation only account for five percent of total fracture deformation based on his cylindrical asperity model. Obviously, this statement mislead the truth.

The variable *l* in Equation (8.1) is the displacement of half-space in response to uniformly distributed load. It can be calculated from the Boussinesq solution for displacement of an elastic half-space under a uniformly distributed load. The variable σ can be calculated from the total force divided by region area of interest.

To compare the difference of these two stress-displacement models, a simple model is constructed to analyze its force distribution under specified displacement boundary condition. Five asperities with equal height are located between two half-pace. Hemispherical and cylindrical asperities are differently analyzed. The sketch is illustrated in Figure 8.5. The Young's modulus and Poisson's ratio for both asperities and half-space are the same, 50 GPa and 0.25. The radius of asperity is 0.5 mm and the height of cylinder is 1 mm. The specified displacement is 0.1 mm.

The force distribution in both cases are shown in Figure 8.6. It presents the same profile as Figure 4.6. The asperity at the edge sustains most loading and the asperity in

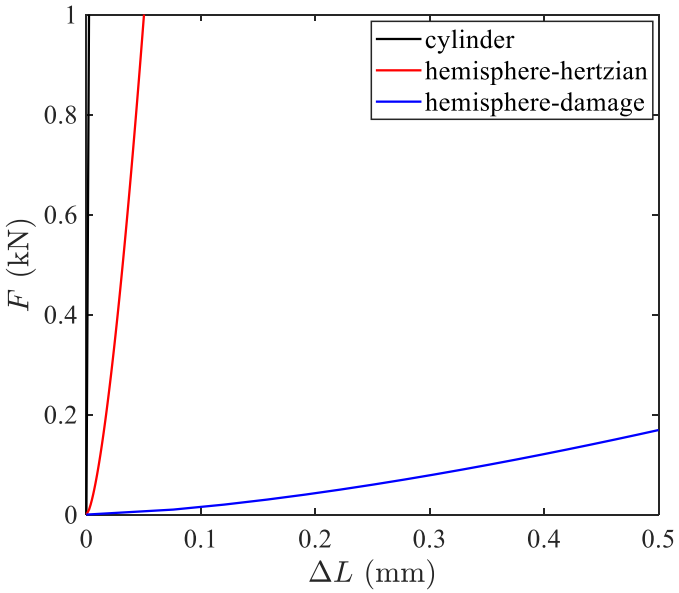

Figure 8.4 Force versus Displacement Curve for Three Models.

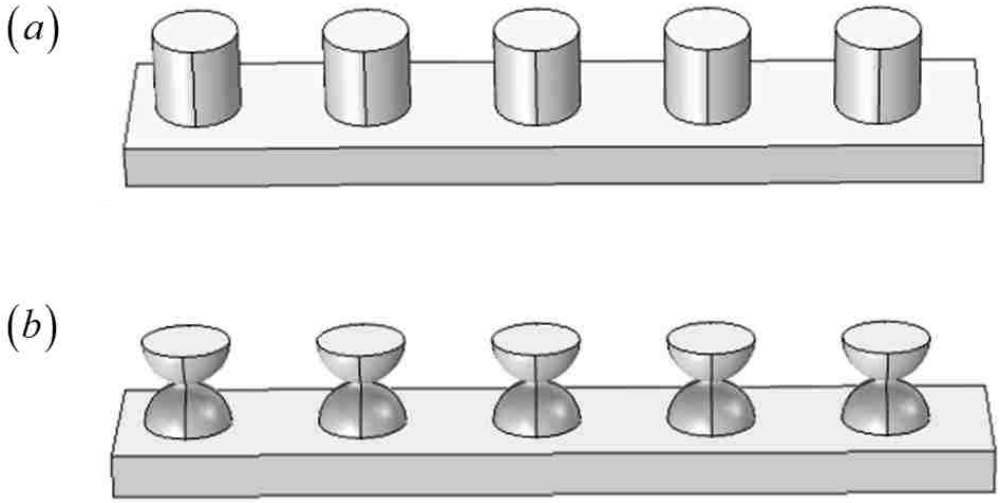

Figure 8.5 Five Asperities with Equal Height between Two Half-Space.

the center has least loading. This trend holds for both asperity geometries. However, the value of force has large difference. It shows that hemispherical asperity sustains much less force than cylindrical asperity which is confirmed in Figure 8.4. For the enhanced geothermal system, the fracture is subjected to in situ stress condition, fracture

deformation is critical to fluid flow and heat conduction. For specified force boundary condition of F = 1 kN, the deformation of half-space and asperity at the edge are 0.0203 mm and 0.0255 mm for cylindrical asperity; the deformation of half-space and asperity at the edge are 0.0203 mm and 0.477 mm cylindrical asperity. It says that asperity compression takes most portion of displacement than half-space displacement, which is different from Hopkins statement[13]. That means, asperity geometry shows importance on the fracture deformation. If the asperity is hemisphere, the mechanical interaction and half-space is negligible. However, if the asperity is cylinder, the mechanical interaction and half-space in significant. In this section and next section, all compression components are included for better accuracy.

Summing up the total force acting on all asperities, the normal stiffness can be calculated by Equation (8.1). The area used is the occupied region by largest distance, A = 1 mm × 37 mm. The stiffness is calculated assuming that the total area is the same for all cases. It shows that normal fracture stiffness is about six times difference for two asperity model. The x axis dist is the distance between two neighboring asperities. It intends to illustrate the effect of distance between asperities on normal fracture stiffness. This information is also presented for cylindrical asperities in Section 5. The result is re-confirmed in this graph. For a constant total area, dispersed contact points form a stiffer interface than clustered contacts. The other aspect is that height, spatial distribution and geometry of asperity have importance on normal stiffness. With increasing displacement, the normal stiffness is constant for equal 8.7. However, if the asperities have varying heights, the normal stiffness would change. This is the nonlinear feature in fracture closure in Figure 8.2. The nonlinearity in the stress-strain curve for fracture in Figure 8.2

is due to increasing numbers of asperities coming into contact with increasing load. In numerical simulation of fracture deformation, all of them require careful characterization before simulation.

Based on characterization in Section 2, fracture aperture and asperity height follows lognormal distribution. That is, low asperities take most portion and tall asperities are a small portion. Therefore, random number generator is used in MATLAB to set the

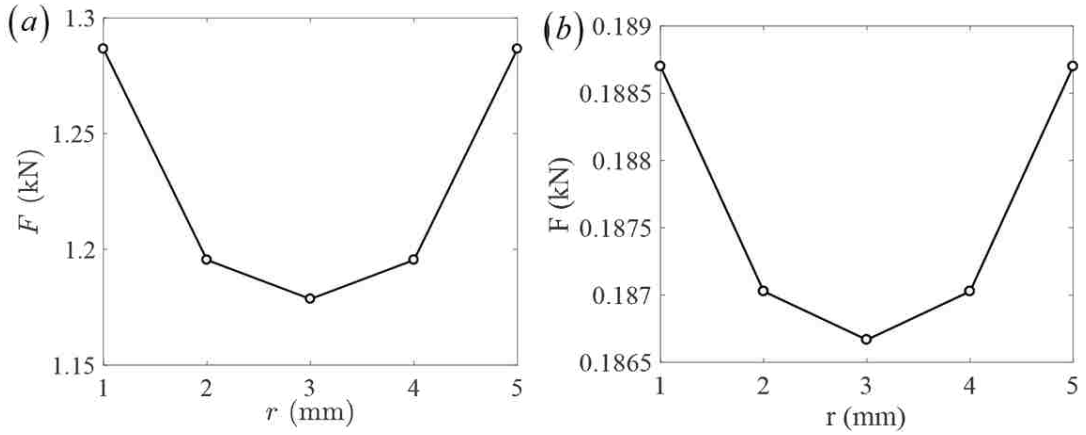

Figure 8.6 The Force Distribution along the Row on Asperities: (a) For cylindrical asperity and (b) for hemispherical asperity.

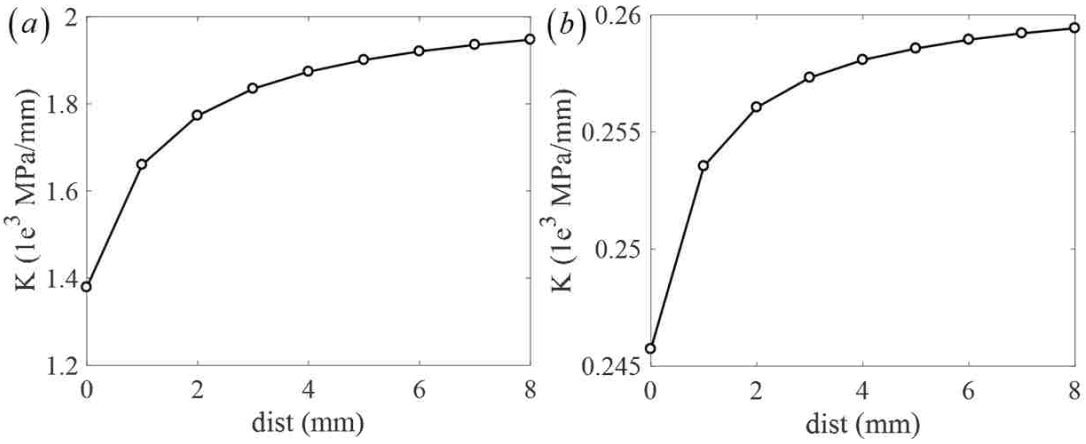

Figure 8.7 The Normal Fracture Stiffness versus Distance between Two Neighboring Asperities for Two Models: (*a*) Cylindrical asperity and (*b*) hemispherical asperity.

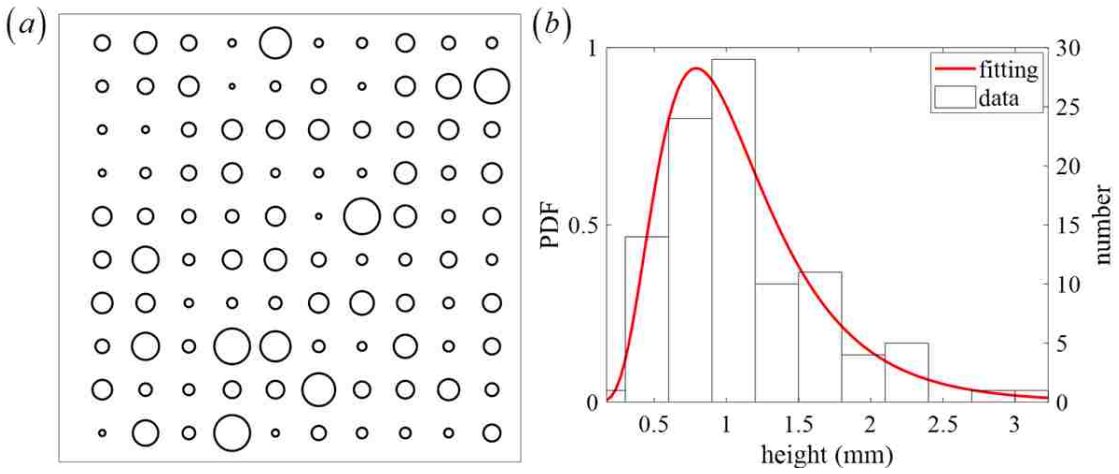

Figure 8.8 The Setting of Asperity with Lognormal Distribution of Height. (a) The positions of asperity and (b) the height distribution.

set asperity height for 100 asperities as shown in Figure 8.8. The random number follows lognormal distribution. The used height distribution and number are plotted in Figure 8.8b. The fitting is used to reassure the distribution of height. The arithmetic mean of height is 1.0618 mm and the maximum height is 3.361 mm. The different radii of circle in Figure 8.8a is due to relation of height and radius. This is the constraint from hemispherical asperity and applies to both cases.

The stress displacement curve for two asperity models are shown in Figure 8.9. The area used to calculate stress is 169 mm^2. The stress for cylindrical model is about five times that for hemispherical model, consistent with the result in Figure 8.7. The curves shape have similar trend as Figure 8.2 from experimental data. Normal stiffness, the slope of curve, increases gradually with more closure of fracture.

It is worth mentioning the relation of preceding result to fracture information. As analyzed in Section 2, two fracture surface and fracture aperture follows lognormal distribution. Composite topography is the sum of surface height from two reference

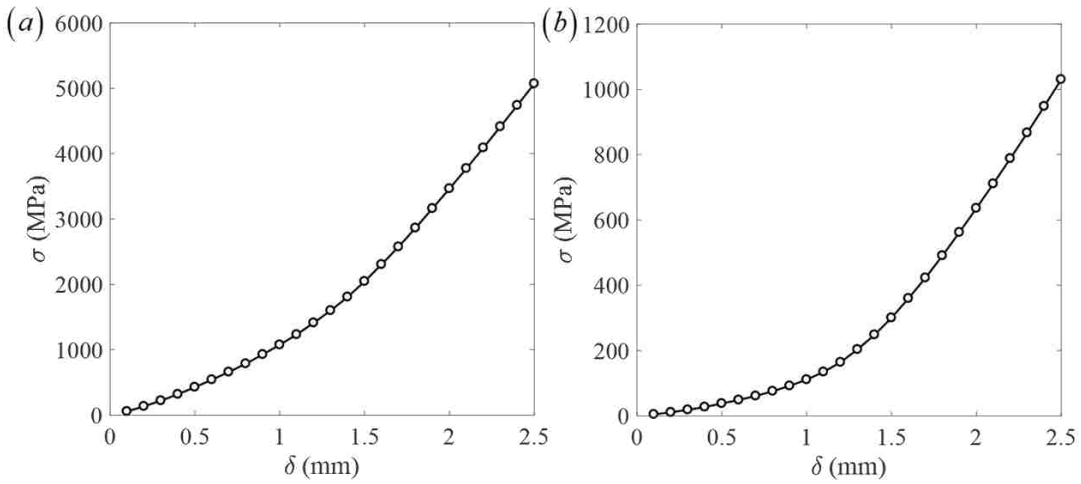

Figure 8.9 Stress versus Displacement Curve for Two Asperity Models: (a) Cylindrical asperity and (b) hemispherical asperity.

planes. It is the negative of fracture aperture. That means, composite topography is complementary to fracture aperture. The lognormal distribution of asperity height used is similar to simulate composite topography. The information about individual fracture surface is embedded together. In other words, the correlation length, scaling feature and other properties on composite topography or fracture aperture can apply to asperity height in this model. The preceding example only represents the distribution property. More comprehensive illustration is based on characterization of fracture aperture.

The stratified continuum percolation model established in Section 3 meets this need. Because the scaling feature, correlation length and other properties have been presented in stratified continuum percolation model. The site density in each pixel follows lognormal distribution. The site density can be used to represent asperity height. Using this approach, the fracture is modeled by two half-spaces separated by an arrangement of hemispherical asperities. The asperities are arranged on a regular lattice

with heights determined by the aperture distribution generated by the stratified continuum percolation algorithm. The radii of the asperities are set such that they are half of their height. The same size of area as Pyrak-Nolte and Morris [22] is used: 300 by 300 pixel. It represents 0.1 m area, giving an asperity radius of 0.1667 mm. for this analysis, the physical properties of both asperity and half-spaces refer to Table 5.1. The geometric constraint in Section 4 is used to update the height of asperity when in contact.

8.3. POROSITY EFFECT

The porosity effect is analyzed on the deformation of asperity in both mechanical loading and thermomechanical loading process in Section 4. The equivalent reduction of stiffness by the porosity is considered in the constitutive curve in Figure 6.1c. From the damage contour display, the porosity has more significant effect on the potential failure of asperity not partial damage on the contact region. This can also be represented in the normal fracture stiffness curve. The deformation curve for single asperity with porosity and without porosity is shown in Figure 8.10.

It shows that porosity has negligible effect on the normal stiffness of asperity deformation. Therefore, without consideration of abrupt failure or crush, the porosity can be ignored in the fracture deformation model. For simplicity, the porosity is not considered in the following analysis.

8.4. FRACTURE DEFORMATION

Based on the stratified continuum percolation model, the fracture geometry can be generated. However, due to constraint of computational resource, the geometry size

cannot set too large. The calculation of individual force on asperity is based on global calculation is very computational intensive. To reduce the computational time, a small model is generated. The size is 50 × 50 pixels to mimic the real fracture region of 100 mm × 100 mm. 4 stratified layers are used in the calculation. The scaling factor is 2.37. The number of squares in each layer is 6. Therefore, the total asperity is 2500. The model geometry is shown in Figure 8.11.

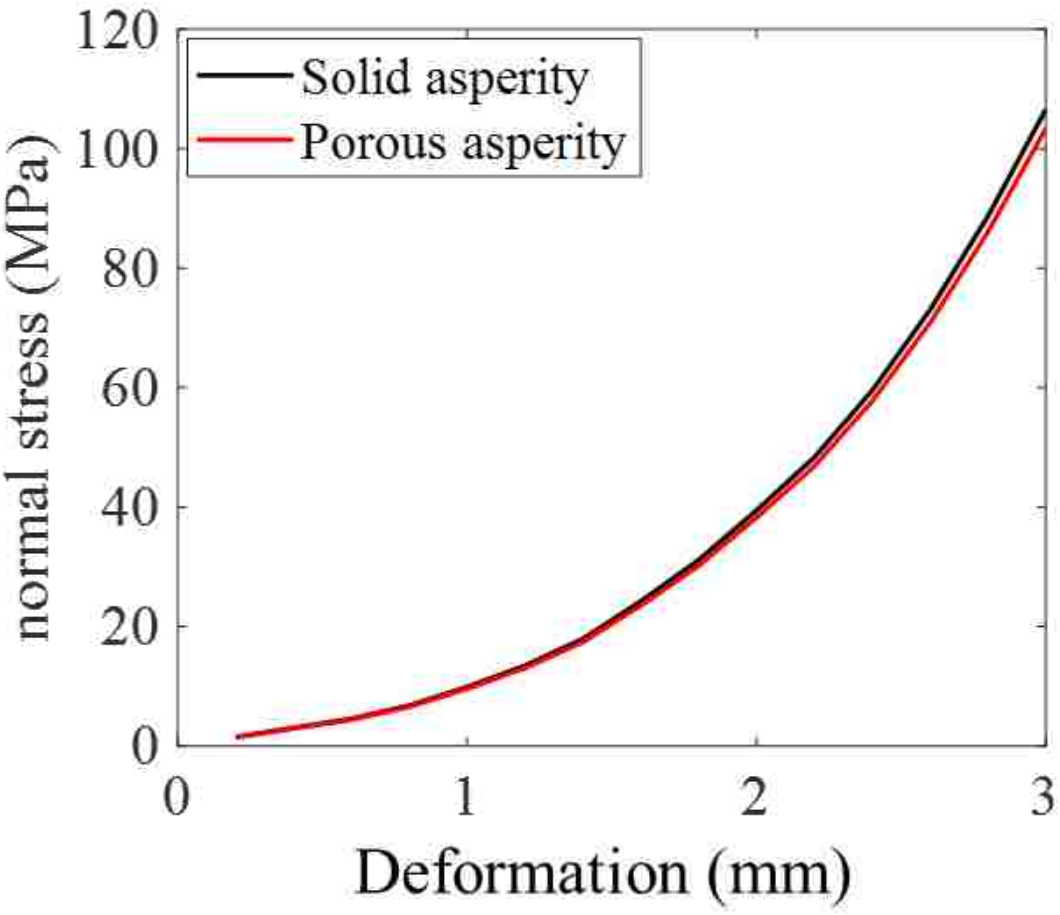

Figure 8.10 The Normal Stiffness Curve for Asperity Deformation.

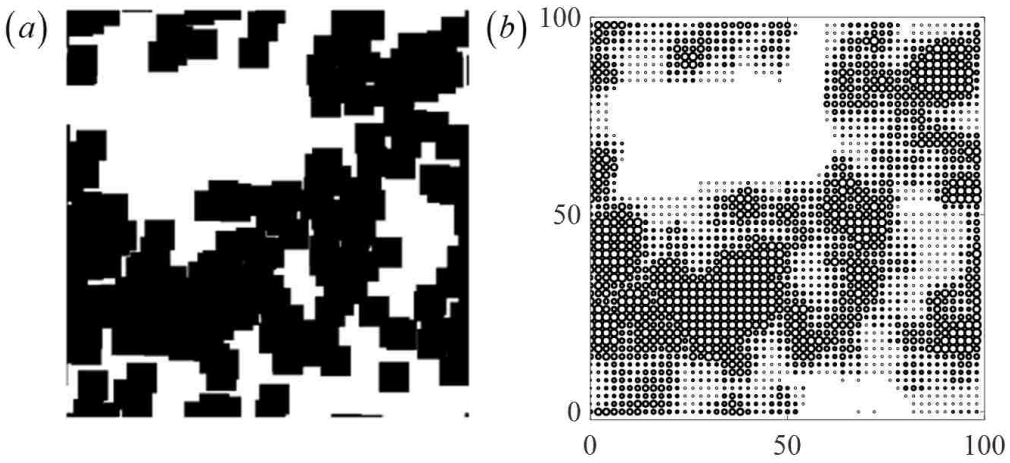

Figure 8.11 The Model Geometry of Fracture: (a) The stratified percolation model by squares and (b) the stratified percolation model by hemispherical asperities.

8.4.1. Mechanical Loading. For the geometry in Figure 8.10*b*, the far field displacement is applied and the force is calculated and then summed to obtain the total force. The total force can be used to obtain the loading, because the fracture area is 0.01 m^2. With different loadings, the asperity displacement are displayed in Figure 8.12.

It shows that with higher stress loading, the fracture aperture reduces significantly. The yellow region in initial state becomes cold color at σ = 100 MPa. The height information of asperity can be extracted and presented in Figure 8.13.

The height changes is more pronounced in Figure 8.13. The number of asperity height of 0 mm increases substantially. It means that more parts of model is closed by stress loading. It is interesting to notice that there is still some small asperity heights even at σ = 100 MPa. If they are connected, they are able to provide flow path for percolation. Therefore, the flow transmissivity highly depends on the initial geometry of asperity positions.

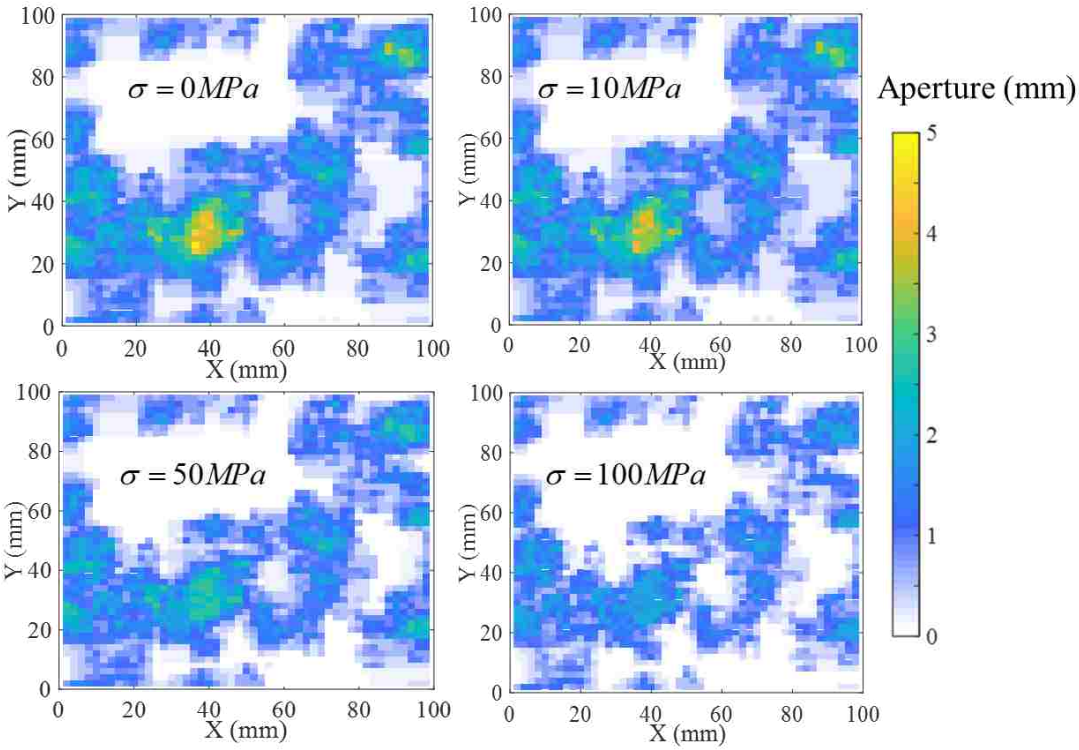

Figure 8.12 The Fracture Aperture at Different Loading Stresses.

8.4.2. Thermomechanical Loading. To account for the potential failure of asperity, the artificial damage is forced randomly on the asperity. Ten percent of contacting asperity is forced to be damaged totally. This is artificial setting of damage, more accurate setting of potential damage can come from the hydrothermal simulation of fracture and analyze the temperature distribution in the fracture. When the temperature is higher than the critical damage temperature, the fracture can be set to be damaged. In this circumstance, the upstream in the fracture has more damage than the downstream. In present study, random selection of certain percentage of damage oversimplify this complicated process. More accurate analysis will be conducted in the future. The geometry and corresponding numerical scheme are shown in Figure 8.14.

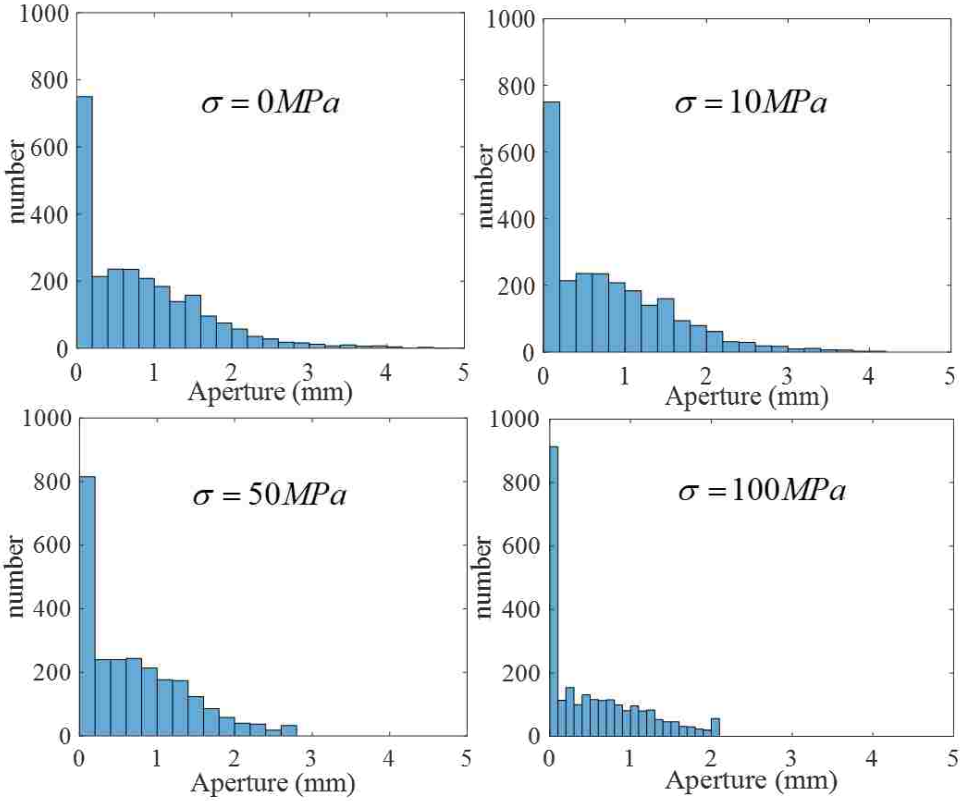

Figure 8.13 Asperity Height Histogram at Different Loading Stresses.

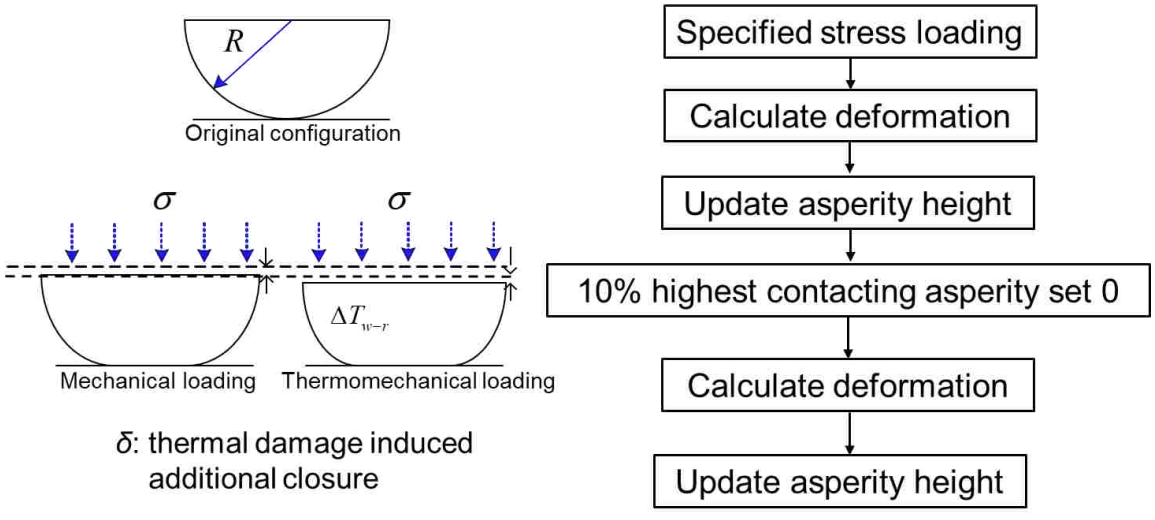

Figure 8.14 The Sketch of Thermomechanical Loading and Numerical Scheme Used in Simulation.

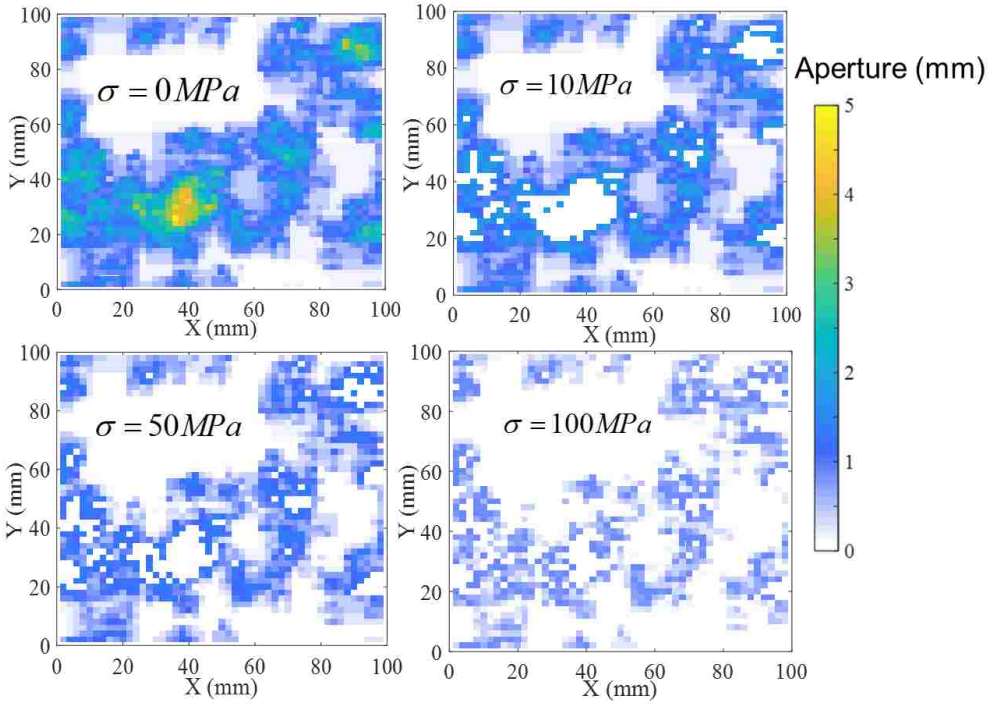

Figure 8.15 The Fracture Aperture at Different Loading Stresses.

The corresponding fracture deformation can be obtained and shown in Figure 8. 14 and 8.15. The presentation maintains the same as in Figure 8.12 and Figure 8.13. Due to damage of contacting asperities, the closure of fracture is more remarking than mechanical loading. At σ = 100 MPa, most asperities almost closed and the connection is become invisible indicating the almost disconnection of flow channels. It shows the significant effect of thermal effect by damage of asperities. In Figure 8.16, the symbol δ denotes the thermal damage induced additional closure. The δ is displayed in the graphs. It shows that thermal induced closure is more significant for high stress loading, which is follows the common sense.

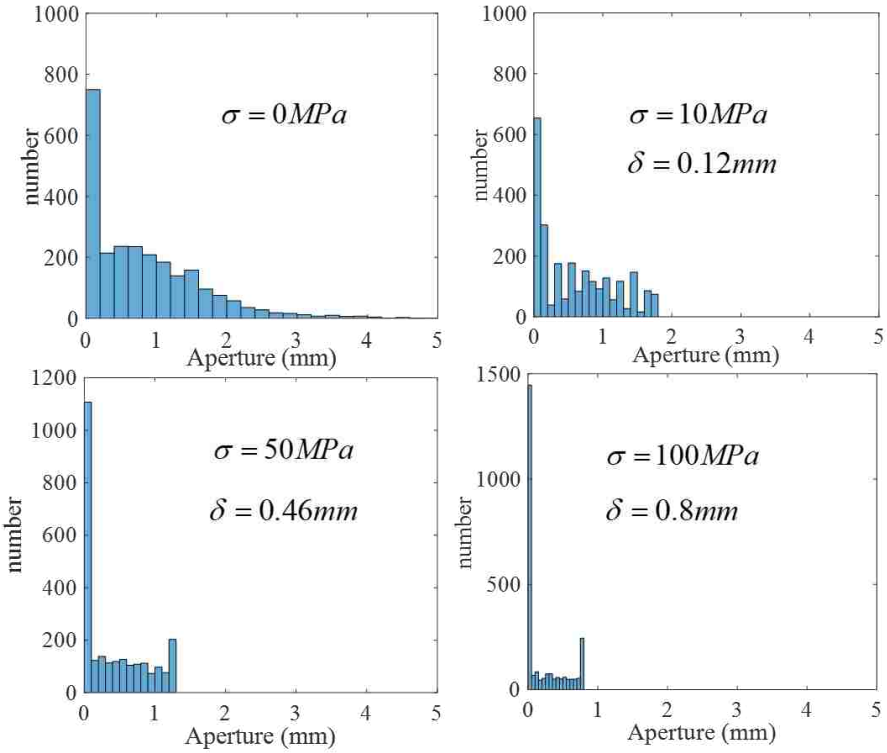

Figure 8.16 Asperity Height Histogram at Different Loading Stresses.

9. CONCLUSION

This dissertation deals with fracture deformation with effect of thermal and mechanical analysis. Due to the rough fracture surface, the direct finite element analysis is infeasible. The contacting asperities consume high computational cost. To alleviate this obstacle, a statistical percolation model is used to analyze the deformation. The deformation of asperity is separately characterized by numerical simulation. The general stress-deformation curve is extracted for individual asperity. This stress-deformation curve is used in the stratified percolation model to analyze the overall closure of fracture.

The abrupt crush and additional closure of fracture can be analyzed by this method. It shows that at high loading stress, thermal closure is significant and has more impact on the fluid flow. The porosity effect is also analyzed in this dissertation. It has negligible effect on the normal stiffness of fracture.

To extend this work, the comparison with experimental data can be done and verify this model. In additional, the fluid flow and transport can be analyzed in this model as well. The remaining aperture between fractures determines the flows channel for fluid flow and contaminant transport. Therefore, this model can serve as a basic framework to analyze more hydrological phenomena in geoscience.

APPENDIX A.

SPECTRAL SYNTHESIS METHOD

The spectral synthesis method is programmed in MATLAB. This code implements approximation of the spectral analysis and inverse Fourier transform. The XA and XB are matrices of bottom surface and top surface respectively. The standard deviation of height is not applied in this code. After the matrices XA and XB are plotted. The height data can be imposed by setting standard deviation.

```
function [XA,XB] =
SpectralSynthesisFM2D(H,Aniso,Rplus,Rminus,tao,lambdac)
% the algorithm based on Oglive et al. (1998)
% Argument:
% X --- doubly indexed array of complex variables of size N^2
% N --- size of array X along one direction
% H --- 0<H<1 determines fractal dimension D = 3-H
% Aniso --- anisotropy factor
% Rplus --- max matching fraction, (0,1)
% Rminus --- min matching fraction, (0,1)
% tao --- transition length, mm
% lambdac --- mismatch wavelength, mm
% Size --- physical size, mm

% NOTES: the default size N = 512
N = 512;

lambdaminus = lambdac*(2*lambdac+tao)/2/(lambdac+tao);    % minimum
correlation scale
lambdaplus = lambdaminus + tao;    % maximum correlation scale

kminus = 2*pi/lambdaminus;    % wavenumber(-)
kplus = 2*pi/lambdaplus;  % wavenumber(+)


A = zeros(N,N);      % matrix for lower surface
B = zeros(N,N);      % matrix for the upper surface

for ii = 1: N/2+1
    for jj = 1: N/2+1
        if (sqrt(ii*ii+jj*jj)<kplus)
            R = Rplus;
        elseif (sqrt(ii*ii+jj*jj)>kminus)
            R = Rminus;
        else
            R = (Rplus-Rminus)/(kplus-kminus)*(sqrt(ii*ii+jj*jj)-
kplus)+Rplus;
        end
        phase1 = 2*pi*normrnd(0,1);      % for lower surface
        phase2 = 2*pi*normrnd(0,1);
        phase3 = R*phase1 + (1-R)*phase2;    % for upper surface
```

```
        if (ii~=1 || jj~=1)
            rad = power(ii*ii+jj*jj/(Aniso*Aniso),-(H+1)/2);
        else
            rad = 0;
        end
        A(ii,jj) = rad*cos(phase1)+1i*rad*sin(phase1);
        B(ii,jj) = rad*cos(phase3)+1i*rad*sin(phase3);
        if (ii==1)
            i0 = 1;
        else
            i0 = N+2-ii;
        end
        if (jj==1)
            j0 = 1;
        else
            j0 = N+2-jj;
        end
        A(i0,j0) = rad*cos(phase1)-1i*rad*sin(phase1);
        B(i0,j0) = rad*cos(phase3)-1i*rad*sin(phase3);
    end
end
A(N/2+1,1) = real(A(N/2+1,1));
A(1,N/2+1) = real(A(1,N/2+1));
A(N/2+1,N/2+1) = real(A(N/2+1,N/2+1));
B(N/2+1,1) = real(B(N/2+1,1));
B(1,N/2+1) = real(B(1,N/2+1));
B(N/2+1,N/2+1) = real(B(N/2+1,N/2+1));
for ii = 2:N/2
    for jj = 2:N/2
        if (sqrt(ii*ii+jj*jj)<kplus)
            R = Rplus;
        elseif (sqrt(ii*ii+jj*jj)>kminus)
            R = Rminus;
        else
            R = (Rplus-Rminus)/(kplus-kminus)*(sqrt(ii*ii+jj*jj)-
kplus)+Rplus;
        end
        phase1 = 2*pi*normrnd(0,1);     % for lower surface
        phase2 = 2*pi*normrnd(0,1);
        phase3 = R*phase1 + (1-R)*phase2;   % for upper surface
        rad = power(ii*ii+jj*jj/(Aniso*Aniso),-(H+1)/2);
        A(ii,N-jj+2) = rad*cos(phase1)+1i*rad*sin(phase1);
        A(N-ii+2,jj) = rad*cos(phase1)-1i*rad*sin(phase1);
        B(ii,N-jj+2) = rad*cos(phase3)+1i*rad*sin(phase3);
        B(N-ii+2,jj) = rad*cos(phase3)-1i*rad*sin(phase3);
    end
end

% fast inverse Fourier transform in 2 dimensions
XA=ifft2(A);
XB=ifft2(B);

end
```

APPENDIX B.

HIERARCHICAL CASCADES OF SQUARES

The stratified continuum percolation model is implemented in MATLAB. All code is attached in this appendix.

```
%%%%%%%%%%%%%%%%%%%%%%%%%%%%%%%%%%%%%%%%%%%%%%%%%%%%%%%%%%%%%%%%%%%%%%%%%%%%%%%

% Chao Zeng
% 07/2019
% This code creates Stratified Percolation Model

% Inputs
% len: Length of Lattice
%
% Global Declarations
% random: Binary Variable for Traditional(0) or Randum(1) Medium
% b: scaling factor
% N: number of tiers
% d: initial pore size
% L: number of pores to remove in each tiers
%-------------------------------------------------------------------------
---
clear
clc
clf

N=5;              % number of tiers

struct1.L = 2;         %number of squares in each tier
struct1.b = 2.37;         %scale factor
struct1.Len = 300;      %length of intial geometry
struct1.Len_large = struct1.Len;    % the length of largest square

struct1.squres_x_all={};
struct1.squres_y_all={};
struct1.gridmatrix = zeros(round(struct1.Len),round(struct1.Len));

[pts,squres_x,squres_y,struct1] =

my_mante_carlo_Simulation(N+1,struct1);

%%%%%%%%%%%%%%%%%%%%%%%%%%%%%%%%%%%%%%%%%%%%%%%%%%%%%%%%%%%%%%%%%%%%%%%%%%%%%%%

% set(0,'DefaultFigureWindowStyle','docked')
% rng(1); % set reset random seed to a fixed
%
function [pts,squres_x,squres_y,struct1] =
my_mante_carlo_Simulation(N,struct1)


cMap = colormap(gray);

% lowest level
if N<=1

    pts = [0, 0, N, 1, 1];    % [x y tier, parent_tag, child_tag]
```

```
    squres_x = {[pts(1)-struct1.Len/2  pts(1)-struct1.Len/2
pts(1)+struct1.Len/2  pts(1)+struct1.Len/2]};
    squres_y = {[pts(2)+struct1.Len/2  pts(2)-struct1.Len/2  pts(2)-
struct1.Len/2  pts(2)+struct1.Len/2]};
    set(gcf, 'Position',  [100, 100, 386, 386])
    fill(squres_x{1,1}, squres_y{1,1}, 'w','EdgeColor','none');
     set(gca,'xtick',[],'ytick',[])
     set(gca,'xticklabel',[],'ytick',[])
%     set(gca,'Visible','off')
    %box off
    pbaspect([1 1 1])
    hold on
else

    %-----------recursive function call--------------------------------
---
    [pts, squres_x, squres_y,struct1] = my_mante_carlo_Simulation(N-
1,struct1);

    sL = size(pts,1)*struct1.L;
    pts_center=zeros(sL,4);
    pts_center(:,1:2) = repmat(pts(:,1:2),[struct1.L,1]) +
(2*rand([sL,2])-1)*struct1.Len/2;   %ceter point of smaller square
    pts_center(:,3) = N;
    pts_center(:,4) = repmat(pts(:,4),[struct1.L,1]);
    pts_center(:,5) = cumsum(ones(sL,1));
    struct1.Len = struct1.Len/struct1.b;

    %clear the squares_x and squares_y in parent squares
    squres_x = {};
    squres_y = {};

%   %   divide the region for the sites
%   %   with intersection with the border
    for k = 1:size(pts_center,1)
        [squres_x, squres_y] = wraparound_boundary(k,
struct1.Len_large, struct1.Len, pts_center, squres_x, squres_y);
    end

%   display the model
    if N == 5
     for k1 = 1:size(pts_center,1)
         for k2 = 1:size(squres_x,2)
             fill(squres_x{k1,k2},
squres_y{k1,k2},'k','EdgeColor','none');
%              set(gca,'xtick',[],'ytick',[])
%              set(gca,'xticklabel',[],'ytick',[])
%              set(gca,'Visible','off')
             %box off
         end
     end
    end

    %-----------calculate the density distribution in the grid---------
---
```

```
    struct1.gridmatrix =
calculate_density_distribution(struct1.gridmatrix,struct1.Len_large,squ
res_x,squres_y);


    %-----------calculate the total area fraction----------------------
-
%     squres_x_all = {squres_x_all{:,:} squres_x{:,:}};
%     squres_y_all = {squres_y_all{:,:} squres_y{:,:}};
%     total_area = calculate_area_parent(squres_x_all,squres_y_all);
%     total_area_fraction = total_area/(Len_large^2);
%     fprintf('the total area fraction is: %f \n',
total_area_fraction);

    %-----------calculate subtier area fraction-----------------------
-
    subtier_area = calculate_area_parent(squres_x,squres_y);
    subtier_area_fraction = subtier_area/(struct1.Len_large^2);
    fprintf('the subtier area fraction is: %f \n',
subtier_area_fraction);



    pts_center(:,4) = pts_center(:,5);
    pts = pts_center;


end

%%%%%%%%%%%%%%%%%%%%%%%%%%%%%%%%%%%%%%%%%%%%%%%%%%%%%%%%%%%%%%%%%%%%%%%%

function [x, y] = wraparound_boundary(k, Len_large, Len, pts_center,
squres_x, squres_y)

%divide the region for the sites
        % with intersection with the border
        if pts_center(k,1)>(Len_large/2-Len/2)&&
pts_center(k,1)<(Len_large/2+Len/2)
            if pts_center(k,2)> (Len_large/2-Len/2) &&
pts_center(k,2)<(Len_large/2+Len/2)
                flag = 1;
            elseif pts_center(k,2)<-(Len_large/2-Len/2) &&
pts_center(k,2)>-(Len_large/2+Len/2)
                flag = 2;
            elseif pts_center(k,2)<= (Len_large/2-Len/2)&&
pts_center(k,2)>=-(Len_large/2-Len/2)
                flag = 3;
            end
        elseif pts_center(k,1)<-(Len_large/2-Len/2)&& pts_center(k,1)>-
(Len_large/2+Len/2)
            if pts_center(k,2)> (Len_large/2-Len/2) && pts_center(k,2)<
(Len_large/2+Len/2)
                flag = 4;
            elseif pts_center(k,2)<-(Len_large/2-Len/2) &&
pts_center(k,2)>-(Len_large/2+Len/2)
                flag = 5;
```

```
            elseif pts_center(k,2)<= (Len_large/2-Len/2)&&
pts_center(k,2)>=-(Len_large/2-Len/2)
                flag = 6;
            end
        elseif pts center(k,1)>=-(Len_large/2-Len/2) &&
pts_center(k,1)<=(Len_large/2-Len/2)
            if pts_center(k,2)>= (Len_large/2-Len/2) &&
pts_center(k,2)<=(Len_large/2+Len/2)
                flag = 7;
            elseif pts center(k,2)<=-(Len_large/2-Len/2) &&
pts_center(k,2)>=-(Len_large/2+Len/2)
                flag = 8;
            elseif pts_center(k,2)< (Len_large/2-Len/2)&&
pts_center(k,2)>-(Len_large/2-Len/2)
                flag = 9;
            end
        end

        %without intersection with the border
        if pts_center(k,1)>=(Len_large/2+Len/2)
            if pts_center(k,2)>=(Len_large/2+Len/2)
                flag = 11;
            elseif pts_center(k,2)<=-(Len_large/2+Len/2)
                flag = 12;
            elseif pts_center(k,2)>=-(Len_large/2-
Len/2)&&pts_center(k,2)<=(Len_large/2-Len/2)
                flag = 13;
            elseif pts_center(k,2)>-
(Len_large/2+Len/2)&&pts_center(k,2)<-(Len_large/2-Len/2)
                flag = 23;
            elseif pts_center(k,2)>(Len_large/2-
Len/2)&&pts_center(k,2)<(Len_large/2+Len/2)
                flag = 24;
            end
        elseif pts_center(k,1)<=-(Len_large/2+Len/2)
                if pts_center(k,2)>= (Len_large/2+Len/2)
                    flag = 14;
                elseif pts_center(k,2)<=-(Len_large/2+Len/2)
                    flag = 15;
                elseif pts_center(k,2)>=-(Len_large/2-
Len/2)&&pts_center(k,2)<=(Len_large/2-Len/2)
                    flag = 16;
                elseif pts_center(k,2)>-
(Len_large/2+Len/2)&&pts_center(k,2)<-(Len_large/2-Len/2)
                    flag = 25;
                elseif pts_center(k,2)>(Len_large/2-
Len/2)&&pts_center(k,2)<(Len_large/2+Len/2)
                    flag = 26;
                end
        elseif pts_center(k,1)>=-(Len_large/2-Len/2) &&
pts_center(k,1)<=(Len_large/2-Len/2)
            if pts_center(k,2)>=(Len_large/2+Len/2)
                flag = 17;
            elseif pts_center(k,2)<=-(Len_large/2+Len/2)
                flag = 18;
            end
```

```
        elseif pts_center(k,1)>(Len_large/2-Len/2) &&
pts_center(k,1)<(Len_large/2+Len/2)
            if pts_center(k,2)>=(Len_large/2+Len/2)
                flag = 19;
            elseif pts center(k,2)<=-(Len_large/2+Len/2)
                flag = 20;
            end
        elseif pts_center(k,1)>-(Len_large/2+Len/2) &&
pts_center(k,1)<-(Len_large/2-Len/2)
            if pts center(k,2)>=(Len_large/2+Len/2)
                flag = 21;
            elseif pts_center(k,2)<=-(Len_large/2+Len/2)
                flag = 22;
            end
        end

        if flag == 1
            squres_x{k,1} = [pts_center(k,1)-Len/2 pts_center(k,1)-
Len/2 Len_large/2 Len_large/2];
            squres_y{k,1} = [Len_large/2 pts_center(k,2)-Len/2
pts_center(k,2)-Len/2 Len_large/2];
            squres_x{k,2} = [Len_large/2 Len_large/2
pts_center(k,1)+Len/2 pts_center(k,1)+Len/2]-Len_large;
            squres_y{k,2} = [Len_large/2 pts_center(k,2)-Len/2
pts_center(k,2)-Len/2 Len_large/2];
            squres_x{k,3} = [Len_large/2 Len_large/2
pts_center(k,1)+Len/2 pts_center(k,1)+Len/2]-Len_large;
            squres_y{k,3} = [pts_center(k,2)+Len/2 Len_large/2
Len_large/2 pts_center(k,2)+Len/2]-Len_large;
            squres_x{k,4} = [pts_center(k,1)-Len/2 pts_center(k,1)-
Len/2 Len_large/2 Len_large/2];
            squres_y{k,4} = [pts_center(k,2)+Len/2 Len_large/2
Len_large/2 pts_center(k,2)+Len/2]-Len_large;
        elseif flag == 2
            squres_x{k,1} = [pts_center(k,1)-Len/2 pts_center(k,1)-
Len/2 Len_large/2 Len_large/2];
            squres_y{k,1} = [pts_center(k,2)+Len/2 -Len_large/2 -
Len_large/2 pts_center(k,2)+Len/2];
            squres_x{k,2} = [pts_center(k,1)-Len/2 pts_center(k,1)-
Len/2 Len_large/2 Len_large/2];
            squres_y{k,2} = [-Len_large/2 pts_center(k,2)-Len/2
pts_center(k,2)-Len/2 -Len_large/2]+Len_large;
            squres_x{k,3} = [Len_large/2 Len_large/2
pts_center(k,1)+Len/2 pts_center(k,1)+Len/2]-Len_large;
            squres_y{k,3} = [-Len_large/2 pts_center(k,2)-Len/2
pts_center(k,2)-Len/2 -Len_large/2]+Len_large;
            squres_x{k,4} = [Len_large/2 Len_large/2
pts_center(k,1)+Len/2 pts_center(k,1)+Len/2]-Len_large;
            squres_y{k,4} = [pts_center(k,2)+Len/2 -Len_large/2 -
Len_large/2 pts_center(k,2)+Len/2];
        elseif flag == 3
            squres_x{k,1} = [pts_center(k,1)-Len/2 pts_center(k,1)-
Len/2 Len_large/2 Len_large/2];
            squres_y{k,1} = [pts_center(k,2)+Len/2 pts_center(k,2)-
Len/2 pts_center(k,2)-Len/2 pts_center(k,2)+Len/2];
```

```
            squres_x{k,2} = [Len_large/2 Len_large/2
pts_center(k,1)+Len/2 pts_center(k,1)+Len/2]-Len_large;
            squres_y{k,2} = [pts_center(k,2)+Len/2 pts_center(k,2)-
Len/2 pts_center(k,2)-Len/2 pts_center(k,2)+Len/2];
        elseif flag == 4
            squres_x{k,1} = [-Len_large/2 -Len_large/2
pts_center(k,1)+Len/2 pts_center(k,1)+Len/2];
            squres_y{k,1} = [Len_large/2 pts_center(k,2)-Len/2
pts_center(k,2)-Len/2 Len_large/2];
            squres x{k,2} = [-Len large/2 -Len_large/2
pts_center(k,1)+Len/2 pts_center(k,1)+Len/2];
            squres_y{k,2} = [pts_center(k,2)+Len/2 Len_large/2
Len_large/2 pts_center(k,2)+Len/2]-Len_large;
            squres_x{k,3} = [pts_center(k,1)-Len/2 pts_center(k,1)-
Len/2 -Len_large/2 -Len_large/2]+Len_large;
            squres_y{k,3} = [pts_center(k,2)+Len/2 Len_large/2
Len_large/2 pts_center(k,2)+Len/2]-Len_large;
            squres_x{k,4} = [pts_center(k,1)-Len/2 pts_center(k,1)-
Len/2 -Len_large/2 -Len_large/2]+Len_large;
            squres_y{k,4} = [Len_large/2 pts_center(k,2)-Len/2
pts_center(k,2)-Len/2 Len_large/2];
        elseif flag == 5
            squres_x{k,1} = [-Len_large/2 -Len_large/2
pts_center(k,1)+Len/2 pts_center(k,1)+Len/2];
            squres_y{k,1} = [pts_center(k,2)+Len/2 -Len_large/2 -
Len_large/2 pts_center(k,2)+Len/2];
            squres_x{k,2} = [pts_center(k,1)-Len/2 pts_center(k,1)-
Len/2 -Len_large/2 -Len_large/2]+Len_large;
            squres_y{k,2} = [pts_center(k,2)+Len/2 -Len_large/2 -
Len_large/2 pts_center(k,2)+Len/2];
            squres_x{k,3} = [pts_center(k,1)-Len/2 pts_center(k,1)-
Len/2 -Len_large/2 -Len_large/2]+Len_large;
            squres_y{k,3} = [-Len_large/2 pts_center(k,2)-Len/2
pts_center(k,2)-Len/2 -Len_large/2]+Len_large;
            squres_x{k,4} = [-Len_large/2 -Len_large/2
pts_center(k,1)+Len/2 pts_center(k,1)+Len/2];
            squres_y{k,4} = [-Len_large/2 pts_center(k,2)-Len/2
pts_center(k,2)-Len/2 -Len_large/2]+Len_large;
        elseif flag == 6
            squres_x{k,1} = [pts_center(k,1)-Len/2 pts_center(k,1)-
Len/2 -Len_large/2 -Len_large/2]+Len_large;
            squres_y{k,1} = [pts_center(k,2)+Len/2 pts_center(k,2)-
Len/2 pts_center(k,2)-Len/2 pts_center(k,2)+Len/2];
            squres_x{k,2} = [-Len_large/2 -Len_large/2
pts_center(k,1)+Len/2 pts_center(k,1)+Len/2];
            squres_y{k,2} = [pts_center(k,2)+Len/2 pts_center(k,2)-
Len/2 pts_center(k,2)-Len/2 pts_center(k,2)+Len/2];
        elseif flag == 7
            squres_x{k,1} = [pts_center(k,1)-Len/2 pts_center(k,1)-
Len/2 pts_center(k,1)+Len/2 pts_center(k,1)+Len/2];
            squres_y{k,1} = [Len_large/2 pts_center(k,2)-Len/2
pts_center(k,2)-Len/2 Len_large/2];
            squres_x{k,2} = [pts_center(k,1)-Len/2 pts_center(k,1)-
Len/2 pts_center(k,1)+Len/2 pts_center(k,1)+Len/2];
            squres_y{k,2} = [pts_center(k,2)+Len/2 Len_large/2
Len_large/2 pts_center(k,2)+Len/2]-Len_large;
```

```
        elseif flag == 8
            squres_x{k,1} = [pts_center(k,1)-Len/2 pts_center(k,1)-
Len/2 pts_center(k,1)+Len/2 pts_center(k,1)+Len/2];
            squres_y{k,1} = [-Len_large/2 pts_center(k,2)-Len/2
pts center(k,2)-Len/2 -Len large/2]+Len large;
            squres_x{k,2} = [pts_center(k,1)-Len/2 pts_center(k,1)-
Len/2 pts_center(k,1)+Len/2 pts_center(k,1)+Len/2];
            squres_y{k,2} = [pts_center(k,2)+Len/2 -Len_large/2 -
Len_large/2 pts_center(k,2)+Len/2];
        elseif flag == 9
            squres_x{k,1} = [pts_center(k,1)-Len/2 pts_center(k,1)-
Len/2 pts_center(k,1)+Len/2 pts_center(k,1)+Len/2];
            squres_y{k,1} = [pts_center(k,2)+Len/2 pts_center(k,2)-
Len/2 pts_center(k,2)-Len/2 pts_center(k,2)+Len/2];
        elseif flag == 11
            squres_x{k,1} = [pts_center(k,1)-Len/2 pts_center(k,1)-
Len/2 pts_center(k,1)+Len/2 pts_center(k,1)+Len/2]-Len_large;
            squres_y{k,1} = [pts_center(k,2)+Len/2 pts_center(k,2)-
Len/2 pts_center(k,2)-Len/2 pts_center(k,2)+Len/2]-Len_large;
        elseif flag == 12
            squres_x{k,1} = [pts_center(k,1)-Len/2 pts_center(k,1)-
Len/2 pts_center(k,1)+Len/2 pts_center(k,1)+Len/2]-Len_large;
            squres_y{k,1} = [pts_center(k,2)+Len/2 pts_center(k,2)-
Len/2 pts_center(k,2)-Len/2 pts_center(k,2)+Len/2]+Len_large;
        elseif flag == 13
            squres_x{k,1} = [pts_center(k,1)-Len/2 pts_center(k,1)-
Len/2 pts_center(k,1)+Len/2 pts_center(k,1)+Len/2]-Len_large;
            squres_y{k,1} = [pts_center(k,2)+Len/2 pts_center(k,2)-
Len/2 pts_center(k,2)-Len/2 pts_center(k,2)+Len/2];
        elseif flag == 14
            squres_x{k,1} = [pts_center(k,1)-Len/2 pts_center(k,1)-
Len/2 pts_center(k,1)+Len/2 pts_center(k,1)+Len/2]+Len_large;
            squres_y{k,1} = [pts_center(k,2)+Len/2 pts_center(k,2)-
Len/2 pts_center(k,2)-Len/2 pts_center(k,2)+Len/2]-Len_large;
        elseif flag == 15
            squres_x{k,1} = [pts_center(k,1)-Len/2 pts_center(k,1)-
Len/2 pts_center(k,1)+Len/2 pts_center(k,1)+Len/2]+Len_large;
            squres_y{k,1} = [pts_center(k,2)+Len/2 pts_center(k,2)-
Len/2 pts_center(k,2)-Len/2 pts_center(k,2)+Len/2]+Len_large;
        elseif flag == 16
            squres_x{k,1} = [pts_center(k,1)-Len/2 pts_center(k,1)-
Len/2 pts_center(k,1)+Len/2 pts_center(k,1)+Len/2]+Len_large;
            squres_y{k,1} = [pts_center(k,2)+Len/2 pts_center(k,2)-
Len/2 pts_center(k,2)-Len/2 pts_center(k,2)+Len/2];
        elseif flag == 17
            squres_x{k,1} = [pts_center(k,1)-Len/2 pts_center(k,1)-
Len/2 pts_center(k,1)+Len/2 pts_center(k,1)+Len/2];
            squres_y{k,1} = [pts_center(k,2)+Len/2 pts_center(k,2)-
Len/2 pts_center(k,2)-Len/2 pts_center(k,2)+Len/2]-Len_large;
        elseif flag == 18
            squres_x{k,1} = [pts_center(k,1)-Len/2 pts_center(k,1)-
Len/2 pts_center(k,1)+Len/2 pts_center(k,1)+Len/2];
            squres_y{k,1} = [pts_center(k,2)+Len/2 pts_center(k,2)-
Len/2 pts_center(k,2)-Len/2 pts_center(k,2)+Len/2]+Len_large;
        elseif flag == 19
```

```
            squres_x{k,1} = [pts_center(k,1)-Len/2 pts_center(k,1)-
Len/2 Len_large/2 Len_large/2];
            squres_y{k,1} = [pts_center(k,2)+Len/2 pts_center(k,2)-
Len/2 pts_center(k,2)-Len/2 pts_center(k,2)+Len/2]-Len_large;
            squres x{k,2} = [Len large/2 Len large/2
pts_center(k,1)+Len/2 pts_center(k,1)+Len/2]-Len_large;
            squres_y{k,2} = [pts_center(k,2)+Len/2 pts_center(k,2)-
Len/2 pts_center(k,2)-Len/2 pts_center(k,2)+Len/2]-Len_large;
        elseif flag == 20
            squres x{k,1} = [pts_center(k,1)-Len/2 pts_center(k,1)-
Len/2 Len_large/2 Len_large/2];
            squres_y{k,1} = [pts_center(k,2)+Len/2 pts_center(k,2)-
Len/2 pts_center(k,2)-Len/2 pts_center(k,2)+Len/2]+Len_large;
            squres_x{k,2} = [Len_large/2 Len_large/2
pts_center(k,1)+Len/2 pts_center(k,1)+Len/2]-Len_large;
            squres_y{k,2} = [pts_center(k,2)+Len/2 pts_center(k,2)-
Len/2 pts_center(k,2)-Len/2 pts_center(k,2)+Len/2]+Len_large;
        elseif flag == 21
            squres_x{k,1} = [pts_center(k,1)-Len/2 pts_center(k,1)-
Len/2 -Len_large/2 -Len_large/2]+Len_large;
            squres_y{k,1} = [pts_center(k,2)+Len/2 pts_center(k,2)-
Len/2 pts_center(k,2)-Len/2 pts_center(k,2)+Len/2]-Len_large;
            squres_x{k,2} = [-Len_large/2 -Len_large/2
pts_center(k,1)+Len/2 pts_center(k,1)+Len/2];
            squres_y{k,2} = [pts_center(k,2)+Len/2 pts_center(k,2)-
Len/2 pts_center(k,2)-Len/2 pts_center(k,2)+Len/2]-Len_large;
        elseif flag == 22
            squres_x{k,1} = [pts_center(k,1)-Len/2 pts_center(k,1)-
Len/2 -Len_large/2 -Len_large/2]+Len_large;
            squres_y{k,1} = [pts_center(k,2)+Len/2 pts_center(k,2)-
Len/2 pts_center(k,2)-Len/2 pts_center(k,2)+Len/2]+Len_large;
            squres_x{k,2} = [-Len_large/2 -Len_large/2
pts_center(k,1)+Len/2 pts_center(k,1)+Len/2];
            squres_y{k,2} = [pts_center(k,2)+Len/2 pts_center(k,2)-
Len/2 pts_center(k,2)-Len/2 pts_center(k,2)+Len/2]+Len_large;
        elseif flag == 23
            squres_x{k,1} = [pts_center(k,1)-Len/2 pts_center(k,1)-
Len/2 pts_center(k,1)+Len/2 pts_center(k,1)+Len/2]-Len_large;
            squres_y{k,1} = [pts_center(k,2)+Len/2 -Len_large/2 -
Len_large/2 pts_center(k,2)+Len/2];
            squres_x{k,2} = [pts_center(k,1)-Len/2 pts_center(k,1)-
Len/2 pts_center(k,1)+Len/2 pts_center(k,1)+Len/2]-Len_large;
            squres_y{k,2} = [-Len_large/2 pts_center(k,2)-Len/2
pts_center(k,2)-Len/2 -Len_large/2]+Len_large;
        elseif flag == 24
            squres_x{k,1} = [pts_center(k,1)-Len/2 pts_center(k,1)-
Len/2 pts_center(k,1)+Len/2 pts_center(k,1)+Len/2]-Len_large;
            squres_y{k,1} = [pts_center(k,2)+Len/2 Len_large/2
Len_large/2 pts_center(k,2)+Len/2]-Len_large;
            squres_x{k,2} = [pts_center(k,1)-Len/2 pts_center(k,1)-
Len/2 pts_center(k,1)+Len/2 pts_center(k,1)+Len/2]-Len_large;
            squres_y{k,2} = [Len_large/2 pts_center(k,2)-Len/2
pts_center(k,2)-Len/2 Len_large/2];
        elseif flag == 25
            squres_x{k,1} = [pts_center(k,1)-Len/2 pts_center(k,1)-
Len/2 pts_center(k,1)+Len/2 pts_center(k,1)+Len/2]+Len_large;
```

```
            squres_y{k,1} = [pts_center(k,2)+Len/2 -Len_large/2 -
Len_large/2 pts_center(k,2)+Len/2];
            squres_x{k,2} = [pts_center(k,1)-Len/2 pts_center(k,1)-
Len/2 pts_center(k,1)+Len/2 pts_center(k,1)+Len/2]+Len_large;
            squres y{k,2} = [-Len large/2 pts center(k,2)-Len/2
pts_center(k,2)-Len/2 -Len_large/2]+Len_large;
        elseif flag == 26
            squres_x{k,1} = [pts_center(k,1)-Len/2 pts_center(k,1)-
Len/2 pts_center(k,1)+Len/2 pts_center(k,1)+Len/2]+Len_large;
            squres y{k,1} = [pts center(k,2)+Len/2 Len_large/2
Len_large/2 pts_center(k,2)+Len/2]-Len_large;
            squres_x{k,2} = [pts_center(k,1)-Len/2 pts_center(k,1)-
Len/2 pts_center(k,1)+Len/2 pts_center(k,1)+Len/2]+Len_large;
            squres_y{k,2} = [Len_large/2 pts_center(k,2)-Len/2
pts_center(k,2)-Len/2 Len_large/2];
        end

        x = squres_x;
        y = squres_y;

end

%%%%%%%%%%%%%%%%%%%%%%%%%%%%%%%%%%%%%%%%%%%%%%%%%%%%%%%%%%%%%%%%%%%%%%%%%%%%%%%

function gridmatrix =
calculate_density_distribution(gridmatrix,Len_large,squres_x,squres_y)

%NOTE: length of unit is 1
M = round(Len_large);    % horizontal direction
N = round(Len_large);    % vertical direction

for k1 = 1: size(squres_x,1)
    for k2 = 1: size(squres_x,2)
        if isempty(squres_x{k1,k2})
            continue
        end
        % the vector info of squres
        x1 = squres_x{k1,k2}(2);
        x2 = squres_x{k1,k2}(3);
        y1 = squres_y{k1,k2}(2);
        y2 = squres_y{k1,k2}(1);
        width = x2 - x1;
        height = y2 - y1;
        temp_B = [x1 y1 width height];
        % the vector info of units
        i1 = floor(x1)+M/2+1;
        i2 = floor(x2)+M/2+(x2~=M/2);
        j1 = floor(y1)+N/2+1;
        j2 = floor(y2)+M/2+(y2~=N/2);
        if i1 == i2
            i2 = i2 + 1;
        end
        if j1 == j2
            j2 = j2 + 1;
        end
        for i = i1:i2
```

```
            for j = j1:j2
                coord_x = i-M/2-1;
                coord_y = j-N/2-1;
                temp_A = [coord_x coord_y 1 1];
                if rectint(temp A, temp B) > 0.5
                    gridmatrix(i,j) = gridmatrix(i,j) + 1;
                end
            end
        end
    end
end

end



%%%%%%%%%%%%%%%%%%%%%%%%%%%%%%%%%%%%%%%%%%%%%%%%%%%%%%%%%%%%%%%%%%%%%%%%%%%%%%%

function total_area = calculate_area_parent(squres_x,squres_y)


% sort all squares according to their x-values of right edges
squres_x_array = {};
squres_y_array = {};
squres_x_array = {squres_x_array,squres_x{:,:}};
squres_y_array = {squres_y_array,squres_y{:,:}};
squres_x_matrix = cell2mat(squres_x_array(2:end));
squres_y_matrix = cell2mat(squres_y_array(2:end));
squres = [squres_x_matrix(2:4:end-2)' squres_x_matrix(4:4:end)'
squres_y_matrix(2:4:end-2)' squres_y_matrix(4:4:end)'];
rangeOfX = [squres_x_matrix(2:4:end-2)'; squres_x_matrix(4:4:end)'];

squres = sortrows(squres,2);
IDX = 1:size(squres,1);

%sort a vector of all x-values
rangeOfX = sort(rangeOfX);
% diffX = diff(rangeOfX);
% total_area = 0.0;
%
% for i = 1: size(rangeOfX)-1
%     idx = IDX(squres(:,1) <= rangeOfX(i) &squres(:,2) >=
rangeOfX(i+1));
%     rangeOfY = [squres(idx,3);squres(idx,4)];   % extract the y
coordinate info
%     rangeOfY = sort(rangeOfY);   %sort a vector of all y-values
%     diffY = diff(rangeOfY);     % the distance of neighbouring points
%     total_length_Y = 0.0;
%     for j = 1: size(rangeOfY)-1
%         if sum(squres(idx,3)<=rangeOfY(j) &
squres(idx,4)>=rangeOfY(j+1)) > 0
%             total_length_Y = total_length_Y + diffY(j);
%         end
%     end
%     total_area = total_area + diffX(i)*total_length_Y;
% end
```

```
%
% end

N = size(rangeOfX,1);           %number of x-range
total_area = 0.0;

for i = 1:N-1

     idx = IDX(squres(:,1) <= rangeOfX(i) &squres(:,2) >=
rangeOfX(i+1));
     rangeOfY = [squres(idx,3) squres(idx,4)];   % extract the y
coordinate info
     iter = numel(idx);

    %------Merge the overlapping Y--------------------------
    if iter == 0
        continue
    else
    rangeOfY = sortrows(rangeOfY,1);   % sort based on bottom
coordinate
    gap = 0.0;
    end

    if iter > 1
        for k = 2:iter    %check top coordinate
            max_Y = max(rangeOfY(1:k-1,2));
            if rangeOfY(k,1) > max_Y  % no overlapping
                gap = gap + rangeOfY(k,1)-max_Y;
            end
        end
    end
    total_area = total_area + (rangeOfX(i+1)-
rangeOfX(i))*(max(rangeOfY(:,2))-rangeOfY(1,1)-gap);

end

end
```

APPENDIX C.

FRACTAL FEATURES

Fractal features analysis in section three resorts to a box-counting method. The box-counting method is used to numerically estimate fractal dimension and lacunarity of the pattern. The calculated dimension is called box-counting dimension, and is different from value calculated from other methods, but is the default way to approximately measure fractal dimension. It has two parts, fix-grid scan for fractal dimension and sliding grid scan for lacunarity. The associated code to calculate each of these is attached. The code is validated by FracLac plug-in in ImagJ software. This code is based on code snippets from the MALTAB community and their contributions are sincerely appreciated (the authors and data is noted in code as comments).

The multifractal analysis is also included in this appendix as an indispensable component on heterogeneity of structure. The code is programmed and attached.

```
%%%%%%%%%%%%%%%%%%%%%%%%%%%%%%%%%%%%%%%%%%%%%%%%%%%%%%%%%%%%%%%%%%%%%%%%%%%%

NOTE: This code is revised upon the MATLAB code online by F. Moisy, 2008.

His contribution to the original code is appreciated.

function [n,r] = boxcount(c,varargin)
% control input argument
narginchk(1,2);
% check for true color image (m-by-n-by-3 array)
if ndims(c)==3
    if size(c,3)==3 && size(c,1)>=8 && size(c,2)>=8
        c = sum(c,3);
    end
end
warning off
c = logical(squeeze(c));
warning on
dim = ndims(c); % dim is 2 for a vector or a matrix, 3 for a cube
if dim>3
    error('Maximum dimension is 3.');
end
% transpose the vector to a 1-by-n vector
if length(c)==numel(c)
    dim=1;
    if size(c,1)~=1
        c = c';
    end
end
```

```
width = max(size(c));    % largest size of the box
p = log(width)/log(2);   % nbre of generations
% remap the array if the sizes are not all equal,
% or if they are not power of two
% (this slows down the computation!)
if p~=round(p) || any(size(c)~=width)
    p = ceil(p);
    width = 2^p;
    switch dim
        case 1
            mz = zeros(1,width);
            mz(1:length(c)) = c;
            c = mz;
        case 2
            mz = zeros(width, width);
            mz(1:size(c,1), 1:size(c,2)) = c;
            c = mz;
        case 3
            mz = zeros(width, width, width);
            mz(1:size(c,1), 1:size(c,2), 1:size(c,3)) = c;
            c = mz;
    end
end
n=zeros(1,p+1); % pre-allocate the number of box of size r
switch dim
    case 1        %------------------- 1D boxcount --------------------
-%
        n(p+1) = sum(c);
        for g=(p-1):-1:0
            siz = 2^(p-g);
            siz2 = round(siz/2);
            for i=1:siz:(width-siz+1)
                c(i) = ( c(i) || c(i+siz2));
            end
            n(g+1) = sum(c(1:siz:(width-siz+1)));
        end
    case 2         %------------------- 2D boxcount -------------------
--%
        n(p+1) = sum(c(:));
        for g=(p-1):-1:0
            siz = 2^(p-g);
            siz2 = round(siz/2);
            for i=1:siz:(width-siz+1)
                for j=1:siz:(width-siz+1)
                    c(i,j) = ( c(i,j) || c(i+siz2,j) || c(i,j+siz2) ||
c(i+siz2,j+siz2) );
                end
            end
            n(g+1) = sum(sum(c(1:siz:(width-siz+1),1:siz:(width-
siz+1))));
        end
    case 3         %------------------- 3D boxcount -------------------
--%
        n(p+1) = sum(c(:));
        for g=(p-1):-1:0
            siz = 2^(p-g);
```

```
            siz2 = round(siz/2);
            for i=1:siz:(width-siz+1)
                for j=1:siz:(width-siz+1)
                    for k=1:siz:(width-siz+1)
                        c(i,j,k)=( c(i,j,k) || c(i+siz2,j,k) ||
c(i,j+siz2,k) ...
                            || c(i+siz2,j+siz2,k) || c(i,j,k+siz2) ||
c(i+siz2,j,k+siz2) ...
                            || c(i,j+siz2,k+siz2) ||
c(i+siz2,j+siz2,k+siz2));
                    end
                end
            end
            n(g+1) = sum(sum(sum(c(1:siz:(width-siz+1),1:siz:(width-
siz+1),1:siz:(width-siz+1)))));
        end
end
n = n(end:-1:1);
r = 2.^(0:p); % box size (1, 2, 4, 8...)
if any(strncmpi(varargin,'slope',1))
    s=-gradient(log(n))./gradient(log(r));
    semilogx(r, s, 's-');
    ylim([0 dim]);
    xlabel('r, box size'); ylabel('- d ln n / d ln r, local
dimension');
    title([num2str(dim) 'D box-count']);
elseif nargout==0 || any(strncmpi(varargin,'plot',1))
    loglog(r,n,'s-');
    xlabel('r, box size'); ylabel('n(r), number of boxes');
    title([num2str(dim) 'D box-count']);
end
if nargout==0
    clear r n
end


% box-accounting technique

% add the sub-directory into the path
cd IMAGE_EXPORT;

% export the image
axe_handle = gca;
export_fig(axe_handle,'-transparent','-tif','-m1')

cd C:\Users\zc727\Desktop\Upscaling-Dissertation
% extract the binary matrix of image (black--0; white---1)
imgmatrix = imread('C:\Users\zc727\Desktop\Upscaling-
Dissertation\IMAGE_EXPORT\export_fig_out.tif');
imgmatrix = imgmatrix < 100;

% display the fractal dimension vs box size
Figure(2)
boxcount(1-imgmatrix,'slope')
```

```
%%%%%%%%%%%%%%%%%%%%%%%%%%%%%%%%%%%%%%%%%%%%%%%%%%%%%%%%%%%%%%%%%%%%%%%%%%%%
NOTE: This code is revised upon the MATLAB code online by Tegy J. Vadakkan,
2009. His contribution to this fractal analysis is appreciated. The
algorithms is based on the work by Tolle et al., Physica D, 237,306-315,
2008

cd IMAGE_EXPORT;

% export the image
axe_handle = gca;
export_fig(axe_handle,'-transparent','-tif')

cd C:\Users\zc727\Desktop\Upscaling-Dissertation
a = imread('C:\Users\zc727\Desktop\Upscaling-
Dissertation\IMAGE_EXPORT\export_fig_out.tif');
a = a > 30;
[rows, cols] = size(a);
a = 1 - a;
%%
n = 2;
while(n <= rows)
nn = n-1;
rnn = rows - nn;
cnn = cols - nn;
index = uint8(log2(n));
count(index)= rnn*cnn;
sigma(index) = 0.0;
sigma2(index) = 0.0;
for i=1:rnn
    for j=1:cnn
        sums = sum(sum(a(i:i+nn,j:j+nn)));
        sigma(index) = sigma(index) + sums;
        sigma2(index) = sigma2(index) + power(sums,2);
    end
end
n = n * 2;
end
%%
for i=1:index
    M(i,1)= (count(i)*sigma2(i))/(power(sigma(i),2))-1;
end
sprintf('the average lacunarity is: %.5f\n',sum(M)/double(index))




%%%%%%%%%%%%%%%%%%%%%%%%%%%%%%%%%%%%%%%%%%%%%%%%%%%%%%%%%%%%%%%%%%%%%%%%%%%%
NOTE: a is the matrix from density of sites in stratified continuum
percolation model. This code is revised upon the MATLAB code online by
```

```
Tegy J. Vadakkan,2009. His contribution to this multifractal analysis is
appreciated. The algorithms is based on the work by Posadas et al., Soil
Sci. Soc. Am. J. 67:1361-1369, 2003.

function multifractal_analysis(a)

npix = sum(sum(a));

width = max(size(a));    % largest size of the box
p = log(width)/log(2);   % nbre of generations
if p~=round(p) || any(size(a)~=width)
    p = ceil(p);
    width = 2^p;
    mz = zeros(width, width);
    mz(1:size(a,1), 1:size(a,2)) = a;
    a = mz;
end

max_boxes = power(width,2)/power(2,2);
nL = double(zeros(max_boxes,p));
for g=(p-1):-1:0
    siz = 2^(p-g);
    sizm1 = siz - 1;
    index = log2(siz);
    count = 0;
    for i=1:siz:(width-siz+1)
        for j=1:siz:(width-siz+1)
            count = count + 1;
            sums = sum(sum(a(i:i+sizm1,j:j+sizm1)));
            nL(count,index) = sums;
        end
    end
end
%----------------------Log of L-----------------------------------------
--
qran = 10;
logl = zeros(p,1);
for l=1:p
    logl(l) = log(power(2,l));
end

%-----------------normalized masses-----------------------------------
---
pL = double(zeros(max_boxes,p));
for l=1:p
    nboxes = power(width,2)/power(power(2,l),2);
    norm = sum(nL(1:nboxes,l));
    if(norm ~= npix)
        FPRINTF('error');
    end
    for i=1:nboxes
        pL(i,l) = nL(i,l)/norm;
    end
end
```

```
%---------------------calculate the parameters-------------------------
---
%------------f(alpha), alpha, tao(q) etc.-----------------------------
---
for l=1:p

    count = 0;
    nboxes = power(width,2)/power(power(2,l),2);

    for q = -qran:+0.1:qran

        %denominator of muiql
        qsum = 0.0;
        for i=1:nboxes
            if(pL(i,l) ~= 0)
                qsum = qsum + power(pL(i,l),q);
            end
        end

        fqnum = 0.0;
        aqnum = 0.0;
        smuiqL = 0.0;
        for i=1:nboxes
            if(pL(i,l) ~= 0)
                  muiqL = power(pL(i,l),q)/qsum;
                  fqnum = fqnum + (muiqL * log(muiqL));
                  aqnum = aqnum + (muiqL * log(pL(i,l)));
                  smuiqL = smuiqL + muiqL;
            end
        end
        if(uint8(smuiqL)~=1)
            FPRINTF('error');
        end

        count = count + 1;
        fql(l,count) = fqnum;
        aql(l,count) = aqnum;
        qval(count) = q;
        taoql(l,count) = log(qsum);
    end
end

% ==============calculate the R^2 in the
fitting=========================
%--------------tao(q)-------------------------------------------------
--
for i=1:count
    line = polyfit(logl,taoql(:,i),1);
    tao(i) = line(1);
end

% -------------alpha(q)-----------------------------------------------
---
for i=1:count
     line = polyfit(logl,aql(:,i),1);
     aq(i) = line(1);
```

```
     yfit = polyval(line,logl);
     sse = sum(power(aql(:,i)-yfit,2));
     sst = sum(power(aql(:,i)-mean(aql(:,i)),2));
     ar2(i) = 1-(sse/sst);
end

%----------------f(q)-----------------------------------------------------
---
for i=1:count
     line = polyfit(logl,fql(:,i),1);
     fq(i) = line(1);
     yfit = polyval(line,logl);
     sse = sum(power(fql(:,i)-yfit,2));
     sst = sum(power(fql(:,i)-mean(fql(:,i)),2));
     fr2(i) = 1-(sse/sst);
end

%================plot result
==============================================
Figure
plot(qval,tao,'r:o');
legend('tao(q)');
xlabel('q','FontSize',14);
%
Figure
plot(qval,aq,'r:o',qval,fq,'g:o');
legend('alpha(q)','f(q)');
xlabel('q','FontSize',14);
%
Figure
plot(aq,fq,'r:o');
xlabel('alpha(q)','FontSize',14);
ylabel('f(q)','FontSize',14);
%
line=polyfit(aq,fq,2);
pfit = polyval(line,aq);
Figure
plot(aq,fq,'r:o',aq,pfit,'g:o');
legend('f(q)','Parabolic fit to f(q)');
xlabel('alpha(q)','FontSize',14);
```

APPENDIX D.

FRACTURE DEFORMATION MODEL

This MATLAB code intends to solve the force on each elastic asperity between two semi-infinite surfaces. The mechanical interaction of asperities, asperities deformation and deformation of surrounding rock are all included.

```
%%%%%%%%%%%%%%%%%%%%%%%%%%%%%%%%%%%%%%%%%%%%%%%%%%%%%%%%%%%%%%%%%%%%%%%%%%%%

function result = TESTI(h,position,step)
%NOTE: the commented variables entail input in advance!

% test I case with 50 asperity in a row
N = length(h);    % number of asperities
%position = 0:2.5:2.5*N;
%h = 3.5;

C = zeros(N,N);
for i = 1:N     % the order of asperity
    for j = 1:i
        Length = sqrt((position(i,1)-position(j,1))^2+(position(i,2)-
position(j,2))^2);
        [dii_bar, dij_bar,
Delta_h]=displacement_component(Length,h(i));
        if i == j
            C(i,j) = Delta_h + 2*dii_bar;
        else
            C(i,j) = 2*dij_bar;
        end
    end
end
C = C' + C;
C(1:N+1:end) = diag(C)/2;

d = step;

force = quadprog(C,[],-C,max(h)-d-h);

result = sum(force);   %total force

end

%%%%%%%%%%%%%%%%%%%%%%%%%%%%%%%%%%%%%%%%%%%%%%%%%%%%%%%%%%%%%%%%%%%%%%%%%%%%

function [dii_bar, dij_bar, Delta_h]=displacement_component(R,h)


a = 0.5;    %radius of asperity, mm
v = 0.25;  %Poisson's ratio
E1 = 20;   %Young's modulus of inifite plate, GPa
E2 = 20;  % Young's modulus of disk, GPa
%R = 5;      % length between centers of asperity, mm
f = 1;      % the force, kN
%h = 3;      % initial height of asperity, mm
```

```
N = 12;     % Gaussian quadrature points
if R == 0
    R1 = 0;
else
    R1 = R-a;
end
R2 = R+a;
[theta,w1]=lgwt(N,0,pi/2);
[r,w2]=lgwt(N,R1,R2);
dij = 0;     % units: mm
dii = 0;     % units: mm

for i=1:N     %theta
    for j=1:N    %r
        if R == 0
            dii = dii + w2(j)*2*pi*r(j)*4*(1-
v^2)*f/(pi^2*a*E1)*w1(i)*sqrt(1-r(j)^2/a^2*sin(theta(i))^2);
        else
            dij = dij + w2(j)*2*r(j)*acos((R^2+r(j)^2-
a^2)/(2*R*r(j)))*4*(1-v^2)*f*r(j)/(pi^2*E1*a^2) ...
                  *w1(i)*(sqrt(1-a^2/r(j)^2*sin(theta(i))^2)-(1-
a^2/r(j)^2)/sqrt(1-a^2/r(j)^2*sin(theta(i))^2));
        end
    end
end

dij_bar = dij/(pi*a^2);
dii_bar = dii/(pi*a^2);
Delta_h = f*h/(pi*a^2*E2);

end
```

BIBLIOGRAPHY

1. Muffler, L., *Tectonic and hydrologic control of the nature and distribution of geothermal resources.* Geo-Heat Center Quarterly Bulletin;(United States), 1993. **15**(2).

2. Luo, J., et al., *Experimental investigation of the hydraulic and heat-transfer properties of artificially fractured granite.* Scientific reports, 2017. **7**: p. 39882.

3. Isaka, B.L.A., et al., *An Influence of Thermally-Induced Micro-Cracking under Cooling Treatments: Mechanical Characteristics of Australian Granite.* Energies, 2018. **11**(6): p. 1338.

4. Zhu, D., et al., *Experimental study on the damage of granite by acoustic emission after cyclic heating and cooling with circulating water.* Processes, 2018. **6**(8): p. 101.

5. McDermott, C. and O. Kolditz. *Hydraulic-geomechanical effective stress model: determination of discrete fracture network parameters from a pump test and application to geothermal reservoir modelling*. in *Proc. 29th Workshop on Geothermal Reservoir Engineering, Stanford, California, pp SGP-TR-175*. 2004.

6. Tran, D.V.D., *Effects of Thermally-Induced Secondary Cracks on Hydraulic Fractures*. 2013, University of Calgary.

7. Chen, T.S. and R.L. Marovelli, *Analysis of stresses in a rock disk subjected to peripheral thermal shock.* Rep. Invest.-US, Bur. Mines;(United States), 1966. **6823**.

8. Perkins, T. and J. Gonzalez, *The effect of thermoelastic stresses on injection well fracturing.* Society of Petroleum Engineers Journal, 1985. **25**(01): p. 78-88.

9. Kocabas, I. *An analytical model of temperature and stress fields during cold water injection into an oil reservoir*. in *Abu Dhabi International Conference and Exhibition*. 2004. Society of Petroleum Engineers.

10. Ghassemi, A., S. Tarasovs, and A.D. Cheng, *Integral equation solution of heat extraction-induced thermal stress in enhanced geothermal reservoirs.* International journal for numerical and analytical methods in geomechanics, 2005. **29**(8): p. 829-844.

11. Ogilvie, S., et al., *Characterization of rough-walled fractures in crystalline rocks.* Geological Society, London, Special Publications, 2003. **214**(1): p. 125-141.

12. Nolte, D. and L. Pyrak-Nolte, *Stratified continuum percolation: Scaling geometry of hierarchical cascades.* Physical Review A, 1991. **44**(10): p. 6320.

13. Hopkins, D., *The implications of joint deformation in analyzing the properties and behavior of fractured rock masses, underground excavations, and faults.* International Journal of Rock Mechanics and Mining Sciences, 2000. **37**(1-2): p. 175-202.

14. Brown, S.R., R.L. Kranz, and B.P. Bonner, *Correlation between the surfaces of natural rock joints.* Geophysical Research Letters, 1986. **13**(13): p. 1430-1433.

15. Brown, S.R. and C.H. Scholz, *Broad bandwidth study of the topography of natural rock surfaces.* Journal of Geophysical Research: Solid Earth, 1985. **90**(B14): p. 12575-12582.

16. Yoshioka, N. and C.H. Scholz, *Elastic properties of contacting surfaces under normal and shear loads: 1. Theory.* Journal of Geophysical Research: Solid Earth, 1989. **94**(B12): p. 17681-17690.

17. Yoshioka, N. and C.H. Scholz, *Elastic properties of contacting surfaces under normal and shear loads: 2. Comparison of theory with experiment.* Journal of Geophysical Research: Solid Earth, 1989. **94**(B12): p. 17691-17700.

18. Amadei, B. and T. Illangasekare. *A mathematical model for flow and solute transport in non-homogeneous rock fractures*. in *International Journal of Rock Mechanics and Mining Sciences & Geomechanics Abstracts*. 1994. Elsevier.

19. Brown, S.R., *Simple mathematical model of a rough fracture.* Journal of Geophysical Research: Solid Earth, 1995. **100**(B4): p. 5941-5952.

20. Wang, J. and T.N. Narasimhan, *Hydrologic mechanisms governing fluid flow in a partially saturated, fractured, porous medium.* Water Resources Research, 1985. **21**(12): p. 1861-1874.

21. Glover, P., et al., *Synthetic rough fractures in rocks.* Journal of Geophysical Research: Solid Earth, 1998. **103**(B5): p. 9609-9620.

22. Pyrak-Nolte, L. and J. Morris, *Single fractures under normal stress: The relation between fracture specific stiffness and fluid flow*. International Journal of Rock Mechanics and Mining Sciences, 2000. **37**(1-2): p. 245-262.

23. Saupe, D., *Algorithms for random fractals*, in *The science of fractal images*. 1988, Springer. p. 71-136.

24. Russ, J.C., *Fractal surfaces*. 2013: Springer Science & Business Media.

25. Brown, S.R. and C.H. Scholz, *Closure of random elastic surfaces in contact.* Journal of Geophysical Research: Solid Earth, 1985. **90**(B7): p. 5531-5545.

26. Båth, B., *Spectral analysis in geophysics*. 2012: Elsevier.

27. Power, W. and T. Tullis, *Review of the fractal character of natural fault surfaces with implications for friction and the evolution of fault zones*, in *Fractals in the Earth Sciences*. 1995, Springer. p. 89-105.

28. Power, W.L. and T.E. Tullis, *The contact between opposing fault surfaces at Dixie Valley, Nevada, and implications for fault mechanics.* Journal of Geophysical Research: Solid Earth, 1992. **97**(B11): p. 15425-15435.

29. Isakov, E., P. Glover, and S. Ogilvie. *Use of synthetic fractures in the analysis of natural fracture apertures*. in *8th European Congress for Stereology and Image Analysis, 8th ECS & IA*. 2001. Leeds.

30. Bendat, J.S. and A.G. Piersol, *Random data: analysis and measurement procedures*. Vol. 729. 2011: John Wiley & Sons.

31. Méheust, Y. and J. Schmittbuhl, *Scale effects related to flow in rough fractures.* Pure and Applied Geophysics, 2003. **160**(5-6): p. 1023-1050.

32. Xie, H., J.-a. Wang, and E. Stein, *Direct fractal measurement and multifractal properties of fracture surfaces.* Physics letters A, 1998. **242**(1-2): p. 41-50.

33. Mandelbrot, B.B., *The fractal geometry of nature*. Vol. 173. 1983: WH freeman New York.

34. Stanley, H.E., *Phase transitions and critical phenomena*. 1971: Clarendon Press, Oxford.

35. Aharony, A., *Percolation, fractals, and anomalous diffusion.* Journal of Statistical Physics, 1984. **34**(5-6): p. 931-939.

36. Salat, H., R. Murcio, and E. Arcaute, *Multifractal methodology.* Physica A: Statistical Mechanics and its Applications, 2017. **473**: p. 467-487.

37. Leyton-Pavez, C., et al., *Fractal analysis of growing cities and its relationship with health centre distribution.* Труды Института системного программирования РАН, 2017. **29**(2).

38. Kirkpatrick, S., *Percolation and conduction.* Reviews of modern physics, 1973. **45**(4): p. 574.

39. Pike, G. and C. Seager, *Percolation and conductivity: A computer study. I.* Physical review B, 1974. **10**(4): p. 1421.

40. Schmittbuhl, J., F. Schmitt, and C. Scholz, *Scaling invariance of crack surfaces.* Journal of Geophysical Research: Solid Earth, 1995. **100**(B4): p. 5953-5973.

41. Heitjans, P. and J. Kärger, *Diffusion in condensed matter: methods, materials, models*. 2006: Springer Science & Business Media.

42. AN, K., *The local structure of turbulence in a compressible liquid for very large Reynolds numbers.* CR (Dokl) Acad Sci URSS, 1941. **30**: p. 301-305.

43. de Godoy Stênico, J.W. and L.L. Ling, *Modern network traffic modeling based on binomial multiplicative cascades.* The Journal of Supercomputing, 2015. **71**(5): p. 1712-1735.

44. Council, N.R., *Rock fractures and fluid flow: contemporary understanding and applications*. 1996: National Academies Press.

45. Pyrak-Nolte, L.J. and D.D. Nolte, *Approaching a universal scaling relationship between fracture stiffness and fluid flow.* Nature communications, 2016. **7**: p. 10663.

46. Meakin, P., et al., *Scaling properties for the surfaces of fractal and nonfractal objects: An infinite hierarchy of critical exponents.* Physical Review A, 1986. **34**(4): p. 3325.

47. Meakin, P., *Invasion percolation and invading Eden growth on multifractal lattices.* Journal of Physics A: Mathematical and General, 1988. **21**(17): p. 3501.

48. Redner, S., *Random multiplicative processes: An elementary tutorial.* American Journal of Physics, 1990. **58**(3): p. 267-273.

49. de Arcangelis, L., S. Redner, and A. Coniglio, *Anomalous voltage distribution of random resistor networks and a new model for the backbone at the percolation threshold.* Physical Review B, 1985. **31**(7): p. 4725.

50. Muralidharan, V., et al. *Investigating fracture aperture distributions under various stress conditions using X-ray CT scanner*. in *Canadian International Petroleum Conference*. 2004. Petroleum Society of Canada.

51. Pyrak-Nolte, L.J., N.G. Cook, and D.D. Nolte, *Fluid percolation through single fractures.* Geophysical Research Letters, 1988. **15**(11): p. 1247-1250.

52. Archard, J., *Contact and rubbing of flat surfaces.* Journal of applied physics, 1953. **24**(8): p. 981-988.

53. Archard, J., *Elastic deformation and the laws of friction.* Proceedings of the Royal Society of London. Series A. Mathematical and Physical Sciences, 1957. **243**(1233): p. 190-205.

54. Dyson, J. and W. Hirst, *The true contact area between solids.* Proceedings of the Physical Society. Section B, 1954. **67**(4): p. 309.

55. Halliday, J., *Surface examination by reflection electron microscopy.* Proceedings of the Institution of Mechanical Engineers, 1955. **169**(1): p. 777-787.

56. Greenwood, J. and J.P. Williamson, *Contact of nominally flat surfaces.* Proceedings of the royal society of London. Series A. Mathematical and physical sciences, 1966. **295**(1442): p. 300-319.

57. Williamson, J. and R.T. Hunt, *Asperity persistence and the real area of contact between rough surfaces.* Proceedings of the Royal Society of London. A. Mathematical and Physical Sciences, 1972. **327**(1569): p. 147-157.

58. Pullen, J. and J. Williamson, *On the plastic contact of rough surfaces.* Proceedings of the Royal Society of London. A. Mathematical and Physical Sciences, 1972. **327**(1569): p. 159-173.

59. Gangi, A.F. *Variation of whole and fractured porous rock permeability with confining pressure*. in *International Journal of Rock Mechanics and Mining Sciences & Geomechanics Abstracts*. 1978. Elsevier.

60. Timoshenko SP, G.J., *Theory of Elasticity*. 3rd edn. ed. 1970, New York Toronto London: McGraw-Hill International Book Company.

61. Bertani, R., *Geothermal power generation in the world 2010–2014 update report.* Geothermics, 2016. **60**: p. 31-43.

62. Tester, J.W., et al., *The future of geothermal energy: Impact of enhanced geothermal systems (EGS) on the United States in the 21st century.* Massachusetts Institute of Technology, 2006. **209**.

63. Zeng, Y.-C., Z. Su, and N.-Y. Wu, *Numerical simulation of heat production potential from hot dry rock by water circulating through two horizontal wells at Desert Peak geothermal field.* Energy, 2013. **56**: p. 92-107.

64. Zeng, Y.-C., et al., *Numerical simulation of heat production potential from hot dry rock by water circulating through a novel single vertical fracture at Desert Peak geothermal field.* Energy, 2013. **63**: p. 268-282.

65. Cheng, W.-L., et al., *Analysis of influencing factors of heat extraction from enhanced geothermal systems considering water losses.* Energy, 2016. **115**: p. 274-288.

66. Mohan, A.R., et al., *Utilization of carbon dioxide from coal-based power plants as a heat transfer fluid for electricity generation in enhanced geothermal systems (EGS).* Energy, 2013. **57**: p. 505-512.

67. White, M., et al., *A suite of benchmark and challenge problems for enhanced geothermal systems.* Geomechanics and Geophysics for Geo-Energy and Geo-Resources, 2018. **4**(1): p. 79-117.

68. Hadgu, T., E. Kalinina, and T.S. Lowry, *Modeling of heat extraction from variably fractured porous media in Enhanced Geothermal Systems.* Geothermics, 2016. **61**: p. 75-85.

69. Jiang, F., et al., *A three-dimensional transient model for EGS subsurface thermo-hydraulic process.* Energy, 2014. **72**: p. 300-310.

70. Borgia, A., et al., *Numerical simulation of salt precipitation in the fractures of a CO2-enhanced geothermal system.* Geothermics, 2012. **44**: p. 13-22.

71. McClure, M. and R. Horne, *Opening mode stimulation or shear stimulation.* Geothermal Resources Council Transactions, 2012. **36**: p. 515-522.

72. Williams, C.F. and J. DeAngelo. *Developing improved methods for the assessment of Enhanced Geothermal Systems*. in *Proceedings, Fourtieth Workshop on Geothermal Reservoir Engineering*. 2015.

73. Pandey, S., A. Chaudhuri, and S. Kelkar, *A coupled thermo-hydro-mechanical modeling of fracture aperture alteration and reservoir deformation during heat extraction from a geothermal reservoir.* Geothermics, 2017. **65**: p. 17-31.

74. Bruel, D., *Impact of induced thermal stresses during circulation tests in an engineered fractured geothermal reservoir: example of the Soultz-sous-Forets European hot fractured rock geothermal project, Rhine Graben, France.* Oil & Gas Science and Technology, 2002. **57**(5): p. 459-470.

75. Tarasovs, S. and A. Ghassemi. *Propagation of a system of cracks under thermal stress*. in *45th US Rock Mechanics/Geomechanics Symposium*. 2011. American Rock Mechanics Association.

76. Finnie, I., G. Cooper, and J. Berlie. *Fracture propagation in rock by transient cooling*. in *International Journal of Rock Mechanics and Mining Sciences & Geomechanics Abstracts*. 1979. Elsevier.

77. Barr, D.T., *Thermal cracking in nonporous geothermal reservoirs*. 1980, Massachusetts Institute of Technology.

78. Murphy, H.D., *Thermal stress cracking and the enhancement of heat extraction from fractured geothermal reservoirs*. 1978, Los Alamos Scientific Lab., N. Mex.(USA).

79. McClure, M.W., *Modeling and characterization of hydraulic stimulation and induced seismicity in geothermal and shale gas reservoirs*. 2012, Stanford University Stanford.

80. Ameli, P., J.E. Elkhoury, and R.L. Detwiler, *High-resolution fracture aperture mapping using optical profilometry.* Water Resources Research, 2013. **49**(10): p. 7126-7132.

81. Ghassemi, A. and G.S. Kumar, *Changes in fracture aperture and fluid pressure due to thermal stress and silica dissolution/precipitation induced by heat extraction from subsurface rocks.* Geothermics, 2007. **36**(2): p. 115-140.

82. Tang, C., et al., *Numerical studies of the influence of microstructure on rock failure in uniaxial compression—part I: effect of heterogeneity.* International Journal of Rock Mechanics and Mining Sciences, 2000. **37**(4): p. 555-569.

83. Valley, B. and K.F. Evans. *Stress state at Soultz-sous-Forêts to 5 km depth from wellbore failure and hydraulic observations*. in *Proceedings, 32nd workshop on geothermal reservoir engineering*. 2007.

84. Dezayes, C., A. Genter, and B. Valley, *Structure of the low permeable naturally fractured geothermal reservoir at Soultz.* Comptes Rendus Geoscience, 2010. **342**(7-8): p. 517-530.

85. Ashby, M. and C. Sammis, *The damage mechanics of brittle solids in compression.* Pure and Applied Geophysics, 1990. **133**(3): p. 489-521.

86. Lockner, D. *The role of acoustic emission in the study of rock fracture*. in *International Journal of Rock Mechanics and Mining Sciences & Geomechanics Abstracts*. 1993. Elsevier.

87. Lemaitre, J., *A continuous damage mechanics model for ductile fracture.* Journal of engineering materials and technology, 1985. **107**(1): p. 83-89.

88. Hawkes, I., M. Mellor, and S. Gariepy. *Deformation of rocks under uniaxial tension*. in *International Journal of Rock Mechanics and Mining Sciences & Geomechanics Abstracts*. 1973. Elsevier.

89. Okubo, S. and K. Fukui. *Complete stress-strain curves for various rock types in uniaxial tension*. in *International journal of rock mechanics and mining sciences & geomechanics abstracts*. 1996. Elsevier.

90. Tapponnier, P. and W. Brace. *Development of stress-induced microcracks in Westerly granite*. in *International Journal of Rock Mechanics and Mining Sciences & Geomechanics Abstracts*. 1976. Elsevier.

91. Tang, C.A. and J.A. Hudson, *Rock failure mechanisms: explained and illustrated*. 2010: CRC.

92. Yang, S., et al., *Experimental investigation on strength and failure behavior of pre-cracked marble under conventional triaxial compression.* International Journal of Solids and Structures, 2008. **45**(17): p. 4796-4819.

93. Lockner, D.A., *A generalized law for brittle deformation of Westerly granite.* Journal of Geophysical Research: Solid Earth, 1998. **103**(B3): p. 5107-5123.

94. Jaeger, J.C., N.G. Cook, and R. Zimmerman, *Fundamentals of rock mechanics*. 2009: John Wiley & Sons.

95. Greenwood, J. and J.P. Williamson, *Contact of nominally flat surfaces.* Proc. R. Soc. Lond. A, 1966. **295**(1442): p. 300-319.

96. Beeler, N. and S. Hickman, *A note on contact stress and closure in models of rock joints and faults.* Geophysical research letters, 2001. **28**(4): p. 607-610.

97. Gelet, R., B. Loret, and N. Khalili, *Thermal recovery from a fractured medium in local thermal non-equilibrium.* International Journal for Numerical and Analytical Methods in Geomechanics, 2013. **37**(15): p. 2471-2501.

98. Zeng, C. and W. Deng, *The effect of radial cracking on the integrity of asperity under thermal unloading process.* In the 52th US Symposium on Rock Mechanics, 2018.

99. Kamali-Asl, A., et al., *Experimental study of fracture response in granite specimens subjected to hydrothermal conditions relevant for enhanced geothermal systems.* Geothermics, 2018. **72**: p. 205-224.

100. Rutqvist, J., *Fractured rock stress-permeability relationships from in situ data and effects of temperature and chemical-mechanical couplings.* Geofluids, 2015. **15**(1-2): p. 48-66.

101. Kumari, W., et al., *Temperature-dependent mechanical behaviour of Australian Strathbogie granite with different cooling treatments.* Engineering Geology, 2017. **229**: p. 31-44.

102. Sharifzadeh, M., Y. Mitani, and T. Esaki, *Rock joint surfaces measurement and analysis of aperture distribution under different normal and shear loading using GIS.* Rock Mechanics and Rock Engineering, 2008. **41**(2): p. 299.

103. Dezayes, C., A. Genter, and G.R. Hooijkaas. *Deep-seated geology and fracture system of the EGS Soultz reservoir (France) based on recent 5km depth boreholes*. in *Proceedings World Geothermal Congress*. 2005.

104. Norbeck, J.H., M.W. McClure, and R.N. Horne, *Field observations at the Fenton Hill enhanced geothermal system test site support mixed-mechanism stimulation.* Geothermics, 2018. **74**: p. 135-149.

105. Ye, Z. and A. Ghassemi. *Experimental study on injection-induced fracture propagation and coalescence for EGS stimulation*. in *43rd Workshop on Geothermal Reservoir Engineering. Stanford, CA, USA*. 2018.

106. Zimmerman, R.W. and G.S. Bodvarsson, *Hydraulic conductivity of rock fractures.* Transport in porous media, 1996. **23**(1): p. 1-30.

107. Vilarrasa, V., A.P. Rinaldi, and J. Rutqvist, *Long-term thermal effects on injectivity evolution during CO2 storage.* International Journal of Greenhouse Gas Control, 2017. **64**: p. 314-322.

108. Barton, N., S. Bandis, and K. Bakhtar. *Strength, deformation and conductivity coupling of rock joints*. in *International journal of rock mechanics and mining sciences & geomechanics abstracts*. 1985. Elsevier.

109. David, C., B. Menéndez, and M. Darot, *Influence of stress-induced and thermal cracking on physical properties and microstructure of La Peyratte granite.* International Journal of Rock Mechanics and Mining Sciences, 1999. **36**(4): p. 433-448.

110. Andersson, J.C., C.D. Martin, and H. Stille, *The Äspö pillar stability experiment: part II—rock mass response to coupled excavation-induced and thermal-induced stresses.* International Journal of Rock Mechanics and Mining Sciences, 2009. **46**(5): p. 879-895.

111. Hettema, M., K.A. Wolf, and C. De Pater, *The influence of steam pressure on thermal spalling of sedimentary rock: theory and experiments.* International Journal of Rock Mechanics and Mining Sciences, 1998. **35**(1): p. 3-15.

112. Wu, C., et al. *Probabilistic modeling of bond behavior of enamel coated steel to mortar*. in *Proceedings of the 2012 Joint Conference of the Engineering Mechanics Institute and the 11th ASCE Joint Specialty Conference on Probabilistic Mechanics and Structural Reliability*. 2012.

113. Tang, C., et al., *Analysis of crack coalescence in rock-like materials containing three flaws—part II: numerical approach.* International Journal of Rock Mechanics and Mining Sciences, 2001. **38**(7): p. 925-939.

114. Lee, S. and A. Ghassemi. *A three-dimensional thermo-poro-mechanical finite element analysis of a wellbore on damage evolution*. in *44th US Rock Mechanics Symposium and 5th US-Canada Rock Mechanics Symposium*. 2010. American Rock Mechanics Association.

115. Min, K.S. and A. Ghassemi. *Simulation of fracture clusters in unconventional reservoir using fully coupled thermo-hydro-mechanical FEM analysis*. in *46th US Rock Mechanics/Geomechanics Symposium*. 2012. American Rock Mechanics Association.

116. Yu, Q., et al., *A mesostructure-based damage model for thermal cracking analysis and application in granite at elevated temperatures.* Rock Mechanics and Rock Engineering, 2015. **48**(6): p. 2263-2282.

117. TANG, C.A., et al., *Influence of Heterogeneity on Crack Propaga-Tion Mode in Brittle Rock.* Chinese Journal of Geophysics, 2000. **43**(1): p. 117-125.

118. Verly, G., *Sequential Gaussian simulation: a Monte Carlo method for generating models of porosity and permeability*, in *Generation, Accumulation and Production of Europe's Hydrocarbons III*. 1993, Springer. p. 345-356.

119. Liu, H., et al., *Numerical studies on the failure process and associated microseismicity in rock under triaxial compression.* Tectonophysics, 2004. **384**(1-4): p. 149-174.

120. Lajtai, E. and L. Bielus, *Stress corrosion cracking of Lac du Bonnet granite in tension and compression.* Rock Mechanics and Rock Engineering, 1986. **19**(2): p. 71-87.

121. Mavko, G., T. Mukerji, and J. Dvorkin, *The rock physics handbook: Tools for seismic analysis of porous media*. 2009: Cambridge university press.

122. Ludovico-Marques, M., C. Chastre, and G. Vasconcelos, *Modelling the compressive mechanical behaviour of granite and sandstone historical building stones.* Construction and Building Materials, 2012. **28**(1): p. 372-381.

123. Salim, N.A.M., Z. Mohamed, and M.N. Berhan, *The Effect of Cyclic Stress on the Strain and Microstructure of Weathered Granite*, in *InCIEC 2015*. 2016, Springer. p. 287-299.

124. Nur, A., et al., *Critical porosity: A key to relating physical properties to porosity in rocks.* The Leading Edge, 1998. **17**(3): p. 357-362.

125. Mukerji, T., et al., *Differential effective medium modeling of rock elastic moduli with critical porosity constraints.* Geophysical Research Letters, 1995. **22**(5): p. 555-558.

126. Weibull, W., *A statistical distribution function of wide applicability.* Journal of applied mechanics, 1951. **18**(3): p. 293-297.

127. Mahabadi, O., B. Tatone, and G. Grasselli, *Influence of microscale heterogeneity and microstructure on the tensile behavior of crystalline rocks.* Journal of Geophysical Research: Solid Earth, 2014. **119**(7): p. 5324-5341.

128. Brace, N., M. Voegle, and H. Pratt, *Porosity. Permeability, and their Relationship in Granite. Basalt, and Tuff*. 1982, ONWI/E512-02900/TR-10, report prepared for Office of Nuclear Waste Isolation, Battelle Memorial Institute, Columbus, OH, October.

129. Watson, G., *On chi-square goodness-of-fit tests for continuous distributions.* Journal of the Royal Statistical Society. Series B (Methodological), 1958: p. 44-72.

130. Pandey, S. and V. Vishal, *Sensitivity analysis of coupled processes and parameters on the performance of enhanced geothermal systems.* Scientific reports, 2017. **7**(1): p. 17057.

131. Johnson, K.L. and K.L. Johnson, *Contact mechanics*. 1987: Cambridge university press.

132. Breede, K., et al., *A systematic review of enhanced (or engineered) geothermal systems: past, present and future.* Geothermal Energy, 2013. **1**(1): p. 4.

133. Yang, S.-Q., et al., *An experimental investigation on thermal damage and failure mechanical behavior of granite after exposure to different high temperature treatments.* Geothermics, 2017. **65**: p. 180-197.

134. Settari, A. and G. Warren. *Simulation and field analysis of waterflood induced fracturing*. in *Rock Mechanics in Petroleum Engineering*. 1994. Society of Petroleum Engineers.

135. Koutsabeloulis, N. and S. Hope. *" Coupled" Stress/Fluid/Thermal Multi-Phase Reservoir Simulation Studies Incorporating Rock Mechanics*. in *SPE/ISRM Rock Mechanics in Petroleum Engineering*. 1998. Society of Petroleum Engineers.

136. Watanabe, N., N. Hirano, and N. Tsuchiya, *Determination of aperture structure and fluid flow in a rock fracture by high-resolution numerical modeling on the basis of a flow-through experiment under confining pressure.* Water Resources Research, 2008. **44**(6).

137. Caulk, R.A., et al., *Experimental investigation of fracture aperture and permeability change within Enhanced Geothermal Systems.* Geothermics, 2016. **62**: p. 12-21.

138. Pyrack-Nolte, L., et al., *Hydraulic and mechanical properties of natural fractures in low-permeability rock.* 1987, Lawrence Berkeley Lab., CA (USA).

139. Pruess, K., J. Wang, and Y. Tsang, *On thermohydrologic conditions near high-level nuclear wastes emplaced in partially saturated fractured tuff: 1. Simulation studies with explicit consideration of fracture effects.* Water Resources Research, 1990. **26**(6): p. 1235-1248.

140. Hu, L., et al. *Laboratory Scale Investigation of Enhanced Geothermal Reservoir Stimulation*. in *50th US Rock Mechanics/Geomechanics Symposium*. 2016. American Rock Mechanics Association.

141. Durham, W.B., W.L. Bourcier, and E.A. Burton, *Direct observation of reactive flow in a single fracture.* Water Resources Research, 2001. **37**(1): p. 1-12.

142. Cook, N.G. *Natural joints in rock: mechanical, hydraulic and seismic behaviour and properties under normal stress*. in *International Journal of Rock Mechanics and Mining Sciences & Geomechanics Abstracts*. 1992. Elsevier.

143. Yasuhara, H., D. Elsworth, and A. Polak, *Evolution of permeability in a natural fracture: Significant role of pressure solution.* Journal of Geophysical Research: Solid Earth, 2004. **109**(B3).

144. Taron, J., D. Elsworth, and K.-B. Min, *Numerical simulation of thermal-hydrologic-mechanical-chemical processes in deformable, fractured porous media.* International Journal of Rock Mechanics and Mining Sciences, 2009. **46**(5): p. 842-854.

145. Lang, P., A. Paluszny, and R. Zimmerman, *Hydraulic sealing due to pressure solution contact zone growth in siliciclastic rock fractures.* Journal of Geophysical Research: Solid Earth, 2015. **120**(6): p. 4080-4101.

146. Bond, A.E., et al., *Development of approaches for modelling coupled thermal–hydraulic–mechanical–chemical processes in single granite fracture experiments.* Environmental Earth Sciences, 2016. **75**(19): p. 1313.

147. Chiappetta, L. and D.R. Sobel, *The temperature distribution within a hemisphere exposed to a hot gas stream.* SIAM Review, 1984. **26**(4): p. 575-577.

148. Ashby, M.F. and D.R.H. Jones, *Engineering materials 1: an introduction to properties, applications and design*. Vol. 1. 2012: Elsevier.

149. Fett, T. and D. Munz, *Stress intensity factors and weight functions*. Vol. 1. 1997: Computational Mechanics.

150. Hutchinson, J.W. and Z. Suo, *Mixed mode cracking in layered materials*, in *Advances in applied mechanics*. 1991, Elsevier. p. 63-191.

151. Ševeček, O., et al., *Assessment of crack-related problems in layered ceramics using the finite fracture mechanics and coupled stress-energy criterion.* Procedia Structural Integrity, 2016. **2**: p. 2014-2021.

152. Goodman, R.E., R.L. Taylor, and T.L. Brekke, *A model for the mechanics of jointed rock.* Journal of Soil Mechanics & Foundations Div, 1968.

153. Goodman, R.E., *Methods of geological engineering in discontinuous rocks*. 1976.

VITA

Chao Zeng began his college study in September 2008 and received a Bachelor of Engineering in Petroleum Engineering from the China University of Petroleum-Beijing in 2012. He continued his studies as a master's student and then received a Master of Science in Oil and Gas Well Engineering from the China University of Petroleum-Beijing in 2015. In August 2015, he began his doctoral studies at Missouri S&T, and focused on the research topics of geotechnical engineering, geomechanics and hydrology. He received the Doctor of Philosophy in Civil Engineering from Missouri University of Science and Technology in December 2019.